Title
Inhibitory pathways in the neocortical microcircuit

Author
Naka, Alexander

Publication Date
2018

Peer reviewed|Thesis/dissertation

Inhibitory pathways in the neocortical microcircuit

By

Alexander S. Naka

A dissertation submitted in partial satisfaction of the

requirements for the degree of

Doctor of Philosophy

in

Neuroscience

in the

Graduate Division

of the

University of California, Berkeley

Committee in charge:

Dr. Hillel Adesnik, Chair
Dr. Daniel Feldman
Dr. Yang Dan
Dr. Polina Lishko

Spring 2018

Abstract

Inhibitory pathways in the neocortical microcircuit

By

Alexander S. Naka

Doctor of Philosophy in Molecular and Cell Biology

University of California, Berkeley

Professor Hillel Adesnik, Chair

Understanding how the canonical circuit implements computations requires that we characterize the components of the circuit and determine how they interact. Cortical components are often equated to the various classes of excitatory and inhibitory neuronal cell-types that occupy the six cortical layers. Excitatory cortical neurons are known to exhibit stereotyped, cell-type specific patterns of connectivity; these excitatory synaptic pathways are a central feature of cortical organization. It has been less clear whether inhibitory neurons are organized according to a similar logic. In this thesis I describe my efforts to map the inhibitory pathways of the neocortex, using the mouse primary somatosensory barrel cortex as a model.

In Chapter 1, I will give an introduction to theories of cortical function and general overview of the organization of cortical circuits. I will also provide a focused review of the inhibitory circuitry in layer 5 of the cortex. This chapter is presented, in part, in the form of reproductions of material from two reviews (one published and one in preparation) that I co-authored with my advisor. In Chapter 2, I describe the discovery of a novel disynaptic inhibitory pathway between layer 4 and layer 5 of the somatosensory cortex, and present evidence that this pathway contributes to selective sensory representations in layer 5. This work is presented as a published manuscript, which I co-authored with Dr. Scott Pluta. In Chapter 3, I describe a series of experiments probing the organization of two subnetworks of dendrite-targeting interneurons. These subnetworks exhibit complementary patterns of connectivity which enable them to differentially modulate the dynamics of cortical activity in a layer-specific manner. This work is presented as a first author manuscript (currently in review). Finally, in Chapter 4 I offer closing thoughts and directions for future work.

Preface

Table of Contents

Acknowledgments

As I approach the final pages of this chapter in my life, it's immensely fulfilling to look back and reflect on how many incredible people have helped write it. Thank you first and foremost to my advisor Hillel. When I give talks, I'm fond of saying that "Hillel taught me half of everything I know." This is because it is true. In my time here, I've learned that there are many different approaches to doing science; one of the great pleasures (and challenges) of my time here has been finding my own style, while also coming to understand and appreciate the diverse scientific philosophies of the people around me. There can be no doubt that Hillel's approach is a special one. He attacks problems in a way that is fearless, tireless, and above all, creative and fun. Beyond this, he's been a great friend and mentor. It's clear that he cares deeply about his science and his people. I am so proud of what the lab has become, and it has been an enormous privilege and honor to have been a part of its formative years.

I've also been tremendously fortunate to benefit from the mentorship of many other people. I'm grateful to Dan Feldman for his invariably insightful advice. Perhaps most telling: when thinking about what my data mean or how to present my work, I have very often tried to imagine what kind of question Dan would ask me about it. Thank you to my committee members Yang Dan and Polina Lishko for their guidance on steering my project through the years. I'm also grateful to Marla Feller for her uncanny ability to offer feedback and encouragement at exactly the moments I've needed these. Thank you to John Ngai for his mentorship, especially during our collaboration. Special thanks also to my undergraduate mentor, Dave McLean, whose support and advice was instrumental in my formative experiences with independent research.

I'll take a somber moment to recognize that the study of the brain incurs a high cost in terms of animal life, and my own research is no exception. When laboratory mice are euthanized, it is common to call this a 'sacrifice.' This is not euphemism; there can be no truer sense of the word.

Throughout my doctorate, I've relied on funding from a number of public and private sources, for which I am extremely grateful. Special thanks to the National Institutes of Health, where I got my start in lab work over a decade ago, with help and guidance from Jim Battey and John Northup. I'm also extremely grateful to the National Institute of Neurological Disorders and Stroke, which sponsors the fellowship that has supported me for the past several years.

I owe many, many thanks to the fantastic community of the Helen Wills Neuroscience Institute. One memory that stands out in particular for me was a retreat in which a large number of the presenters (including the keynote speaker!) conspired to hide pictures of my face on their slides. I can imagine that this might be a really horrifying event in most professional environments, but it made me feel loved and appreciated. I think this really speaks to what kind of community we are; HWNI is truly something special. Huge thanks in particular to Candace Groskreutz, Tony Leonard, Kati Markowitz, Barbara Peterson, and Natalie Terranova, who have collectively helped me out of more jams than I can count.

I am incredibly lucky and thankful to have had so many wonderful people in my life as colleagues, friends, partners, and everything in between. For brevity, I list only their names here and do all the actual thanking in the endnotes at the end of this document. Thanks to: David Arroyo[A,B], Cameron Baker[C], Jenny Brown[D], Kelly Clancy[E,L], Rob Curtis[F], Desi Chu[G], Dennis DiGioia[H], Liz Dressler[I], Kevin Doxzen[J], Andrew Egladyous[G], Justin Elstrott, Sophia Espinoza[K], Charles Frye[B,L], Brian Gailey[H], Rich Hakim[G], Anna Headland, Brian Isett[M], Nick Jourjine[N], George Lin[O], Keven Laboy[B,M], Claire Lee, Amy LeMessurier[M], Evan Lyall[P,Q], Kim Long[R], Alan Mardinly[S], Dan Mossing[Q,T], Ryan Neely[B], Ian Oldenburg[U], Nico Pegard, Professor Scott Pluta[V], Lucy Portnoff[G], Elena Ryapolova[W], Sara Sheriff[X], Mike Silliman[Y], Ben Shababo[Z], Ben Snyder[G], Savitha Sridharan, David Taylor[G], Greg Telian[AA], Silvio Temprana, Ming-Chi Tsai[BB], Moe Turner[CC], Julia Veit[DD], Lucy

Yao[EE], the McElroy clan[FF] and the rest of my family[GG], my cohort[HH], my team[II], and many others[JJ]. I'm so indebted to all of you.

Lastly, thank you to my family. Thanks to my mom for teaching me to appreciate the living creatures of our planet. Thanks to my dad for nurturing my curiosity about the world. Thanks to both of you for teaching me to always try to do the right thing. Thank you to Betsy[KK] and my sisters Adalyn[LL], Naomi[MM], and Marie[JJ], for being constant sources of support, love, and laughter. I love you all so much more than words could ever convey. I strive to be better because of you.

Publications related to this work

1. Naka, A., Veit, J., Shababo, B., Snyder, B., Egladyous, A., Sridharan, S., Chu, D., Chesnov, K., Paninski, L., and Adesnik, H. (2018) Complementary subnetworks of neocortical somatostatin interneurons. *In review*
2. Adesnik, H., Naka. A., (2018) Cracking the function of cortical layers. *In preparation*
3. Naka, A. and Adesnik, H., (2016). Inhibitory circuits in cortical layer 5. *Frontiers in neural circuits*, 10.
4. Pluta, S.*, Naka, A.*, Veit, J., Telian, G., Yao, L., Hakim, R., Taylor, D., and Adesnik, H. (2015). A direct translaminar inhibitory circuit tunes cortical output. *Nature Neuroscience* 18 1631-1640
5. Naka, A. Cell-Type-Specific Manipulation Reveals New Specificity in the Neocortical Microcircuit (2015). *Journal of Neuroscience* 35(24):8976-8.

Chapter 1: Introduction

Reverse-engineering the neocortical microcircuit

The neocortex is thought to perform neural computations that underlie an enormous number of survival-essential functions, including perception, cognition, decision-making, and motor control. Despite this functional diversity, the neural circuits of the cortex appear to share a common cellular organization that is remarkably conserved between different regions of the cortex and across different mammalian species. One influential hypothesis posits that there exists a 'canonical' neocortical microcircuit: a flexible, generalized, modular circuit that serves as a building block for cortical computation (Douglas et al., 1989; Harris and Shepherd, 2015). Concretely, this circuit has often been conceptualized as a cortical column- a cylindrical volume of cortical tissue that contains a cross section through all the layers of the cortex. According to this hypothesis, the cortical sheet is essentially a crystalline lattice assembled from many repeating units of this circuit.

Optimism springs forth from this hypothesis. The complexity of the neocortex cannot be understated; neocortical circuits are an impenetrable jungle. The notion of a canonical circuit is so tantalizing because it carries the potential to be the simplifying abstraction that is so desperately needed. The hope is that by achieving a mechanistic understanding of the basic computational building block of the cortex, we might be able to 'build-up' toward a more generalized understanding of the cortical hierarchy at large. This pursuit requires that we understand how the various components of neocortical circuits cooperate to implement computation. Prerequisite to this are more basic questions. *What are the components of cortical circuits? How do they fit together?*

The layered structure of the neocortex is very likely at the heart to the answers of these questions. The layers of the cortex have long been understood to be a central feature of its organization. Cortical layers have long been known to host sets of neurons with profound anatomical and functional differences. Accordingly, in the original formulation of the canonical circuit, layers could be understood to be the components. More recently, the field's understanding of cortical organization has evolved past a focus on layers *per se* and toward a focus on cortical cell-types. Cortical neurons can be classified into a hierarchical taxonomy of cell-types. At the highest level of this hierarchy is the dichotomy between glutamatergic excitatory cells, which make up the bulk (~80%) of cortical neurons, and GABAergic inhibitory 'interneurons,' which make up the remainder of cortical neurons.

For excitatory cortical neurons, cell-type and layer are inextricably intertwined. While each layer harbors multiple excitatory cell-types, these cell-types are unique to their home layers; each excitatory cell-type lives in one and only one layer. It is less clear if the same is true for inhibitory interneurons, since interneurons which ostensibly share the same phenotype can be found in multiple layers. For example, very distinctive interneurons such as chandelier cells or Martinotti cells can be found both in L2/3 and L5 (Markram et al., 2004). This is perhaps in part explained by the very distinct developmental processes by which interneurons and excitatory neurons arrive in the cortex. As I will discuss in more depth below, our understanding of excitatory pathways in the cortex centers around the idea of layer-crossing or 'translaminar' synaptic pathways. However, the apparent disregard of inhibitory neurons for laminar boundaries, along with the emerging (if controversial) notion that inhibitory connectivity might be non-specific in general (Fino et al., 2013; Karnani et al., 2014), make it reasonable to ask: do analogous translaminar inhibitory pathways exist in the neocortex? If inhibitory circuits wire up irrespective of laminar boundaries, this would place important constraints on the functional roles of inhibition in cortical function. Alternatively, if

inhibitory pathways do exist, how are they organized? How might they contribute to cortical computation? These are the questions which have motivated my work over the last five years.

As a starting point, I will provide an introduction to theories of cortical function and an overview of the organization of cortical circuits across the different layers. I make heavy use of material from two review articles (co-authored with my advisor, Hillel Adesnik) in this section. The following section (**Cracking the function of cortical layers**) is a partial reproduction of our more recent review. This section will serve as an introduction to some of the conceptual frameworks that have shaped cortical sensory physiology. It also provides an overview of what is known about the neural circuitry of the different layers, with a particular focus on the excitatory circuits. It concludes with a discussion of the promises and perils of perturbative manipulations of cortical layers (the subject of Chapter 2). Following this section, I shift the focus toward layer 5 (the subject of most of my research) in the final section (**Inhibitory circuits of cortical layer 5**), which provides an overview of the major classes of inhibitory interneurons and a detailed look at inhibitory circuits in layer 5. I close this chapter with a discussion of the role of inhibition in cortical circuits and how inhibitory circuits might integrate with the excitatory pathways of the canonical microcircuit.

Cracking the function of cortical layers

Summary

Understanding how cortical activity generates sensory perceptions requires a detailed dissection of the function of cortical layers. Despite our relatively extensive knowledge of their anatomy and wiring, we have a limited grasp for what each layer contributes to cortical computation. We need to develop a theory of cortical function that is rooted solidly in each layer's component cell types and fine circuit architecture, and produces predictions that can be validated by specific perturbations. We will review existing data that support and explain what we do know, and suggest future experiments that can address what we do not. The new technologies that can crack the function of cortical layers are finally on the immediate horizon.

Adesnik, H., Naka. A., (2018) Cracking the function of cortical layers. *In preparation*

Introduction

> "At present we have no direct evidence on how the cortex transforms the incoming visual information. Ideally, one should determine the properties of a cortical cell, and then examine one by one the receptive fields of all the afferents projecting upon that cell." – Hubel and Wiesel, 1962, *Journal of Physiology*

A primary goal of cortical physiology is to explain how the cortex transforms incoming information to generate perceptions. Despite more than half a century since the above statement was made, a detailed understanding of cortical transformations across the cortical layers remains remarkably incomplete. However, recent technological advances finally allow for the execution of the experiment that Hubel and Wiesel prescribed, as well as many other sophisticated assays that can overcome this conceptual challenge. First, we review how existing data have motivated the available theories on the function of cortical layers, primarily with respect to sensory transformations. Next, we highlight the key data we lack that could confirm or invalidate these models or motivate new ones. Finally, we propose the new technologies and experiments that are needed to obtain the data that will allow us to arrive at a much more mechanistic, circuit-driven theory for the unique contributions of layer-specific circuits in sensory perception.

The cortical generation of sensory percepts can be thought of as a synthetic, hierarchical process, as one based largely in statistical inference, or as a mixture thereof. In the hierarchical model, neurons integrate their inputs to filter the sensory data, and transform it into an output spike train that encodes features of stimulus. A simple feed-forward architecture composed of many neurons filtering their input in this manner should ultimately enable complex computations to mediate object identification and scene analysis (Hubel and Wiesel, 1962; Marr, 1982). The apparent feed-forward architecture of the primate visual system might help explain why object recognition is fast (Thorpe et al., 1996). In the framework of statistical inference, cortical circuits encode a generative model of the sensory environment, and recurrent interactions between cortical processing stages compare the expectations of the internally generated model with incoming data from the sensory apparatus (Bastos et al., 2012).

Two of the most compelling examples of the synthetic process are the encoding of edge orientation in the primary visual cortex (Hubel and Wiesel, 1959, 1962), and that of object or face selectivity in the inferotemporal cortex (Bruce et al., 1981; Gross et al., 1972). The emergence of orientation tuning stands of one the few concrete examples of a *de novo* transformation that occurs in

a layer of the primary visual cortex (V1), and can be well-explained by a simple feed-forward model involving the integration over a specific set of center-surround thalamic relay neurons (Hubel and Wiesel, 1962). Although the mechanistic details of an analogous feed-forward circuit for the generation of face selectivity are lacking, one can conceptualize a similar process where neurons exhibiting increasingly sophisticated feature tuning are built by summating over neurons with more elementary filtering properties (e.g., edges to contours, and contours to faces)(Liu et al., 2016b).

While ample data collected across cortical areas is consistent with the synthetic model, this framework has provided remarkably few, if any compelling examples of *de novo* transformations that can be observed between cortical layers of a single sensory area, such as V1. Orientation tuning, direction selectivity, ocular dominance, and binocular disparity tuning are all observable within layer 4 neurons (Hubel and Wiesel, 1962; Sun et al., 2016). In other cortical areas, such as the somatosensory cortex, we have similarly little insight into the synthesis of new response properties among neurons even within layer 4 (Brecht, 2017). Receptive fields in the rodent barrel cortex of cat visual tend to grow or change sub-structure across layers (Brecht et al., 2003a; Martinez et al., 2005), and some evidence supports the *de novo* generation of complex cells and contextual properties such as end-stopping between L4 and L2/3 in cats (Alonso and Martinez, 1998; Hubel and Wiesel, 1962; Martinez and Alonso, 2001). Yet the striking lack of concrete examples akin to orientation tuning implies that the laminar circuity in a single cortical area is not set up to generate new types of feature selectivity. Alternatively, the synthetic model fails to capture these transformations, despite its success in artificial neural networks (Fukushima, 1980; Hassabis et al., 2017). Furthermore, this framework fails to account for a wide range of context-dependent phenomena observed in cortical activity, nor does it provide a compelling explanation for the profuse amount of feedback connections from higher cortical areas to lower ones.

In contrast, the alternative framework that sees sensory processing as probabilistic inference can explain these 'top down' phenomena. In this scheme neurons in different cortical layers have unique roles to play in computing the conditional probabilities that a given pattern of afferent neural input represents a specific sensory stimulus (Bastos et al., 2012; Rao and Ballard, 1999). The core notion is that cortical neurons, moment to moment, compare afferent input from each preceding stage with an internal generative model of the sensory environment, a model based on both the recent past and accumulated experience. Predictions of this model are passed from higher to lower stages (both across layers in individual areas and between areas) through feedback connections, and neurons in preceding stages compare these predictions to errors indicated by deviation from the afferent, 'bottom-up' sensory data. In one version of this theory, principal cells in superficial cortical layers of primary sensory areas encode prediction errors, while those in deeper layers encode conditional expectations from which predictions are made (Bastos et al., 2012). Inhibitory interneurons within each cortical layer might be critical for canceling errors when the predictive model matches the sensory data. This conceptual framework is attractive since can assign specific functions to cells in different layers and cell types that should be experimentally testable. However, at present, data supporting it is largely indirect and extremely limited. An intriguing variant on this theme is a 'body model' for somatosensory cortex, in which the goal of S1 is to generate mental simulations of planned body actions. This model also assigns specific functions to each layer: body simulation to L4, sensory memory storage to L2/3, motor memory storage in L5, and relay of top-down drive from M1 through L6 and back to L4(Brecht, 2017). Additional computational models attempt to integrate much of the known circuitry of the primary visual cortex to propose specific functions for different layers, but similarly require experimental validation (Raizada, 2003).

An updated view of the 'canonical microcircuit'

Our empirical knowledge of cortical layers from which we can build theories of their function comes from four types of exploration: 1) anatomy of single cells and their projections, 2) connectivity of pairs of cells according to their laminar location and cell type, 3) physiological responses to sensory stimuli, and 4) activation or suppression of neurons in discrete layers. Anatomy and connectivity are the most absolute in that they do not depend on brain state or type of sensory stimulation. They constrain the types of computations layer can perform and the dynamics they can exhibit, but on their own provide limited insight into function. Conversely, physiology and activity perturbations are much less absolute in that the data obtained will likely depend on the brain state and context in which they were obtained. However, they should provide the most direct insight into the different functions of cortical layers. Clearly, all four approaches taken together are needed to address this question, although arguably, anatomy and connectivity have so far proved the most influential.

The often-repeated (although just as often maligned) dogma of the 'cortical canonical microcircuit' is largely based on studies of anatomy and connectivity in rodents, primates and cats. These data have converged on a core model where thalamic input drives activity in a feed-forward and sequential fashion from L4, to L2/3, to L5 and out to other cortical and subcortical regions (Armstrong-James et al., 1992; Binzegger, 2004; Lefort et al., 2009; Rodney et al., 1991). While numerous examples of alternate connections exist (e.g., thalamus to other layers, L5 to L2/3, L4 to L5), the anatomy of these neurons (i.e., their intracortical axons and dendrites) matches well with paired electrophysiological recording and circuit mapping via optical approaches. As these and other pathways in the cortex have been extensively reviewed elsewhere (Douglas and Martin, 2004; Feldmeyer, 2012; Harris and Shepherd, 2015; Thomson, 2007) we will focus on data revealing the physiology and functional impact of different cortical layers.

However, a key point that has emerged from this circuit mapping work (that has gone largely unappreciated) is the remarkable increase in specificity of translaminar output through the standard feed-forward intracortical architecture (see Fig. 1 and full citations below). Primary sensory thalamus, constituting the input stage of the hierarchy, provides at least some input to every cortical layer. L4, the primary cortical input stage, sends significant output to the three main other layers. L2/3 is more selective, and largely targets L5 (both L5 intratelencephalic 'IT' and L5 pyramidal tract 'PT' neurons), and to a minor extent, L6. L5IT neurons target L5PT neurons. Thus what appears to organize a serial 'hierarchy' among the cortical layers is not the density of certain projection pathways, but the ratio between the number of each layer's targets compared to its number of inputs. We place L4 at the first level of the hierarchy because it sends broad translaminar output but receives hardly any feedback; successive stages send increasingly selective output (i.e., to fewer and fewer target layers) but receive increasingly convergent input (Fig 1A). L6 output is still mysterious. In the mouse, L6 corticothalamic neurons appear to only make strong synapses on L5a pyramidal cells (PCs) and otherwise synapse on interneurons (cats and mice, see below), and the output of the L6 IT cells is mostly uncertain (Fig. 1B).

In addition to this underlying structural principal, the projection neurons of each layer are also organized according to their long-range targets: IT cells in L2/3 and L5 target other cortical areas and the dorsal striatum; L5 PT cells send widely divergent projections to subcortical nuclei, and L6 PCs target either thalamus or other cortical areas (Fig. 1C). How the relationship between the local architecture and the long-range circuitry of cortical layers might help explain to their function is perhaps one of the key questions to address in the coming years.

The size of the neuronal population at the different stages of this hierarchy varies considerably. Interestingly, the number of neurons in a given population appears to be inversely

correlated with how sparsely that population encodes sensory stimuli (Fig. 1D). For example, the large populations in L4 and L2/3 exhibit high levels of population sparseness in rodents (Crochet et al., 2011; O'Connor et al., 2010). Each of these layers contains at least an order of magnitude more neurons than the topographically corresponding region of primary thalamus (e.g. there are ~4500 L4 excitatory neurons in a rat barrel column versus ~250 neurons in the corresponding thalamic 'barreloid') (Meyer et al., 2010a). It has been proposed that the thalamocortical expansion into a much higher dimensional representation in L4 contributes to the creation of an overcomplete sparse code (Olshausen and Field, 2004). In addition to being energetically advantageous, the transformation into a sparser code confers potential computational benefits (Favorov and Kursun, 2011). Conversely, in rodents the less numerous L5 IT and especially L5 PT neurons employ a denser code (de Kock et al., 2007; Sakata and Harris, 2009a), which may be necessary in order to transmit information through the bottleneck of their long-range axonal projections with sufficient bandwidth (Ganguli and Sompolinsky, 2012).

Primer on vertical and horizontal circuits of the neocortex

We shall briefly review the defining anatomical and physiological features of each layer; this is not meant to be exhaustive, but simply to capture those key attributes that have largely led to conceptual frameworks for the functional roles of each layer. While circuit features vary across species as well as across sensory cortical areas, we will focus on data collected particularly in the visual and somatosensory cortical areas, and primarily in rodents and cats.

Layer 4 (L4): excitatory circuits in L4, among all four major layers, receive the densest innervation from primary thalamocortical neurons, but also receive dense recurrent excitatory feedback from nearby L4 neurons, but little feedback from other layers in both cats and mice (Lefort et al., 2009). L6 PCs do synapse in L4, but might selectively innervate L4 interneurons, at least in cats (McGuire et al., 1984). These facts rest on ample tracing (both bulk and single cell) from thalamus to cortex, single cell reconstructions of individual L4 neurons, and *in vitro* and *in vivo* electrophysiology. Furthermore, compared to other layers, L4 receives very little long-range feedback from higher cortices. This circuit architecture leads to the clear notion that L4 neurons represent the primary input stage to the cortical hierarchy. Through precise patterns of convergence from thalamic afferents onto single L4 neurons, key sensory computations are thought to be implemented, such as orientation tuning and direction selectivity (Hubel and Wiesel, 1962).

Despite the relatively strong input from the thalamus, perturbation studies indicate that local (i.e., 'intra-columnar'), recurrent synaptic input might in fact exceed the thalamic contribution. Cooling or optogenetically silencing cortical recurrence appears to linearly divide sensory-evoked excitation in cats and rodents, implying that its primary function is to amplify input without substantially altering its tuning (Ferster et al., 1996; Li et al., 2013a, 2013b; Lien and Scanziani, 2013; Malina et al., 2016). Despite the elegance of these studies, they provide little insight into the role of recurrent inhibition in L4, which is potently recruited by the same intralaminar excitatory circuits. Thus it remains to be determined what the net impact of cortical recurrence is on L4 spiking when inhibition is taken into account, and if this impact if context-dependent. Inhibition in L4 is thought to balance excitation on fast timescales, counteracting amplification by recurrent excitatory circuitry. The rapid nature feed-forward inhibition in L4 has been proposed to enforce precise spike timing in the barrel cortex (Gabernet et al., 2005a) and may allow it to actively cancel slow self-generated sensory signals due to the movement of the whiskers, while selectively amplifying fast, synchronous inputs created by externally generated touch (Yu et al., 2016). Recurrent inhibition in L4 (as well as in L2/3) is thought to make it act as an inhibition stabilized network, which can explain a variety of non-linear phenomenon in their sensory responses. If inhibition is not simply co-tuned, or in fact

dampens response in a stimulus-specific manner (Pinto, 2003), the net impact of recurrence might be quite different from linear amplification. Horizontal circuits are much sparser in L4 compared to other layers, but can influence sensory responses in rodents (Fox et al., 2003) and may contribute to how surround whiskers potently influence responses properties of L4 neurons (Pluta et al., 2017).

Although it has received less attention, the striking lack of excitatory feedback to L4 from other layers or higher cortical areas solidifies the notion that L4 is a feed-forward processing circuit whose computational role is largely independent of any direct output of other layers. Conversely, L4 appears unique among cortical layers in sending substantial synaptic to most other layers, perhaps only exceeded in the divergence of its output by the thalamus itself. L4, like all layers, is subject to neuromodulation (Radnikow and Feldmeyer, 2018) and can be suppressed by disynaptic inhibition via L6 activity in mice (Olsen et al., 2012), but paired recording and optogenetic stimulation of L2-5 reveals little to no excitatory or disynaptic inhibitory input to L4 (Adesnik and Scanziani, 2010; Lefort et al., 2009). Because of the relative simplicity of its anatomical input-output structure, L4 represents an attractive starting point for mechanistic interrogation of cortical function.

Layer 2/3 (L2/3): L2/3 neurons are major targets of ascending axons from L4, although many L2/3 cells can also receive direct input from the thalamus across species (Morgenstern et al., 2016; Petreanu et al., 2009). One of their most defining features are their long-range horizontal projections, which can extend many millimeters in cats or primates (Rockland and Lund, 1982), implying that individual L2/3 cells have access to much more widespread sensory input than their afferent L4 cells provide, a fact consistent with their larger sub-threshold receptive fields observed in rats (Brecht et al., 2003a). These horizontal circuits have intrigued cortical physiologists for decades as they provide an anatomical substrate for spatial summation, contextual modulation (Angelucci and Bressloff, 2006; Chisum and Fitzpatrick, 2004), and long-range synchronization (Gray et al., 1989; Veit et al., 2017) from mice to primates. By sharing information across the topographic map of sensory space these tangential axons should, in theory, be sufficient to generate new types of feature selectivity (i.e., *de novo* transformations) that could facilitate the analysis of larger object and natural environments. However, although new types of representations in L2/3 have emerged at the population level (Pluta et al., 2017), novel feature selectivity at the level of single neurons has largely eluded investigators, if it exists at all.

Instead, a defining physiological feature of individual L2/3 neurons, often attributed to these horizontal circuits, is surround suppression, a form of lateral inhibition observed broadly throughout the visual cortex (Bair et al., 2003; Hubel and Wiesel, 1965). Stimuli presented outside a neuron's 'classical receptive field' (CRF) suppresses responses to those within it – a circuit motif found widely throughout sensory systems and across species that appears to be particularly potent in L2/3 neurons (Nienborg et al., 2013; Ozeki et al., 2009; Self et al., 2014). Evidence indicates that surround suppression (at least the component due to stimuli proximal to the CRF) is cortical in origin and may operate via the recruitment of intra-areal inhibitory circuits by L2/3 horizontal axons (Adesnik, 2017; Nurminen and Angelucci, 2014). The net impact of these highly suppressive interactions is to generate a sparse and efficient population code for sensory stimuli that is optimal for readout downstream (Crochet et al., 2011; Froudarakis et al., 2014; O'Connor et al., 2010; Sachdev et al., 2012; Vinje and Gallant, 2000).

If horizontal circuits in L2/3 primarily generate lateral inhibition, how might components of a large sensory object be 'bound' together? One possibility, albeit highly controversial, is that spatial integration for the perception of object contour or shape depends on temporal coding through synchronizing spiking (Gray, 1999). A notable feature of upper layer circuits in the primary visual cortex from mice to primates, particularly for L2/3, is the prominence of visually-induced rhythmic activity in the gamma band (Gieselmann and Thiele, 2008; Gray et al., 1989; Veit et al., 2017; Xing et

al., 2012). These rhythms can phase lock principal neurons across large retinotopic distances, and most intriguingly depend on a match between the attributes of the stimuli (such as orientation, phase, or direction of motion) (Gray et al., 1989; Veit et al., 2017). Recently, it has been found that these rhythms, as well as surround suppression itself, depend on intracortical inhibition mediated by dendrite-targeting somatostatin (SST interneurons in awake mice (Adesnik et al., 2012; Chen et al., 2017). Note that while many, but not all naturalistic stimuli generate obvious gamma band activity, as measured in the local field potential (LFP) (Brunet et al., 2015; Hermes et al., 2015), they might still evoke potent synchronized spiking that would serve the same function. Since coincident activity is a potent mechanism for driving downstream activity, the mechanism by which L2/3 populations might drive the encoding of extended contours downstream is not through increased firing rates but through increases in their synchronized activity. This notion could be tested by measuring contour encoding in secondary cortical areas while eliminating synchronization in primary areas by inactivating SST neurons. In addition, unlike L4, neurons in L2/3 receive a substantial amount of long-range corticocortical feedback that is also thought to contribute to contextual effects such as surround suppression (Nassi et al., 2013), particularly from regions of sensory space that are farther afield than those represented by intra-areal horizontal connections (D'Souza and Burkhalter, 2017). These 'top-down' afferents have also been implicated in anticipatory activity and 'mismatch' responses in rodents, consistent with a role in conveying predictions about the incoming sensory data (Leinweber et al., 2017; Zmarz and Keller, 2016). Furthermore, they likely contribute to attentional modulation, possibly through frequency dependent coupling as observed in monkeys (Bastos et al., 2015), as well as learning and plasticity (Makino et al., 2015).

The major outputs of L2/3 include L5 neurons within the same cortical area, higher cortical areas, as well as the striatum (Adesnik and Scanziani, 2010; Callaway, 1998; Lefort et al., 2009; Mao et al., 2011a; Shepherd et al., 2003). In the case of the latter two, these inter-areal projections appear to emerge from non-overlapping subsets of L2/3 neurons (Chakrabarti and Alloway, 2006; Chen et al., 2013). An interesting distinction between mammalian species is that the L2/3 feed-forward projections to higher cortical areas have target different layers in primates, cats, and rodents (D'Souza and Burkhalter, 2017). Within the primary sensory area, L2/3 provides little input to L4 and a minor projection to L6 (Briggs and Callaway, 2001; Denardo et al., 2015). It can potently recruit inhibitory neurons in L2/3 and L5, particularly of the SST sub-class (Adesnik et al., 2012; Kapfer et al., 2007). They also synapse onto both parvalbumin (PV) and vasoactive intestinal peptide (VIP) positive neurons (Karnani et al., 2016c; Pala and Petersen, 2015), but the physiological conditions under which L2/3 drives these inhibitory neurons are still being worked out.

Layer 5 (L5): It is perilous to attempt to draw broad conclusions about the local circuits of L5 PCs. They are highly diverse, whether they are probed morphologically, physiologically, or transcriptionally, with estimates of, at minimum, seven unique classes, but likely even more (Kim et al., 2015a; Lur et al., 2016a; Narayanan et al., 2015a; Tasic et al., 2016a). They are similarly heterogeneous when compared across cortical areas, and so the 'cardinal types' of L5 neurons identified in visual cortex (and perhaps L2/3 neurons as well) might be quite different from those identified in the somatosensory, auditory or higher order cortices. Since L5 neurons can be considered to compose the major output of most cortical areas, this high diversity makes intuitive sense: each cortical area is most likely computing various key features of sensory input that must be distributed to a unique set of downstream regions depending on the modality, type of stimulus, and current behavioral demands. Interestingly, some L5 neurons in the rodent barrel cortex may receive sufficient input directly from the primary somatosensory thalamus to encode subtypes of sensory stimuli (Constantinople and Bruno, 2013) and even drive simple behavioral responses through their subcortical projections (Matyas et al., 2010).

Nevertheless, we can summarize some fundamental features of their circuits. L5 neurons are unique in that their dendrites often span all the cortical layers in their local circuit, implying that they can receive input from any local or long-range sources. Paired recording and optical mapping studies in mice confirm this notion: L5 neurons receive input from primary and secondary thalamus, all other cortical layers, as well as higher cortical areas, (Denardo et al., 2015; Lefort et al., 2009; Petreanu et al., 2009). By having access to every type of local and long-range input, L5 neurons might be considered the fulcrum of fundamental cortical computations. Perhaps as a consequence, they exhibit high firing rates under both spontaneous and sensory evoked conditions (O'Connor et al., 2010; Pluta et al., 2015a), as a population show low sparsity (de Kock and Sakmann, 2009; Sakata and Harris, 2009a), and can potently modulate performance on operant perceptual tasks (Znamenskiy and Zador, 2013). This low sparsity might also arise since the high convergence of mixed inputs onto L5 neurons, and their limited divergence back onto other layers makes them a bottleneck for information flow.

A second defining (although not necessarily unique) feature of L5 neurons is the electrically excitable properties of their long dendrites, particularly the apical dendrite that extends all the way to the pial surface (Larkum, 2013). Even in species such as the mouse, which have relatively thinner cortices, the electrotonic distance of the L5 apical tuft is so great that some theories consider it a practically independent functional compartment with its own computational properties. As a corollary, it might only exert its influence on axonal output through propagating dendritic spikes and not through passive electronic spread of synaptic potentials. The apical tuft is particularly intriguing since it accesses L1, which, though harboring few cortical neurons, contains numerous long-range axons from higher cortical and secondary thalamic areas that likely encode more processed information or predictions about incoming sensory data (D'Souza and Burkhalter, 2017). Thus the synaptic integration zone of L5 neurons in L1 might represent a key node for numerous aspects of cortical computation. This same site is also the major target of deep cortical interneurons of the SST subtype that can potently modulate how apical dendritic output propagates to the spike initiation zone (Murayama et al., 2009a). Both experimental and theoretical considerations imply that this zone is critical for behavioral detection of sensory stimuli (Manita et al., 2015a; Takahashi et al., 2016), 'top-down' modulation during selective attention (Stanisor et al., 2013), and plasticity (Cichon and Gan, 2015).

Locally, L5 neurons make few synapses onto L4 or L2/3 neurons, at least in mice (Lefort et al., 2009)(Lefort et al., 2009), although the few L5 PCs that do project intracortically could have a significant impact on activity in these layers, such as the generation of UP states or reverberant activity during memory recall (Adesnik, 2018; Beltramo et al., 2013). Within L5 recurrent connectivity is more common, but still the overall statistics of intralaminar connectivity appear to be substantially sparser than in other layers (Lefort et al., 2009), although between corticocortical and corticotectal L5 neurons in mouse connectivity rates can be much higher (Brown and Hestrin, 2009). This key finding highlights that L5 PCs not only project to different downstream regions, but preferentially interact with specific ensembles of L5 neurons that may have discrete functions. From this perspective, L5 begins to appear as multiple sub-layers that are not necessarily neatly organized along the vertical axis. Nevertheless, L5 is often sub-divided into sub-lamina (termed 'a' and 'b') with a predominance of slender tufted striatal and motor cortex projecting neurons in superficial L5a, and a predominance of thick-tufted thalamic and pontine-projecting neurons in L5b, but these rules are not absolute (Narayanan et al., 2017).

[A section on inhibitory circuits of L5 is omitted here, since it is reviewed in greater depth below.]

Layer 6 (L6): In many ways, the physiology and functional importance of neurons in L6 are the most enigmatic (Briggs, 2010; Thomson, 2010). L6 principal neurons also compose multiple subtypes, but can be broadly divided in to cortico-thalamic (CT) projecting and cortico-cortical (CC) projecting neurons (Briggs, 2010; Olsen et al., 2012; Wiser and Callaway, 1996). L6 neurons receive synaptic input from thalamus (L6 CC more than L6 CT (Crandall et al., 2017)), from within L6 (Beierlein and Connors, 2002) as well as excitatory input, albeit sparse, from L4 and L5 (Lefort et al., 2009). There is little excitatory input from L2/3 in rodents (Adesnik and Scanziani, 2010; Lefort et al., 2009), except onto a specific subset L6 PCs in monkeys (Briggs and Callaway, 2001). Some L6 neurons project their apical dendrite nearly to the pia, while others stop in L4 or L2/3, and others barely leave the infragranular layers (Briggs and Callaway, 2001). To match their relatively sparse intracortical input, mouse L6 neurons, even of the cortico-cortical projection subtype, appear to make few excitatory connections onto principal neurons in other layers (Lefort et al., 2009), but may synapse more broadly on GABAergic neurons (Bortone et al., 2014; McGuire et al., 1984). When genetically labeled in mice, L6 CT neurons clearly send axonal ramification to upper L5, excite these neurons, and can even drive them spike (Kim et al., 2014). However, the dominant impact of functional activation of L6 appears to be intracortical suppression, at least in part to fast-spiking GABAergic neurons in L6 that send translaminar axons to most other cortical layers (Bortone et al., 2014; Olsen et al., 2012). One study argued that in cat visual cortex, L6 neurons, which exhibit large receptive fields, are critical for surround suppression in the upper layers (Bolz and Gilbert, 1986), but this result is a matter of debate (Grieve and Sillito, 1991).

However, the defining, and perhaps best-known feature of L6 is the dense connection many of these neurons make onto cells in the thalamus and the thalamic reticular nucleus (nRT)(Bourassa and Deschˆnes, 1995), in additional to a much less studied output to the claustrum (Katz, 1987; Thomson, 2010). A substantial fraction of synapses onto thalamic neurons comes from the cortex (Erişir et al., 1997), implying that CT input to thalamus should have profound impacts on what information is passed back to cortex from the thalamus (Briggs and Usrey, 2008). Few other long-range connections from the cortex have inspired more experimentation or greater debate, and strikingly, despite extensive literature, their still remains little consensus on the functional impact or importance of this connection. It is known to be topographic, but as it simultaneously synapses onto thalamic relay neurons and GABAergic nRT neurons, it might be net facilitating, net suppressive, show no effect, synchronize thalamic firing depending on the location, features or context of a stimulus, or control the precision of spike timing (Denman and Contreras, 2015; Hasse and Briggs, 2017; Li and Ebner, 2007; Olsen et al., 2012; Przybyszewski et al., 2000; Sillito et al., 1994; Temereanca and Simons, 2004). More recently, *in vitro* experiments in rodents have tried to address this confounding literature by arguing that the net impact depends on the frequency of L6 spiking (Crandall et al., 2015).

To match the confusing and enigmatic nature of their functional impact, the physiological responses of L6 neurons are similarly obscure. Studies in rodents have often found only weak sensory responses in L6, potentially explained by a unique reversal of the standard excitatory-inhibitory sequence normally observed in cortical neurons during sensory stimulation (Zhou et al., 2010), but might also be explained by recording in anesthetized or passive conditions. The data that exists implies that CT cells fire extremely sparsely and show high levels of tuning (e.g., to orientation), while CC neurons are more heterogeneous and show less tuning to stimulus features (Vélez-Fort et al., 2014). Intriguingly, subsets of L6 neurons in S1 are principal targets of afferents from motor cortex (Kinnischtzke et al., 2016; Vélez-Fort et al., 2014), and L6 CT neurons V1 are targets of the retrosplenial cortex (in V1). Both of these areas convey information about body position to L6 (head position for V1, and whisker position for S1). Clearly, more work is needed to

assess the functional role of L6 in various aspects of sensory computation. An excellent mouse L6-specific driver line exists for L6 CT cells (Gong et al., 2007) for genetically targeting vectors for activation or suppression, and these cells should also be accessible in non-genetically tractable species through intersectional viral approaches employing retrograde transporting vectors. The design of driver line for the other subtypes of L6 neurons is critically needed.

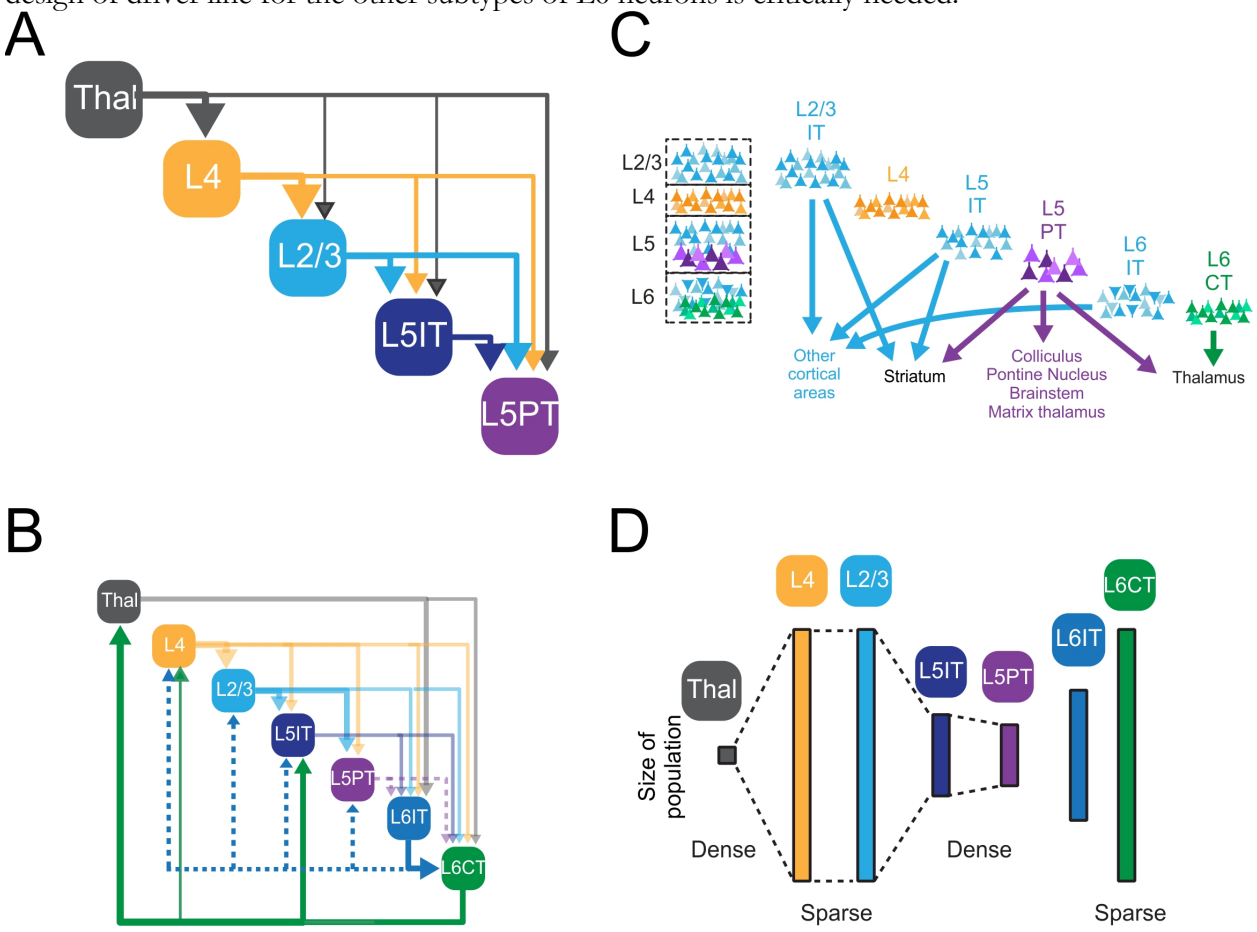

Figure 1.1: Architectural principles of the cortical layers.
A) Schematic of the 'feed-forward' architecture of the neocortex, emphasizing the increase in the specificity of translaminar targets across the layers. The hierarchy can be constructed based on the principal that the ratio of laminar targets to laminar inputs decreases uniformly. B) Inclusion of L6 principal neurons in the hierarchy; much of their input and output circuitry remains uncertain (dashed lines). C) Organization of the principal cells in each layer based on their long-range projection targets. D) Schematic of the change in population size of principal cells in each layer and the corresponding sparsity of their population responses to sensory stimuli. The length of the vertical bars approximates the relative size of the population of principal neurons in each laminar subdivision.

Layer-specific perturbations: insights and challenges

Understanding any neural circuit requires perturbing it. Although the anatomy and physiology of the neurons in any layer can help us build theories and propose hypotheses for what layers might do, only manipulating the activity of specific layers or subsets of layers can test and validate these theoretical hypotheses. Prior to the advent of cell-type specific perturbations (via opto- or chemo-genetics) the primary tools for perturbation were chemical lesions (reversible or irreversible), cortical cooling, and electrical micro-stimulation. The weakness of all these tools is that precisely calibrating the spread of any inactivating chemical (e.g, sodium channel blockers of GABA receptor agonists) or electrical stimulation is extremely challenging, although careful experiments with iontophoresis or very low current electrical stimulation can get close. Nevertheless, as is clear from the anatomical

features enumerated above, any application of a chemical or electrical stimulus to any layer will necessarily impinge on cells in multiple layers, since most cortical neurons have dendrites or axons that stretch across laminar boundaries (and across columnar boundaries as well, if they exist). This issue of specificity is largely overcome with layer-specific targeting of optogenetic or chemogenetic actuators, and both the number of available layer-specific driver lines, and the data from layer-specific perturbations grows quickly.

A striking result of these various manipulations of cortical layers is a frequent incongruence between the predictions of the 'canonical model' and the impact of these perturbations. For instance, reversibly blocking L4 activity (through chemically silencing specific layers of the visual thalamus) does not block much of the sensory evoked responses in L2/3 of the visual cortex of anesthetized cats (Malpeli, 1983) (but see (Martinez and Alonso, 2001)), but simultaneously suppressing higher visual cortex areas does (Mignard and Malpeli, 1991). In a similar vein, direct application of the action potential blocker lidocaine to the superficial layers of somatosensory cortex in has essentially no effect on whisker-evoked activity in L5 PCs in sedated and paralyzed rats (Constantinople and Bruno, 2013)(but see (Wright and Fox, 2010)). Direct optogenetic suppression of L4 in awake, locomoting mice leads to a reduction in sensory evoked activity in L2/3 of V1 or S1, albeit modest, but strikingly leads to a potent disinhibition of activity in L5, an effect attributed to a previously unappreciated disynaptic translaminar inhibitory circuit between L4 and L5 (Pluta et al., 2015a). Optogenetic suppression of L6 in awake mice also largely has a disinhibitory effect across most layers of cortex, an effect attributed to deactivating a broadly inhibiting translaminar inhibitory neuron (Bortone et al., 2014; Olsen et al., 2012). In one study, optogenetic activation of L4, L2/3, or L5 in brain slices from mouse primary visual cortex revealed a slightly more generalizable principle with an underlying synaptic mechanism: activation of each of these layers suppressed activity within their own layer by recruiting potent recurrent inhibition, but could facilitate activity in downstream layers by generating a more favorable excitation/inhibition ratio (Adesnik, 2018), a feature previously identified in for L2/3 of the barrel cortex (Adesnik and Scanziani, 2010). Clearly, as for the L6 CT to thalamus projection, different results are obtained concerning the functional impact of layers, possibly explained by a combination of the type of manipulation (chemical vs. optogenetic), sign of the perturbation (activation vs. suppression), or state of the experimental preparation (brain slice vs. anesthetized vs. sedated vs. awake). While something can be learned from each of these studies, a more conclusive picture almost surely necessitates more physiological forms of perturbations in the most functionally relevant context.

However, a major problem persists even with layer-specific genetic manipulations: owing to the highly inter-connected nature of neurons across layers, perturbation to cells in one layer will almost necessarily impact activity in other layers. Therefore, any measurable physiological or behavioral effect is difficult to assign to the action of the pharmacologically or optogenetically targeted layer. While this is a criticism that can be more generally leveled at any sort of brain perturbation (whether it be within a single cortical area or between distant but connected brain regions) (Otchy et al., 2015), it stands as one of the key challenges in interpreting data gained from perturbation studies. Arguably, this problem must overcome by addressing the same question from multiple vantage points: layers (or cell types or brain areas) should be perturbed with multiple tools, at varying levels of intensity, in different conditions, and while the neural activity in multiple layers or areas are simultaneously monitored. Finally, the data obtained from these perturbations should ultimately be able to be predicted from more holistic computational models of cortical circuits, although this is probably a long way off. But perhaps an even greater challenge with circuit perturbations is that they can have major effects on circuit dynamics and behavior due to unobserved effects in downstream brain structures. For instance, silencing L2/3 in S1 may impact L5 not only through its direct projections to L5 within in S1, but also indirectly through its impact

on S2, and S2's feedback to S1. Therefore, to best interpret the impact of any layer or cell-type specific perturbation, it is critical to monitor effects on other downstream structures to rule out or rule in their contributions to the observed effects.

[Continued in Chapter 4]

Acknowledgements

The authors thank Dan Feldman for a critical reading of the manuscript.

Inhibitory circuits of cortical layer 5

Foreword

Most of the present work is focused on circuits involving the inhibitory interneurons of cortical layer 5, the primary output layer. Below I present published work that includes an in-depth review of the circuitry in L5. [1]

Naka, A. and Adesnik, H., (2016). Inhibitory circuits in cortical layer 5. *Frontiers in neural circuits*, 10.

Summary

Inhibitory neurons play a fundamental role in cortical computation and behavior. Recent technological advances, such as two photon imaging, targeted in vivo recording, and molecular profiling, have improved our understanding of the function and diversity of cortical interneurons, but for technical reasons most work has been directed towards inhibitory neurons in the superficial cortical layers. Here we review current knowledge specifically on layer 5 inhibitory microcircuits, which play a critical role in controlling cortical output. We focus on recent work from the well-studied rodent barrel cortex, but also draw on evidence from studies in primary visual cortex and other cortical areas. The diversity of both deep inhibitory neurons and their pyramidal cell targets make this a challenging but essential area of study in cortical computation and sensory processing.

The diversity of layer 5 excitatory neurons

Before surveying the existent literature on layer 5 (L5) inhibitory neurons, we briefly review current knowledge on the connectivity and physiological properties of L5 pyramidal cells (PCs), as it provides important context for understanding L5 inhibitory circuits. One feature that distinguishes L5 from other cortical layers is the diversity of its PCs, which send a myriad of long-range projections to other cortical and sub-cortical structures (Aronoff et al., 2010; Harris and Shepherd, 2015; Hattox and Nelson, 2007; Lévesque et al., 1996; Veinante et al., 2000). This simple anatomical fact establishes L5 as a primary cortical layer involved in the top-down control of other brain areas. Exactly how L5 circuits parse information to influence downstream circuits and control behavior is one of the central questions in neuroscience. Even though L5 is conventionally thought of as primarily an output layer, L5 PCs also receive direct thalamocortical input (Agmon and Connors, 1992; Meyer et al., 2010b; Oberlaender et al., 2012; Rah et al., 2013; Wimmer et al., 2010) and can be driven by thalamic activity alone (Constantinople and Bruno, 2013), suggesting that L5 is an important input layer as well. L5 PCs also receive input from all cortical layers and are thus uniquely positioned to integrate nearly every local and afferent pathway in the cortex (Markram et al., 2015). Without exception, signals transmitted via these pathways invoke a mixture of synaptic excitation

[1] Note that this review was written after the completion of the work described in Chapter 2 and indeed makes reference to the results of that work. However, because it serves the purpose of introducing the circuits that are the main topic of this dissertation, I believe it is most logical that this work goes up above the descriptions of my primary research efforts. As an aside: a running joke among the Adesnik lab is that L5 only 'goes up,' which originated from the observation that activity in L5 neurons increases (seemingly invariably) in response to a wide variety of perturbations of cortical activity. Accordingly, it seems only fitting that a review on L5 *goes up* above the other chapters. Nonetheless, apologies to the reader for the chronological hiccup!

and inhibition (Isaacson and Scanziani, 2011). Thus inhibition onto L5 PCs, the focus of this review, is crucial for nearly every aspect of L5 function.

L5 PCs can be broadly subdivided based on their projection targets into 1) the pyramidal tract (PT) neurons, which project to subcortical regions, are located mainly in layer 5B, and display impressive 'thick-tufted' apical dendritic morphologies, and 2) intratelencephalic (IT) neurons, which project mainly to other cortical regions and striatum, are found mainly in layer 5A, and have smaller and less complex dendrites (Hattox and Nelson, 2007; Larsen et al., 2007). PT and IT cells interconnect asymmetrically: while IT cells form excitatory synapses onto PT cells as well as other IT cells, PT cells preferentially connect to other PT cells (Brown and Hestrin, 2009; Harris and Shepherd, 2015; Kiritani et al., 2012; Lefort et al., 2009; Perin et al., 2011; Fig. 1.2A). The two cell types are also distinguished by their intrinsic properties (Agmon and Connors, 1989, 1992; Chagnac-Amitai et al., 1990; Schubert et al., 2001), plasticity (Greenhill et al., 2015; Jacob et al., 2012), and more (Table 1). Furthermore, both PT and IT neurons can be further sub-divided based on their unique subsets of sub-cortical or cortical targets (Hattox and Nelson, 2007).

As a whole, L5 PCs have distinct physiological properties *in vivo* that distinguish them from excitatory neurons in other layers. First, L5 PCs display very broad sensory tuning (Brecht et al., 2003b; Kim et al., 2015b; de Kock et al., 2007; Lur et al., 2016b; Manns et al., 2004; Sakata and Harris, 2009b). Second, L5 PCs, especially PT cells, fire at high rates both spontaneously and during sensory responses (Hires et al., 2015; de Kock et al., 2007; O'Connor et al., 2010; Sakata and Harris, 2009b). Third, many L5 PCs exhibit reductions in their firing rate during sensory stimulation or behavior, a feature not often seen in other cortical neurons, which might serve to expand their dynamic range (Krupa et al., 2004a; Pluta et al., 2015b; Sofroniew et al., 2015). These properties suggest that L5 PCs employ a dense coding strategy (Harris and Mrsic-Flogel, 2013), which stands in contrast to the sparse code that has been observed in L2/3 (Brecht et al., 2003b; Clancy et al., 2015; Crochet et al., 2011; Kerr et al., 2007; Peron et al., 2015) and other layers (Barth and Poulet, 2012; de Kock and Sakmann, 2009; de Kock et al., 2007; O'Connor et al., 2010). L5 PCs are highly intrinsically excitable, and can integrate excitatory inputs from many different sources – both of which probably help establish this dense code (Hooks et al., 2011; Schnepel et al., 2015; Schubert et al., 2001, 2006; Zarrinpar and Callaway, 2014). Another major factor is the diverse cast of inhibitory circuits impinging onto L5 PCs.

Type (other common nomenclatures)	**Pyramidal Tract (PT)** (Thick tufted, intrinsic bursting)	**Intratelencephalic (IT)** (Slender tufted/short, regular spiking)
Morphology (Larsen and Callaway, 2006; Narayanan et al., 2015b; Oberlaender et al., 2011; Ramaswamy and Markram, 2015; Schubert et al., 2006)	Broad, thick-tufted apical dendritic arbor, often with a prominent bifurcation in L4 or L2/3. Local axonal ramification is sparse and mostly restricted to infragranular layers, but spans multiple columns. Preferentially occupy L5B	Smaller dendritic arbor, with a slender apical tuft or no apical tuft Local axonal ramification is dense, spans multiple columns and often ascends to supragranular layers. Preferentially occupy L5A
Projection targets (Groh et al., 2010; Hattox and Nelson, 2007; Lévesque et al., 1996; Veinante et al., 2000; Wise and Jones, 1977)	Spinal cord, brainstem, superior colliculus, pontine nucleus, ipsilateral striatum, higher-order thalamus	Ipsilateral and contralateral striatum, contralateral S1, M1 and other cortical areas
Intrinsic properties (Grewe, 2010; Groh et al., 2010; Larkum et al., 1999a, 1999b, 2009; Schubert et al., 2006)	Can fire bursts or doublets, Prominent dendritic spiking, Non-adapting after burst	Regular or doublet spiking, Little dendritic excitability Adapting somatic spikes
Local excitatory connectivity (Feldmeyer et al., 2005; Frick et al., 2008; Hooks et al., 2011; Kim et al., 2014; Kiritani et al., 2012; Krieger et al., 2007; Lefort et al., 2009; Markram, 1997; Perin et al., 2011; Schubert et al., 2006, 2001; Song et al., 2005)	Receive excitatory input from PCs in all cortical layers; strong inputs from L3, L5PT Engage in reciprocally connected subnetworks with other PT cells but rarely connect to L5 IT	Receive excitatory input from PCs in all cortical layers; strong inputs from L2, L4, L5IT, L6 corticothalamic cells Reciprocally connected to other L5 IT; provide excitation to L5 PT
Long-range inputs (Agmon and Connors, 1992; Constantinople and Bruno, 2013; Oberlaender et al., 2012; Petreanu et al., 2007, 2009; Rah et al., 2013; Wimmer et al., 2010; Xu et al., 2012)	Strong input from ventral posteriomedial nucleus of thalamus (VPM) Weak input from posteromedial nucleus of thalamus (POm) Primary motor cortex and other cortical areas	Weak or no input from VPM Strong input from POM Primary motor cortex and other cortical areas

Table 1.1 Properties and connectivity of layer 5 pyramidal neurons

Major subtypes of layer 5 inhibitory neurons

Cortical interneurons can be broadly sub-divided into distinct cell types based on their morphology, connectivity, molecular and developmental identity, and electrophysiological and synaptic properties (Ascoli et al., 2008; DeFelipe et al., 2013; Markram et al., 2004). Increasingly, these cell types are being linked to specific functional specializations (Gentet, 2012; Kepecs and Fishell, 2014; Petersen, 2014; Petersen and Crochet, 2013; Roux and Buzsáki, 2014; Womelsdorf et al., 2014). Cortical inhibitory interneurons can be grossly separated into three essentially non-overlapping groups based on their expression of the molecular markers parvalbumin (PV), somatostatin (SOM), or the serotonin receptor 5HT3aR (Rudy et al., 2011). Each molecular group can be subdivided into multiple cell types, though exactly how many remains unclear. The diversity of inhibitory cell types in the neocortex has been reviewed extensively elsewhere (Ascoli et al., 2008; Huang, 2014; Kepecs and Fishell, 2014; Kubota, 2014; Markram et al., 2004; Rudy et al., 2011; Taniguchi, 2014), so we will limit our discussion to the most relevant aspects for inhibitory circuits in L5 (Table 2).

PV neurons

PV-expressing GABAergic neurons constitute the largest sub-class of L5 interneurons (Gonchar, 2008; Lee et al., 2010; Xu et al., 2010). All PV cells share a distinctive "fast-spiking" electrophysiological phenotype. In addition to their eponymous fast action potentials (sometimes also called thin or narrow), these neurons also display little or no spike-frequency adaptation, rapid membrane kinetics, and rapid synaptic conductances, which collectively allow them to fire precisely timed spikes at high rates (Hu et al., 2014). Importantly, the fast-spiking phenotype has allowed experimenters to distinguish PV cells from other types of neurons (such as PCs or SOM interneurons, which typically have broader spikes) during extracellular recording *in vivo*. The vast majority of information we have on L5 interneurons *in vivo* primarily derives from this type of analysis.

Most PV cells in L5 are basket cells whose axons densely target the perisomatic compartments of PCs, allowing them to impose rapid and powerful inhibition on the surrounding network (Xiang et al., 2002). Anatomically, basket cells take on a range of morphologies that have been described as 'large', 'small' and 'nest' derived from the unique and diverse structure of their intracortical axons (Gupta et al., 2000; Wang et al., 2002), and these different axonal phenotypes may correlate to functional distinctions (Bortone et al., 2014; Buchanan et al., 2012a). However the differential circuit connectivity and function of these various basket subtypes remain to be fully elucidated.

Chandelier cells are the second major subtype of PV cells. These neurons have a highly distinctive and characteristic axonal morphology and primarily synapse on PC axons. Yet they are technically challenging to study due to their relative scarcity and current barriers to specific genetic access to them (Huang, 2014; Taniguchi et al., 2013). While chandelier cells are GABAergic, in some conditions they can actually depolarize postsynaptic PCs due to the locally elevated chloride reversal potential in the axon initial segment. However, the questions of whether and when chandelier cells exert excitatory or suppressive effects on their postsynaptic targets remain open (Glickfeld et al., 2009; Szabadics, 2006; Woodruff et al., 2010, 2011). Interestingly, while chandelier cells have been observed to occupy the infragranular layers (Inda et al., 2009; Taniguchi et al., 2013), to the best of our knowledge no direct evidence of connections from L5 chandelier cells onto L5 PCs has been published; these may be comparatively rare (Peters et al., 1982). However, connections onto L5 PCs have been observed originating from chandelier cells located in the supragranular layers, where they are more common (Jiang et al., 2013; Lee et al., 2014a).

SOM neurons

The second largest class of L5 GABAergic neurons are SOM cells. In contrast to PV neurons, SOM cells primarily target the dendrites of excitatory neurons and receive facilitating excitatory input (Markram et al., 2004; Reyes et al., 1998; Silberberg and Markram, 2007). The best-studied type of SOM cell is the Martinotti cell, which is a subclass found across layers 2-6, but especially prevalent in L5. The axons of L5 Martinotti cells characteristically ascend to upper cortical layers, particularly to L1, where they ramify and form a dense axonal plexus innervating the distal apical dendrites of L5 PCs. Some Martinotti axons also target L4, and overall Martinotti cells display considerable morphological and molecular heterogeneity (McGarry et al., 2010; Wang et al., 2004). This heterogeneity has been demonstrated in a study comparing two transgenic reporter mouse lines (the 'X98' line and the more commonly used 'GIN' line), which appear to label distinct sets of Martinotti cells with mostly non-overlapping phenotypes (Ma et al., 2006b). Another reporter, the 'X94' line, labels a third subset of non-Martinotti SOM cells present in both L5 and L4 which display a quasi-fast-spiking electrophysiological phenotype and target their axons almost exclusively to L4 rather than L1. A distinctive feature of X94 cells in L5 is that they receive robust excitatory input from thalamocortical axons, indicating that they may play a key role in feed-forward inhibition from thalamus to cortex (Porter et al., 2001; Tan et al., 2008). On the other hand, Martinotti cells receive little or no thalamocortical input in the mature animal (Cruikshank et al., 2010; Ji et al., 2015), though recent results indicate that they may play a transient role in feedforward inhibition during development (Marques-Smith et al., 2016a; Tuncdemir et al., 2016a).

5HT3aR neurons

The last major group of L5 GABAergic neurons express the serotonin receptor, 5HT3aR (Lee et al., 2010; Vucurovic et al., 2010). Even more so than L5 PV and SOM neurons, this sub-group is highly heterogeneous. While 5HT3aR neurons represent half of the GABAergic cells in L2/3, they comprise only a small fraction (~10-25%) of L5 interneurons (Lee et al., 2010; Rudy et al., 2011; Xu et al., 2010). This group includes interneurons expressing the molecular marker vasoactive intestinal peptide (VIP). These neurons have bipolar or bitufted dendritic morphologies and vertically oriented axonal arborizations (Prönneke et al., 2015; Vucurovic et al., 2010). In L2/3, VIP cells have recently been shown to target other interneurons as a part of dedicated disinhibitory circuits. However, VIP cells in L5 appear morphologically distinct from those in upper layers and comparatively little is known about them (Prönneke et al., 2015). Other 5HT3aR expressing interneurons, such as neurogliaform cells, are known to exist but rarely observed in L5 (Jiang et al., 2015; Oláh et al., 2009). Overall, data on 5HT3aR interneurons in L5 are scarce and much further experimentation is needed.

Type (other common nomenclatures)	**Parvalbumin (PV) expressing interneurons** (Fast-spiking, narrow-spiking, thin-spiking)		**Somatostatin (SOM) expressing interneurons** (Low-threshold spiking, regular spiking nonpyramidal)		**Serotonin receptor (5HT3aR) expressing interneurons** (Irregular spiking)	
Subtype	**Basket**	**Chandelier**	**Martinotti**	**X94**	**VIP**	**Neurogliaform cells**
Fraction of L5 interneurons (Gonchar, 2008; Lee et al., 2010; Meyer et al., 2011; Rudy et al., 2011; Sohn et al., 2014; Xu et al., 2010)	45-60%		20-50%		5-15%	
Morphology (Buchanan et al., 2012a; Ma et al., 2006b; Oláh et al., 2009; Prönneke et al., 2015; Silberberg and Markram, 2007; Taniguchi et al., 2013; Wang et al., 2002, 2004; Xiang et al., 1998)	Bi/multipolar dendritic morphology Dense axonal arbor, can be intra or translaminar. Axons target the perisomatic compartment of PCs	Bi/multipolar dendritic morphology Dense, hanging axonal arbor. Cartridge-like synapses onto axon initial segments give the appearance of a chandelier	Bitufted or bi/multipolar dendrites Radially oriented, translaminar axon ascending to layer 1. Innervates distal dendrites.	Bitufted or bi/multipolar dendrites Radially oriented, translaminar axon densely targets a single barrel in L4 but avoids L1	Radially oriented, bipolar/bitufted dendrites Radially oriented axons, mostly restricted to infragranular layers. Target dendrites of PCs but somata of PV neurons	Multipolar dendrites Dense, local axon
Molecular Markers (Gonchar, 2008; Huang, 2014; Kubota et al., 2011; Leão et al., 2012; Ma et al., 2006b; Rudy et al., 2011; Sohn et al., 2014; Xu et al., 2010)	PV		SOM Preprodynorphin Calretinin NPY		5HT3aR NPY CCK Calretinin	
			Chrna2 Calbindin		VIP	Reelin nNOS
Intrinsic properties (Galarreta and Hestrin, 2002; Ma et al., 2006b, 2012; Markram et al., 2004; Oláh et al., 2009; Prönneke et al., 2015)	Fast-spiking Non-adapting Large, fast AHP Low input resistance		Regular, adapting spiking, High input resistance, Can perform a low-threshold spike on rebound from hyperpolarization	Quasi fast-spiking phenotype, Some adaptation Low input resistance, No low-threshold spike	Regular or irregular spiking, Adapting High input resistance	Late spiking or irregular spiking Adapting
Local excitatory inputs (Angulo et al., 2003; Apicella et al., 2012; Le Bé et al., 2007; Buchanan et al., 2012a; Jiang et al., 2015; Jin et al., 2014; Kapfer et al., 2007; Kim et al., 2014; Marques-Smith et al., 2016a; Otsuka and Kawaguchi, 2009; Pluta et al., 2015b; Silberberg and Markram, 2007; Staiger et al., 2002)	L2/3, L4, L5 (PT and IT), L6 CT	?	L5 PT L2/3	?	L5 PT	?
Long-range inputs (Cruikshank et al., 2010; Ji et al., 2015; Karayannis et al., 2006; Kinnischtzke et al., 2014; Lee et al., 2013; Rock and Apicella, 2015; Sun et al., 2013; Tan et al., 2008; Zhang et al., 2014)	VPM, M1, contralateral S1		?	VPM	Long-range corticocortical inputs in L2/3, unknown in L5	?
Synaptic targets (Blazquez-Llorca et al., 2014; Buchanan et al., 2012a; Hioki et al., 2013; Jiang et al., 2015; Kruglikov and Rudy, 2008; Ma et al., 2006b; Packer and Yuste, 2011; Pfeffer et al., 2013; Silberberg and Markram, 2007; Walker, 2016; Xiang et al., 2002; Xu et al., 2013)	PCs, other PV cells, Martinotti Mostly but not exclusively intralaminar	PCs, other PV cells Mostly intralaminar	All neurons except other SOM cells Intralaminar or translaminar	? Neurons in L4 Preferentially target PV cells	PV, SOM	Chemical and electrical connectivity with all interneurons, intralaminar

Table 1.2 Properties and connectivity of layer 5 GABAergic interneurons.

Boxes containing a question mark indicate areas where direct experimental evidence is not available or lacking.

Recurrent, intralaminar inhibition within layer 5

Somatic Inhibition

PV basket-type interneurons mediate a major component of recurrent inhibition within L5. L5 PCs powerfully excite L5 PV cells (Angulo et al., 2003; Jiang et al., 2015; Jin et al., 2014; Pluta et al., 2015b) and likely do so in a highly convergent and non-selective manner (Bock et al., 2011; Hofer et al., 2011; Scholl et al., 2015a). In turn, L5 PV cells connect onto surrounding L5 PCs at a very high rate, and diverge massively, with one recent study estimating that each L5 PV cell inhibits >1000 L5 PCs (Packer and Yuste, 2011). This has led to the proposal that PV cells may provide a blanket of dense, non-specific inhibition to all excitatory cells (Fino et al., 2013). Despite this promiscuous connectivity, some studies suggest that the PV population may preferentially inhibit specific PC subtypes (Ye et al., 2015), though reports in L5 conflict over whether IT or PT cells receive more inhibition (Fariñas and DeFelipe, 1991; Lee et al., 2014b; Rock and Apicella, 2015). Unlike Martinotti cells (see below), PV cells generally require multiple, co-occurring excitatory inputs in order to spike. However, they are more numerous than Martinotti cells in L5, and paired recordings suggest that the conductance of a PV to PC synapse in L5 is several fold larger than that of a Martinotti to PC synapse (Kruglikov and Rudy, 2008; Xiang et al., 2002), though this is likely partially confounded by the limited ability of somatic recordings to measure distal conductances (Williams and Mitchell, 2008). Thus, PV basket cells are poised to exert direct control over the spiking output of PCs and are likely the dominant inhibitory force in L5.

PV to PC inhibition is likely to be preferentially important during certain moments of cortical activation by sensory stimuli. Excitatory synapses onto PV cells are powerful, but exhibit prominent synaptic depression, and the outputs of PV cells onto L5 PCs depress substantially during trains of action potentials (Galarreta and Hestrin, 1998; Silberberg and Markram, 2007; Xiang et al., 2002). Thus, as has been demonstrated in the hippocampus and other cortical circuits, PV neurons are typically recruited extremely reliably upon the first action potential in a PC spike train, but may stop firing shortly thereafter (Gabernet et al., 2005b; Pouille and Scanziani, 2001). Due to these temporal dynamics, PV-mediated somatic inhibition may impose a temporal window on synaptic integration in L5 PCs, preventing summation of non-coincident inputs. The net consequence of this would be to precisely time the first few spikes in a sensory-driven PC spike train (Silberberg and Markram, 2007), similar to what has been shown for PV cells in L4 for thalamocortical input (Gabernet et al., 2005b). The enforcement of such a precisely timed integration window may contribute to neuronal tuning in the whisker system (Wilent and Contreras, 2005), and enable temporal coding of stimulus features such as texture or object location (Jadhav et al., 2009; Petersen et al., 2002; Pitas et al., 2016). In agreement with this notion, *in vivo* recordings show that fast-spiking (putatively PV) cells in L5, and especially L5B, encode a high degree of information about the temporal features of a sensory stimulus and may play an important role in initiating precisely timed sequences of spikes during sensory responses (Reyes-Puerta et al., 2015a, 2015b).

Dendritic inhibition

While PV neurons chiefly inhibit the soma and proximal dendrites of L5 PCs, SOM cells are thought to primarily target PC dendrites. In fact, one of the best understood recurrent inhibitory circuits within L5 is a motif in which L5 Martinotti cells mediate frequency dependent disynaptic inhibition (FDDI) between L5 PCs. FDDI is generated when an L5 PC fires a high-frequency burst of action potentials and excites a postsynaptic L5 Martinotti cell (Silberberg and Markram, 2007). Because excitatory synapses onto Martinotti cells undergo strong short term facilitation, high frequency input from only one or a few PCs is sufficient to drive spiking in the Martinotti cell and

inhibit the dendrites of nearby PCs (Berger et al., 2010; Kapfer et al., 2007; Kwan and Dan, 2012; Silberberg, 2008). This motif is widespread and occurs in the visual, auditory, motor, and prefrontal cortices in addition to somatosensory cortex (Berger et al., 2009).

The FDDI motif allows a small number of PCs to spread inhibition widely to the surrounding network - as few as four L5 PCs firing at high frequency is enough to drive inhibition in virtually all nearby L5 PCs (Berger et al., 2010). FDDI seems to recruit a relatively small number of L5 Martinotti cells, but these diverge extensively onto the surrounding PC network (Fino and Yuste, 2011; Jiang et al., 2015). FDDI-mediated connections between PT cells appear to be structured, since FDDI occurs reciprocally between two PT cells much more often than would be expected by chance (Berger et al., 2009). This enhanced reciprocity is reminiscent of motifs found in excitatory connectivity between PCs, and suggests that the indirect connectivity created by FDDI might complement the structured subnetworks that have been observed in cortical microcircuits (Kampa et al., 2006; Perin et al., 2011; Yoshimura et al., 2005). At first glance, this result is difficult to reconcile with the promiscuous, non-selective outputs of SOM cells (Fino and Yuste, 2011); this could potentially be resolved by specificity in excitatory connectivity onto SOM cells (Otsuka and Kawaguchi, 2009, 2013; Yoshimura and Callaway, 2005), or by 'soft' structure in the synaptic weights of a densely connected PC-SOM network that shapes how Martinotti cells are recruited.

While FDDI can also occur outside of L5 (Kapfer et al., 2007), FDDI within L5 appears to be specific to PT (thick-tufted) PCs, since it is not observed between pairs of IT cells in L5 (Le Bé et al., 2007). The mechanism of this specificity is unclear, since Martinotti cells seem to target pyramidal cells non-selectively (Fino and Yuste, 2011; Jiang et al., 2015), and both PT and IT cells in prefrontal cortex receive equal amounts of SOM-mediated inhibition (Lee et al., 2014b). One possibility is that L5 IT cells are simply less efficacious than PT cells at recruiting Martinotti cells to spike (Fig. 1.2B). Future experiments utilizing paired recordings between identified L5 IT cells and Martinotti cells could resolve this. Another open question is whether PT cells can drive Martinotti-mediated FDDI onto the dendrites of L5 IT cells. If so, this disynaptic motif would represent an interesting inversion of the asymmetric connectivity from IT cells onto PT cells. Emerging evidence suggests that indirect circuits of this sort underlie stereotyped inhibitory interactions between excitatory cell types in cortex (Adesnik and Scanziani, 2010; Olsen et al., 2012; Xue et al., 2014; Yamawaki and Shepherd, 2015); these circuits might be thought of as inhibitory 'pathways' in the cortical microcircuit (Naka, 2015) and will be an important topic for future study.

More broadly, FDDI might represent an avenue for PT cells to broadcast inhibition throughout the local microcircuit. While PT cells receive and integrate input widely, they do not locally excite many other excitatory neurons, except for other PT cells (Brown and Hestrin, 2009; Harris and Shepherd, 2015; Jiang et al., 2015; Lefort et al., 2009; Yamawaki and Shepherd, 2015). However, by harnessing the massive divergence of Martinotti cells, L5 PT cells can potentially route inhibition to a large cohort of neurons across multiple layers. Burst firing by one or a small number of L5 PT cells might therefore represent a 'call to order', quieting activity throughout an entire cortical column by activating FDDI.

FDDI may serve several functional roles during sensory processing. Most simply, it can act as negative feedback, inhibiting PCs in response to sustained epochs of high activity. More subtly, it can alter synaptic integration in L5 PCs by suppressing electrogenic events in the dendrites. The apical dendrites of L5 PCs can couple with the somatic compartment via dendritic calcium and NMDA spikes (Larkum, 2013; Larkum et al., 1999a; Major et al., 2013), which are highly sensitive to dendritic inhibition (Larkum and Zhu, 2002; Larkum et al., 1999a; Marlin and Carter, 2014). By suppressing the initiation of dendritic spikes FDDI could modulate the gain of the input/output function in L5 PCs (Larkum et al., 2004; Murayama et al., 2009b), influence temporal correlations between L5 PCs (Berger et al., 2010), and shape tuning (Lavzin et al., 2012; Xu et al., 2012). In the

same vein, since dendritic spikes are thought to be crucial for burst spiking, particularly in PT cells, FDDI can control the firing mode of L5 PCs by reducing burst firing. Lastly, since L5 PC apical tufts in the barrel cortex are major targets of 'top-down' axons from higher cortical areas, including from frontal and motor areas (Manita et al., 2015b; Mao et al., 2011b; Petreanu et al., 2009, 2012), FDDI may act as a gate for feedback input to the primary somatosensory cortex. Since corticocortical feedback axons convey contextual and behavior related information to S1, FDDI is in a position to powerfully influence how context and brain state influence sensory processing (Larkum, 2013).

In addition to directly hyperpolarizing or shunting their postsynaptic targets via ionotropic $GABA_a$ receptors, a recent study has shown that SOM cells in L2/3 can also reduce the probability of release at pyramidal-to-pyramidal synapses via a form of $GABA_B$ mediated presynaptic inhibition (Urban-Ciecko et al., 2015). It is not yet known if this phenomenon affects excitatory transmission onto L5 PCs, nor if L5 SOM cells also engage in this form of inhibition.

Inhibition onto other interneurons in L5

L5 interneurons also form circuits with other interneurons. L5 PV cells form both electrical and chemical synapses with other PV cells at a high rate (Galarreta and Hestrin, 1999, 2002). These densely coupled PV networks have been implicated in driving network synchrony and generating oscillations (Hestrin and Galarreta, 2005). In contrast, SOM cells generally seem to inhibit each other rarely or not at all, but do inhibit PV cells (Jiang et al., 2015; Ma et al., 2012; Pfeffer et al., 2013; Tuncdemir et al., 2016a; Zhang et al., 2014). This asymmetric connectivity pattern among interneurons suggests that L5 SOM cell activity might redistribute inhibition along the somato-dendritic axis of L5 PCs, driving dendritic inhibition while simultaneously disinhibiting the somatic compartment by suppressing PV cells. SOM cells also inhibit other interneurons, including VIP cells (Chen et al., 2015; Jiang et al., 2015; Pfeffer et al., 2013).

In L2/3, VIP cells have emerged as specialists for disinhibition, which can release PC networks from inhibition by selectively suppressing other interneurons, especially SOM cells (Fu et al., 2014; Karnani et al., 2016a, 2016b; Lee et al., 2013; Pfeffer et al., 2013; Pi et al., 2013). This effect has not yet been investigated in deeper layers, but seems likely to occur in some form. In L5, both PV and SOM cells are innervated by VIP inhibitory synapses (Dávid et al., 2007; Pfeffer et al., 2013). In the case of PV cells, VIP boutons preferentially target the soma, suggesting that VIP-mediated inhibition likely has a powerful influence over PV spiking in the same manner that PV neurons themselves yield control over PC spiking (Hioki et al., 2013). While VIP neurons are comparatively scarce in L5, the axons of L2/3 VIP neurons descend into deeper layers and connect to L5 PCs and interneurons (Jiang et al., 2013; Walker, 2016).

The set of interneuron-to-interneuron connectivity motifs described above has recently emerged as a 'canonical' motif in cortical microcircuits (Fig. 1.2D). However, other circuits outside of this scheme are also known to exist. Within L4 of the barrel cortex, PV cells provide dense reciprocal inhibition back onto SOM cells. Studies in V1 indicate that PV to SOM connectivity is much weaker in L5 (Jiang et al., 2015; Pfeffer et al., 2013), but it may still be fairly strong in L5 of the barrel cortex (Walker, 2016). Furthermore, PV cells also inhibit VIP cells to some extent in barrel cortex and V1 (Karnani et al., 2016a; Pfeffer et al., 2013; Staiger, 1997; Staiger et al., 2002). Thus connectivity between these classes of interneurons is actually all-to-all, albeit with some connections being much stronger than others.

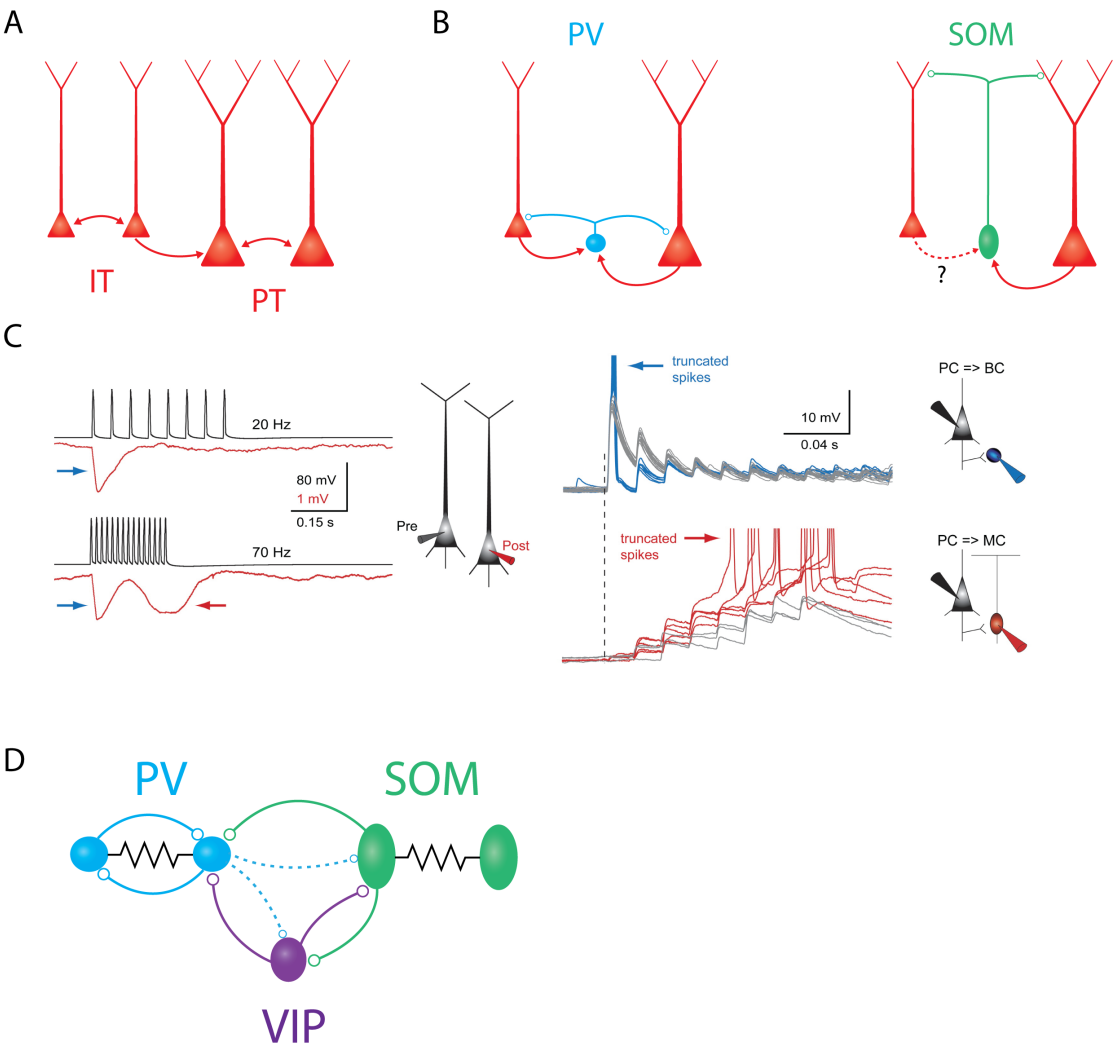

Figure 1.2 Schematic overview of major intralaminar circuits in L5.

(A) Both the slender-tufted IT cells (left) and thick-tufted PT cells (right) form homotypic excitatory synaptic connections. IT cells additionally connect to PT cells, but PT cells connect to IT cells only very rarely. IT→IT and IT→PT connections both occur at a fairly high rate (Brown and Hestrin, 2009; Kiritani et al., 2012; Lefort et al., 2009). PT→PT connectivity occurs less frequently, but is structured into strongly interconnected subnetworks (Perin et al., 2011; Song et al., 2005). **(B)** Left: Both IT and PT cells (red) excite PV cells (blue) and receive perisomatic inhibition from PV cells(Angulo et al., 2003; Kruglikov and Rudy, 2008; Silberberg and Markram, 2007). Right: SOM/Martinotti cells (green) inhibit the distal dendrites of both PT and IT cells. These interneurons receive excitatory input from PT cells, but it is unknown if IT cells also excite them. **(C)** Experimental evidence for disynaptic inhibitory circuits between L5 PCs. Left: Example traces showing two types of disynaptic inhibitory responses in a postsynaptic PC (red) driven by spiking in a presynaptic PC (black). Firing the presynaptic cell at 20 Hz (top traces) drives a transient, frequency-independent disynaptic inhibitory response (indicated by the blue arrow) which is likely mediated by activation of a PV/basket cell at the onset of spiking. Firing the same cell at 70 Hz (bottom traces) reveals a second, frequency-dependent form of disynaptic inhibition (indicated by the red arrow) which is likely due to delayed recruitment of a (SOM) Martinotti cell. Right: Membrane potential responses of different interneurons to high-frequency stimulation of an L5 PC. Top: (PV) basket cells receive strong excitatory postsynaptic potentials (EPSPs) at the onset of stimulation, which can drive subthreshold (gray traces) or suprathreshold depolarization (blue traces). In either case, the postsynaptic response is initially strongly, but then depresses rapidly. Bottom: EPSPs in Martinotti cells are weak and unreliable at the onset of L5 PC firing, but these facilitate and can eventually drive postsynaptic spiking, leading to FDDI (gray traces, subthreshold responses, red traces- suprathreshold responses). Reproduced with permission from Silberberg and Markram, 2007. **(D)** Schematic of interneuron-to-interneuron connectivity in L5. PV cells (blue) form reciprocal chemical and electrical synapses with other PV cells. SOM cells are electrically but not chemically connected to other SOM cells, and form chemical synapses onto PV cells and VIP cells. VIP cells inhibit PV cells and SOM cells. Dashed lines indicate two weaker outputs from PV cells onto SOM cells and VIP cells.

Feed-forward, translaminar inhibition of L5

In addition to intralaminar circuits, L5 is subject to a number of inhibitory influences from other cortical layers in the local circuit. Translaminar inhibition of L5 can derive either from input from

GABAergic cells in other cortical layers that target L5 PCs, or from the synaptic activation of GABAergic cells within L5 through translaminar excitatory afferents. With respect to the former scenario, studies using axonal reconstruction, paired intracellular recordings, and viral tracing methods indicate that L5 PCs receive input from a substantial number of interneurons in L2/3, L4, and L6, albeit at a lower frequency than from L5 interneurons (DeNardo et al., 2015; Helmstaedter et al., 2009a, 2009b, 2009c; Jiang et al., 2013; Lee et al., 2014a). Connections from several different varieties of interneurons in layers 1 and 2/3 have been observed onto L5 PCs (Jiang et al., 2013, 2015). Interestingly, different L2/3 interneurons appear to target specific dendritic domains of L5 PCs (Jiang et al., 2013), a result which has been mirrored by recent work in the hippocampus (Bloss et al., 2016). Since dendritic inhibition can be quite spatially precise (Chiu et al., 2013; Marlin and Carter, 2014; Müllner et al., 2015), this organization might allow for cell-type specific control over the distinct spatial domains of the various types of dendritic spiking that occur in L5 PCs (Larkum et al., 2009). Studies in mouse V1 have described a translaminar inhibitory circuit in which a subclass of L6 PV neurons can powerfully suppress PCs across all other cortical layers, including L5 (Bortone et al., 2014; Olsen et al., 2012). If this circuit also exists in the barrel cortex, it could play a major role in L5 gain control during sensory activity.

Despite the existence of these direct translaminar inhibitory pathways, optogenetic experiments mapping inhibitory inputs to L5 PCs (either from GABAergic non-specifically, or selectively from PV neurons) suggest that inhibition onto L5 PCs most strongly originates from interneurons within L5 (Brill and Huguenard, 2010; Kätzel et al., 2011; Pluta et al., 2015b; Schubert et al., 2001, 2006). Thus the major source of translaminar inhibition to L5 PCs is more likely to be through the synaptic recruitment of L5 interneurons by afferent axons from other cortical layers (Fig. 1.3B).

With the exception of L1, all cortical layers make excitatory axonal projections onto L5, which can recruit L5 interneurons to fire. This recruitment, often termed "feed-forward inhibition" (FFI), is a nearly ubiquitous motif in cortical microcircuits where afferent excitatory input simultaneously recruits local inhibitory neurons that provide inhibition to the same cells receiving excitation. Circuits for FFI have been well studied at the projections from thalamus to L4 (Bruno and Simons, 2002; Cruikshank et al., 2007, 2010; Daw et al., 2007; Gabernet et al., 2005b; Gibson et al., 1999; Sun, 2006; Swadlow, 2003; Wilent and Contreras, 2005), and from L4 to L2/3 (Adesnik et al., 2012; Elstrott et al., 2014; Helmstaedter et al., 2008; House et al., 2011; Li et al., 2014; Xu and Callaway, 2009; Xue et al., 2014). In these pathways, incoming axons primarily recruit PV interneurons in the recipient layer. PV-mediated FFI serves many functions: it enhances the temporal specificity of incoming signals (Gabernet et al., 2005b; Pouille and Scanziani, 2001), extends the dynamic range of the downstream population response (Pouille et al., 2009a), and imposes a synchrony filter on incoming inputs (Bruno, 2011). FFI is surprisingly poorly understood in L5. We recently described a translaminar inhibitory circuit in which descending excitatory axons from L4 synapses on L5 PV neurons, which in turn drives inhibition in L5 PCs (Pluta et al., 2015b). FFI mediated through this circuit has the net effect of suppressing L5 PCs, sharpening their spatial tuning to tactile stimuli. Although it remains unexplored, we hypothesize that the L4-L5 translaminar inhibitory circuit may also be crucial for the precise timing of touch-evoked spiking in L5 PCs. Another recent study found that L6 PCs can drive disynaptic inhibition onto L5 PCs, specifically to PCs in L5a (Kim et al., 2014). Interestingly, both of these studies found that afferent input to L5 was much more effective at driving PV neurons than Martinotti cells. Thus inhibition in the L4→L5 and L6→L5 pathways appears to be organized similarly to other translaminar circuits by operating through PV neurons.

Notably, there is a gap in our understanding of FFI in the L2/3 to L5 pathway, one of the densest projections in the cortical microcircuit. Stimulation of L2/3 generates robust FFI in L5 PCs (Adesnik and Scanziani, 2010; Pouille et al., 2009a), but preliminary evidence suggests that the mechanisms of L2/3→L5 FFI may be unique. Surveys of connectivity onto L5 PV cells in S1 (Jin et al., 2014; Pluta et al., 2015b), V1 (Jiang et al., 2015), and other cortical areas (Apicella et al., 2012; Otsuka and Kawaguchi, 2009) expose only moderate excitatory input from L2/3. In contrast, L5 Martinotti cells appear to receive strong input from L2/3 (Apicella et al., 2012; Jiang et al., 2015; Kapfer et al., 2007; Otsuka and Kawaguchi, 2009). This suggests that L2/3→L5 FFI may operate primarily through SOM, rather than PV neurons, and thus predominantly routes inhibition to the L5 PC dendrites, similar to what occurs between the olfactory bulb and the piriform cortex (Stokes and Isaacson, 2010). Because of the filtering cable properties of the apical dendrites, dendritic FFI is likely suboptimal for enforcing rigid temporal control over the somatic spiking of L5 PCs per se, but is instead poised to directly regulate the integration of excitatory inputs from L2/3 PCs to the apical compartment of an L5 PC.

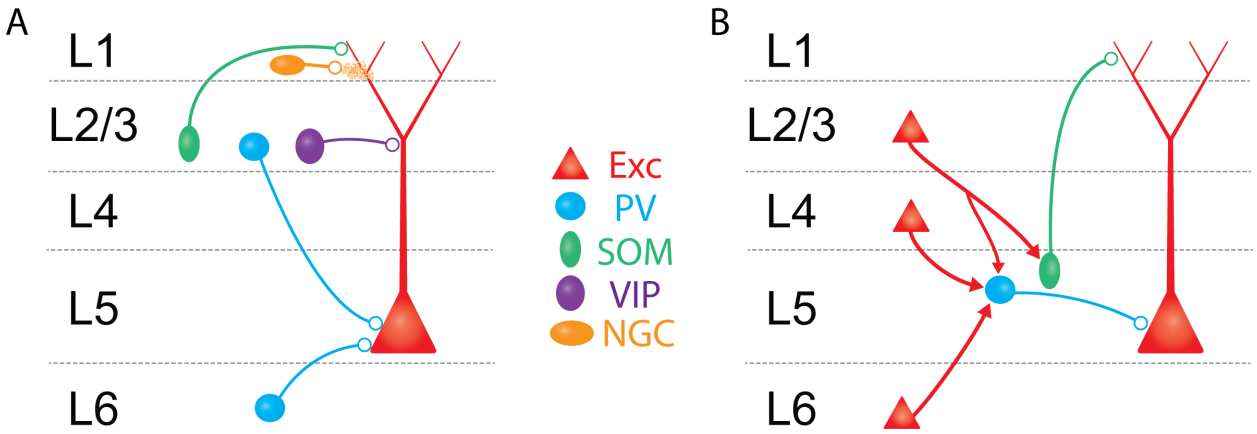

Figure 1.3. Schematic overview of major translaminar inhibitory circuits impinging on L5 PCs.
(A) Inhibition arises from multiple types of interneurons outside of L5. In L1, 5HT3aR/Neurogliaform cells (NGCs, mustard) inhibit L5 PCs via volume release of GABA. In L2/3, SOM/Martinotti cells (green) and VIP cells (purple) target the apical dendrites of L5 PCs, while PV/basket cells (blue) synapse onto the perisomatic compartment via descending axons. In L6, translaminar PV/basket cells inhibit L5 PCs via ascending axons. **(B)** Excitatory translaminar pathways recruit L5 interneurons. Excitatory cells in L2/3, L4, and L6 can target PV/basket cells. Additionally, L2/3 PCs synapse onto L5 SOM/Martinotti cells.

Interareal recruitment of L5 inhibition

Long-range axons from the thalamus, motor cortex, and contralateral S1 that innervate L5 PCs, also recruit L5 inhibitory neurons. For example, ascending axons from primary thalamus (VPM) can recruit both L5 PV and SOM cells driving various forms of FFI. Interestingly, as described for FFI circuits in hippocampal CA1 (Pouille and Scanziani, 2004), during sustained activity, VPM afferents will initially recruit L5 PV cells, but then switch to driving a subpopulation of L5 non-Martinotti SOM cells labeled by the X94 line (Tan et al., 2008), although it is still unclear if these L5 X94 neurons project inhibition onto L5 PCs. In contrast, L5 Martinotti cells are not driven by VPM afferents and thus do not appear to participate in thalamocortical FFI (Cruikshank et al., 2010; Ji et al., 2015). Motor cortex afferents to S1 appear to target L5 PV neurons and not L5 Martinotti cells (Kinnischtzke et al., 2014), whereas inputs from contralateral cortex drive inhibition in L5 PCs through at least two distinct circuits. First, callosal projections likely drive FFI using the familiar motif of activating L5 PV neurons, though this has not yet been directly demonstrated in barrel cortex (Karayannis et al., 2006; Lee et al., 2014b; Rock and Apicella, 2015). However, these

projections also drive an unusual form of slow, GABAB-dependent inhibition onto the dendrites of L5 PCs, which is mediated by the recruitment of neurogliaform cells in layer 1 (Palmer et al., 2012, 2013). Because callosal projections can synapse onto both the basal and apical compartments of L5 PCs, these dual pathways may allow FFI to be spatially matched to the same subcellular compartments as feed-forward excitation. As many other long-range inputs also form synapses at the distal apical tufts of L5 PCs (Cauller and Connors, 1994; Cauller et al., 1998; Larkum and Zhu, 2002; Manita et al., 2015b; Mao et al., 2011b; Petreanu et al., 2009, 2012; Xu et al., 2012), it will be interesting to see if these circuits also possess similar capabilities to generate dendritic inhibition.

How might inhibition contribute to communication in these long-range circuits? Long-range afferents to S1 can convey a variety of information, including data on whisker kinematics (Curtis and Kleinfeld, 2009; Petreanu et al., 2012), attentional focus (Harris, 2013; Zagha et al., 2013), and cognitive features in decision-based tasks (Yang et al., 2016). FFI in these circuits will powerfully influence how activity in these afferent pathways is integrated with ongoing local cortical activity. Do these circuits incorporate all L5 PCs in the same manner? PT and IT cells both send and receive long-range inputs in a cell-type specific manner. For example, since the axons of PT cells do not cross the corpus callosum, only L5 IT cells will be able to directly activate the circuits for interhemispheric inhibition mentioned above. Furthermore, while both PT and IT cells receive long-range callosal input, two recent studies found that optogenetic activation of callosal fibers generates inhibition in a manner specific to cell-type. Interestingly, this effect appears to be regionally specialized. In auditory cortex IT neurons are more strongly inhibited, while in prefrontal cortex PT neurons are more strongly inhibited (Lee et al., 2014b; Rock and Apicella, 2015). This type of specialization is intriguing, since it might provide a means to direct and gate the flow of activity between different regions of the cortex. More research is needed to determine if similar specificity is seen in other cortical areas or other types of long-range circuits.

Future directions

Many recent advances in the understanding of cortical inhibitory circuits can be attributed to the widespread adoption of cell-type specific Cre recombinase driver lines (Taniguchi et al., 2011a). These lines have allowed investigators to target subsets of cortical interneurons with optical reporters for targeted electrophysiological recording or functional imaging. Experiments using these lines *in vivo* have revealed how the various interneuron subtypes modulate their responses to different sensory stimuli (Adesnik et al., 2012; Bock et al., 2011; Gentet et al., 2012; Hofer et al., 2011; Kerlin et al., 2010; Ma et al., 2010; Runyan et al., 2010; Scholl et al., 2015a) and shifting behavioral states (Fu et al., 2014; Lee et al., 2013; Pi et al., 2013; Polack et al., 2013; Reimer et al., 2014). By expressing optogenetic actuators rather than reporters in these inhibitory cell types, many groups have begun to manipulate interneurons with cell-type specificity to assess their specific contributions to cortical computation and behavior (Adesnik et al., 2012; Atallah et al., 2012; Lee et al., 2012; Seybold et al., 2015; Wilson et al., 2012).

Nevertheless, the recent and widespread reliance on just a few Cre lines (particularly the PV-SOM- and VIP-Cre lines) can also lead to unintended problems. First, these lines are not completely non-overlapping. Up to ~10% of Cre expressing cells in the widely used SOM-IRES-Cre line may actually be PV expressing, fast-spiking interneurons (Hu et al., 2013). Second, the availability of only a few Cre driver lines for interneurons, along with the paucity of more specific alternatives, has ushered in a new era of 'lumping' in the study of interneurons. While this reunification is conceptually beneficial in many ways, it is undoubtedly an over simplification; each of these major subtypes (PV, SOM and 5HT3aR) are highly heterogeneous groups, as described above; for example, the PV-Cre line labels both basket and chandelier cells, while the SOM-Cre line labels both Martinotti and X94 neurons. Third, and perhaps most problematically, all of these Cre lines label

interneurons non-specifically across all cortical layers. This is particularly an issue for *in vivo* optogenetic manipulations where one-photon illumination will non-specifically activate or suppress Cre-expressing interneurons across all cortical layers. This makes it difficult to ascribe results gained with these manipulations to interneurons in specific laminae.

However, there are potential solutions to these problems. The first would be the development and adoption of new transgenic lines that target highly specific inhibitory cell types (Shima et al., 2016; Taniguchi et al., 2011b). In the short term, further characterizing existing Cre-driver lines that might fractionate the three major interneuron subgroups, such as the Chrna2-Cre line for SOM cells (Leão et al., 2012), or retrofitting existing highly specific GFP lines for Cre expression (Tang et al., 2015a), could be extremely valuable. In the long term, advances in single cell transcriptional profiling of cortical neurons could provide quantitative genetic data which may aid in the much more complete delineation of new GABAergic cell types (Armañanzas and Ascoli, 2015; Tasic et al., 2016b; Zeisel et al., 2015). At the same time, these data will hopefully identify highly differentially expressed genes between the various subtypes that will provide genetic handles to develop transgenic lines (including Cre reporters) that will permit targeting and optogenetic control of many more subclasses of interneurons. While doing so may depend on sophisticated intersectional strategies involving multiple recombinases, such technology already exists.

As we alluded to above, the recent explosion of functional information on inhibitory subtypes *in vivo* has mostly focused on superficial interneurons due to the technical difficulty of imaging deeper cells in the cortex due to light scattering, and the practical challenges of maneuvering recording pipettes into deeper layers under visual guidance. A number of recent technical advantages should overcome these challenges. These include adaptive optics for deeper *in vivo* imaging (Wang et al., 2015), implantable optics such as prisms (Andermann et al., 2013) or GRIN lenses (Barretto et al., 2009), three photon imaging (Horton et al., 2013), regenerative amplification of ultrafast pulses (Mittmann et al., 2011), and red-shifted fluorophores that are much less affected by optical scattering in brain tissue. Recent advances in red-shifted calcium and voltage dyes hold particular promise (Gong et al., 2015; Huang et al., 2015; Inoue et al., 2014).

New optical methods will also open new avenues for manipulation of interneuron activity. Novel techniques for spatial light modulation are poised to provide unprecedented optogenetic precision, enabling experimenters to arbitrarily target manipulations to single cells or even specific ensembles of neurons (Bovetti and Fellin, 2015). Furthermore, these manipulations are flexible and can be altered online, opening the door to new methods for adaptive/closed-loop experiments to probe network dynamics and structure (Grosenick et al., 2015). However, even in the best of circumstances it is not straightforward to interpret optogenetic perturbations of neurons embedded in recurrent networks (Kumar et al., 2013; Seybold et al., 2015). To account for this, it will be necessary to embrace more complicated, nonlinear models of cortical dynamics- and to incorporate these into experimental design (Litwin-Kumar et al., 2016; Rubin et al., 2015). By combining these new technologies with much more specific and sophisticated genetic tools, it should be possible to make considerable progress in understanding the function and impact of L5 interneurons in the coming few years

Acknowledgements

H.A. is a New York Stem Cell Foundation Robertson Investigator. This work was supported by NINDS grant DP2NS087725-01 and NEI grant R01EY023756-01. We thank Jenny Brown, Evan Lyall, Alan Mardinly, Ian Oldenburg, Ming-Chi Tsai, and Julia Veit for helpful comments and feedback.

The role of inhibition in the canonical microcircuit

Inhibition is essential to every aspect of cortical computation (Isaacson and Scanziani, 2011). From the start, models of the canonical microcircuit have included inhibition as a key component (Douglas et al., 1989; Potjans and Diesmann, 2011, 2014). However, inhibition is usually incorporated in a relatively simplified manner. At the same time, the advent of new genetic technologies in recent years has produced an explosion of new knowledge about inhibitory circuits, cell-types, and computation (Tremblay et al., 2016). As reviewed above, it is now apparent that many functionally distinct inhibitory systems exist within the cortical circuit. A major challenge for cortical physiologists is to determine exactly how these systems integrate with the excitatory pathways of the neocortex. One key question is to determine the extent to which excitatory-inhibitory interactions are specific or non-specific. Ample evidence for specificity in inhibitory circuits exists. Interneurons connect with other interneurons in a highly cell-type dependent manner (Jiang et al., 2015; Pfeffer et al., 2013), and also exhibit specific preferences in how they target the subcellular compartments of excitatory neurons (Jiang et al., 2013; Markram et al., 2004). At the same time, at the level of cells and networks, evidence is mixed for whether interneurons wire up with excitatory cells in a specific fashion, with some studies pointing to specificity (Krook-Magnuson et al., 2012; Lu et al., 2017; Wilson et al., 2017; Znamenskiy et al., 2018) and others pointing to a non-selective scheme (Fino and Yuste, 2011; Fino et al., 2013; Hofer et al., 2011; Karnani et al., 2014; Packer and Yuste, 2011; Packer et al., 2012; Scholl et al., 2015b).

Resolving this issue is important, since the action of the excitatory components of the microcircuit can only be understood when inhibition is taken into account. Previous work by my advisor suggested that optogenetically activating specific excitatory cell-types generates unique, cell-type specific mixtures of excitation and inhibition in downstream (Adesnik and Scanziani, 2010). This work and other similar studies (Adesnik, 2018; Olsen et al., 2012; Yamawaki and Shepherd, 2015)support the idea that interactions between excitatory neurons might exhibit characteristic, pathway-specific excitation/inhibition ratios (Naka, 2015). This implies that in order to understand the action of an excitatory pathway in the cortical microcircuit, it necessary to take into account both its monosynaptic excitatory effects and its polysynaptic inhibitory effects. The following chapter focuses on exactly this.

Chapter 2: A direct translaminar inhibitory circuit tunes cortical output

Foreword

In the next chapter, I present work from the first half of my doctorate which examines a circuit linking L4 and L5. One of the central experiments in this work involved perturbative manipulations of the excitatory cells of L4, which produced the surprising results alluded to in an earlier section (see "Layer-specific perturbation: insights and challenges" in Chapter 1). I had the great pleasure of collaborating very closely on this project with my colleague Dr. Scott Pluta. My primary contribution to this work involved mapping the inhibitory pathway that we advance as a mechanism for our counter-intuitive *in vivo* results. Many others made crucial contributions to this work; notably, Dr. Julia Veit and my advisor, Dr. Hillel Adesnik collected key datasets.

Pluta, S.*, Naka, A.*, Veit, J., Telian, G., Yao, L., Hakim, R., Taylor, D., and Adesnik, H. (2015). A direct translaminar inhibitory circuit tunes cortical output. *Nature Neuroscience* 18 1631-1640

Summary

Anatomical and physiological experiments have outlined a blueprint for the feed-forward flow of activity in cortical circuits: signals are thought to propagate primarily from the middle cortical layer, L4, up to L2/3, and down to the major cortical output layer, L5. Pharmacological manipulations, however, have contested this model and suggested that L4 may not be critical for sensory responses of neurons in either superficial or deep layers. To address these conflicting models we reversibly manipulated L4 activity in awake, behaving mice using cell-type specific optogenetics. In contrast to both prevailing models, we show that activity in L4 directly suppresses L5, in part by activating deep, fast spiking inhibitory neurons. Our data suggest that the net impact of L4 activity is to sharpen the spatial representations of L5 neurons. Thus we establish a novel translaminar inhibitory circuit in the sensory cortex that acts to enhance the feature selectivity of cortical output.

Introduction

The sensory neocortex is organized along its vertical axis into discrete layers (Gilbert and Kelly, 1975)[1, 2]. A wealth of data characterizing the anatomy and synaptic connectivity of cortical neurons has implied the existence of a core circuit arranged vertically across these layers (Douglas and Martin, 2004; Feldmeyer, 2012; Lefort et al., 2009; Thomson, 2007). According to this model, thalamus drives L4, L4 drives L2/3, and L2/3 drives L5 (Douglas and Martin, 2004). However, alternative synaptic pathways within the cortex – both local and long range – are known to exist, and evidence suggests that these alternative pathways might even be key drivers of cortical output, acting independently of L4 activity (Constantinople and Bruno, 2013; Malpeli, 1983) .

One recent study pharmacologically inactivated superficial cortical layers in sedated rats and found no effect on sensory responses in L5, suggesting a disconnect between the upper and lower layers of the cortex during sensory processing (Constantinople and Bruno, 2013). Other studies found that silencing L4 in the visual cortex of the anesthetized cat had no effect on the responses of the L2/3 neurons (Malpeli, 1983; Mignard and Malpeli, 1991). Precise latency analysis of sensory evoked spikes in the rodent's barrel cortex also suggest a more complex picture than proposed by the canonical circuit model (Armstrong-James et al., 1992). However, no study has directly addressed these competing models using cell type-specific manipulations or in awake, behaving animals – a state in which cortical dynamics are known to be very different from anesthetized, sedated, or non-alert conditions (Haider et al., 2013; Krupa et al., 2004b; Niell and Stryker, 2010). Thus the neural circuits that govern the flow of sensory activity in the cortex under physiological conditions remain largely unresolved.

Using layer specific optogenetic manipulation, we found that L4 activity in awake, behaving mice simultaneously drives L2/3, but suppresses responses in L5. The descending suppression of L5 is mediated significantly by a direct, translaminar circuit in which L4 excitatory neurons drive fast spiking inhibitory neurons in L5 – a translaminar connection not previously recognized. The functional consequence of this L4 to L5 suppression is to sharpen sensory representations of L5 cortical projection neurons. This circuit is active in both somatosensory and visual cortex, suggesting it may represent a conserved feature of the cortical circuit to improve sensory coding at the primary output stage of the neocortex.

Results

Layer specific optogenetic suppression of L4 activity in awake, behaving mice

To directly assess the functional impact of L4 activity within a physiological context, we expressed the optogenetic silencer eNpHR3.0-YFP (Gradinaru et al., 2010) in L4 excitatory neurons of the rodent somatosensory cortex using a Cre-dependent AAV vector (Atasoy et al., 2008) and the scnn1-tg3-Cre (Madisen et al., 2010) mouse. In this strain transgene expression is largely specific to excitatory neurons in L4, with the 'barrels' of rodent somatosensory cortex clearly visible (Fig 1a and Supp. Fig. 1a, b). Thus we could use Cre-dependent AAV viral expression of optogenetic actuators in this Cre line to achieve specific manipulation of L4 activity.

Next we devised an experimental preparation in which we could generate reproducible sensory-evoked responses in the barrel cortex of awake, behaving mice. Mice were head-fixed and habituated to running on a free-spinning circular treadmill (Fig. 1b). While running, mice rhythmically sweep their whiskers back and forth. This allowed us to present a tactile stimulus (a vertical bar) to different positions in the whisking field and drive reproducible, contact-evoked responses in the barrel cortex under conditions of active sensation (Fig. 1c) (Krupa et al., 2004b). Neural activity was recorded with laminar silicon probes. We confirmed the laminar depth of electrodes on the silicon probe using a combination of approaches (Supp. Fig. 2). This allowed us to assign each isolated unit to a specific layer in the barrel cortex (Supp. Fig. 2d, e). We recorded units across multiple layers (L2 – L6), often in the same experiment.

We separated regular spiking (RS) from fast spiking (FS) cells (Niell and Stryker, 2008) (see Methods), with the former group largely representing excitatory cells, and the latter primarily corresponding to inhibitory neurons (although a subset of FS neurons may correspond to fast spiking excitatory neurons (Nowak et al., 2003)). Although L5 excitatory neurons can be separated into regular spiking and bursting subtypes (Agmon and Connors, 1992), the majority of non-FS neurons in L5 showed a heterogeneous distribution of a tendency to spike in bursts (see Methods and Supp. Fig. 11) and are thus considered as one group, referred to here as 'RS' cells.

Under these conditions, cortical neurons showed sensory responses that were well tuned to the spatial position of the vertical bar, consistent with previous studies (Curtis and Kleinfeld, 2009; O'Connor et al., 2010) (Fig. 1d). This tuning likely reflects a combination of the somatotopic organization of barrel cortex (which whiskers contact the bar at a given position) and information about the relative position of the whiskers at the time of contact with the stimulus (Curtis and Kleinfeld, 2009; Diamond et al., 2008). At each position two to three whiskers contacted the stimulus bar, with 3-5 out of 8 stimulus positions contacting the principal whisker. Nearby units, sorted off the same electrode, typically exhibited co-tuning for space, while the preferred spatial position of units varied across the whisker map (Supp. Fig. 5f, g).

Illuminating the cortical surface with red light (30-80 mW, 1mM optical fiber) reliably suppressed the activity of L4 units (Fig. 1e-h), demonstrating the effectiveness of our optogenetic approach. On a unit-by-unit basis the majority (64%) of L4 RS units exhibited a significant reduction in firing during illumination, while the remaining units showed no significant change – perhaps reflecting incomplete infection of the eNpHR3.0 virus in L4 and/or incomplete penetrance of Cre expression.

The illumination area was set to suppress L4 across nearly all of barrel cortex. Importantly, the same light level proportionally reduced L4 firing across all stimulus positions (Supp. Fig. 1c), indicating that we could reduce L4 activity by the same fraction for both preferred and non-preferred stimuli. Illumination in control mice expressing only YFP had no significant effect (Supp.

Fig. 3). Moreover, suppressing L4 optogenetically did not result in changes the kinematics of whisking (Supp. Fig. 4). Therefore with this experimental system we could reliably and specifically test the functional impact of L4 on cortical sensory activity in the absence of any changes in the sensory stimulus.

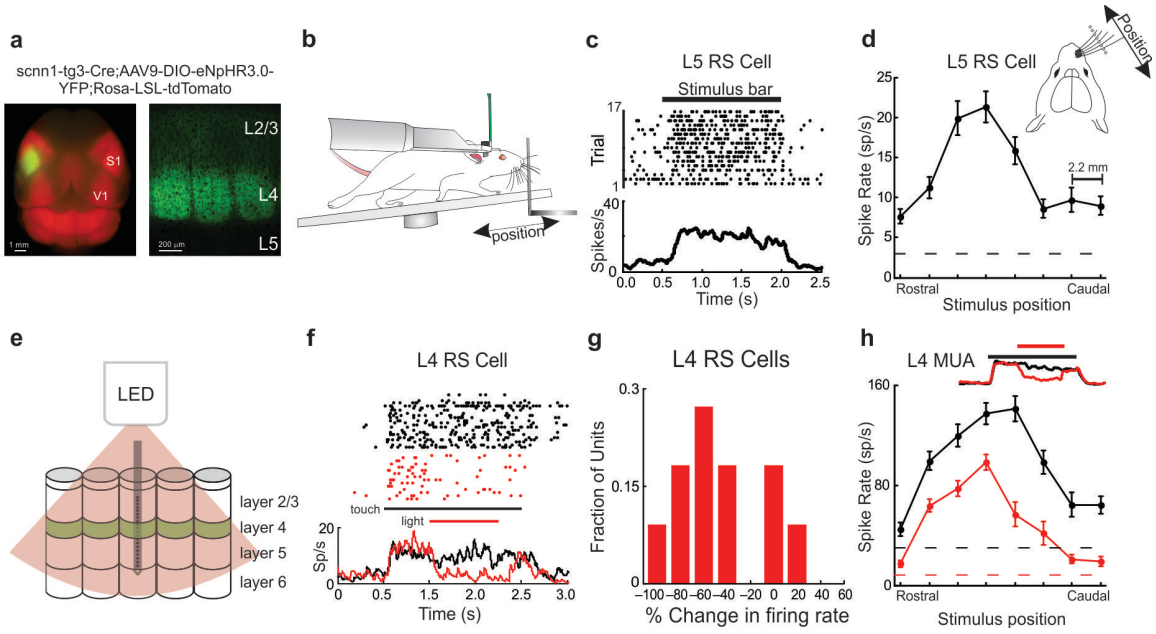

Figure 2.1 Optogenetic control of cortical layer 4 during active sensation.

a, Left: whole brain epifluorescence image of the scnn1-tg3-Cre line crossed to a ROSA26-LSL-tdTomato reporter line. The left barrel cortex was injected with an eNpHR3.0-YFP Cre-dependent virus (yellow). Right: coronal section through the barrel cortex showing eNpHR3.0-YFP expression. b, Schematic of the experimental configuration. A mouse is head-fixed on a free-spinning circular treadmill. A vertical bar moved by a stepper motor acts as a tactile stimulus. c, Raster plot (top) and peri-stimulus time histogram (PSTH, bottom) of an isolated RS unit from L5 during presentation of the tactile stimulus. d, Plot of firing rate vs. stimulus position of the same L5 unit showing tuning to stimulus position. Dashed grain line indicates spontaneous firing in the absence of a stimulus. e, Schematic of the optogenetic suppression of L4 neurons with light. f, Raster plot (top) and PSTH (bottom) of an L4 RS unit that was completely suppressed by illumination of the cortex. Black line indicates the tactile stimulus; red line indicates the period of illumination. g, Frequency histogram of the percent change in firing to the preferred stimulus of L4 RS units during illumination. Mean reduction in firing was 35±14% ($p = 9.1 \times 10\text{-}6$, n = 11 cells from 6 mice, 2-way ANOVA, f(1)=21). h, PSTHs (top) and tuning curves (bottom) of multi-unit activity in L4 during illumination of the cortex. Dashed lines indicate average spontaneous firing rates during control (black) and illumination conditions (red). All error bars are s.e.m.

L4 drives L2/3 but suppresses L5

The major prediction of the conventional model of the neocortex is that inactivating L4 would reduce firing of neurons in L2/3 and L5, whereas the alternative models would predict little or no effect on either L2/3 (Malpeli, 1983) or L5 (Constantinople and Bruno, 2013). To address these contrasting notions we optogenetically suppressed L4 while recording neuronal firing across the cortical layers. First, we focused on neurons in L2/3. We analyzed firing rates under both control and photo-suppression conditions at the steady-state portion of the sensory response (see Fig. 1). Photo-hyperpolarizing L4 neurons resulted in a reduction in the sensory responses of L2/3 RS units (Fig. 2a). At their preferred stimulus position, the firing rates of L2/3 RS units were reduced by 39.3±8% ($p = 3.9 \times 10^{-6}$, n= 33 cells from 5 mice, paired t-test, t(32) = 5.5). This result confirms that L4 input is involved in driving L2/3 RS neuron activity and provides *in vivo* validation of one prediction of the conventional model of the neocortex.

Next we focused on the functional impact of L4 suppression on L5 RS neurons. In contrast to all existing models of cortical function, we found that L4 photo-hyperpolarization enhanced L5

firing (Fig. 2a). On a unit by unit basis, 45/75 L5 RS cells exhibited a significant (threshold: $p < 0.05$, 2-way ANOVA) enhancement during sensory stimulation. We computed an optogenetic modulation index (OMI, see Methods) for each isolated unit that characterized how L4 photo-suppression affected its firing rate. A histogram of OMI (averaged across all conditions) versus cortical depth shows that illumination of the cortex suppressed L4 and L2/3 (OMI < 0), but facilitated L5 (OMI > 0) (Fig. 2b).

Next we tested whether generating activity in L4, via expression of ChR2, would produce the opposite effects; namely, facilitating activity in L2/3 while suppressing L5. The light intensity was set so as to optogenetically generate firing rates in L4 neurons that were similar to what we observed physiologically (4.8±1.6 Hz). Under these conditions, photo-activation of L4 facilitated the activity of L2/3 RS units (OMI: 0.37±0.15, n=19, Fig. 2c) while simultaneously suppressing activity in L5 (OMI: –0.27±0.09, n=49, Fig. 2c). A plot of OMI versus cortical depth quantifies this effect across layers (Fig. 2d). Although optical stimulation cannot recapitulate the spatiotemporal characteristics of sensory drive, taken together with the previous experiments using photo-suppression, these results indicate that L4 activity is both necessary and sufficient to positively control neural activity in L2/3 while negatively controlling L5 responses.

To examine if the L4-mediated suppression of L5 activity was a general feature of cortical circuits, we repeated the same experiment in mouse primary visual cortex (V1). Head-fixed, running mice were presented with drifting gratings at various orientations, sizes and contrasts (see Methods). Photo-hyperpolarization of L4 neurons in V1 had a similar effect of enhancing L5 activity for a wide range of stimuli (Fig. 2e, f). Illumination in control mice had no effect (3.5±2.7%, $p=0.82$, $n = 23$ units from 4 mice, Wilcoxon signed rank test, $z = -0.23$). Conversely, photo-stimulation of L4 in mice expressing ChR2 drove a significant suppression in the majority (24/45 units) of units in L5 (mean firing rate reduction: 55±5.7%, $p = 1.81 \times 10^{-5}$, $n = 24$ units from 3 mice, Wilcoxon signed rank test, $z = 4.29$). This suggests that suppression of L5 by L4 activity is likely to be a conserved feature across sensory cortical areas.

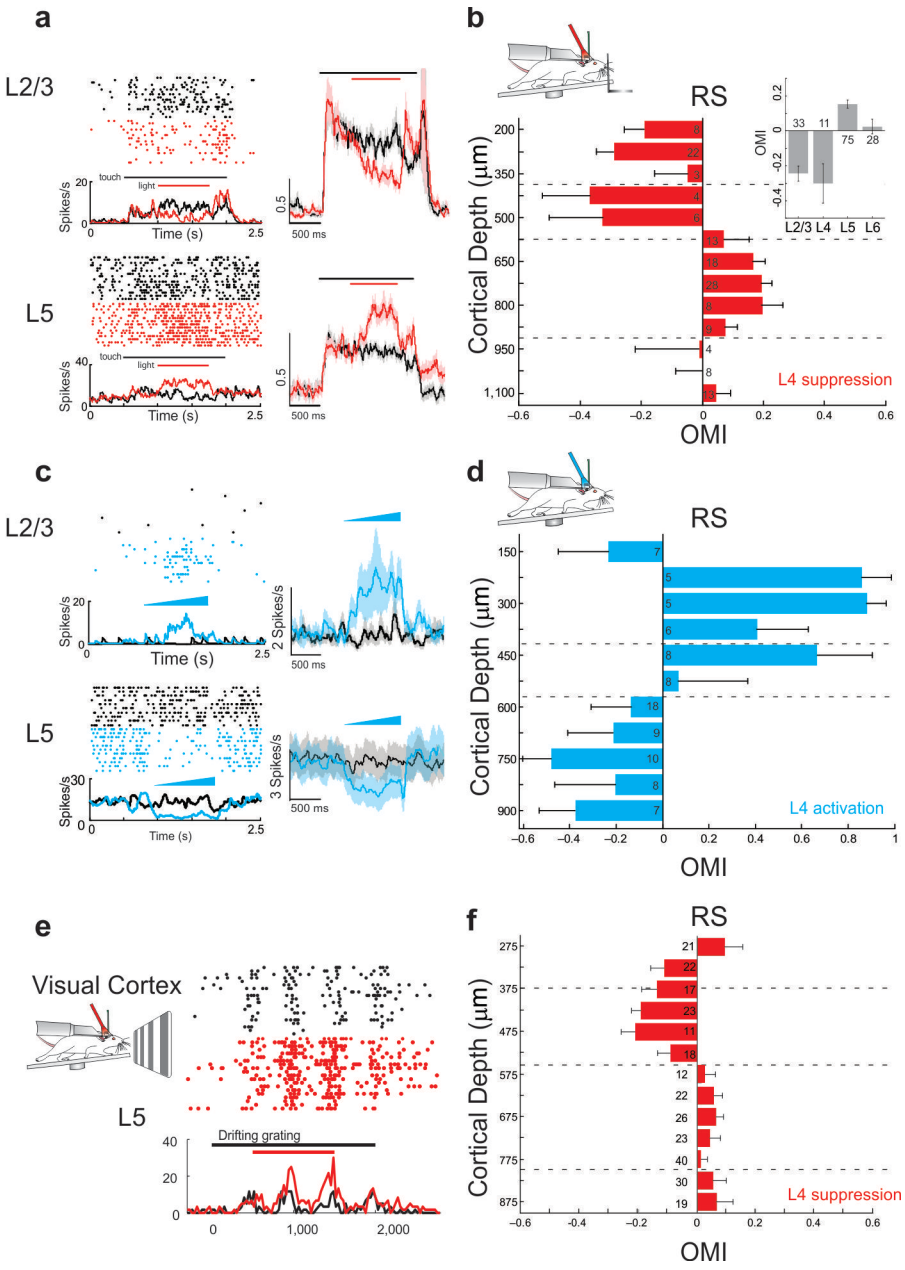

Figure 2.2 Optogenetic suppression of L4 deactivates L2/3 but facilitates L5.

a_i, Left: Raster plot (top) and PSTH (bottom) of a representative isolated L2/3 RS unit under control conditions (black) and during photo-suppression of L4 (red). Right: Population PSTH showing a reduction in evoked response ($p = 3.9 \times 10^{-6}$, n= 33 units from 5 mice, paired t-test, $t(32) = 5.5$) of L2/3 RS units during suppression of L4. a_{ii}, Left: As in a_i) except for an L5 RS unit. Right: Population PSTH (n=75) showing an enhancement in firing ($p < 10^{-6}$, n = 75 cells from 6 mice, 2-way ANOVA, $f(1) = 27$) during suppression of L4. b, Histogram of optogenetic modulation index (OMI) during photo-suppression of L4 for all isolated RS units binned according to depth in the cortex. Each bin contains units spanning 25 µm above and below its marked center. c-d, As in a-b) except for photo-activation of L4 with ChR2 (L2/3: $p = 0.015$, n = 19 units from 3 mice, Wilcoxon signed rank test, $z = 2.4$; L4: $p = 0.0026$, n = 20 units from 3 mice, Wilcoxon signed rank test, $z = 3.0$; L5: $p = 0.046$, n = 49 units from 3 mice, Wilcoxon signed rank test, $z = 2.4$). Blue ramp indicates time of illumination. e, Left: schematic of the recording configuration from visual cortex. Right: Raster plot (top) and PSTH (bottom) for an example L5 RS unit during photo-suppression of L4 in V1 (red) and under control conditions (black). f, Histogram of OMI vs. cortical depth for all isolated RS units in V1 during photo-suppression of L4. All error bars are s.e.m. L4: 24±4.9% reduction in mean firing rate, $p < 10^{-6}$, n = 59 cells from 11 mice, Wilcoxon signed rank test, $z = 5.78$; L5: 14.2±3.9% enhancement in mean firing rate, $p = 9.78 \times 10^{-5}$, n = 123 units from 11 mice, Wilcoxon signed rank test, $z = 3.9$. All error bars are s.e.m.

L4 sharpens sensory tuning in L5

How does the suppressive influence of L4 on L5 shape sensory representations? To address this question we determined whether photo-hyperpolarizing L4 altered spatial tuning in L5 RS cells measured by presenting the stimulus bar in different locations along the horizontal axis. We computed a tuning index for each unit across the eight stimulus positions (Brumberg et al., 1996) (see Methods). Photo-hyperpolarizing L4 broadened the representation of horizontal space across the population of L5 RS units (Fig. 3a, b). We also computed the width of each neuron's tuning curve (see Methods) and found that for units that were well fit by a Gaussian model (44/75 units, $r^2 > 0.75$), there was a strong and statistically significant increase in tuning width across the population (Fig. 3c, d). This detuning could not be explained by a 'ceiling effect' on L5 firing. First, intrinsic limits on the spike rate of L5 excitatory neurons (measured with intracellular current injection in brain slices) readily exceed the average maximum firing rates observed *in vivo* (11.6±1.2 Hz *in vivo* vs 42.4± 7.0 Hz *in vitro*). Second, L4 photo-suppression had no significant effect on the Fano factor of L5 RS cells ($p = 0.405$, n = 75 units from 9 mice, 2-way ANOVA, $f(1) = 0.69$).

Do L4's effects on the spatial tuning of L5 neurons depend on surround interactions from other whiskers? To address this question, we optogenetically suppressed L4 in mice in which we trimmed all except the principal whisker (PW), restricting sensory activation to the PW's representation in the barrel cortex. Under these conditions, both the enhancement of L5 RS unit firing and the reduction of L5 FS unit firing persisted (Supp. Fig. 5d, e). This indicates that surround whisker input is not required for these effects, and that they are mediated, at least in part, by descending circuits within the PW barrel column, although lateral inhibition from adjacent whisker representations may still contribute to the observed effects (see below, and supp. Fig. 9).

To assess how L4 photo-suppression influenced stimulus-response functions of cortical neurons, we plotted the normalized firing rate of isolated units as a function of response magnitude for each stimulus. Photo-suppression of L4 scaled down the stimulus-response function of L2/3 RS units proportionally across all stimuli (Fig. 3e). In contrast, L4 suppression shifted stimulus-response functions of L5 RS units and drove a disproportionate enhancement for non-preferred stimuli (Fig. 3f).

To further examine how the impact of photo-suppression of L4 varies as a function of stimulus strength, we plotted OMI for each stimulus position versus stimulus preference (by rank ordering stimuli from least to most preferred according to sensory driven firing rate). For L2/3 units there was a marginal absolute increase in OMI for stronger stimuli (Fig. 3g). In contrast, we observed a strong negative relationship for L5 units, with OMI sloping towards zero for the most preferred stimuli (Fig. 3h).

On a unit-by-unit basis within L5, OMI was significantly larger for the least preferred stimulus position, as compared to the most preferred (Supp. Fig. 5a). In addition, 77% (58/75) of L5 units exhibited a negative correlation (mean r^2=-0.33) between stimulus preference and the absolute number of spikes added by L4 photo-suppression. Thus L4 photo-suppression disproportionally enhanced L5 RS neuron firing for non-preferred stimuli (Supp. Fig. 5b, c), broadening the spatial tuning of the L5 RS population as a consequence (Fig. 3b). These results indicate that the normal role of L4 is to sharpen sensory representations of L5 cortical neurons.

While we analyzed how neurons are tuned for space, the suppressive action of L4 on L5 persisted even in the absence of external contact with the stimulus bar (Fig. 3f, blue dot), indicating that even ongoing activity in L5 is under tonic suppressive control by L4 output ($p < 10\text{-}6$, n = 75 from 9 mice, Wilcoxon sign-rank, $z = 6.5$). Thus L4 may generally sharpen L5 neurons' sensory tuning by reducing spontaneous activity and suppressing responses to non-optimal stimuli.

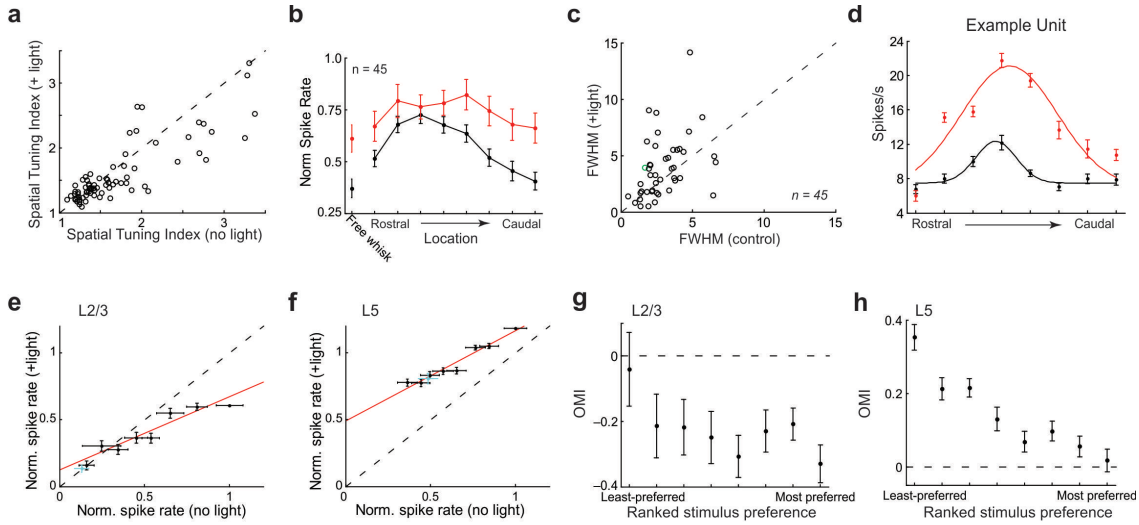

Figure 2.3 Suppression of L4 alters spatial tuning in L5.

a, Scatter plot of the spatial tuning index for L5 RS units during photo-suppression of L4 ($p = 0.003$, n = 75 units from 9 mice, paired t-test, $t(74) = 3.1$). b, Population average spatial tuning curve of L5 RS units under control (black) and during photo-suppression of L4 (red) for units showing significant tuning under control conditions (n = 45, $p < 0.001$, 2-way ANOVA). The unconnected points are for the non-contact, free-whisking condition. c, Scatter plot of the full-width half maximum of the Gaussian fit to well-fit spatial tuning curves of individual neurons during photo-suppression of L4 ($p = 0.016$, n = 45 units from 9 mice, Wilcoxon signed rank test, $z = 2.42$). d, Tuning curves with (red) and without (black) photo-suppression of L4. e, Plot of the normalized spike rate under light vs. control conditions in L2/3 RS units for rank-ordered stimulus preference (n = 33 units from 5 mice). The blue point indicates the control (non-contact) position. f, As in c) but for L5 RS units (n = 75 units from 9 mice). Blue dot: firing in the absence of tactile stimulus (OMI: 0.23±0.04, $p < 10^{-6}$, n = 75 units from 9 mice, Wilcoxon signed rank test, $z = 6.5$) g, Plot of average optogenetic modulation index (OMI) across L2/3 RS units as a function of rank-ordered stimulus preference ($p = 0.653$, n = 33 units from 5 mice, Kruskal-Wallis test, $\chi(7) = 5.0$). h, OMI vs ranked stimulus preference for L5 RS units ($p < 10^{-6}$, n = 75 units from 9 mice, Kruskal-Wallis test, $\chi(7) = 82$). All error bars are s.e.m.

L4 drives synaptic inhibition in L5

What could account for the suppressive action of L4 on L5 activity? L4 is known to drive both feed-forward (Helmstaedter et al., 2008) and recurrent (Tarczy-Hornoch et al., 1998) inhibition through fast spiking (FS) interneurons in the superficial cortical layers. Thus we tested whether L4 might also drive FS inhibitory neurons *in vivo*, which could potentially account for an important component of the suppression of L5 RS neurons. During photo-suppression of L4 (as above), we observed a pronounced reduction in FS neuron firing rates across layers, including FS units in L5 (OMI: -0.25±0.03), computed as a negative OMI across all cortical depths (Fig. 4a, b and Supp. Fig. 6). Although the largest percent reduction in FS unit firing was in L4 (– 52±3%, n = 35 units from 6 mice, $p < 10^{-6}$, 2-way ANOVA, $f(1) = 26.6$), strong reductions were also observed both for L5 (–30±5%, $p < 10^{-5}$, n = 53 units from 9 mice, 2-way ANOVA, $f(1) = 24$) and L2/3 (–31±3%, $p = 0.005$, n = 50 units from 5 mice, 2-way ANOVA, $f(1) = 9.13$) FS units, with the largest absolute reduction in firing rate observed in L5 FS units (Supp. Fig. 6). FS units in L6 were not significantly affected ($p = 0.55$, n = 25 from 3 mice, 2-way ANOVA, $f(1) = 0.36$), suggesting that L4 activity does not substantially influence inhibition originating from L6 FS units (Bortone et al., 2014) (Supp. Fig. 6). Conversely, photo-activation of L4 increased the firing rate of most FS neurons outside of L6 (mean rate increase: 3.9±0.43 Hz, mean OMI: 0.39±.05; Fig. 4a, Supp. Fig. 6). Thus activity in L4 RS neurons is both necessary and sufficient to drive a component of the activity of FS neurons in L2/3, L4, and L5.

These results implicate FS interneurons as possible mediators of L5 suppression. Thus we hypothesized that L4 suppresses L5 by driving interneurons that inhibit L5 RS cells. If so, photo-suppressing L4 should reduce sensory-evoked synaptic inhibition in L5 RS cells. To test this idea we

measured synaptic currents from L5 neurons using whole-cell patch clamp recordings in the same conditions as above; namely, head-fixed, but freely locomoting mice. First, we established a stabilized preparation so that neurons could be recorded in the whole-cell voltage clamp mode for prolonged periods and with low access resistances (see Methods), in order to better estimate excitatory and inhibitory currents. As the mouse actively contacted the stimulus bar with its whiskers we observed barrages of excitatory and inhibitory synaptic inputs, (Fig. 4d). Spontaneous excitation and inhibition exhibited an average ratio of ~1:2 (mean excitatory charge: 56±2 pC/s; mean inhibitory charge 100±0.07 pC/s, n = 11 cells in 9 mice, Figure 4e). Thus L5 neurons were under a tonic inhibitory drive, consistent with the spontaneous firing rates of FS units we observed during extracellular recording (3.3±0.6 Hz in L5 FS cells, n = 53). During sensory stimulation, when FS units show a profound increase in their firing rate, photo-hyperpolarizing L4 excitatory neurons resulted in a significant reduction in evoked inhibitory input to L5 RS neurons, sometimes reducing it to below baseline levels (control: 117±25 pC; light: 67±20 pC, n = 11, $p < 0.04$; Fig. 4f). In contrast, we observed no significant change in synaptic excitation (control: 40±5 pC; light: 65±25 pC, n = 12, $p = 0.49$), even though L4 excitatory neurons are known to monosynaptically innervate L5 pyramidal cells (Feldmeyer et al., 2005). This lack of change in excitatory drive in L5 RS neurons during L4 suppression may be explained by the increased recruitment of recurrent excitatory inputs from within L5 (Feldmeyer and Sakmann, 2000) since L4 suppression enhances L5 RS unit firing. These results demonstrate that L4 activity is responsible for a substantial component of the synaptic inhibition in L5 neurons.

How might L4 generate inhibition in L5? Our extracellular recordings suggest that L4 could drive spiking in FS cells, which then inhibit L5 RS neurons. We hypothesized that L5 FS cells in particular might be a primary mediator, since these cells are known to densely target L5 pyramidal cells (Helmstaedter et al., 2009a; Jiang et al., 2013; Priebe and Ferster, 2008). If L4 generates inhibition in L5 through L5 FS cells, then L4 photo-suppression should reduce excitatory input in L5 FS cells. We addressed this by analyzing a subset of the L5 neurons that we recorded in whole-cell mode *in vivo* that we categorized as putative FS (pFS) neurons based on their intrinsic synaptic properties, a classification we could confirm by comparing such measurements from positively identified FS neurons in brain slices, and for a subset of neurons *in vivo* in which we collected action potentials in the cell-attached or current clamp mode prior to voltage clamping (see Supp. Fig. 7 and Methods). When we optogenetically hyperpolarized L4 excitatory neurons, we observed a pronounced reduction in their excitatory input, and in 5/6 cells the time-averaged excitatory charge was reduced to below baseline levels (average OMI: 2.4±1.0; control: -8±4C, light: 8±4 pC, $p = 0.035$, n = 6, Fig. 4g). Interestingly, although synaptic inhibition in L5 cells drops rapidly following the onset of light, excitation to pFS neurons decays more slowly. This may be explained by the non-linearity imposed by the action potential threshold in L5 FS cells, such that even a partial drop in their excitatory input can profoundly reduce their firing rate, and thus their inhibitory output. These results demonstrate that L4 activity drives excitation in L5 pFS neurons, which is consistent with the reduced firing of L5 FS neurons during L4 photo-suppression.

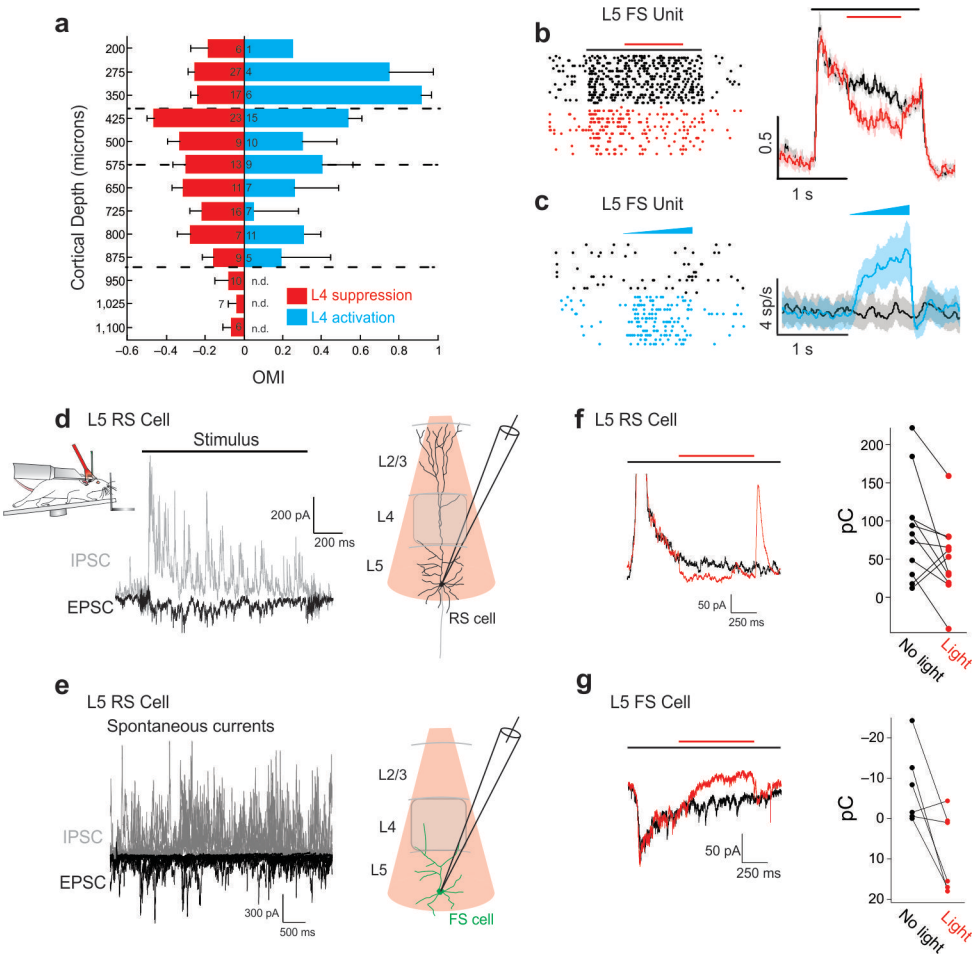

Figure 2.4 Layer 4 drives FS neurons and synaptic inhibition in L5.

a, Histogram of OMI of FS units vs. cortical depth for L4 photo-suppression (red bars) and L4 photo-activation (blue bars). b, Representative example raster plot of an L5 FS unit (left) and population PSTH of L5 FS units (right) during L4 photo-suppression (red) or control conditions (black), (OMI: –0.25±0.03, $p = 1.1 \times 10^{-6}$, n = 53 units from 9 mice, 2-way ANOVA, f(1) = 24). c, As in b) except for photo-activation of L4 (p = 0.001, n = 35 units from 3 mice, Wilcoxon signed rank test, z = 3.4). d, Example traces of synaptic excitation (black) and inhibition (grey) recorded in whole-cell voltage clamp mode from an L5 neuron during tactile stimulation in head-fixed, locomoting mice. Right:Schematic of the recording configuration from L5 putative RS cells. e, Left: Example traces of synaptic excitation (black) and inhibition (grey) during locomotion but in the absence of any external tactile stimulus. Right: schematic of the recording configuration from L5 putative FS cells. f, Left: average traces of synaptic inhibition under control conditions (black) or during L4 photo-suppression for all recorded L5 RS cells. Right:Plot of net inhibitory synaptic charge in L5 neurons under control conditions (black points) or during photo-suppression of L4 (red points, n = 11 cells in 9 mice, p=0.048, paired t-test, t(10)=2.2). g, Left: average traces of synaptic excitation for all putative L5 FS cells under control conditions (black) or during L4 photo-suppression. Right: plot of net excitatory synaptic charge in putative L5 FS cells under control conditions (black points) or during photo-suppression of L4 (red points), (n = 6 cells in 5 mice, p =0.035, paired t-test, t(5)=-2.9). All error bars are s.e.m.

A direct translaminar feed-forward inhibitory circuit from L4 to L5

The results above suggest a possible circuit to account for the suppressive influence of L4 on L5: L4 might directly recruit L5 inhibitory neurons, generating disynaptic somatic inhibition in L5 pyramidal cells. Although it is well known that L4 excitatory neurons synapse on L5 pyramidal cells (Feldmeyer et al., 2005), to our knowledge, the direct L4 innervation of L5 inhibitory neurons has never before been observed. Thus we sought to verify its existence using acute brain slices from the barrel cortex. Photo-stimulation of L4 *in vitro* resulted in fast excitatory and inhibitory currents in both L2/3 and L5 pyramidal cells (Fig. 5a). The observed inhibition was almost entirely abolished by glutamatergic antagonists (Supp. Fig. 1d), demonstrating that it was mediated by synaptic recruitment of inhibitory

interneurons. The onset latencies of inhibition in L2/3 and L5 pyramidal cells showed no significant difference (Fig. 5b), indicating that L4 might directly activate inhibitory neurons that suppress L5, and not operate poly-synaptically through L2/3 pyramidal cells (also see below, Fig. 6).

To address the existence of direct circuit linking L4 and L5 FS neurons, we first made whole-cell recordings from electrophysiologically identified FS neurons in L5 (see Methods). Photo-stimulation of L4 resulted in large, short latency (mean: 3.77±0.48 ms) excitatory synaptic currents, and in most cases reliably drove action potentials in the recorded L5 FS neurons (8/14 cells; Fig. 5c, d). To demonstrate directly that this is a monosynaptic connection, we made paired intracellular recordings from L4 excitatory neurons and L5 PV^+/FS neurons (labeled in the PV-Cre;ROSA-LSL-tdTomato line) located within the same barrel column. Out of a total of 55 tested connections, we observed 9 positive connections with an average unitary conductance of 0.66±0.10 nS (Fig. 5e) on the first presynaptic action potential. This is comparable to the connectivity rate observed between L4 and L2/3 FS cells (Helmstaedter et al., 2008). When we restricted our estimate of connection probability to postsynaptic PV^+/FS cells showing at least one monosynaptic connection with an excitatory neuron in L4, connection probability rose to 39% (9/23 connections). In one L5 $PV^{+/}$ FS cell 3/7 tested connections were positive (Fig. 5f). This result suggests that L4 neurons may preferentially innervate a subset of L5 PV cells.

To estimate the laminar pattern of intracortical excitatory connectivity onto L5 inhibitory neurons, we used a digital micromirror device (DMD) to spatially control optogenetic photo-stimulation and mapped the excitatory input to L5 FS neurons across barrel columns and cortical layers (Fig. 5g). ChR2 was expressed in excitatory neurons throughout the cortex using the emx1-Cre line(Gorski et al., 2002). ChR2-expressing neurons were photo-activated primarily within 50 microns of the illumination spot, ensuring sublaminar spatial resolution (Supp. Fig. 8a-d). Illumination was specifically chosen to limit polysynaptic activity and prevent activation of axons of passage (see Methods). Although all L5 FS neurons received some excitatory input from L5 (Fig. 5h, left, Supp. Fig.8e-i), ~23% (7/31) received their densest excitatory input from L4 of the same barrel column (Fig. 5h, right Supp. Fig. 8i), consistent with paired recordings.

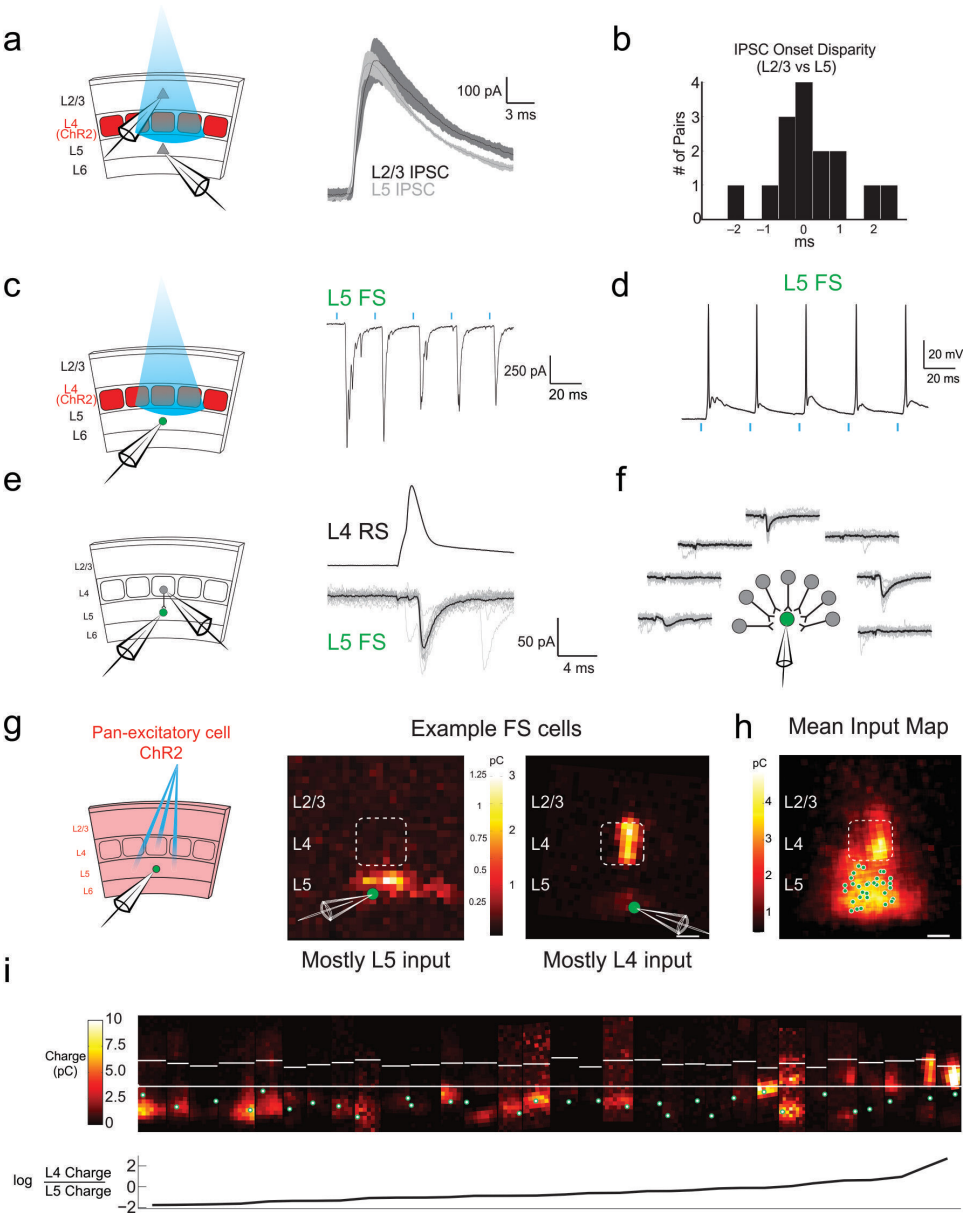

Figure 2.5 Mapping a direct translaminar inhibitory circuit from L4 to L5 via L5 FS cells.

a, Left: recording schematic of a pair of simultaneously recorded L2/3 and L5 pyramidal cells in mice expressing ChR2 in L4. Right: example traces of light evoked synaptic inhibition in a L2/3 (dark grey) and a L5 (light grey) pyramidal cell. b, Histogram of the difference in mean onset latency of light evoked synaptic inhibition in simultaneously recorded pairs of L2/3 and L5 neurons (L2/3: 4.9±0.4 ms vs L5: 4.7±0.4 ms, p=0.49, n = 13 pairs in 10 slices from 5 mice, paired t-test, t(12) = 0.70). c, Left: recording schematic of an intracellularly recorded L5 FS neuron in mice expressing ChR2 in L4. Right: example traces of light-evoked synaptic excitation in a L5 FS neuron. Blue lines indicate 1 ms pulses of blue light. d, Example trace of the first five synaptically evoked action potentials in a L5 FS neuron during a train of photo-stimulation of L4. e, Left: Recording schematic of a simultaneously recorded L4 excitatory cell and a L5 FS neuron. Right: example traces of an evoked action potential in the L4 excitatory neuron (top trace) and unitary EPSCs (grey, single trials; black, average) in a connected L5 FS neuron. f, Schematic of an example recording in which seven candidate presynaptic L4 excitatory neurons were recorded in a pair with a L5 FS neuron. g, Left: Recording schematic of a digital-micromirror based optogenetic mapping system in emx1-IRES-Cre mice injected with a flexed-ChR2 AAV vector. Right: Two example excitatory input maps from FS neurons exhibiting mostly L5 input (left) or mostly L4 input (right). Scale bar: 100 µm. h, The grand average excitatory input map from all recorded L5 FS neurons (n=31 FS cells in 26 slices from 13 mice), aligned by the position of the L4 barrel above each neuron. Green dots indicate the location of the somata of the recorded FS neurons. Scale bar: 100 µm. i, All individual excitatory input maps recorded L5 FS neurons. Green dots indicate the location of the somata of the recorded FS neurons. White lines indicate the top and bottom boundaries of L4. Bottom: Maps from the recorded FS cells are rank-ordered according to the L4:L5 ratio of home column input (quantified as mean charge transfer per unit area). All error bars are s.e.m.

Next, to test if L2/3 was dispensable *in vitro* for L4-generated inhibition in L5 pyramidal cells, we surgically removed L2/3 entirely. In these slices – even in the complete absence of L2/3 – we observed that photo-stimulation of L4 was still sufficient to generate disynaptic inhibition in L5 pyramidal cells (Fig. 6a-c). This result demonstrates that neither excitatory nor inhibitory cells in L2/3 are required for L4 to drive inhibition in L5. Since this transection also severs the apical dendrites of L5 pyramids, it further indicates that the remaining inhibition is either somatic or targeted to L5 neurons' proximal dendrites.

To support the notion that L4 activates L5 FS cells directly, which in turn generates synaptic inhibition in L5, we made paired recordings from connected L5 FS and L5 pyramidal cells while photo-stimulating L4. As above, light pulses to L4 drove firing in L5 FS cells and generated inhibitory currents in L5 pyramidal cells. When we prevented the synaptic activation of the recorded L5 FS cell by holding it in voltage clamp, we observed a significant (threshold: $p < 0.05$) and reversible reduction in the photo-induced IPSC in the L5 pyramidal cell in 5/7 connected pairs (mean reduction: 12±6%; Fig. 6e, f).

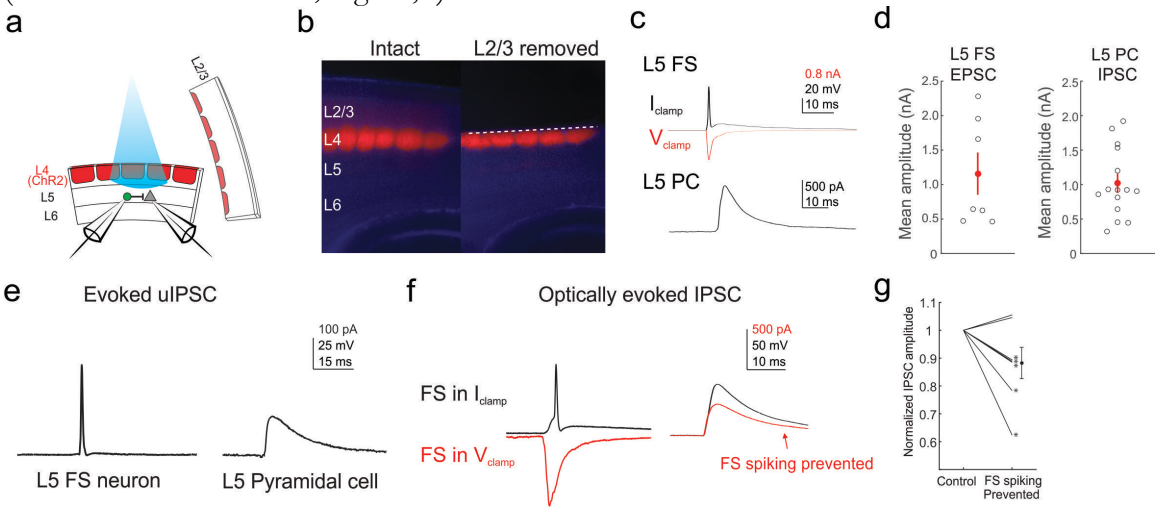

Figure 2.6 L4 to L5 translaminar inhibition through L5 FS neurons persists in the absence of L2/3.

a, Recording schematic: L2/3 is surgically removed from the brain slice, while a paired recording is made from a L5 FS and a L5 pyramidal cell. b, Example images from an intact slice expressing ChR2-TdTomato in L4 (left), and a slice with L2/3 surgically removed (right). c, Top: example average light evoked response recorded in a L5 FS neuron after removal of L2/3. Black: current clamp; red: voltage clamp. Bottom: Evoked IPSC in a L5 pyramidal cell. d, Scatter plot of the mean amplitude of the evoked EPSCs in L5 FS cells (left, n = 7 cells in 7 slices from 3 mice), and of IPSCs in L5 pyramidal cells (PC, right, n = 15 cells in 12 slices from 3 mice). e, Left: Action potential evoked by current injection in a connected L5 FS-L5 PC pair. Right: unitary IPSC recorded in the postsynaptic pyramidal cell. f, Same pair as in e). Left: Optically evoked response of the L5 FS in current clamp (black), and during voltage clamp (red). Right: Optically evoked IPSC in the L5 pyramidal cell when the FS cell is allowed to spike (black) or prevented from spiking (red). g, Scatter plot of the mean change in the optically evoked IPSC in the L5 pyramidal cell when the presynaptic L5 FS cell is prevented from spiking by voltage clamping. Asterisk denotes $p<0.05$ (range: $p = 10^{-12} – 0.21$, n = 7 pairs in 5 slices from 3 mice t-test). All error bars s.e.m.

Contributions to L5 suppression by other inhibitory circuits

Taken together, these results establish a direct translaminar inhibitory circuit connecting L4 with L5 pyramidal cells via FS inhibitory neurons. Nevertheless, other intracortical circuits likely contribute to L4's ability to suppress L5 excitatory neurons, including FS neurons in other layers, polysynaptic recruitment of L5 FS neurons through L2/3 pyramidal cells, and non-FS inhibitory neurons. Thus we sought to systematically test whether each of these other possibilities might play a contributing role in L4 to L5 translaminar suppression.

Since photo-suppressing L4 neurons reduced FS neuron firing rates across L2/3-L5, we quantitatively measured the relative strength of inhibitory input onto L5 pyramidal cells from FS

neurons in different layers to address the potential relative contributions to translaminar inhibition. We expressed ChR2 selectively in PV^+ inhibitory neurons using the PV-Cre line and used the same DMD-based mapping approach as above (Supp. Fig. 9). Consistent with previous studies (Kätzel et al., 2011; Li et al., 2014), L5 pyramidal cells received the majority of their monosynaptic PV^+ mediated-inhibition from PV cells within L5 (>70% of total charge transfer, Supp. Fig.9 a, b, e). Taken together with the finding that L5 FS cells also display the largest absolute decrease in firing rate during L4 photo-suppression, this suggests that the majority of FS-mediated L4 to L5 inhibition is routed through FS cells in L5.

Next we asked whether L5 FS neurons might be recruited poly-synaptically through L2/3 excitatory neurons. To address this question we optogenetically suppressed L2/3 excitatory neurons using the drd3-Cre driver line (Gong et al., 2007) which labels L2/3 pyramidal cell in the barrel cortex (Supp. Fig. 10a). Despite a pronounced suppression of L2/3 excitatory neurons, L5 FS neurons as a population were not significantly reduced, in contrast to when we photo-suppressed L4 (Supp. Fig. 10b). The lack of a consistent effect on L5 FS cells is consistent with reports that L2/3 pyramidal cells in agranular cortex selectively excite L5 SOM^+ and not L5 PV^+ neurons (Apicella et al., 2012; Otsuka and Kawaguchi, 2009). This experiment suggests that the decrease in L2/3 activity during L4 photo-suppression probably only makes a minor contribution to the disinhibition of L5 neurons through FS cells. However, we cannot rule out a contribution from L2/3 that operates independently of FS neurons.

Finally, we asked whether non-FS GABAergic interneurons could significantly contribute to the L4-mediated suppression of L5 excitatory cells. We addressed this possibility in two ways. First we asked whether L4 excitatory neurons also monosynaptically innervate L5 SOM^+ Martinotti cells. We made paired intracellular recordings from L4 excitatory neurons and GFP^+ neurons in the GIN line, which exclusively labels SOM^+ Martinotti cells (Ma et al., 2006b; Oliva et al., 2000). In contrast to the frequent connectivity onto L5 PV^+ neurons, we never observed direct connections from L4 excitatory neurons onto GFP^+ cells in the GIN line (52 connections tested onto 18 L5 GIN GFP+ cells; 0/18 L5 GIN GFP^+ versus 5/12 L5 PV^+/FS received at least one monosynaptic connection, $p=0.0056$, Fisher's exact test, DF = 1), likely excluding them from playing a direct role in the L4 to L5 translaminar suppressive circuit. Next, we asked if photo-suppressing L4 *in vivo* results in an increase in the burst rate of L5 neurons, as would be expected for a reduction in dendritic inhibition[38]. However, we found that despite robustly increasing L5 RS unit firing rates, L4 suppression did not lead to a significant increase in the tendency of L5 RS units to fire spikes in bursts in S1 or V1(Supp. Fig. 11a-e). As a positive control, directly suppressing SOM^+ neurons (by expression of eNpHR3.0 in SOM-Cre mice) increased the tendency of L5 neurons to burst (Supp. Fig 11g, h). Although other inhibitory circuits are likely to contribute, these three lines of experiments lend additional support to the model that L4 excitatory neurons monosynaptically drive L5 FS neurons, which in turn potently suppress L5 excitatory neurons during sensory stimulation.

Discussion

This study reveals a novel translaminar inhibitory circuit directly connecting the input and output layers of the cortex. The functional consequence of this circuit is to enhance the feature selectivity of cortical output. More generally, our results lead us to rethink the nature of signal propagation in neocortical circuits. On one hand, anatomical and physiological data support the notion of a simple feedforward excitatory circuit in which L4 drives L2/3, and L2/3 drives L5. On the other hand, pharmacological manipulations in anesthetized or sedated animals suggest that L4 activity may not be required for sensory responses in L2/3 or in L5. Our data support a new model to accurately describe functional interactions in the cortex during sensory processing in behaving animals. Consistent with the model of Constantinople and Bruno (Constantinople and Bruno, 2013), we find that L4 activity is not required for sensory responses in L5. In contrast with this model, we find that L4 actually exerts an inhibitory effect on L5 activity. This might have been missed previously owing to the exceptionally low firing rates of superficial cortical neurons in sedated animals (Constantinople and Bruno, 2013), the strong adaptation of intracortical activity during passive conditions (Fanselow and Nicolelis, 1999; Khatri, 2004), or the absence of a neuromodulator that is only present during active brain states, rendering this suppressive mechanism inactive under these reduced states and only detectable in awake, behaving animals.

With respect to signal propagation to L2/3, our results are consistent with the more conventional model, as we found that L4 is involved in driving L2/3 in response to sensory stimuli. However, we cannot rule out the involvement of cortical feedback from other areas, such as secondary somatosensory cortex or primary motor cortex, which may explain, in part, the incomplete deactivation of L2/3 when photo-suppressing L4. Taken together, our results suggest a revised model of signal flow through the cortical layers: sensory input propagating through L4 drives L2/3 but simultaneously suppresses L5 through disynaptic inhibition.

Our results suggest that L4 to L5 suppression can be attributed, at least in part, to a previously unrecognized circuit in which L4 excitatory neurons directly activate a subpopulation of FS inhibitory neurons in L5, which in turn suppress L5 projection neurons and sharpen their sensory representations. This model is supported by several lines of evidence based on the optogenetic suppression and activation of L4 excitatory neurons in vivo and in brain slices. Although we provide data that L5 Martinotti cells and FS cells in other layers are not likely to substantially contribute to the translaminar inhibitory circuitry studied here, other inhibitory circuits that we did not directly examine could also contribute. For example, other subtypes of cortical inhibitory interneurons that target L5 pyramidal cells (Helmstaedter et al., 2009a; Jiang et al., 2013), including SOM^+ non-Martinotti cells (Ma et al., 2006b) and non-FS inhibitory neurons in more superficial layers may receive excitatory input from L4, and could provide alternative sources of translaminar inhibition. These will be important questions to address in the future.

Notably, we observed that L4 to L5 translaminar suppression disproportionally affects non-preferred stimuli. Thus the net impact of this suppression is to sharpen sensory tuning curves, in this case for horizontal space. This suppression is likely due to an increase in inhibition from FS inhibitory neurons, which, when combined with the nonlinearity of action potential threshold in L5 pyramidal cells, preferentially suppresses pyramidal cells' responses to non-optimal stimuli (Priebe and Ferster, 2008). We note that we observed changes in spatial tuning in both S1 and V1, which is akin to a broadening of their spatial receptive fields.

There is ample evidence that inhibitory circuits control tuning in the somatosensory cortex (Adesnik and Scanziani, 2010; Brumberg et al., 1996) and in other cortical areas (Hirsch et al., 1998; Isaacson and Scanziani, 2011; Ozeki et al., 2009). Unlike other inhibitory circuits that have been proposed to enhance tuning to specific stimulus features, the L4 to L5 inhibitory circuit we describe

here might generally enhance tuning to multiple sensory features, not just for space. This notion is supported by the fact that L4 suppresses L5 even when no external stimulus is present. By reducing a component of the ongoing or 'non-sensory' firing of L5 projection neurons, the L4 to L5 translaminar inhibitory circuit should enhance the relative modulation of cortical neurons to all sensory stimuli.

Furthermore, since we observed this suppression in both somatosensory and visual cortices, this mechanism might generally improve coding at the output level of the cortex in many cortical areas. It will be interesting to test whether the synaptic connection between L4 excitatory neurons and L5 interneurons is under control from higher cortical areas. If so, it might represent a key node for dynamically sharpening stimulus representations in different brain states or under different behavioral demands.

Miscellaneous

Acknowledgements

We are grateful to K. Deisseroth and S. Sternson for optogenetic reagents, and to D. Kleinfeld for spike sorting software. This work was supported by NINDS grant DP2NS087725-01 and NEI grant R01EY023756-01, and a Whitehall foundation grant to H.A. J.V. was supported by a grant from the Swiss National Foundation.

Author Contributions

H.A. and S.P. conceived of the study. S.P. performed all in vivo extracellular barrel cortex experiments. H.A. performed all in vivo patch experiments. A.N. performed all in vitro circuit mapping experiments. J.V. performed all visual cortex experiments. G.T. collected all whisker tracking data and performed laminar boundary analysis. R.H., L.Y. and D.T. provided technical assistance. H.A. wrote the paper. A.N. and S.P. contributed equally to this study.

Methods

All experiments were performed in accordance with the guidelines and regulations of the Animal Care and Use Committee of the University of California, Berkeley.

Transgenic mice

Mice used for experiments in this study were either wild type (ICR white strain, Charles River), heterozygous for the scnn1-tg3-Cre allele (JAX stock # 009613), or heterozygous for drd3-Cre (strain KL196, MMRRC). A subset of mice carried the Ai9 Rosa-LSL-tdTomato allele (JAX stock # 007909) to help quantify the infection rate of Cre^+ cells. The scnn1-tg3-Cre and drd3-Cre lines were outcrossed several generations into the ICR white background to improve habituation to locomotion under head fixation. Mice used for visual cortical physiology were than backcrossed to C57/B6 mice for one generation to produce mice with pigmented eyes. For a subset of experiments in brain slices we used the emx1-IRES-Cre line (JAX stock #005628), PV-cre line (B6;129P2-$Pvalb^{tm1(cre)Arbr/J}$; JAX stock #008069), or the GIN line (FVB-Tg(GadGFP)45704Swn/J; JAX stock #003718). For in vivo experiments mice were between 4-8 weeks old. For labeling all inhibitory neurons we used GAD67-GFP mice (Tamamaki et al., 2003). To quantify the fraction of L4 excitatory neurons that express Cre we analyzed slices from scnn1-tg3-Cre;GAD67-GFP mice injected with AAV-flexed-tdTomato and were counterstained for NeuN. We found that tdTomato+ cells in these mice constituted 85±3% of excitatory L4 neurons. Mice were housed in cohorts of five or less with a light:dark cycle of 12:12 hours, and were used for experimentation during their subjective night.

Viral Infection

Neonatal scnn1-tg3-Cre mice (P3-P6) were injected transcranially with ~20 nl of AAV9-DIO-ef1a-eNpHR3.0-YFP at 3 locations in S1 or V1. Viral infection at this age gave us reliable, dense and broad infection across most of either S1 or V1 and avoided toxicity we observed when injecting high titer AAV- eNpHR3.0 in adult mice. For *in vivo* ChR2 expression, AAV-2/1-DIO-Ef1a-ChR2-YFP was injected at P21-P24. For in *vitro experiments,* neonatal scnn1-tg3-Cre, PV-cre, or emx1-cre mice were injected with AAV9-CAG-flexed-Chr2-tdTomato at P0-P4. Viruses were acquired from the University of Pennsylvania Vector Core. Undiluted viral aliquots were loaded into a Drummond Nanoject injector. Neonates were briefly cryo-anesthetized and placed in a head mold. With respect to the lamba suture coordinates for S1 were: 2.0 mm AP; 3.0 mm L; 0.3 mm DV; For V1 they were: 0.0 mm AP; 2.2 mm L; 0.3 mm DV.

Preparation for in vivo recording

Mice were anesthetized with isoflurane (2.5%). The scalp was removed, the fascia retracted, and the skull lightly etched with a 20 gauge needle. Following application of Vetbond to the skull surface, a custom stainless steel headplate was fixed to the skull with dental cement (Metabond). Two days after surgery mice were habituated for 2-7 days to head-fixation on a free-spinning circular treadmill. On the day of recording mice were briefly anesthetized with isoflurane (2%), the skull over S1 or V1 was thinned, and a small (<250 micron) craniotomy was opened over S1 or V1 with a fine needle. In some cases S1 was previously identified with intrinsic optical imaging. The small size of the craniotomy ensured a stable preparation for both extracellular and intracellular recording.

Tactile Stimulus presentation

While mice ran on the treadmill, they rhythmically swept their whiskers in a stereotyped manner (see Supp. Fig. 4). To stimulate the whiskers a vertical metal bar (0.5 mm diameter) was rapidly (~50 ms) moved into the whisking field using a stepper motor with submicron precision (Oriental Motor) and controlled by digital signals (National Instruments PCIe-6353). The bar was presented at eight different positions, evenly spanning the entire rostral-caudal axis of the whisking field, in a randomly ordered sequence. An additional ninth position that did not contact the whiskers was used to compute non-contact evoked firing rates. The horizontal distance between adjacent stimulus positions was 2.2 mm, and controlled by moving the stepper motor on a linear stage with submicron precision (Zaber Technologies). Most mice habituated quickly to the presentation of the tactile stimulus assessed by lack of a change in whisking or running speed during stimulus presentation. Mice that did not habituate were excluded from this study. Mice were neither punished nor rewarded for any aspect of their behavior. Most mice ran consistently for hundreds of trials. In all cases we recorded from the C1-C3 or B1-B3 columns verified by a combination of intrinsic optical imaging and/or electrophysiology. Out of 8 stimulus positions, 3-5 contacted the principal whisker, and at each position, 2-3 whiskers contacted the stimulus, as assayed by separate experiments in which we tracked a single row of whiskers with high speed imaging. In a subset of mice, after physiological identification of the principal whisker, the surround whiskers were trimmed from the face to prevent contact with the object.

In the AAV-2/9-eNpHR3.0 experiments, five mice were used for recordings focused on collecting data from L2/3. In six separate mice, recordings focused on collecting data from L4 and L5, and in three additional mice, recordings focused on recording from L5 and L6. In the AAV-2/1-DIO-Ef1a-ChR2-YFP experiments, three mice were used to record across layers 2 through 5. In the YFP control experiments, two mice were used to collect data from layers 2 through 5.

Visual Stimulation

Visual stimuli were generated with Psychophysics Toolbox running on a Mac Mini and were presented on a gamma corrected 23" Eizo FORIS FS2333 LCD display with a 60Hz refresh rate. Stimuli consisted of drifting square wave gratings at 0.04 cycles/° and 2 cycles/s of 8 different directions (0-315° in steps of 45°) and either 5 different contrast levels (10% to 100% in logarithmic steps) or 5 different sizes (8, 13, 21, 36, 60 visual degrees), centered on the average receptive fields of all simultaneously recorded neurons. Gratings drifted for 2 seconds with 1 second inter-trial intervals with the red LED (Lumencor) switched on for one second starting 0.5 seconds after start of the visual stimulus in 50% of the trials. Suppression index was calculated as the difference between the peak response and the response to the largest stimulus, divided by the peak response $(FR_{PS} - R_{LS})/FR_{PS}$.

In vivo extracellular multi-electrode electrophysiology

A 16- or 32-channel linear electrode (NeuroNexus, A1x16-3mm-25-177-A16 or A1x32-5mm-25-177-A32), or a subset of experiments a four shank 'Buzsaki32' style probe, was guided into the brain using a micromanipulator (Sutter Instruments) and a stereomicroscope (Leica). Electrical activity was amplified (A-M Systems), digitized at 30 kHz (National Instruments PCIe-6353), and stored on a computer hard drive. The cortical depth of each electrical contact was determined by zeroing the bottom contact to the surface of the brain. To ensure the electrode trajectory was close to perpendicular to the brain surface, the animal's skull was tilted relative to the vertically mounted electrode. After each recording a laminar probe coated with the lipophilic dye DiI was used to mark

the electrode track and quantitatively assess insertion angle and depth. The laminar depth of recorded units was corrected for this insertion angle and the local curvature of the neocortex. In a subset of recordings we also assessed electrode depth by computing the current source density during sensory stimulation and identifying a sink corresponding to L4 (Niell and Stryker, 2008). All three metrics (micromanipulator depth, DiI labeling, and CSD analysis) were in close correspondence (Suppl. Fig. 2). Laminar boundaries, consistent with published values (Lefort et al., 2009), were measured from several lines of layer-specific Cre driver mice (scnn1-tg3-Cre, drd3-Cre, Rbp4-Cre, and Ntsr1-Cre, Suppl. Fig. 2) cross to ROSA26-LSL-tdTomato.

Optogenetic stimulation in vivo

For optogenetic stimulation of eNpHR3.0 *in vivo* we used red light (30-80 mW/mm^2) from the end of a 1 mm diameter multimode optical fiber coupled either to a red laser diode (Ultralasers) or a solid state source (Lumencor Spectra X) controlled by analog and digital outputs (NI PCIe-6353). The fiber was placed as close to the craniotomy as possible (<3 mm). For activation of ChR2 we used blue light from a fiber coupled LED (Thorlabs). The illumination area was set to cover the entire macrovibrissal barrel cortex.

Analysis of multi-electrode neural data

Spike detection was performed using the UltraMega Sort package (Hill et al., 2011) in Matlab (Mathworks). After detection, spikes were automatically sorted into clusters of discrete units. Units were then manually sorted to meet criteria for inclusion while simultaneously preventing pseudo-replication. Quality metrics included analysis of spike amplitude, spike rate, auto-correlation, inter-spike interval, outlier removal, distance from threshold, and cortical depth of largest waveform. With the exception of a small group of fast-spiking or burst firing units, included units had no more 1% of their individual waveforms violating a refractory period of 2.5ms.

In sorted units mean firing rates were computed from counting spikes in a 550ms window starting 200ms after the onset of the red LED, and 700ms after the onset of moving the bar into the whisker field. This window was chosen because within 700ms of the bar entering the whisker field, neuronal firing rates reached a stable steady-state. Trials containing stimulation periods where the animal's average running speed during the stimulus period deviated by more than 1.3 standard deviations of its mean velocity were excluded, to ensure consistency in behavior across trials. The depth of each unit was assigned based on the calculated depth of the electrode on the array that exhibited its largest amplitude sorted waveform. Layer boundaries follow (Lefort et al., 2009)and were confirmed experimentally in a subset of recordings with current source density analysis (Niell and Stryker, 2008) and histological assessment. CSDs were calculated from the trial-averaged local field potential (0.5 – 300Hz) measured at each electrode contact, as previously published (Nicholson and Freeman, 1975; Reyes-Puerta et al., 2015a, 2015b). We estimated the layer 4/5 boundary as the base of the current sink corresponding to layer 4.

Statistically significant differences between conditions were determined using standard parametric or nonparametric tests, including a 1-way or 2-way ANOVA, student's t-test, and a Wilcoxon sign-rank test. Tests for normality were performed with a Lilliefors test. An optogenetic modulation index (OMI) for each condition was computed as the difference of the firing rates of a given unit between the light and no light condition, divided by their sum. Thus an $OMI < 0$ indicates suppression, $OMI > 0$ indicates facilitation, and $OMI = 0$ indicates no change. A small subset of L5 units (5/128, or 3.9%) displayed OMIs close to -1 indicating nearly complete suppression, and were statistical outliers. These neurons most likely correspond to a small subset of Cre^+ neurons in L5 that expressed eNpHR3.0, and were excluded from analysis.

The effect of layer 4 suppression on L5 sensory tuning was assessed using the following methods: An index of spatial tuning was calculated by dividing the firing rate at the peak of the tuning by the mean spike rate across all eight conditions (similar to a previous study that using this approach to measure angular tuning) (Brumberg et al., 1996). Using this metric, a tuning index of one (STI = 1) indicates no preference for any stimulus, while a tuning index of eight (STI = 8) indicates a selective response to only one stimulus. The slope of a least squares linear regression was used to determine how the effect of L4 suppression changed as a function of sensory drive. To calculate the full width at half max, a Gaussian function was fit to neuronal spatial tuning curves using the method of least squares with upper and lower boundaries limited by the peak-evoked and spontaneous firing rate of each neuron, respectively.

Neuronal burst rate was calculated using a Poisson surprise method (Legéndy and Salcman, 1985). High frequency spikes were counted as the number of spikes with at least one neighboring spike occurring in less than 10 ms. The coefficient of variation (CV) of interspike intervals (ISIs) was used to provide a quantitative description of spiking regularity. Bursting neurons have more irregular firing patterns, and are therefore characterized by a large CV. As the firing rate of a neuron approaches its refractory period, variation across trials necessarily decreases. Fano factor provides a reliable metric of this "ceiling effect".

Individual units were classified as either fast-spiking or regular spiking using a k-means cluster analysis of spike waveform components. One major component of waveform classification was the normalized difference between the two positive-going peaks. The other major component was the trough-to-peak latency of the large negative-going deflection. Fast-spiking units were categorized by a larger 2nd positive-going peak (positive difference), and a short (less than 0.33 ms) trough-to-peak latency, following a previously established approach (Reyes-Puerta et al., 2015a) (see Supp. Fig. 7a, b). A subset of units on the border between the classification as FS or RS was excluded from analysis, although their inclusion did not change the significance of any results.

In vivo intracellular recording and analysis

Mice were prepared identically as for extracellular recording. To make blind whole cell patch clamp recordings a glass borosilicate pipette (Sutter) was pulled to a long taper and a low resistance (3-5 Megaohms) and inserted axially through the dura mater under high positive pressure. Electrode solution was the same as for brain slice recording for voltage clamp (see below, containing cesium, QX-314, and TEA). Signals were amplified with an Axopatch 200B (Molecular Devices), filtered at 2 kHz, and digitized with a National Instruments DAQ device (PCIe-6323).

The depth of the electrode was set to zero when the pipette encountered the dural surface, which was easily identified electrically by a large, transient increase in pipette resistance. The pipette was then advanced to L5 (~575-900 microns below the dura) under high pressure (~180 mbar). At the entry point of L5 pressure was quickly lowered to <30 mbar to search for neurons in the blind configuration. The pipette was advanced in 2 micron steps and following a sudden and transient increase in pipette resistance the positive pressure was released. Following gigaseal formation brief suction ruptured the membrane providing whole cell access. The cell was dialyzed for 2-3 minutes prior to obtaining data on synaptic excitation, and an additional 5-10 minutes prior to voltage clamping to the reversal potential of synaptic excitation to isolate inhibitory currents. Initial uncompensated access resistance averaged 17±2 MΩ (range: 7-23 MΩ), and cells were excluded if this changed by more than 20% during the duration of the recording. Illumination trials were interleaved with control trials for all experiments to ensure that any slow drift in cell stability would not impact the results.

Excitatory and inhibitory synaptic charge was calculated as the integral under the current record at the corresponding apparent reversal potentials for GABA and glutamate. Most neurons exhibited a high rate of tonic synaptic excitatory and inhibitory currents. To calculate a baseline for charge measurements during sensory or optogenetic stimulation, current records for each trial were automatically scanned for a 50 ms period of the lowest variance during the second before the stimulus entry, and the mean of this interval was subtracted from the entire trace. Due to the high ongoing rate of inputs optogenetic suppression of L4 often resulted in a reduction below baseline of either inhibition in L5 RS cells (5/10 cells) or excitation in L5 FS cells (5/6 cells). Statistical significance of optogenetic changes in excitatory and inhibitory charge were assessed with a paired t-test.

Putative FS neurons were identified either by the width of their spikes recorded in the cell-attached configuration prior to membrane rupture, or, in the absence of spikes, by the fast decay of spontaneous excitatory postsynaptic currents (sEPSCs, Supp. Fig. 7d). Based on the decay kinetics of sEPSCs from intracellularly recorded FS neurons in brain slices, we were able to set a criterion of $\tau < 2$ ms for FS neurons (Supp. Fig. 7c, d). Out of the 16 intracellularly recorded neurons in this study used for analysis in Fig. 4, 6 were classified as FS neurons based on these criteria, and all cells showing fast action potentials in cell-attached also exhibit fast decaying sEPSCs.

Brain slice recording and optogenetic stimulation

Acute thalamocortical slices were prepared from the left hemisphere 2-4 weeks later as previously described (Adesnik and Scanziani, 2010) . Slices were placed in a recording chamber and constantly perfused with oxygenated artificial cerebro-spinal fluid (NaCl 119 mM, KCl 2.5 mM, $MgSO_4$ 1.3 mM, NaH_2PO_4 1.3 mM, glucose 20 mM, $NaHCO_3$ 26 mM, $CaCl_2$ 2.5 mM) maintained at 32°. Slices were oriented with the caudal surface facing up in the recording chamber. Slices were visually inspected with epifluorescence to confirm dense, even expression of ChR2-tdTomato in L4 (scnn1-tg3-Cre experiments) or across the entire cortex (emx1-Cre and PV-cre experiments). Slices in which expression appeared faint or uneven were discarded. Slices were further inspected under 40x magnification to confirm that Layer 5 pyramidal cell apical dendrites stayed roughly parallel with the surface of the slice or receded slightly deeper as they progressed apically, otherwise the slice was discarded.

In a subset of scnn1-tg3-Cre experiments, we removed L2/3 prior to recording. While briefly visualizing L4 with epifluorescence, a fine blade was used to sever the slice below the border between L2/3 and L4. L2/3 was then completely separated from the lower layers and discarded. Multiple cuts were performed to ensure complete horizontal coverage of barrel cortex and surrounding regions. Generally this also removed one third to one half of the volume of L4 in recorded areas, but preserved the basal most regions of L4, as well as its descending axons. Recorded neurons did not appear noticeably unhealthy and could be recorded from for extended periods with stable resting membrane potentials and input resistances.

Whole cell recordings were performed using glass micropipettes (2-3MΩ resistance) pulled on a Sutter P-1000 Micropipette Puller. For recording pyramidal cells, pipettes were filled with a Cs^+ based internal ($CsMeSO_4$ 135 mM, NaCl 8 mM, HEPES 10 mM, Na_3GTP 0.3 mM, MgATP 4 mM, EGTA 0.3 mM, QX-314-Cl 5 mM, TEA-Cl 5mM). For recording interneurons and for connectivity testing, pipettes were filled with a potassium gluconate based internal (K-gluconate 135 mM, NaCl 8 mM, HEPES 10 mM, Na_3GTP 0.3 mM, MgATP 4 mM, EGTA 0.3 mM). In some experiments, Alexa Fluor 488 Hydrazide (5μM) or biocytin (1%) was dissolved into the internal solution to enable morphological recovery. Voltage recordings were not corrected for the junction potential, which was 13 mV. Series resistance was monitored with negative voltage steps during each trial, and was

compensated up to 60%. Data were analyzed from recordings in which series resistance was below 25MΩ and did not change by more than 25% during the course of the experiment. Data were acquired and filtered at 2 kHz using a Multiclamp 700B Amplifier (Axon Instruments) and digitized at 20 kHz (National Instruments). All data were acquired using custom written MATLAB (Mathworks) software. Fast-spiking cells could be distinguished on the basis of their non-adapting response to current injection and short duration action potentials (Supp. Fig. 7).

Photo-stimulation in vitro

Laser light was generated using a 1W 445nm diode laser (Ultralasers) and routed via a liquid light guide into a CEL5500 digital micromirror device (DMD) (Digital Light Innovations). The projection from the DMD was then collimated and integrated into the light path of the microscope, before being focused onto the slice chamber using a 5x or 40x objective lens (Olympus). For Scnn1-tg3-Cre experiments, the DMD passively reflected but not spatially modulate light. Prior to photo-stimulation, infrared and epifluorescence images were captured using an IR-1000 CCD camera (DAGE-MTI) and imported into MATLAB. For mapping experiments, these images were used define the borders of a grid for photo-stimulation. For Emx1-cre experiments, this was an area extending from just below the L1-L2 border to upper layer 6 (~810-870 μm) and covering 2-5 columns laterally (~400 to ~1000 μm). For PV-cre experiments, the slice was rotated to achieve complete or nearly complete coverage of all cortical layers. The DMD was used to pattern light into a square region (30-40μm on a side). Each stimulation site was spaced 25-30μm apart from adjacent ones, resulting in some overlap of adjacent stimuli. During mapping, a 50ms ramp of light (1.25 mW/mm^2 final intensity) was applied to one of these regions at a time. Ramps minimize activation of fibers of passage (Adesnik and Scanziani, 2010). Ten regions were stimulated per second in a serial, pseudorandom order, with 4 second breaks after every 10 seconds of mapping. Control experiments were performed using identical stimulation conditions while recording from $ChR2^+$ neurons in all layers. To account for the different excitability of PV neurons, for PV-cre mapping experiments were performed at room temperature (~20°), and light stimuli measured 50μm to each side. Control experiments recording spiking from ChR2 expressing cells confirmed that this yielded comparable efficacy and precision to the photostimulation protocol used in Emx1-Cre experiments (Supp. Fig. 9c, d).

All data were analyzed using custom written MATLAB software. For mapping experiments, the DC component was removed from traces by subtracting a down-sampled and median-filtered duplicate of the trace. Charge was calculated as the integral of the EPSC/IPSC during photostimulation and the subsequent 50 milliseconds. Population maps were generated by first rotating the average map collected in each experiment in order to horizontally orient the laminar boundaries of the mapped area. Maps were next translated vertically to align the L4-L5 laminar boundary, and translated horizontally to align either the home column or the soma position of the recorded cell, before being averaged to yield a population map. Average values are expressed as mean ± s.e.m. Statistical tests were performed using the paired t-test (latency data, Fig. 5b).

Paired recording connectivity testing

Experiments were performed in slices prepared from either PV-cre; Flex-TdTomato or GIN-GFP mice. We first targeted whole-cell recordings to a fluorescent L5 interneuron, and then subsequently recorded from one or multiple neurons in L4 of the same column. Monosynaptic connectivity was tested by driving spiking in L4 neurons using trains of 1.5 ms, 2nA current injections, while monitoring EPSCs in a reporter-labeled cell in L5. Stimulation was repeated at least 15 times in all pairs tested. For PV-cre experiments, connections were tested by driving trains of 3 spikes in L4

cells at 10 Hz, though in connected pairs a single spike was sufficient to drive a robust EPSC. In contrast, excitatory synapses onto Martinotti cells exhibit high rates of failure on the first spike but display facilitating EPSCs during trains of high frequency firing[55]. We therefore tested connections onto GIN GFP+ cells by driving trains of 10 spikes at 70 Hz in the presynaptic cell. As a positive control, we confirmed that we could use this protocol to observe monosynaptic EPSCs in GIN GFP+ cells by recording from pairs of L5 pyramidal neurons and L5 GIN GFP+ (data not shown). The distance between the somata of recorded cells was 122 ±41 μm for L4-L5 GIN pairs, and 180 ±39 μm for L4-L5 PV pairs. To perform statistical tests, we created a contingency table by categorizing L5 interneurons based on two criteria: cell-type (as established by genetic labeling) and whether or not that interneuron received at least one connection from L4. We then used Fisher's exact test on these categorical data. For further confirmation, we also fit a generalized linear mixed-effects model to our connectivity data. This model allowed us to account for the non-independence and varying amount of observations of connectivity onto each L5 interneuron, which would invalidate standard binomial tests. We found a statistically significant effect of cell type on connectivity rate (data not shown), corroborating our previous analysis.

Whisker imaging and automated tracking

A high-speed camera (Basler acA2000-340km) was placed below the running wheel; whiskers were imaged from below using a telecentric lens (Edmund Optics NT58-257) and a mirror angled at 45 degrees. Whiskers were backlit from above using high-powered diffused infrared LEDs (CMVision-IR200). High-speed videos were acquired with a framegrabber (Silicon Software) at 495fps with a 100us exposure and were synchronized with electrophysiology data via external triggers. Whisker tracking was performed offline using "Whisk" (Clack et al., 2012) (Janelia Farms, HHMI) which returned whisker angles and positions for every frame. Tracking data was further processed and analyzed using custom MATLAB scripts written to extract whisker contacts, set-point, amplitude, phase, and frequency. Whisker contacts were defined as the moment a whisker trace entered a user specified region of interest placed around the border of the stimulus bar. Contact accuracy was verified by watching a subset of videos from each experiment.

Statistics

All analyses were performed using MATLAB (Mathworks). The analyses performed were: 2-way ANOVA, student's t-test, paired t-test, Wilcoxon signed rank test, Kruskal-Wallis test, and Fisher's exact test. Where relevant, all tests were two-sided. Shapiro-Wilk and Kolmogorov-Smirnoff tests were used to formally assess normality of data in cases where parametric tests were used. No statistical methods were used to pre-determine sample sizes, but we collected sample sizes similar to those reported in previous publications. Blinding was not used in this study. In experiments involving multiple different stimuli (visual/tactile stimulation in awake mice, or *in vitro* optogenetic mapping), different stimuli were randomly interleaved. Unless noted, all plots with error bars are reported as mean ± s.e.m.

Supplementary Figures

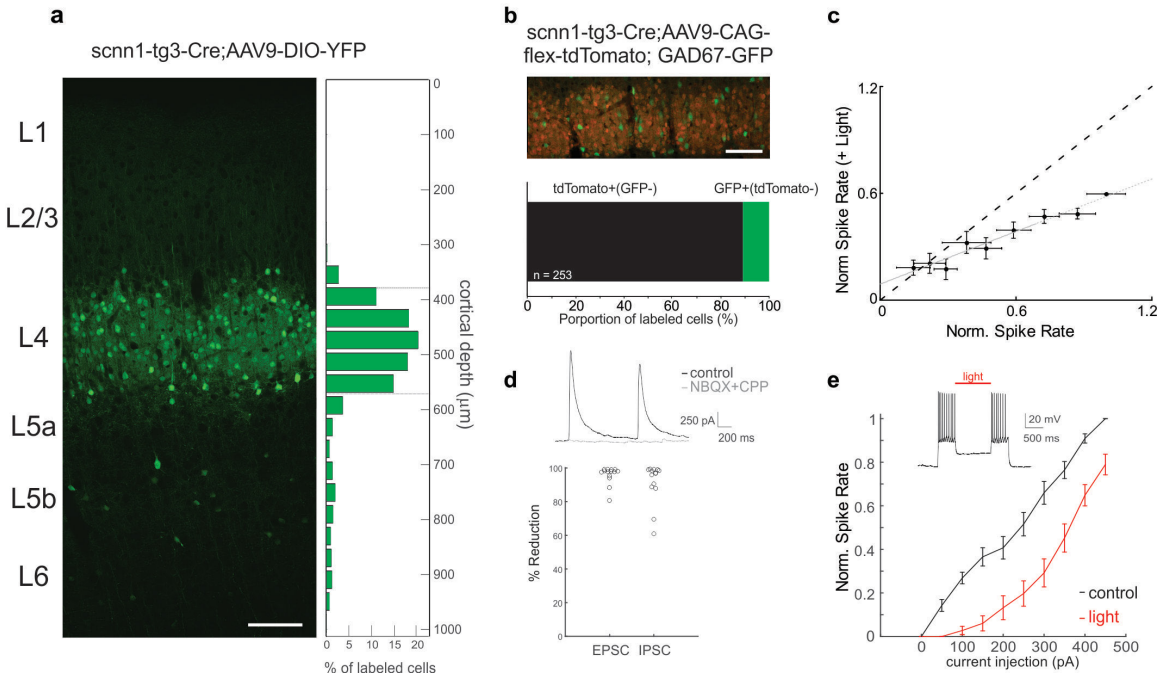

Supplementary Figure 2.1 Scnn1-tg3-Cre line labels excitatory cortical neurons preferentially in layer 4.

a, Left: Laser scanning confocal image of an scnn1-tg3-Cre mouse injected with AAV9-ef1a-DIO-YFP. Scale bar: 100 µm. Right: histogram of the proportion of labeled cells observed vs. cortical depth. b, Top: Example image from L4 of an scnn1-tg3-Cre;Rosa-LSL-tdtomato; GAD67-GFP mouse. Bottom: Quantification of the number of cells expressing tdTomato (85%) or GFP (15%). No cells co-expressing GFP and tdTomato were observed. Scale bar: 100 µm. c, Plot of normalized spike rate under light vs. control conditions in L4 RS units for rank- ordered stimulus preference. d, Plot of the proportion of synaptic excitation and synaptic inhibition blocked by application of the glutamatergic antagonists NBQX and CPP (10 µM each, $p = 0.00012$, $n = 14$ cells in 14 slices from 5 mice, Wilcoxon signed rank test, $z = 3.28$). e, Firing rate vs current injection plots of L4 eNpHR3.0-expressing excitatory neurons under control conditions (black) and during illumination of the slice ($n = 8$ cells in 4 slices from 3 mice). Inset: example trace showing light evoked suppression of action potential firing.

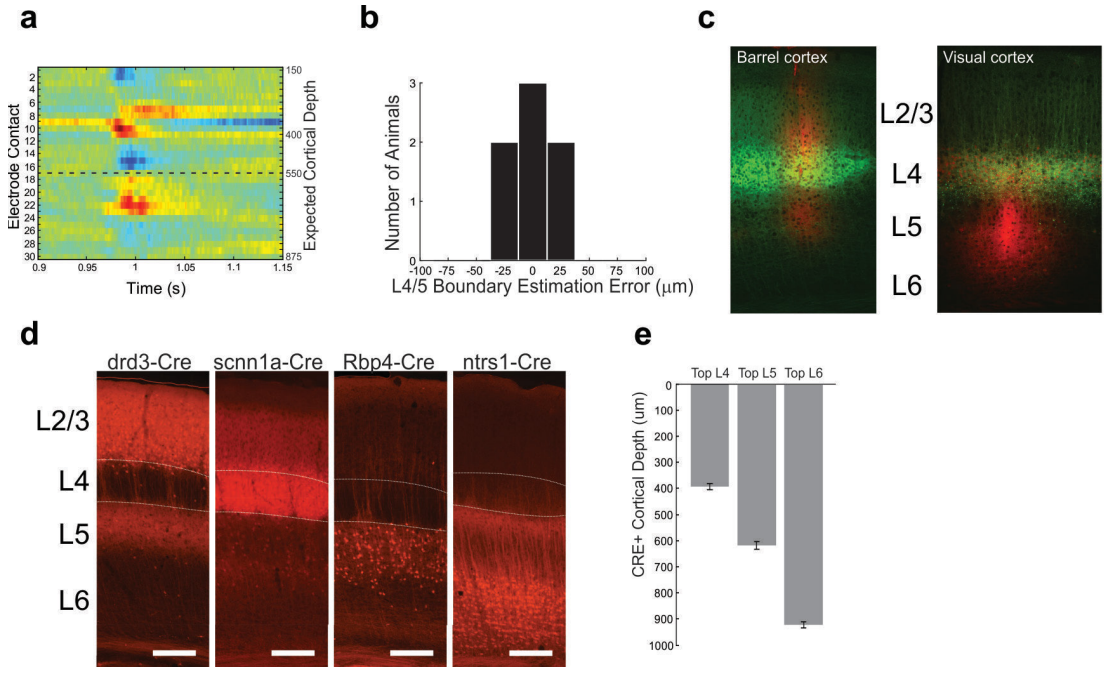

Supplemental Figure 2.2 Verification of depth estimates of extracellularly recorded units.

a, Example current source density plot computed from a 32-channel laminar probe inserted into S1 during whisker deflection. b, Histogram of the computed error in L4/5 boundary by comparing depth from the micromanipulator reading to the depth indicated by CSD analysis. c, Left: example imaging of a DiI track of a recording electrode inserted into the barrel cortex. Green: eNpHR-YFP, red: DiI. Right: same but for V1. d, Example images from four layer-specific Cre lines crossed to a Rosa-LSL-tdTomato reporter line used to compute laminar boundaries. e, Average laminar boundaries measured from the layer-specific Cre lines (n = 2 Drd3-Cre mice, n = 3 scnn1a-cre mice, n = 2 Rbp4-Cre mice, n = 1 Ntsr1 mouse, measurements in multiple sections for each mouse).

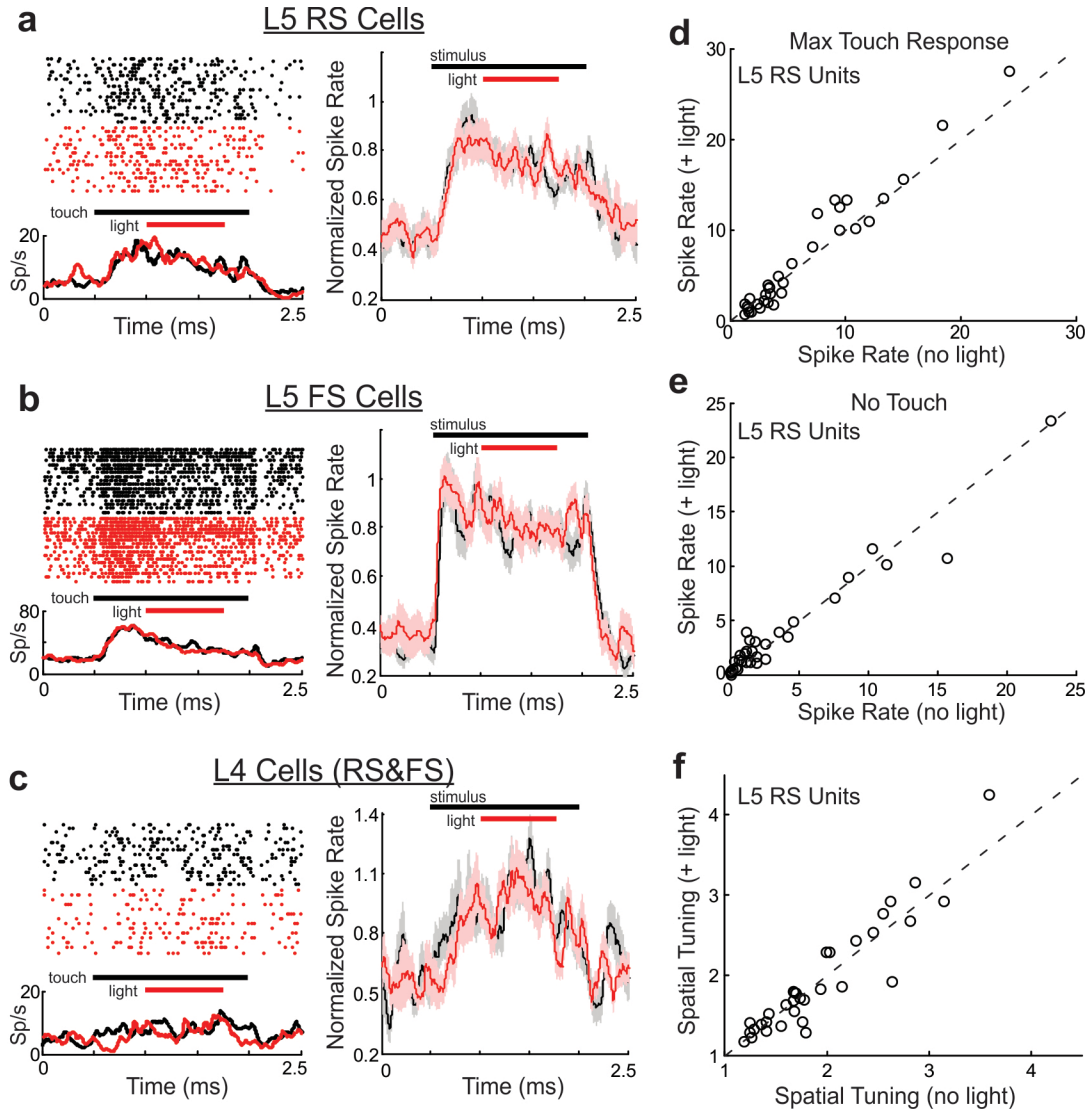

Supplementary Figure 2.3 Illumination of the cortex in mice expressing YFP alone shows no effect.

a, Left: Raster plot (top) and PSTH (bottom) of an example L5 RS unit during illumination of the cortex. Middle: Population PSTH under control conditions (black) and during illumination (red). Light had no effect on the spatial tuning curve of L5 RS units ($p = 0.36$, $n = 33$ units from 3 mice, 2-way ANOVA, $f(1) = 0.8445$). b, As in a) but for L5 FS neurons ($p = 0.7$, $n = 19$ units from 3 mice, 2-way ANOVA, $f(1) = 0.1108$). c, As in a) but for L4 units ($p = 0.5$, $n = 16$ units from 3 mice, 2-way ANOVA, $f(1) = 0.45$). d, Scatter plot of neuronal firing rates of L5 RS units under control and photo-suppression conditions for their preferred tactile stimulus ($n = 33$ from 3 mice, $p = 0.15$, paired t-test). e, As in d) but for the non-contact condition ($p = 0.62$, paired t-test). f, Scatter plot of the spatial tuning index of L5 RS units under control and illumination conditions ($p = 0.95$, paired t-test).

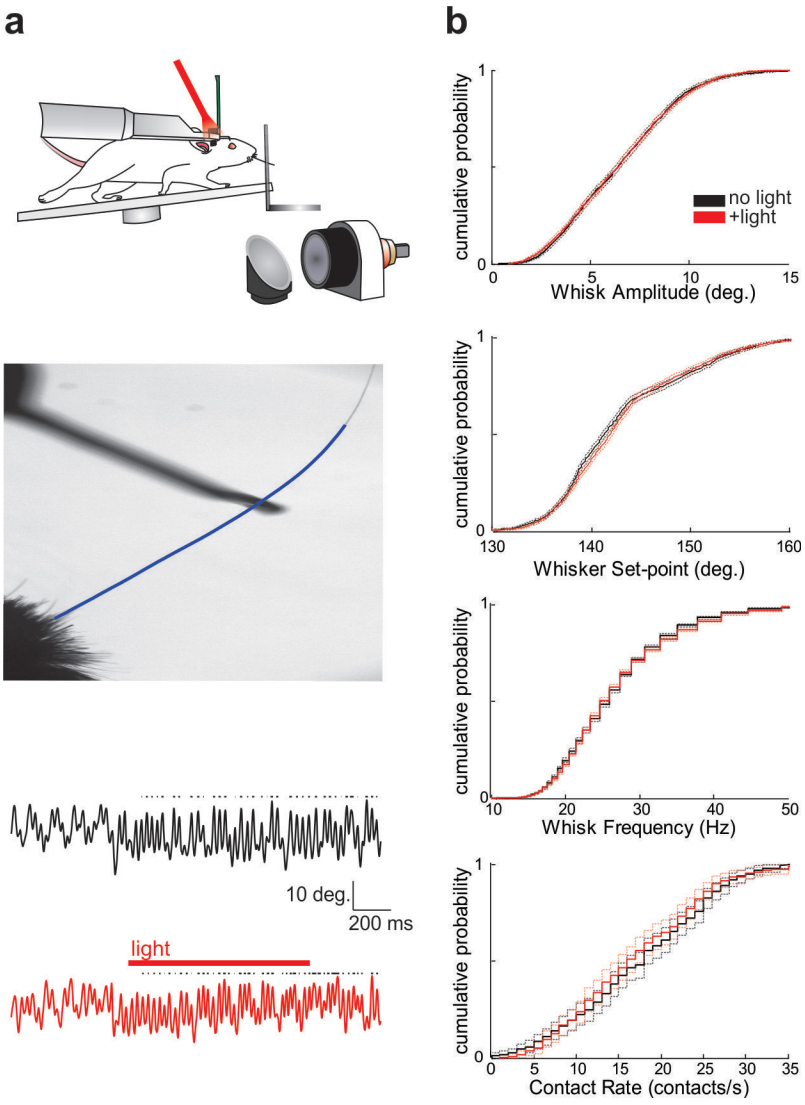

Supplementary Figure 2.4 Photo-suppression of L4 does not alter whisking behavior.

a, Top: Imaging schematic with a high-speed camera for whisker tracking. Middle: example image and tracked whisker (blue line) from the high-speed imaging stream. Bottom: example traces of whisker movement under control conditions (black) and during photo-suppression of L4. Black dots indicated contacts with the tactile stimulus bar. b, Top: Cumulative distribution plot of whisk amplitudes ($p = 0.71$, $n = 422$ whisk cycles in 4 mice, 2-way ANOVA, $f(1) = 0.14$) ; whisker set point ($p = 0.56$, $n = 422$ whisk cycles in 4 mice, 2-way ANOVA, $f(1) = 0.33$), whisk frequency ($p = 0.47$, $n = 422$ whisk cycles in 4 mice, 2-way ANOVA, $f(1) = 0.51$), and contact rate ($p = 0.38$, 2-way ANOVA) under control (black) and during L4 photo-suppression (red) (±95% confidence intervals, dotted lines).

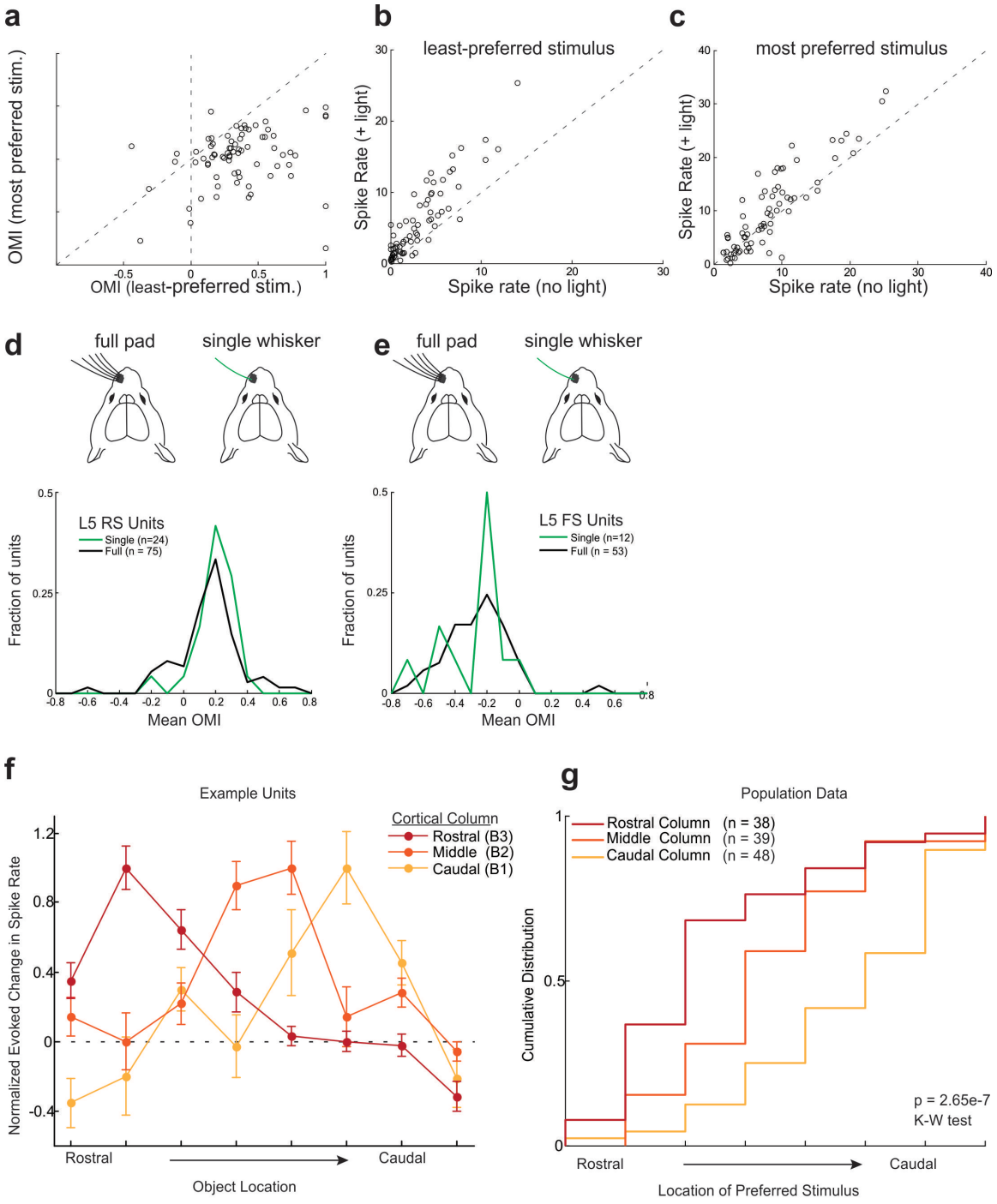

Supplemental Figure 2.5 Photo-suppression of L4 preferentially enhances L5 firing for non-optimal stimuli.

a, Scatter plot comparing OMI for the non-preferred stimulus position vs. the preferred stimulus position (mean $OMI_{non\text{-}preferred}$: 0.35±0.04; mean $OMI_{preferred}$: 0.02±0.03; $p < 10^{-6}$, n = 75 units from 9 mice, paired t-test, t(74) = 8.2). b, Scatter plot of raw firing rates of L5 RS units for the least-preferred stimulus position comparing control and L4 photo-suppression conditions ($p < 10^{-6}$, n = 75 units from 9 mice, paired t-test, t(74) = 7.9). c, As in b) except for the most-preferred stimulus position (p = 0.0006, n = 75 units from 9 mice, paired t-test, t(74) = 3.7). d, Histograms of a mean OMI of L5 RS units between animals tested will all the whiskers intact ('full pad', black), and those trimmed to the principal whisker (green). e, As in d) except for L5 FS units. L4 suppression significantly ($p = 1.3\times10^{-4}$, n = 24, f(1) = 15) enhanced L5 RS cells and significantly (p<0.002, n = 12, f(1) = 10) suppressed L5 FS cells during single whisker stimulation (2-way ANOVA). OMI distributions for L5 RS and L5 FS units were not significantly

different between full and single whisker stimulation ($p = 0.34$ and 0.69, respectively, two-tailed t-test). f, Example spatial tuning curves for three units recorded on adjacent shanks of a multi-shank probes (200 μm spacing), with adjacent shanks in three neighboring barrel columns. g, Cumulative distribution plots of the preferred positions of units recorded on multi-shank laminar probes ($p < 10^{-6}$, $n = 125$, Kruskal-wallis). Note the smooth shift in preferred position across the probe shanks.

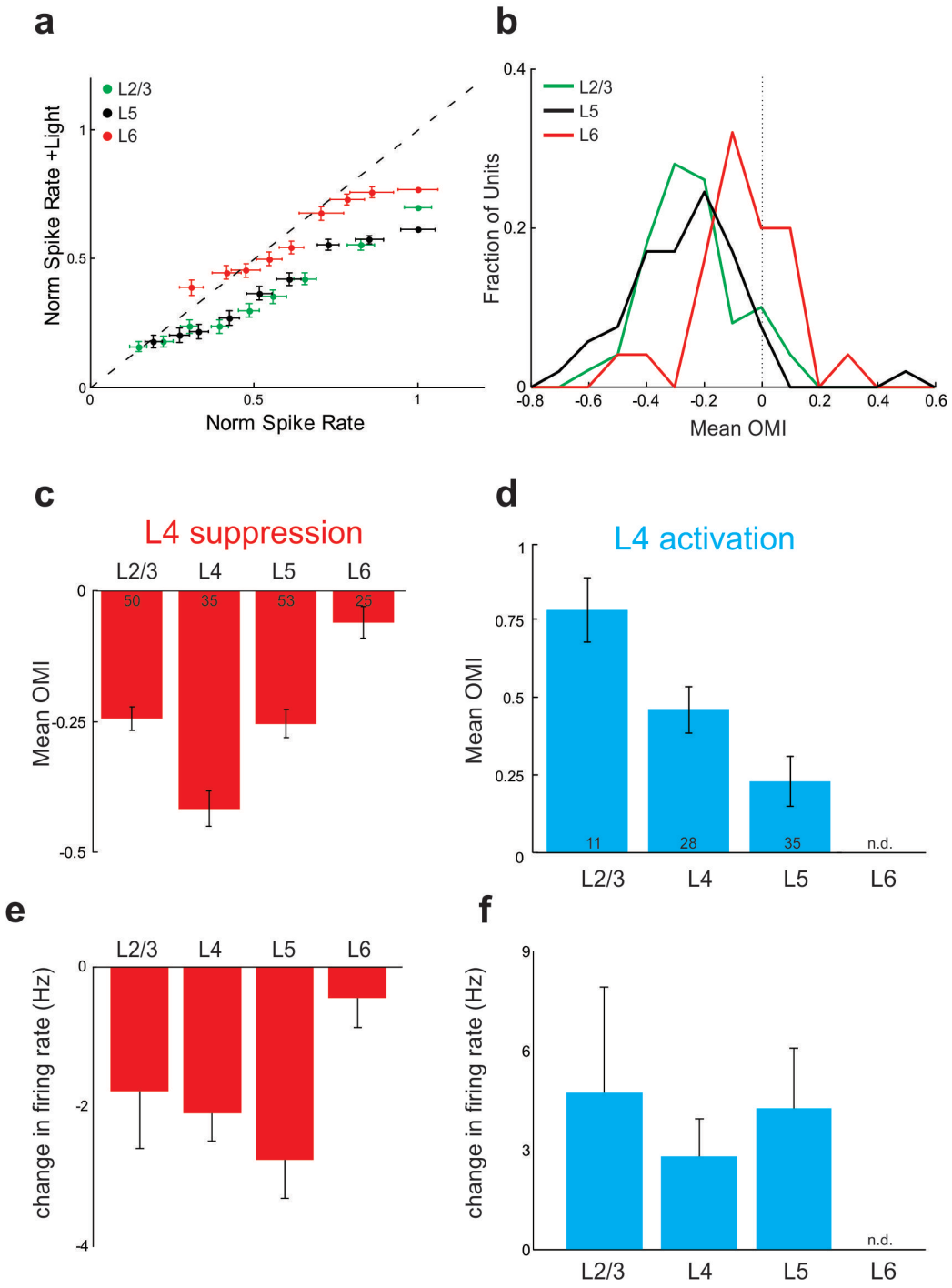

Supplemental Figure 2.6 The impact of L4 photo-suppression on FS units across layers.

a, Plot of the average normalized spike rates for FS units across L2/3, L5 and L6 between control and L4 photo-suppression conditions, grouped by ranked stimulus response. b, Histograms of the mean OMI for FS units across these layers across all stimulus conditions. c, Plot of the mean OMI across all stimulus conditions for FS units across all layers during photo-suppression of L4. d, As in c) but for L4 photo-activation (n.d., not done). e-f As in c) and d) but showing changes in the raw firing rates of FS units across layers.

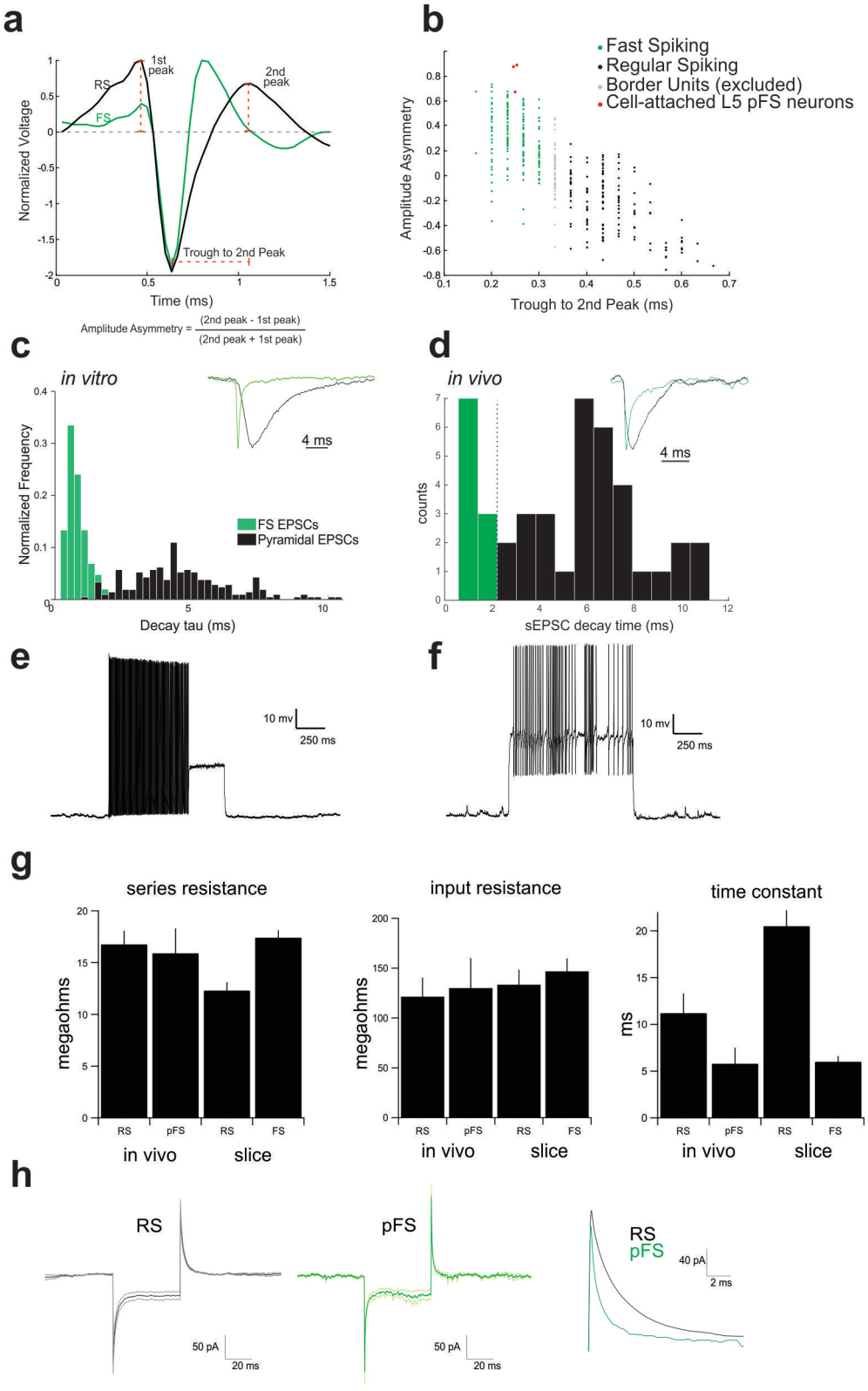

Supplemental Figure 2.7 Separation of FS and RS units.

a, Example waveforms for units categorized as FS (green) or RS (black) based on several waveform parameters. b, Scatter plot of amplitude asymmetry vs. trough to 2nd peak for recorded units. Units were categorized by k-means clustering. FS units: green, RS units: black, grey: excluded units, red: cells

recorded in cell-attached mode prior to intracellular recording. c, Histogram of sEPSC decay time constants in identified FS (green) or RS neurons (black) from acute brain slices. Cells were identified by their firing characteristics to current injection in the whole-cell mode. Inset: example average sEPSCs from an FS neuron (green) and an RS neuron (black). d, As in c) but for neurons recorded using the blind patch technique *in vivo*. e, Example supra-threshold response of a PV^+ neuron recorded with a K^+-based internal solution in a brain slice to current injection showing the characteristic non-adapting high frequency firing. f, As in e) but for a blind-patched pFS L5 neuron *in vivo*. Note that the variance in spike timing likely arises due to fluctuations in the background synaptic conductance *in vivo*. g, Average estimated series resistance (left), input resistance (center), and membrane time constant (right) for recorded RS and FS L5 cells *in vivo* (17 cells, 12 mice) and *in vitro* (*in vitro*: n = 42 cells in 36 slices from 17 mice). h, Average responses to a -4 mV voltages step in the RS (left) and pFS (center) neurons recorded *in vivo*. Right: expansion of the average current relaxation in RS and pFS cells after the end of the voltage step.

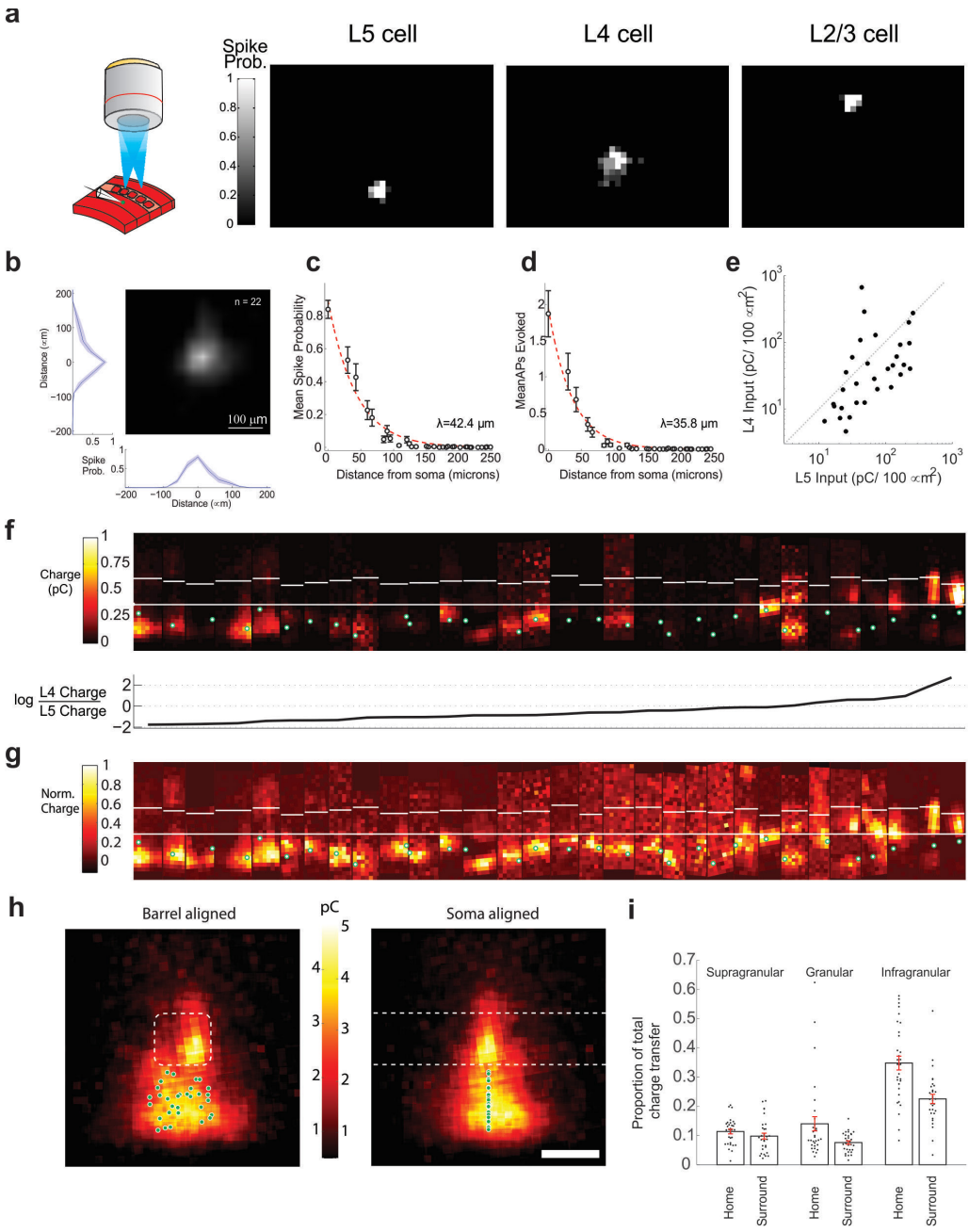

Supplemental Figure 2.8 Spatial resolution of DMD-based mapping and L5 FS input maps.

a, Left: schematic of DMD-based setup for photo-stimulation. Right: Example spike probability maps of an example excitatory neuron in L5, L4, and L2/3. b, Spatial resolution of light-evoked spiking in ChR2$^+$ excitatory neurons in the emx1-Cre line. c, Plot of spike probability vs. distance of the photo-stimulation light from the soma of the recorded neuron. d, As in c) but for mean number of action potentials evoked per photo-stimulation trial. e, Scatter plot of the mean excitatory input of recorded L5 FS neurons comparing input from L4 and L5. f, Top: All 31 excitatory input maps of L5 FS neurons ranked ordered according to the ratio of their mean excitatory input from L4 to L5. Maps have been rotated and cropped to show only the region corresponding to the barrel column in which each FS cell was located. White lines correspond to the upper and lower borders of L4. Green and white dots indicate the soma location of the recorded cell. Bottom: Corresponding log value of the ratio of mean charge transfer per unit area of L4 to mean charge transfer per unit area of L5 for each map. g, As in top panel of f), but with each map normalized to its range. h, Left: Average excitatory input map for all L5 FS cells (n = 31 cells in 26 slices from 13 mice), after aligning the barrel of the home column of each recorded cell. Right: As in left panel, but after horizontally aligning maps to the soma of each recorded cell. Scale bar: 200 µm. i, Quantification of the proportion of excitatory charge transfer to L5 FS cells originating from within the home column versus surrounding columns across cortical layers, normalized to total charge transfer in each map.

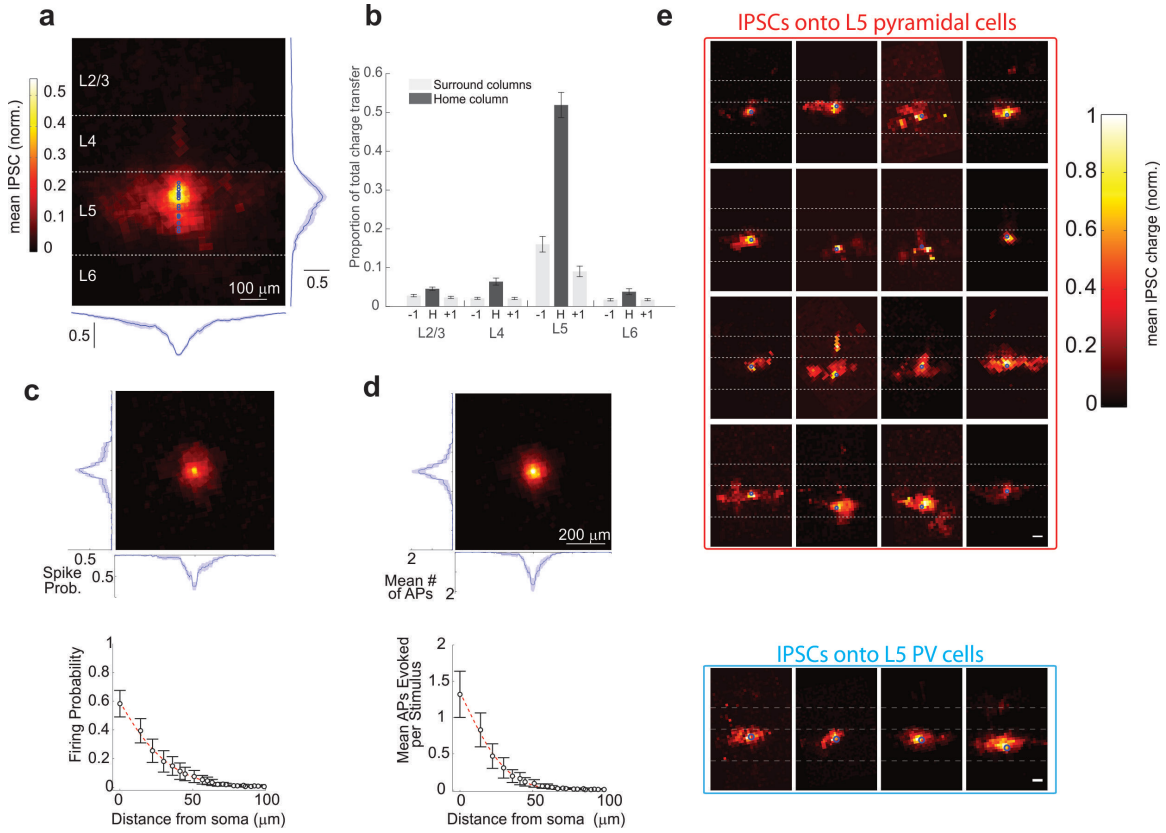

Supplemental Figure 2.9 PV interneuron mediated inhibitory input to L5 cells.

a, Average of normalized inhibitory input maps for all L5 pyramidal cells (n = 16 cells in 9 slices from 4 mice) recorded in PV-Cre;flexed-ChR2 brain slices. Maps are vertically aligned to laminar borders and horizontally aligned to the soma of the recorded cell (blue circles). b, Plot of the mean proportion of inhibitory input onto L5 pyramidal cells from PV neurons in each cortical layer, separated by barrel column. H: home column. ±1: adjacent barrel column. Dark gray: mean proportion of home column inhibitory input; light gray: same, but for the surrounding two columns. c, Top: Average spike probability map for all recorded PV neurons (n = 19 ChR2+ PV cells in total, in 11 slices from 5 mice; n = 4 in L2/3; n = 6 in L4; n = 7 in L5; n=2 in L6) under the photo-stimulation conditions using for mapping inhibitory input to L5 PCs. Bottom: Plot of firing probability versus distance from the soma of the recorded PV neuron. d, As in c) except for mean number of action potentials evoked in PV neurons during each photo-stimulus. e, Top: All 16 individual inhibitory input maps for L5 pyramidal cells. Bottom: four example inhibitory input maps in intracellularly recorded PV neurons (recorded at the reversal potential of the ChR2-photocurrent).

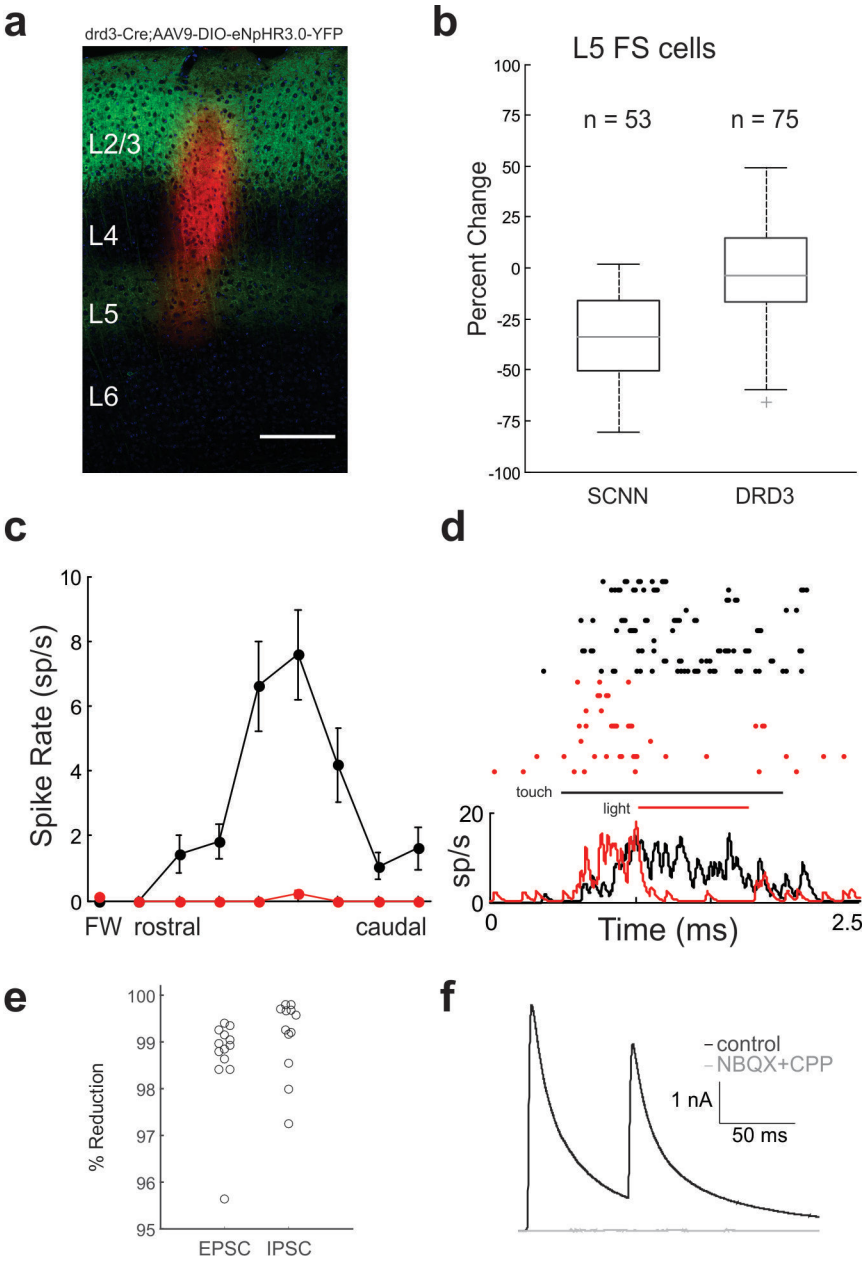

Supplemental Figure 2.10 Impact of photo-suppression of L2/3 excitatory neurons on L5 FS units.

a, Example image from a Drd3-Cre mouse injected with a DIO-eNpHR3.0-YFP (green) and recorded with a DiI-labeled laminar multi-electrode array. Scale bar: 200 μm B, Box and whisker plot of the average percent change in L5 FS unit firing rate when photo-suppressing L4 (in the scnn1-tg3-Cre line) or L2/3 (in the Drd3-Cre line). Mean firing rate in the L2/3 FS population is not significantly reduced by L2/3 photo-suppression ($p = 0.7$, $n = 75$ units from 7 mice, 2-way ANOVA, $f(1) = 0.144$). c, Spatial tuning curve of an example photo-suppressed L2/3 RS unit with (red) and without (black) light. d, Raster plot (top) and PSTH (bottom) of the example unit in c) during photo-suppression of L2/3 during sensory stimulation. e, Plot of the proportion of synaptic excitation and synaptic inhibition blocked by application of the glutamatergic antagonists NBQX and CPP ($p = 0.00024$, $n = 13$ cells in 8 slices from 4 mice, Wilcoxon signed rank test, $z = 3.16$). f, Example traces of light evoked IPSCs recorded in a L5 pyramidal cells in drd3-cre mice injected with flexed-ChR2. Black: control, grey: after application of glutamatergic antagonists, showing near 100% block.

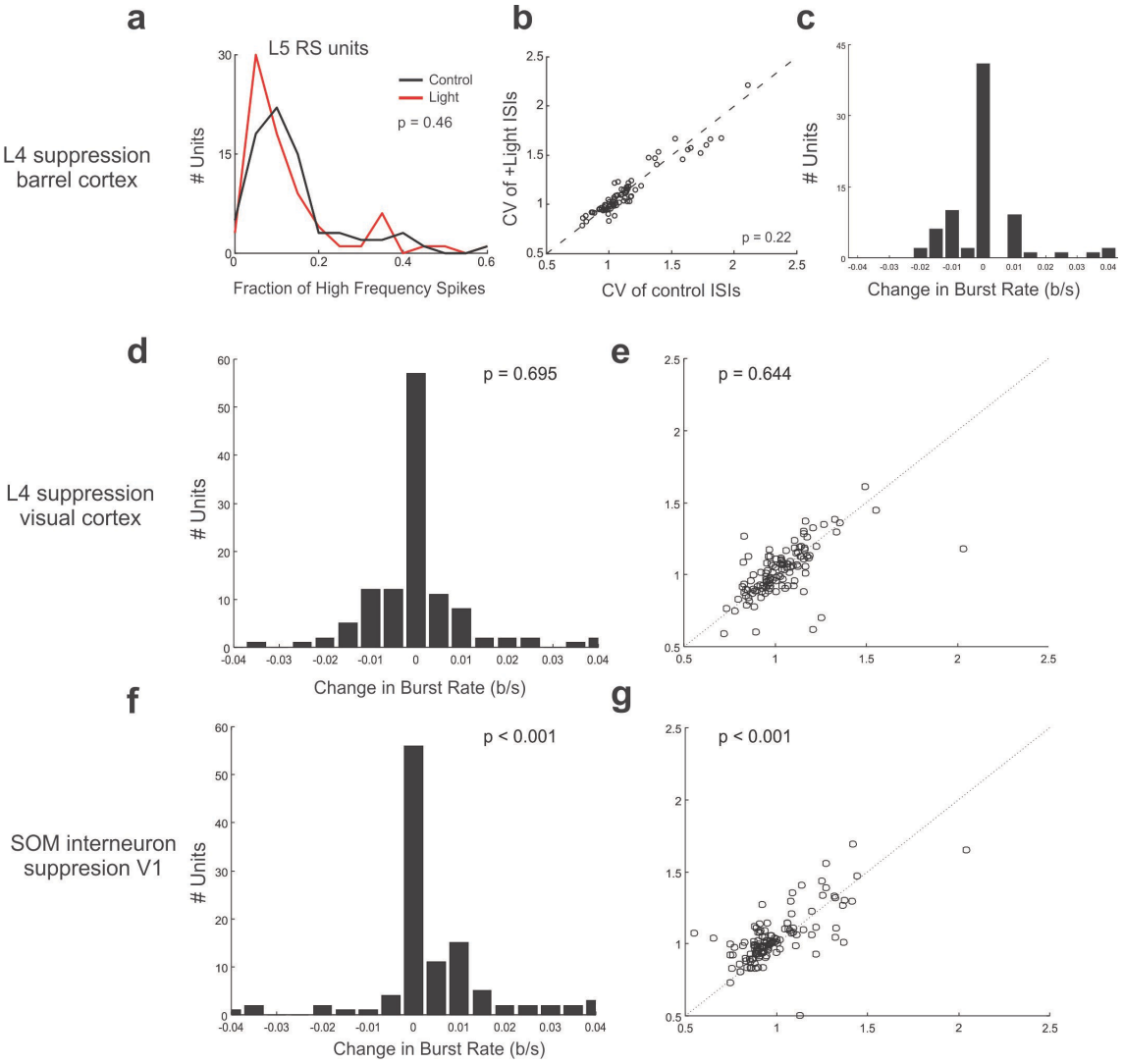

Supplemental Figure 2.11 Photo-suppression of L4 does not increase burst rate of L5 RS cells.

a, Histogram of the fraction of high frequency spikes (see Methods) for L5 RS units with (red) and without (black) photo-suppression of L4 (p=0.46, n=75 units from 9 mice, Wilcoxon signed rank test). b, Scatter plot of the coefficient of variation of the inter-spike-intervals (ISIs) of L5 RS units with and without photo-suppression of L4 (light vs no light, p=0.22, n=75 units from 9 mice, Wilcoxon signed rank test). c, Histogram of the change in burst rate of L5 RS units during photo-suppression of L4 (p=0.67, n=75 units from 9 mice, Wilcoxon signed rank test). d, As in d) but for L5 RS units recorded in the visual cortex. e, As in c) but for V1 units. f, As in e) but for photo-suppression of SOM^{+} inhibitory neurons. g, As in f) but for SOM photo-suppression. In figure panels d), e) and g), burst rate was calculated using a Poisson surprise algorithm[53].

Interlude

In the closing phases of the work described in the previous chapter, we were interested in determining whether other inhibitory interneurons in L5 might contribute to L4-driven suppression of L5 PCs. Other work suggested that most synaptic inhibition of L5 PCs originates from interneurons within L5. The large majority of interneurons in L5 can be classified into two broad groups: PV-expressing interneurons, and somatostatin (SST) expressing interneurons. Accordingly, we hypothesized that the next most likely candidate circuit that might allow L4 to drive inhibition onto L5 PCs would operate through L5 SST cells. To address this, I conducted paired recordings between L4 excitatory neurons and L5 SST cells. I used two different mouse lines to target L5 SST cells for these experiments, which produced entirely discrepant results: experiments in one line showed no connections between L5 SST cells and L4, while experiments in the other line showed plentiful connections! The project described in the chapter to follow was born from this discrepancy; in some ways, the entire project is a loose end run amok. Fortunately it led to an interesting biological finding: different classes of L5 SST cells with highly selective laminar connectivity.

To provide context for this work, I return to the concept of the canonical cortical circuit. The preceding chapters dealt with this circuit primarily discussed local patterns of connectivity in cortical circuits. However, as is alluded to several times, the laminar structure of the cortex also organizes the long-range inputs and outputs of the cortical circuit. Understanding the organization of these projections is also likely indispensable to discovering principles of how the canonical circuit might function, because of the simple fact that these circuits never operate in isolation. If canonical circuits exist, the must do so as nodes in a vast network, subsumed by a much larger hierarchy. Their function can very likely only be understood in this juxtaposition.

While long-range pathways of cortical circuits are less understood than local ones, they are also organized by layer. Perhaps most notably, afferents from different areas target certain layers. The specifics of this vary by area, but obey a general (though loose) logic based on whether they originate in areas that are higher or lower in the corticothalamic hierarchy than the target area. Broadly: afferents from lower areas preferentially target L4 (for example, afferents from primary sensory thalamus targeting primary sensory cortex) whereas afferents from higher areas preferentially connect to neurons in L2/3 and L5/6, in part by densely targeting their dendrites in L1, while avoiding L4 (D'Souza and Burkhalter, 2017; Markov et al., 2013).

Observations indicating that the functional connectivity between cortical regions is highly dynamic suggest that the effective strength of long-range corticocortical pathways can be adjusted. One possible way that this could be achieved is through local gating or modulation of afferent axonal inputs via synaptic inhibition. However, this idea is currently only speculation; indeed, it has been unclear if the circuitry exists that would permit such a scheme. The following work, suggests that the necessary machinery may be in place. We delineate new inhibitory pathways in which distinct subtnetworks of SST cells target specific layers. These pathways might allow the cortex to selectively adjust how much it 'listens' to different input streams to the local circuit.

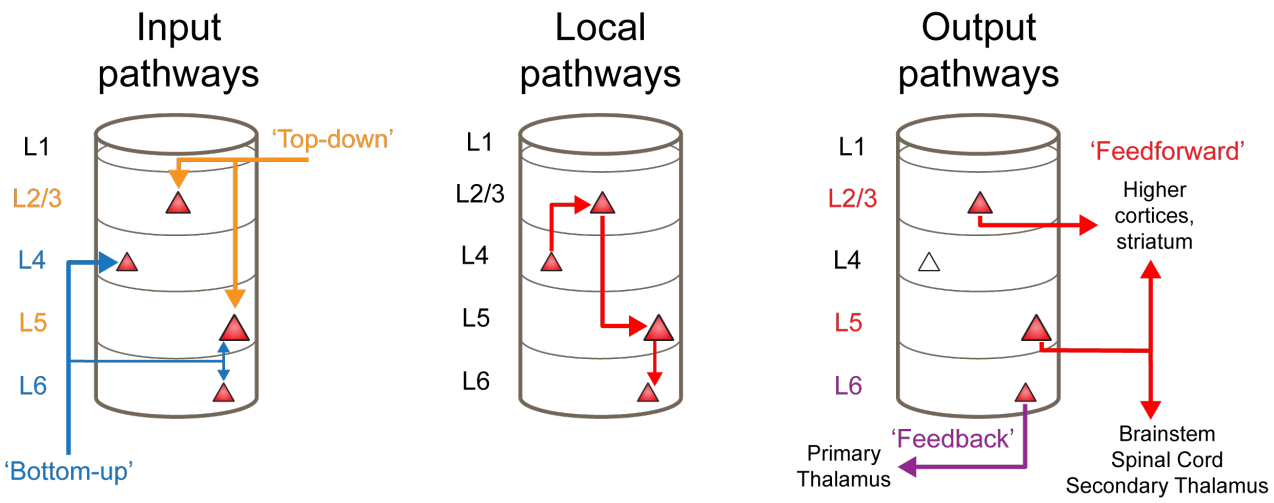

Figure I.1 Schematic of afferent, local, and efferent pathways in the different cortical layers

Chapter 3: Complementary networks of neocortical somatostatin interneurons

Foreword

This chapter contains work from the second half of my doctorate. It is presented in the form of a manuscript, which is currently under review. I had the great fortune to collaborate with many incredible scientists while working on this project. I am particularly thankful to Dr. Julia Veit, who contributed the *in vivo* recordings, Benjamin Shababo, who conducted and analyzed the 2-photon mapping data. Not included in this text but instrumental to the scientific progress of the project was a collaboration with a small team including Dr. Davide Risso, Dr. Rebecca Chance, and Dr. David Stafford (under the guidance of Professor John Ngai) to perform single-cell RNA sequencing.

One important note: somatostatin, sometimes abbreviated as 'SOM' in above chapters is hereafter abbreviated as 'SST.' I apologize for the inconvenience; this change was implemented at the suggestion of one of our peer reviewers.

Naka, A., Veit, J., Shababo, B., Chance, R., Risso, D., Stafford, D., Snyder, B., Egladyous, A., Sridharan, S., Chu, D., Paninski, L., Ngai, J., and Adesnik, H. (*in review*) Complementary subnetworks of neocortical somatostatin interneurons

Summary

The connectivity patterns of excitatory and inhibitory microcircuits are fundamental to computation in the neocortex. Highly specific excitatory projections form a stereotyped microcircuit linking the six cortical layers, but it is unclear whether inhibitory circuits are structured according to a similar layer-based logic or instead wire up non-selectively across the different layers. Understanding principles of inhibitory wiring is critical, since they constrain the computational operations that cortical inhibition can perform. If subnetworks of inhibitory neurons target specific functional components of cortical circuits (e.g. cortical input and output layers), these targets could be independently modulated, enabling a richer repertoire of inhibitory computations. Here we use one and two photon optogenetic circuit mapping techniques to demonstrate that two distinct subtypes of spatially intermingled Layer 5 (L5) somatostatin (SST) interneurons form exquisitely selective and complementary intracortical circuits. One subtype connects predominantly with L4 and L6 - the primary cortical input layers, while a second subtype connects nearly exclusively with L2/3 and L5 - the primary cortical output layers. This highly specific architecture suggests that separate SST networks could differentially modulate processing at the input and output stages of the neocortical microcircuit.
Keywords: cerebral cortex; interneuron; somatostatin; neural circuit; inhibition; cortical layers; optogenetics; connectivity

Introduction

Excitatory and inhibitory synaptic connectivity are fundamental to computation in neural circuits. In sensory regions, such as the primary somatosensory cortex (S1), excitatory circuitry follows a modular architecture centered on the 6-layered structure of neocortex. Excitatory principal cells (PCs) in each layer differentially encode and process sensory information, and their inter-connectivity helps define the basic input/output logic of the S1 microcircuit (Feldmeyer, 2012; Harris and Shepherd, 2015). 'Bottom-up' sensory inputs enter S1 via thalamocortical projections that most densely innervate L4, and cortical output emerges primarily from PCs in L2/3 and L5, feeding forward to other brain regions. In between, sensory-driven activity propagates through the different layers via highly specific translaminar pathways. Together, these excitatory pathways comprise a stereotyped microcircuit, which is thought underlie hierarchical transformation and processing of sensory information (Atencio et al., 2009; Martinez et al., 2005).

In contrast, no comparable framework exists for inhibitory circuit organization. While it is well established that the connectivity of many inhibitory circuits is selective with respect to cell-type (especially interneuron-to-interneuron connectivity; Kepecs and Fishell, 2014; Pfeffer et al., 2013), and that many interneurons target specific subcellular compartments of other neurons (Markram et al., 2004; Tremblay et al., 2016), it remains unclear how inhibitory circuits integrate into the layer-based logic of the excitatory microcircuit. One possibility is that interneurons non-selectively interconnect with PCs (Bock et al., 2011; Fino and Yuste, 2011; Hofer et al., 2011; Packer and Yuste, 2011; Scholl et al., 2015b), irrespective of layers; this would suggest that cortical inhibition primarily performs 'global' operations on excitatory neurons, such as non-specific normalization (Carandini and Heeger, 2012; Poo and Isaacson, 2009; Pouille et al., 2009b). Alternatively, interneurons might form synaptic connections with specific layers within the microcircuit, which would suggest that different functional components of cortical circuits can be independently modulated by specific inhibitory pathways, enabling more sophisticated computations.

To resolve this, it is necessary to assess connectivity in inhibitory circuits with respect to both layer and cell-type, since different classes of interneurons likely obey different principles for translaminar wiring. For example, many interneurons, including parvalbumin (PV) cells, the most numerous class of cortical interneuron, are largely local, intralaminar inhibitors (Brill et al., 2016; Koelbl et al., 2015; Levy and Reyes, 2012; Packer and Yuste, 2011; but see Bortone et al., 2014; Buchanan et al., 2012). However, some types of interneurons - most notably, dendrite-targeting somatostatin (SST) interneurons- appear specialized to mediate translaminar inhibition (Denardo et al., 2015; Helmstaedter et al., 2009a; Jiang et al., 2013, 2015; Kätzel et al., 2011; Marques-Smith et al., 2016b; Wang et al., 2004; Xiang et al., 1998). SST cells are critical players in many aspects of neural computation, perception, and cognition (Adesnik et al., 2012; Kim et al., 2016; Kvitsiani et al., 2013; Lee et al., 2012; Makino et al., 2015; Urban-Ciecko and Barth, 2016). Since they integrate excitatory inputs from both intralaminar and translaminar sources and since many SST cells, project extensive translaminar axons they are likely key players in translaminar inhibitory circuitry (Apicella et al., 2012; Kapfer et al., 2007; Karnani et al., 2016c; Otsuka and Kawaguchi, 2009; Silberberg and Markram, 2007; Xu and Callaway, 2009; Yoshimura and Callaway, 2005). How do SST inhibitory networks integrate into the different layers of the cortical microcircuit?

The intralaminar outputs of SST cells onto nearby PCs are thought to be extremely dense (Fino and Yuste, 2011; Jiang et al., 2015), which has led to the hypothesis that SST cells might generate a 'blanket of inhibition' that overlays nearby excitatory circuits (Fino et al., 2013; Karnani et al., 2014). One possibility is that the translaminar connectivity of SST cells is similarly non-selective. However, more sophisticated principles might govern the organization of laminar SST circuits. SST

cells are highly heterogeneous (Urban-Ciecko and Barth, 2016; Yavorska and Wehr, 2016) and can be subdivided into electrophysiologically and genetically distinct subtypes (Tasic et al., 2016a). Emerging evidence indicates that SST subtypes exhibit distinct sensory tuning and coupling to behavior (Kim et al., 2016; Kvitsiani et al., 2013; Ma et al., 2010; Muñoz et al., 2017; Nakajima et al., 2014; Reimer et al., 2014), indicating that different SST subtypes might serve different computational functions. Intriguingly, SST subtypes target their axons to different laminar domains (Ma et al., 2006b; Muñoz et al., 2014, 2017). While most SST cells are Martinotti cells (MCs) with axons that ascend to L1, there is also a substantial population of non-Martinotti cells with axons that primarily target L4 instead of L1. It has been hypothesized that these two distinct SST subtypes could uniquely influence cortical processing by targeting specific components of the cortical microcircuit. However, we lack basic knowledge of the circuit organization of different SST subtypes, which precludes mechanistic understanding of their computational contributions to cortical function. What are the patterns of synaptic input to different types of SST cells, and how might these give rise to differential activation of SST subtypes during sensation and behavior? Do all SST cells generate non-selective inhibitory outputs, or can SST cells provide targeted inhibition to specific components of the cortical microcircuit, such as certain cortical layers?

To address these issues, we used a combination of high-resolution one and two photon optogenetic mapping, paired intracellular recordings, and anatomical reconstructions to probe the logic of SST inhibitory circuits across the six cortical layers. We focused our investigation on L5, since this layer hosts a more diverse population of SST cells than the upper layers, which includes large fractions of both Martinotti and non-Martinotti cells (Markram et al., 2004; Rudy et al., 2011). We found that two subtypes of SST cells exhibit exquisitely specific and strikingly complementary laminar patterns of connectivity. L5 Martinotti cells receive input from L2/3 and L5, whereas L5 non-Martinotti cells receive input from L4 and L6. In turn, L5 Martinotti cells provide reciprocal inhibition to L5 PCs but not L4 PCs, while L5 non-Martinotti cells inhibit L4 PCs but not L5 PCs. Furthermore, *in vivo* optogenetic manipulation of Martinotti and non-Martinotti cells modulated cortical activity in a layer specific manner. These results demonstrate that subtypes of SST cells are wired into separate layer and cell-type specific subnetworks which independently shape different aspects of cortical computation.

Results

Distinct subtypes of L5 SST cells receive complementary patterns of excitatory synaptic input

To probe the structure of L5 SST circuits, we first verified approaches to identify and target different subtypes of SST cells in the barrel cortex. The widely used SST-Cre line allows labeling of SST cells irrespective of subtype (by crossing to the LSL-tdTomato mouse line; hereafter referred to as 'SST-TdT'). Additionally, there exist transgenic GFP reporter lines which have been characterized as labeling smaller subsets of the SST population. We chose two of these lines, the 'X94' line and the 'GIN' line in order to respectively target non-Martinotti and Martinotti cells for whole cell recording in acute barrel cortex slices (Ma et al., 2006b; Oliva et al., 2000; Taniguchi et al., 2011c). GFP+ neurons were clearly visible within L5 in slices from both X94 and GIN animals, consistent with reports that L5 contains both Martinotti and non-Martinotti SST cells. Biocytin fills confirmed that the vast majority of L5 GIN cells were MCs (41/44; 93%) which exhibited an ascending translaminar axon that ramified in L1, L2/3, and L5a (Fig. 1a) and intrinsic properties classically associated with MCs (Fig. S1)(Fanselow et al., 2008; Kawaguchi, 1993; Kinnischtzke et al., 2012; Wang et al., 2004). Similarly, the vast majority of L5 X94 cells were non-Martinotti cells (32/35; 91%) which formed a dense axonal plexus in L4 rather than L1 (Fig. 1a, Fig. S2) and exhibited quasi-fast-spiking electrophysiological phenotypes (Fig. 1b, Fig. S1). While the X94 line labels only ~15% of SST cells in L5 (Ma et al., 2006b), additional recordings from L5 SST-TdT cells suggested that a larger fraction (~30 - 40%; Fig. S1c-g) of L5 SST cells are non-Martinotti, X94-like cells (hereafter termed 'XCs') with most of the remainder being MCs. Thus L5 contains at least two intermingled but qualitatively distinct SST cell subtypes, MCs and XCs, which can reliably be identified using the GIN and X94 lines, respectively (Ma et al., 2006b).

Aligning reconstructions of L5 MCs and XCs revealed that these two populations had strikingly complementary vertical profiles of neurite density: MCs primarily innervated layers 1, 2/3 and 5, and XCs primarily innervated L4 and the L5/L6 border (Fig. 1c). This complementary pattern bears a strong similarity to the axonal projection profile of the two major thalamic input pathways to the barrel cortex: the profile of XCs aligns with the lemniscal pathway projection from the ventro-posterior medial nucleus (VPM), whereas the profile of MCs aligns with the paralemniscal pathway projection from the posterior medial nucleus (POm). These pathways, which carry different aspects of whisker related information, continue intracortically via specific, translaminar pathways; thus this distinction represents an important organizing principle in the excitatory connectivity and function of barrel cortex circuits.

We next asked whether MCs and XCs might differentially wire in to the laminar networks defined by these pathways. To do this, we first sought to determine whether the excitatory inputs to MCs and XCs might arise from different laminar sources. We virally expressed channelrhodopsin-2 (ChR2) in all excitatory neurons and photo-stimulated PCs in different regions of the slice to map the excitatory inputs to L5 MCs and XCs (Fig. 1d,e,f, AAV-flexed-ChR2 in the emx1-Cre line; see methods and Fig. S4). Remarkably, we found that L5MCs and XCs receive inputs from highly specific but largely non-overlapping sources that aligned with the anatomical distributions of their neurites. L5 MCs, but not L5 XCs, frequently received excitatory inputs from either upper L5, L2/3, or from both L2/3 and L5, but received little input from L4 or L6. On average, MCs received stronger inputs from L2/3 than L5 (49 ± 9% of total input from L2/3 versus 26 ± 7% from L5 in n = 15 MCs; $p = 0.008$, paired t-test). These results are consistent with previous studies (Anastasiades et al., 2016; Jiang et al., 2015; Kapfer et al., 2007; Pluta et al., 2015a). In contrast, L5 XCs received strong input from L4 and/or the L5B/L6 border (Fig. 1e,f; input from L4 and L6 was 62 ± 7% of

total input for n = 14 XCs versus 25 ± 3% for n = 15 MCs; $p = 6.5 \cdot 10^{-10}$; two sample T-test; see also Fig. S3) but relatively little input from L2/3 and L5. This input architecture indicates that these two subtypes of L5 SST cells receive almost completely distinct patterns of excitatory innervation from their local circuit. Comparing the average laminar profiles of mapped excitatory input and anatomical reconstructions revealed a striking symmetry in the overall structure of XC and MC intracortical circuits: XCs received input from L4 and 6, and projected most densely to these two layers; MCs received input from L2/3 and 5, and projected preferentially to these same two layers (Fig. 1c,f).

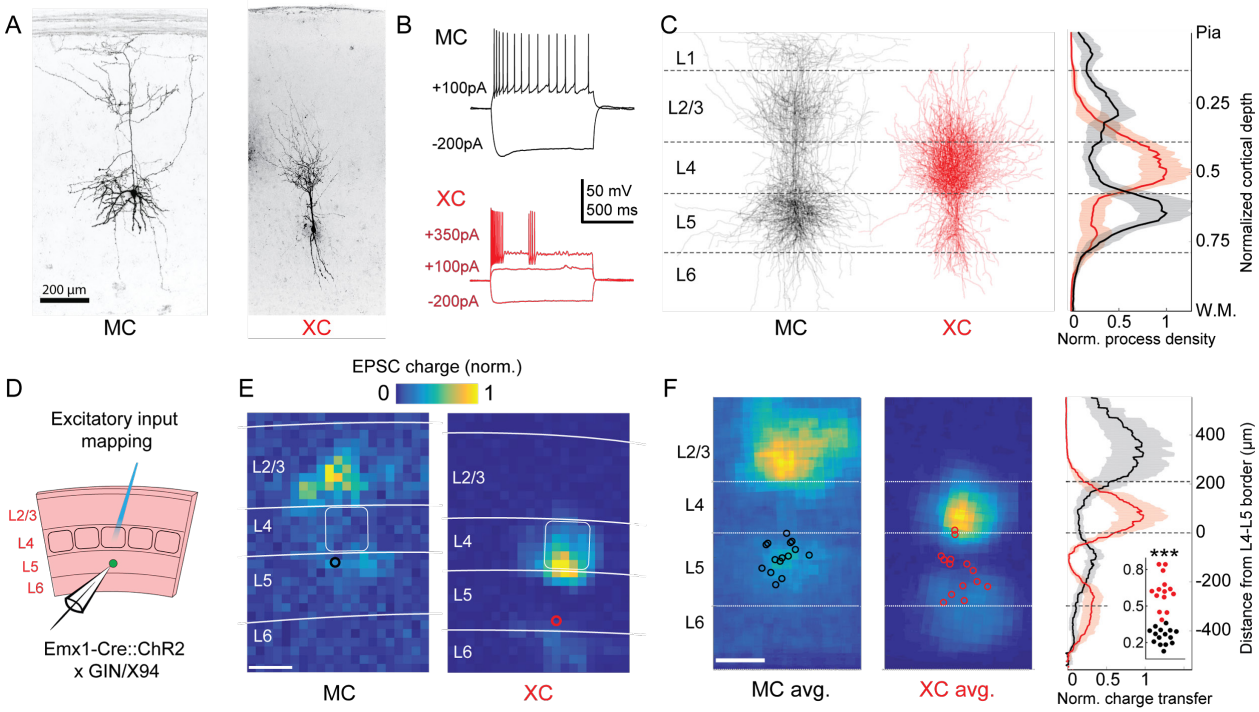

Figure 3.1 Complementary synaptic input patterns to two subtypes of L5 SST cells.

(A) Confocal images of dye filled neurons revealing two morphological phenotypes of L5 SST cells. Left: an L5 GIN cell. Right: an L5 X94 cell. Scale bar: 200 µm. (B) Example traces during current step injections from an L5 GIN cell (black) and an L5 X94 cell (red). (C) Left: Overlaid morphological reconstructions of L5 GIN/MC cells (black, n=14) and L5 X94/XC cells (red, n=10) showing differences in laminar distribution of neurites. Right: Normalized neurite density versus cortical depth for L5 GIN (black) and L5 X94 cells (red). Data are represented as mean ± C.I.(D) Schematic of experimental configuration. A digital micromirror device was used to focally photo-stimulate excitatory cells in different regions of the slice in order to map the spatial profile of excitatory inputs to GFP+ L5 MCs (Emx1-Cre; GIN) or GFP+ L5 XCs (Emx1-Cre; X94).(E) Example heat maps of median EPSC charge transfer evoked at each stimulus site for example L5 SST cells. Left: An L5 MC that received inputs from L5 and L2/3. Right: An L5 XC that received inputs from L4 and the L5/6 border. Soma locations are indicated by red/black bordered white dot). Scale bar: 200 µm.(F) Left: Grand averages of input maps reveal cell-type specific patterns of laminar input. Soma locations are indicated as above. Right: Normalized charge transfer versus distance from L4-L5 border for MC (black) and XC (red) populations. Scale bar: 200 µm. Inset: Swarm plots showing the proportion of total evoked charge transfer in each map that originated from sites in L4+L6, i.e. [L4+L6] / [L2/3+L4+L5+L6] for the MC (black; median, 27%; range, 13-36%) and XC (red; median, 62%; range, 38-84%) populations. Proportions were significantly different between L5 MCs and L5 XCs (25 ± 3% in n = 15 MCs versus 62 ± 7% in n = 14 XCs, mean ± C.I.; $p = 6.5 \cdot 10^{-10}$; two-sample t-test). See also Figures S1-4.

The striking laminar differences in inputs to L5 XCs and MCs suggested that these two types of SST cells should be differentially recruited by activity of different cortical layers. For instance, driving L4 should specifically recruit XCs, but not MCs. To test this possibility, we specifically photo-stimulated L4 excitatory neurons via Cre-dependent expression of ChR2 in scnn1-Cre mice (crossed to GIN or X94; Fig. 2a). L4-specific photostimulation (with two different stimulus protocols, across four different intensities; see methods) drove large EPSCs in XCs but evoked little to no input in MCs under identical conditions (Fig. 2b,c; Fig. S5). Current clamp recordings under the same

conditions showed that L4 photo-stimulation reliably drove spiking in L5 XCs, but not in L5 MCs (Fig. 2b,d; Fig. S5), despite the fact that MCs are intrinsically more excitable than XCs (Fig. S1). The lack of evoked responses in MCs was not due to differences in the degree of L4 activation (see supplemental text and Fig. S5 for controls). Thus, these results indicate a stark difference between L5 XCs and MCs: L4 densely innervates and powerfully drives firing in L5 XCs, but not L5 MCs.

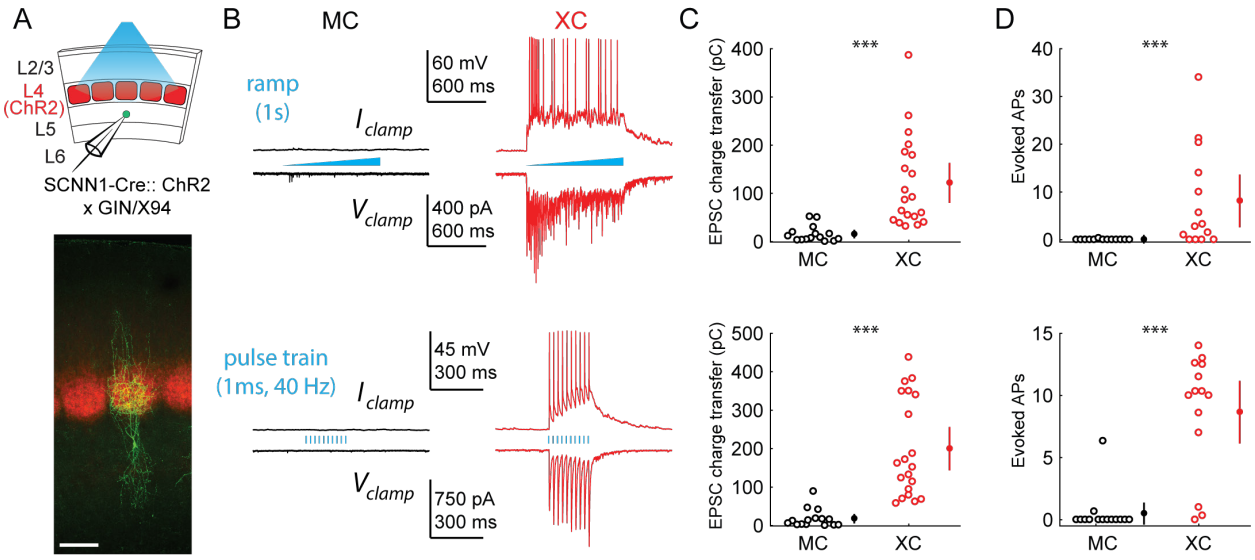

Figure 3.2 L4 photo-stimulation excites L5 XCs but not L5 MCs

(A) Top: Schematic of the experimental configuration. L5 X94 or GIN cells were recorded during photo-stimulation of L4 excitatory neurons. Bottom: Confocal image of a filled L5 X94 neuron (green) with ChR2-TdTomato expression (red) visible in L4. Scale bar: 150 μm. (B) Top row: Example traces recorded in the current clamp (upper traces) or voltage clamp (lower traces) configurations during a 1-second ramp photo-stimulation. Bottom row: As above, but for photo-stimulation with a 40 Hz train of ten 1ms pulses. (C) Quantification of excitatory charge transfer during maximum intensity 1-second ramp stimulation trials. Mean 122 ± 41 pC in n = 20 XCs versus 15 ± 8 pC in n = 15 MCs; $p = 3.9 \cdot 10^{-6}$, Wilcoxon rank sum test.(D) Quantification of the mean number of evoked action potentials during maximum intensity 1-second ramp stimulation trials. Mean 8.1 ± 5.5 spikes per trial in n = 15 XCs versus 0.03 ± 0.05 spikes per trial in n = 15 MCs; $p = 6.6 \cdot 10^{-4}$, Wilcoxon rank sum test. (E) As in C, for maximum intensity 40Hz pulse train stimulation. Mean 200 ± 56 pA in n = 20 XCs versus 18 ± 12 pA in n = 15 MCs; $p = 2.8 \cdot 10^{-6}$, Wilcoxon rank sum test. (F) As in D, for maximum intensity 40Hz pulse train stimulation. Mean 8.7 ± 2.4 spikes per trial in n = 15 XCs versus 0.5 ± 0.9 spikes per trial in n = 15 MCs; $p = 1.5 \cdot 10^{-6}$, Wilcoxon rank sum test. Error bars denote mean ± 95% confidence interval. Three asterisks denotes $p<0.001$. See also Figure S5.

Common input mapping reveals subnetwork structure in L5 SST cell output

Having found that XCs and MCs in L5 receive highly complementary patterns of excitatory synaptic input, we next asked whether XCs and MCs also exhibit layer-specificity in their inhibitory outputs. Since SST cells have been implicated in generating feedback inhibition (Adesnik et al., 2012; Kapfer et al., 2007; Silberberg and Markram, 2007), we hypothesized that MCs and XCs might target their inhibitory outputs in order to reciprocally inhibit the same PC populations that excite them. For example, XCs but not MCs would inhibit L4 PCs, whereas MCs but not XCs inhibit L5 PCs. Alternatively, MCs, XCs, or both cell types could globally target PCs within and across layers non-selectively. These hypotheses are difficult to test using conventional optogenetic approaches since, to our knowledge, Cre-driver lines do not exist for all SST subtypes. An alternative approach is to use high precision photo-stimulation to ask whether the outputs of individual SST cells (in the non-specific SST-Cre line) diverge onto PCs in multiple layers. If individual SST cells target either L4 or L5 PCs, but not both, then we should never observe common input to pairs of L4 and L5 PCs when photo-stimulating single SST neurons. This can be tested by mapping SST inhibitory connections onto multiple PCs simultaneously and analyzing the spatiotemporal coincidence of evoked IPSCs

onto different pairs of PCs, thereby measuring the amount of common input shared between pairs of PCs in different layers (Morgenstern et al., 2016; Yoshimura et al., 2005). Although this approach does not discriminate between MCs and XCs directly, it performs a more stringent test by extending our hypothesis to apply to the structure of the outputs of the L5 SST population as a whole.

In order to conduct comprehensive mapping of individual SST outputs, we developed a novel approach to map neural circuits at high spatiotemporal resolution using two photon optogenetics and a statistical pipeline for detecting synaptic connections (Merel et al., 2016) and evoked inhibitory postsynaptic current (IPSC) synchrony. In addition, we employed a soma-targeted opsin (Wu et al., 2013), which has the advantage of providing far superior spatial resolution during photo-stimulation than non-targeted opsins (Fig. 3a,b,c)(Baker et al., 2016). We expressed a soma-targeted variant of the red-shifted opsin, ChrimsonR, in SST cells using the SST-Cre line, and photo-stimulated SST cells using 2-photon excitation with computer generated holography (Fig. 3a,b; Fig. S9a). Since SST → PC synapses are often located on the distal dendrites of PCs, we recorded IPSCs using a cesium-based internal solution and took additional steps to minimize false negatives (see Methods). Using this method, we simultaneously mapped SST inputs to pairs of L4-L5 PCs and L5-L5 PCs (Fig. 3d,e,f). We found that L5 PCs received SST inputs at more locations than L4 PCs on average (45.3 ± 5.5 inputs out of 441 locations tested per map in n = 30 L5 PC maps versus 12.8 ± 2.3 inputs in n = 10 L4 PC maps, Fig. S10e), but that both cell types received inputs from locations throughout L5 (Fig. S10f).

If individual L5 SST cells target either L4 PCs or L5 PCs but not both, we would expect maps from L4-L5 PC pairs to contain spatially intermixed but non-overlapping input locations. Conversely, when recording a pair of L5 PCs, we would expect a much higher rate of overlap due to common input from MCs. Consistent with this hypothesis, we observe that the probability of detecting an input at the same location in L4-L5 pairs was very low and substantially smaller than for L5-L5 pairs (2.4 ± 1.3% spatially coincident inputs out of all input locations in n = 10 L4-L5 pairs, versus 28 ± 6.7% in n = 10 L5-L5 pairs; $p = 1.2 \cdot 10^{-3}$, Wilcoxon rank sum test). Given that occasionally more than one SST cell might be photostimulated at any given location (Fig. S9d,g), we employed a statistical test for fine time scale synchrony of IPSCs between the patched cells at each candidate location (where both cells received input) to determine whether the IPSCs truly arose from a single SST cell diverging onto both recorded PCs (Amarasingham et al., 2012, see Methods, Fig. 3g, Fig. S10g,h,i,j). Using this far more stringent spatiotemporal test for the detection of common input, we detected no locations in which stimulation evoked common inputs for L4-L5 pairs, whereas we detected at least one common input in 7 of 10 L5-L5 pairs (Fig 3h; no locations in n = 10 L4-L5 pairs versus 13.7 ± 5.1% of all input locations in n = 10 L5-L5 pairs; $p = 1.1 \cdot 10^{-3}$, Wilcoxon rank sum test; see also Fig. S10k). These data argue that individual L5 SST cells connect to either L4 PCs or to L5 PCs, but never to both. In other words, L4 PCs and L5 PCs are inhibited by non-overlapping subnetworks of L5 SST cells.

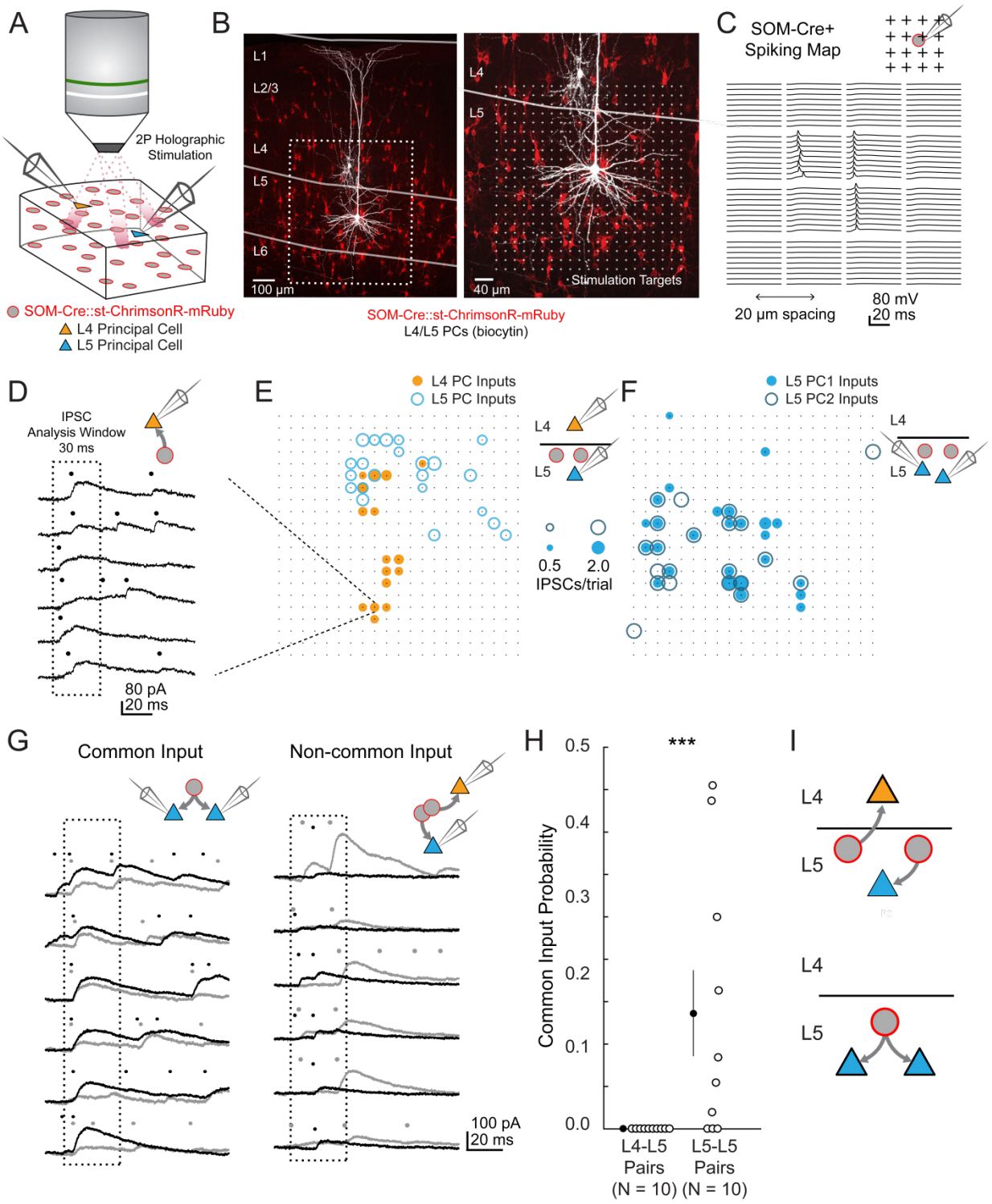

Figure 3.3 L4 and L5 PCs are inhibited by separate populations of L5 SST cells.

(A) Schematic of the experimental configuration. IPSCs are recorded from a pair of PCs (either an L4/L5 pair or an L5/L5 pair) while SST cells expressing soma-targeted ChrimsonR-mRuby2 are focally activated using 2P photo-stimulation and computer generated holography.(B) Left: post-hoc confocal image showing SST cells expressing soma-targeted-ChrimsonR-mRuby2 (red) and biocytin fills of recorded PCs in L4 and L5 (white) at 10x

magnification. Right: Confocal image at 20x magnification showing the grid of photo-stimulated target locations. Both images are max z-projections over 100 μm.(C) Spatial photo-excitation profile of a soma-targeted-ChrimsonR-mRuby2 expressing SST cell. Whole cell current-clamp recordings from this cell showing multiple trials of photo-stimulation at a 4 x 4 subsection of the photo-stimulation grid with 20 μm spacing between stimulation locations. The SST cell is recruited to spike only at a small number of stimulation sites, but does so reliably and with low jitter across trials at these sites. (D) Example traces showing IPSCs recorded from an L4 PC during SST photo-stimulation at a single site (corresponding to black boxed square in E) over multiple trials. Dots above each trace indicate the onset time of detected IPSCs ($p = .0003$, Poisson detection). (E) Example overlay of maps showing the mean number of IPSCs at detected input locations during photo-stimulation for a simultaneously recorded L4 PC-L5 PC pair. Bubble size indicates the mean number of IPSCs evoked (deviation from background rate) per trial.(F) As in E, but for an L5 PC-L5 PC pair.(G) Example traces illustrating method for detection of common SST-mediated inputs to pairs of simultaneously recorded PCs. Left: IPSC traces at a single site recorded simultaneously in two PCs (each PC is indicated by black or grey traces) and corresponding detected IPSCs. IPSCs with synchronous onset occur in many trials, despite the trial-to-trial jitter in IPSC onset, suggesting that a SST cell which diverges onto both recorded PCs is being stimulated at this site ($p = .0005$, synchrony jitter test). Right: IPSC traces from a different site. Evoked IPSCs are observed in both cells, but the lack of synchronicity suggests they arise from separate, neighboring SST cells ($p = .4$). Dots above each trace indicate the estimated onset time of detected IPSCs.(H) Probability of detecting common SST input per photo-stimulated site for pairs consisting of L4 PCs and L5 PCs versus pairs consisting of two L5 PCs. No common input locations were detected in $n = 10$ L4-L5 pairs versus 13.7 ± 5.1% of all input locations locations stimulated in $n = 10$ L5-L5 pairs; $p = 1.1 \cdot 10\text{-}3$, Wilcoxon rank sum test Data are summarized by mean ± S.E.M. (I) Schematic of main result for SST outputting mapping. Individual L5 SST cells form inhibitory connections onto L4 PCs and or L5 PCs but not both. See also Figure S9, S10.

Paired recordings show dense, reciprocal, and selective intra- and translaminar connectivity

We hypothesized that the L4-targeting and L5-targeting populations of L5 SST cells identified with two-photon optogenetic mapping corresponded to XCs and MCs. This would mean that SST cells in L5 are organized into at least two discrete subnetworks, each with its own unique input and output connectivity. If this were the case, one would expect L5 XCs to be reciprocally connected with L4 PCs, but not L5 PCs; conversely, L5 MCs should be reciprocally connected with L5 PCs but not L4 PCs. To address this, we conducted paired intracellular recordings to assess the fine-scale patterns of synaptic connectivity between L4/L5 PCs and L5 MCs/XCs. This strategy is low throughput, but provides unambiguous measurements of synaptic connectivity between identified cell types; furthermore, it complements the above experiments because it is unaffected by issues that potentially limit optogenetic approaches (for example, differences in intrinsic excitability between cell types or variability in opsin expression). In addition to targeting L5 MCs and XCs with the GIN and X94 lines as above, we also used the SST-TdT line to identify L5 SST cells, which we classified as putative MCs or XCs based on their electrophysiological properties (Fig. S1g; Table S1).

First, we address translaminar connections. Paired recordings between L5 XCs and L4 PCs revealed monosynaptic L5 XC→ L4 PC connections, which we observed as short-latency IPSP/IPSCs in the L4 PC membrane potential following induced action potentials in the L5 XC. We observed frequent L5XC→L4PC connections (36/67 pairs tested; 54%; Fig. 4a,b), even across relatively long inter-somatic distances (183 ± 67 μm, mean ± S.D.; Fig. S6), suggesting that L5 XCs connect densely onto L4. We also frequently observed monosynaptic excitatory connections from L4 PCs onto L5 XCs, consistent with the optogenetic experiments above (39/72 pairs tested; 54%). These synapses exhibited profound facilitation during sustained high-frequency firing in the presynaptic cell (Fig. 4a; Fig. S8), the hallmark of excitatory connections onto SST cells (Beierlein et al., 2003; Berger et al., 2009; Kapfer et al., 2007). In cases where we tested connectivity bidirectionally, we frequently observed reciprocal connections (23/56 pairs tested; 41%). Thus, L5 XCs and L4 PCs form a translaminar feedback inhibitory motif. We also observed frequent connections from L5 XCs onto L4 fast-spiking (FS) cells (12/23 pairs tested; 52%; Fig. S7), consistent with a known circuit in which L4 non-Martinotti SST cells inhibit L4 FS cells (Ma et al., 2006b; Xu et al., 2013).

In contrast, we very rarely observed excitatory connections from L4 PCs to L5 MCs (1/95 pairs tested; 1%; Fig. 4a,b) or from L5 MCs onto L4 PCs (4/68 pairs tested; 6%), despite the fact that these pairs were separated by smaller inter-somatic distances than L4PC-L5XC pairs (143 ± 47 μm, mean ± S.D.; Fig. S6), likely due to the fact that MCs and XCs preferentially localize in the

superficial and deeper portions of L5 respectively (Ma et al., 2006b). In a subset of these experiments, we recorded from L4 PCs in the voltage clamp configuration at +10mV (using a cesium-based internal solution), but did not observe connections any more frequently (0/38 pairs tested; 0%). These data suggest that L5 XCs are integrated into the densely interconnected network of L4 PCs and interneurons (Beierlein et al., 2000; Petersen and Sakmann, 2000), whereas L5 MCs are essentially isolated from it. Since our 2P mapping experiments indicated that distinct sets of SST cells inhibit L4 PCs and L5 PCs, we hypothesized that this pattern would be reversed within L5, i.e. L5 MCs but not L5 XCs will interconnect with L5 PCs.

We next examined intralaminar connections between L5 PCs and L5 SST cells. We observed frequent inhibitory connections from L5 MCs onto L5 PCs (24/46 pairs tested; 52%; Fig. 4c,d), in agreement with a large body of work indicating that Martinotti cells diverge profusely onto nearby intralaminar targets (Berger et al., 2010; Fino and Yuste, 2011; Jiang et al., 2015). We also observed excitatory connections from L5 PCs onto L5 MCs, albeit more rarely (4/29 pairs tested; 14%; Fig. 4c,d) but at a rate consistent with the literature (Jiang et al., 2015; Levy and Reyes, 2012). In contrast, we detected very few inhibitory outputs from L5 XCs onto L5 PCs (2/65 pairs tested; 3%; Fig. 4c,d) or excitatory connections from L5 PCs onto L5 XCs (1/60 pairs tested; 2%; Fig. 3c,d), despite the fact that L5 PCs were on average located much closer to L5 XCs than were L4 PCs. The surprising dearth of intralaminar connectivity between L5 PCs and L5 XCs stands in stark contrast to the dense intralaminar connectivity observed between L5 PCs and L5 MCs, as well as in other inhibitory circuits (Fino and Yuste, 2011; Levy and Reyes, 2012; Packer and Yuste, 2011), lending further support to the notion that MC and XC circuits are uniquely and selectively wired (Fig. 4e).

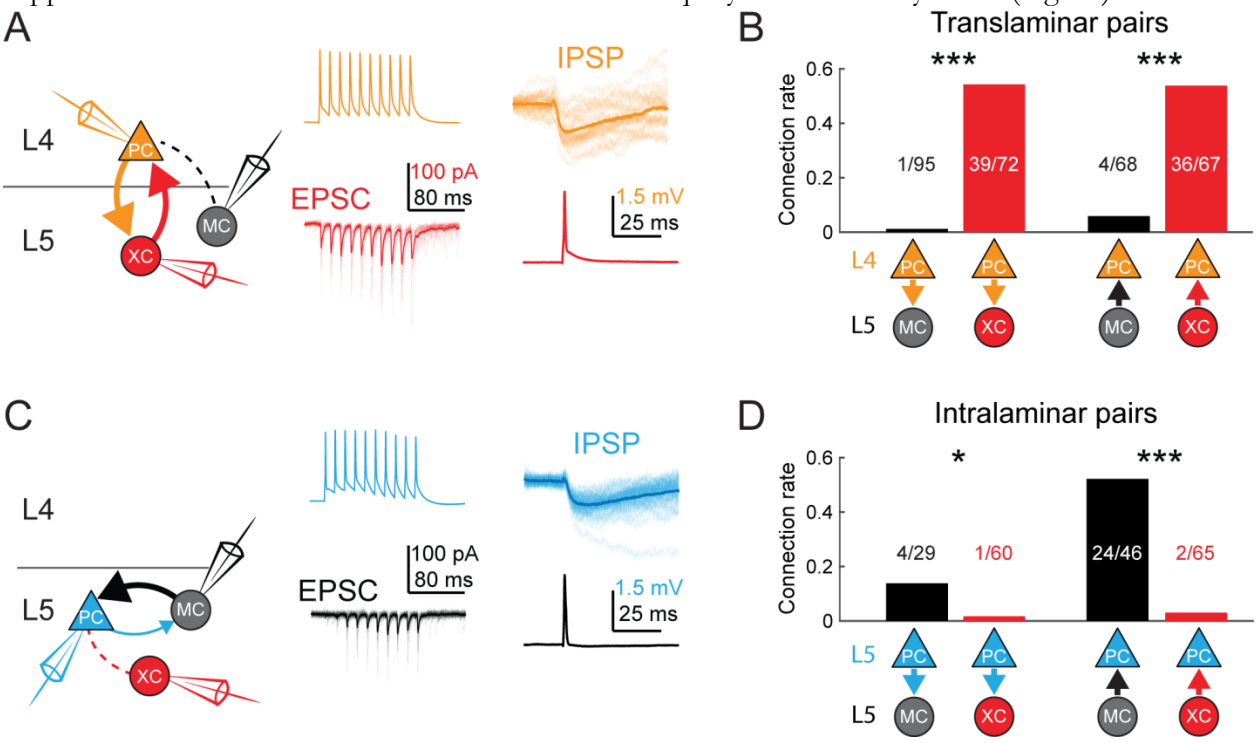

Figure 3.4 MCs and XCs exhibit different patterns of monosynaptic connectivity with L4 and L5 PCs.

(A) Paired recordings of L4 PCs (orange) and L5 XCs/MCs (red/black).). Left: schematic of the tested circuit. Middle: example traces of evoked spikes in a L4 PC (orange) and the excitatory synaptic current in a L5 XC (red). Right: example traces of evoked IPSPs in a L4 PC (orange) in response to a single action potential in a L5 XC (red). (B) Bar graph summarizing translaminar connection rates between L4 PCs and L5 MCs (black bars) and L4 PCs and L5 XCs (red bars). $p < 10^{-6}$ for L4PC→L5MC (n = 95 connections tested onto 39 MCs) versus L4PC→L5XC connection rate (n = 72

connections tested onto 51 XCs); $p = 2 \cdot 10^{-6}$ for L5MC→L4PC (n = 68 connections tested from 35 MCs) versus L5XC→L4PC connection rate (n = 67 connections tested from 51 XCs); Monte Carlo permutation test. (C) As in A, but intralaminar pairs between L5 MCs/XCs and L5 PCs (blue). (D) As in B, but for intralaminar connections with L5 PCs. p = 0.020 for L5PC→L5MC (n = 29 connections tested onto 20 MCs) versus L5PC→L5XC connection rate (n = 60 connections tested onto 35 XCs); $p<10^{-6}$ for L5MC→L5PC (n = 46 connections tested from 30 MCs) versus L5XC→L5PC connection rate (n = 65 connections tested from 37 XCs); Monte Carlo permutation test. See also Figures S6-8 and Table S1.

CRE-DOG enables genetic access to subtypes of SST cells

The highly specific connectivity exposed by our circuit mapping experiments suggests that MCs and XCs are specialized for different functions in cortical computation. If this is the case, we would expect that manipulating the activity of these groups of interneurons will cause different effects on cortical dynamics. We specifically hypothesized that increasing MC activity would primarily affect neurons in L2/3 and L5, but not L4, whereas increasing XC activity would primarily impact neurons in L4, but leave other layers relatively unaffected.

In order to probe how MCs and XCs influence cortical dynamics during sensory processing, we sought to use the CRE-Dependent-on-GFP (CRE-DOG) system to gain genetic access to these cell types. CRE-DOG uses two split fragments of Cre recombinase, which reconstitute into functional Cre only in the presence of GFP, which allows GFP transgenic lines to be retrofitted for use in conditional genetics. We coinjected AAVs to drive expression of the CRE-DOG system, along with flexed ChR2-TdT, into neonatal X94 and GIN mice in order to target ChR2-TdT to GFP+ SOM cells in these mice.

After 2-3 weeks, bright tdT expression was present in the brains of X94 mice injected with this cocktail (referred to hereafter as X94-ChR2 mice). X% of GFP+ cells near the injection site exhibited TdT expression, and a bright band of TdT+ axons was visible in L4, indicating effective labeling of GFP+ XCs (Fig. 5a,b). While nearly all TdTomato expression colocalized with GFP, we did observe a small number of GFP-/TdT+ neurons, which usually were pyramidal neurons. This off-target expression is probably the result of CRE-DOG leakage, since injecting GFP- wildtype animals in the same manner also results in sparse expression of TdT+ in cortical neurons. However, GFP- neurons represented only a very small fraction of the total population of TdT+ neurons, meaning that CRE-DOG allows expression of ChR2-TdT in X94 cells with high specificity. Furthermore, current clamp recordings in acute slices of X94-ChR2 mice showed that GFP+/TdT+ XCs were efficiently driven to spike by photostimulation, indicating that XCs express ChR2 at sufficient levels for photoactivation experiments.

To examine the proximal effects of optogenetically activating XCs, we recorded IPSCs from PCs in layers 2- 6 while activating XCs (Fig. 5c,d). We used widefield photostimulation for these experiments, which activates XCs in all layers, in order to mimic the pattern of activation we would expect to achieve during *in vivo* photostimulation. Consistent with our previous experiments, XC photostimulation reliably evoked powerful IPSCs in L4 PCs, whereas PCs in other layers usually received small IPSCs or showed no response (mean charge transfer ± C.I: L2/3 = 2.0 ± 1.4 pC; L4 = 10.7 ± 4.8 pC; L5 = 0.8 ± 0.5 pC; L6 = 1.1 ± 0.4 pC). At the population level, the evoked IPSC response only significantly exceeded baseline in L4 PCs (L2/3: p = 0.41, n = 20; L4: $p < 10^{-8}$, n = 30; L5: p = 0.67, n = 27; L6: p = 0.84, n = 22; F-test on linear mixed-effects model), though a small number of individual L2/3 PCs did exhibit substantial IPSCs. While this was expected for L2/3 and L5 PCs, the lack of evoked inhibition in L6 PCs is notable, since it suggests that the L6 to XC connection is asymmetric, unlike the highly reciprocal connectivity pattern seen between L4 PCs and XCs. We conducted these experiments while pharmacologically blocking glutamatergic synaptic transmission. We observed small or no EPSCs in response to photostimulation in a subset of experiments carried out in normal ACSF, and evoked IPSC amplitude was unaltered by wash-on of glutamate blockers, suggesting that the inhibition we observed was predominantly monosynaptic.

These results indicate that CRE-DOG can be used with the X94-GFP line to achieve specific optogenetic control of XCs.

Unfortunately, we found that using the same procedure with GIN mice was not suitable for specifically labeling MCs. While GFP+ MCs were efficiently labeled in the brains of these mice, we unexpectedly also observed very bright TdT expression in a large number of L6 neurons (Fig. S11j). Upon closer inspection, we saw that these neurons were part of a fairly numerous population of dimly GFP+ L6 neurons. These neurons were regular spiking, but electrophysiologically and morphologically dissimilar to MCs (Fig. S11l); furthermore, these neurons were not labeled by TdT in a GIN x SST-TdT mouse, suggesting that they are not SST cells (Fig. S11m). This observation, combined with the fact that the GIN line labels a heterogeneous population of SST cells (including some L4 XCs; see Supplementary note), means that the results of CRE-DOG based optogenetic manipulation of neurons in these mice will be difficult to interpret. We therefore turned to an alternative GFP line, X98, which also labels MCs, although a different population of MCs than the GIN line. Injecting CRE-DOG/flexed-ChR2-TdT yielded expression which was strikingly complementary to the expression of X94-ChR2, with bright axonal fluorescence in L1, L2/3, and L5, but virtually none in L4 (Fig. 5b). X98 has been described as labeling MCs primarily in deep L5 and L6, but surprisingly we observed a large number of TdT+ neurons in L2/3 and throughout L5. This discrepancy may be due to changes in GFP expression during development: while most TdT+ L2/3 and upper L5 neurons had dim or no visible GFP in sections taken from adult mice, many GFP+/TdT+ neurons were visible in these layers in juvenile mice. Transient expression of GFP in these neurons may be sufficient to allow CRE-DOG mediated recombination and expression of the flexed-ChR2 construct, which then perdures into adulthood. X98 mice also express GFP in some small, non-neuronal cells in the barrel cortex, but we did not observe any TdT expression in these cells.

Immunohistochemical staining for somatostatin showed that X% TdT+ neurons in X98 mice injected with CRE-DOG/flexed-ChR2-TdT (X98-ChR2 mice) were somatostatin positive. Furthermore, photostimulation of these neurons drove strong inhibition in L2/3 and L5 PCs, but relatively little in L4 and L6 PCs (mean charge transfer ± C.I: L2/3 = 33.9 ± 18.7 pC; L4 = 4.7 ± 3.0 pC; L5 = 17.9 ± 5.0 pC; L6 = 4.9 ± 2.7 pC; Fig. 5d). In contrast to X94-ChR2, in X98-ChR2 slices evoked responses at the population level significantly exceeded baseline only in L2/3 and L5 PCs (L2/3: $p < 10^{-11}$, n = 6; L4: p = 0.46, n = 7; L5: $p < 10^{-6}$, n = 15; L6: p = 0.53, n = 4; F-test on linear mixed-effects model). These results, along with the patterns of axonal fluorescence, suggests that ChR2-TdT+ cells in these mice are a population of non-XC SST cells which likely includes MCs, making X98-ChR2 mice a useful comparison for X94-ChR2 mice.

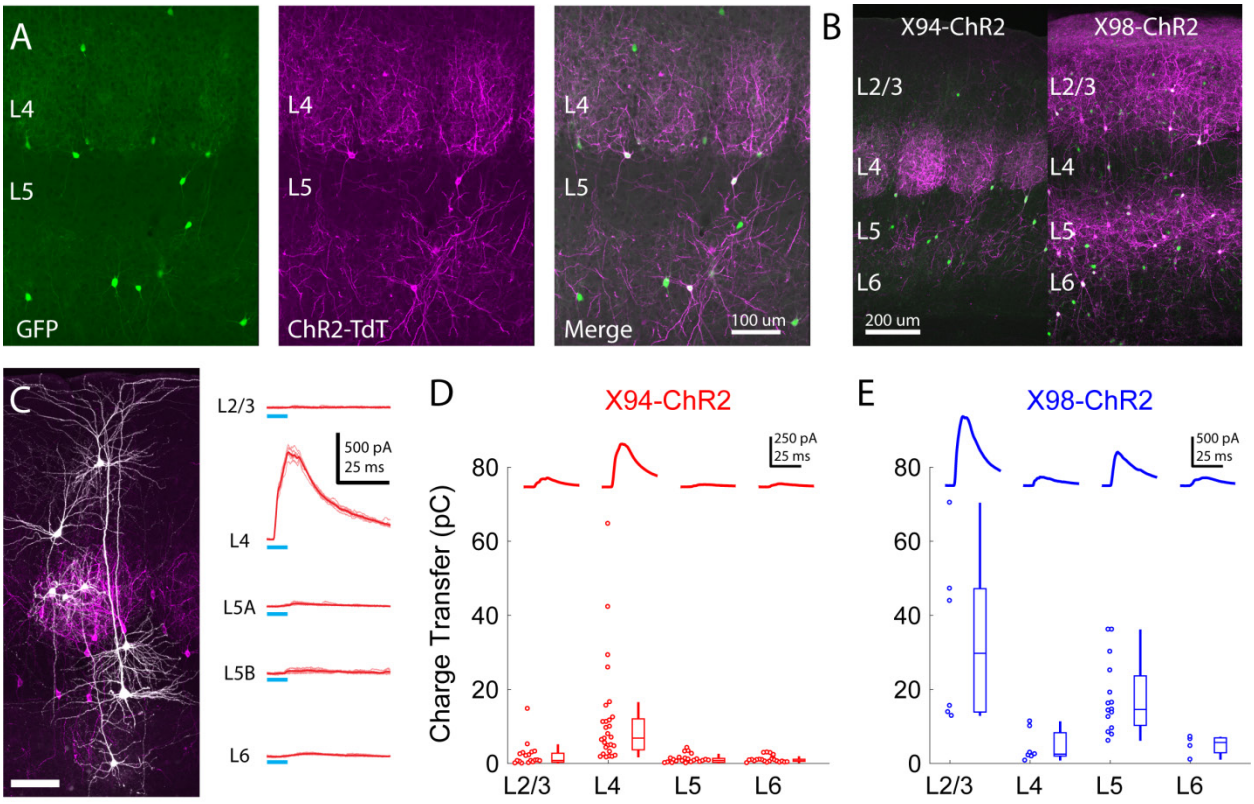

Figure 3.5 Cre-DOG enables optogenetic control of SST subtypes targeting different cortical layers

(A) Confocal image of cortical section from an X94 mouse injected with Cre-DOG AAVs (AAV2/8. EF1a.C-CreintG WPRE.hGH and AAV2/8. EF1a. N-Cretrcintc WPRE.hGH) along with AAV9.CAGGS.Flex.ChR2-tdTomato.WPRE.SV40. Left: X94- GFP cells (green). Middle: ChR2-TdT expression (magenta). Right: Merged image
(B) Side by side comparison of X94-ChR2 mice and X98-ChR2 mice showing laminar differences in localization of ChR2-TdT+ axons
(C) Recording light-evoked IPSCs in X94-ChR2 slices. Left: post-hoc confocal image showing recorded neurons (white) and ChR2-TdT+ XCs (magenta). Right: example traces of light-evoked IPSCs recorded in neurons in different layers
(D) Median charge transfer of evoked IPSCs in each PC recorded in X94-ChR2 slices, grouped by layer and accompanied by box and whisker plots. Top inset: grand average IPSC
(E) As in D, but for X98-ChR2 mice

SST subtypes differentially modulate cortical dynamics during somatosensation

To assess how different SST subtypes impact sensory processing, we next optogenetically enhanced the firing of XCs and non-XC SST cells while recording cortical activity in actively sensing mice. X94-ChR2 and X98-ChR2 mice were head-fixed and habituated to run on a freely spinning circular treadmill. To drive tactile responses, a vertical pole stimulus was presented at 8 different positions within the whisking field, along with optogenetic stimulation of the cortex on randomly interleaved trials. Using silicon laminar probes, we recorded single-unit activity across multiple layers in the barrel cortex, distinguishing regular-spiking (RS, putative excitatory) and fast-spiking (FS, putative PV-expressing interneurons) via their spike waveforms.

Our circuit mapping data predicts that the synaptic outputs of these two sets of SST cells should differentially affect cortical activity in a layer-specific manner: XCs should most powerfully affect units in L4, whereas non-XCs should affect the L4 population minimally, but exert strong effects on L2/3 and L5 units. How these effects will manifest is nonobvious. Studies in V1 and A1 which have optogenetically stimulated SST cells as a whole have observed various forms of suppressive gain modulation in excitatory neurons. However, SST inhibition can also suppress the firing of PV neurons, and under some conditions SST activity can yield a net-disinhibitory effect on

PCs. One possibility is that XCs and non-XCs could produce different net effects on downstream excitatory populations. In particular, Xu et al. proposed that XCs mediate a primarily disinhibitory effect in L4, since L4 XCs inhibit L4 PV cells much more strongly than they inhibit L4 PCs. If this is the case, photostimulating XCs should decrease the firing of L4 FS units while simultaneously increasing the firing of L4 RS units.

Recording from X94-ChR2 mice, we observed that photostimulating XCs powerfully suppressed the firing of L4 FS cells (5.2 ± 1.7 Hz control versus 1.1 ± 0.5 Hz opto; $p < 10^{-6}$, n = 39 L4 FS units), but also suppressed L4 RS units (1.8 ± 1.2 Hz control versus 0.9 ± 0.7 Hz opto; $p < 0.001$, n = 15 L4 RS units). This indicates that enhancing XC firing does not disinhibit L4 excitatory cells and instead produces a net suppression. Suppression of both L4 RS and L4 FS units also occurred during sensory-driven activity (L4 RS: 3.8 ± 1.7 Hz control versus 2.3 ± 1.2 Hz opto; $p < 10^{-6}$, n = 15; L4 FS: 7.1 ± 4.0 Hz control versus 2.9 ± 1.0 Hz opto; $p < 10^{-6}$, n = 39) . Under the same conditions, XC photostimulation caused no reduction or small reductions in the activity of the L5 RS and L6 RS populations (L5 RS spontaneous: 5.1 ± 1.2 Hz control versus 5.1 ± 1.3 Hz opto; p = 0.20, n = 59; L6 RS spontaneous: 1.9 ± 1.0 Hz control versus 1.6 ± 0.7 Hz opto; p = 0.42, n = 13; L5 RS sensory-driven: 5.9 ± 1.2 Hz control versus 5.6 ± 1.3 Hz opto; $p < 10^{-6}$, n = 59; L6 RS sensory-driven: 2.1 ± 1.0 Hz control versus 1.9 ± 0.9 Hz opto; p = 0.04, n = 13), consistent with the lack of XC inhibitory connections to PCs in these layers and supporting the notion that XC-mediated inhibition has layer-specific effects on cortical dynamics. Surprisingly, XC photostimulation also robustly reduced spontaneous and sensory-evoked activity in the L2/3 RS population (L2/3 RS spontaneous: 0.9 ± 0.5 Hz control versus 0.1 ± 0.1 Hz opto; $p < 10^{-4}$, n = 10; L2/3 sensory-driven: 3.4 ± 1.4 Hz control versus 1.5 ± 0.5 Hz opto; $p < 10^{-6}$, n = 10), as well as that of nearly all FS units, including those outside of L4 (L2/3 FS sensory-driven: 8.3 ± 4.0 Hz control versus 5.6 ± 3.0 Hz opto; $p < 10^{-6}$, n = 11; L5 FS sensory-driven: 7.6 ± 2.8 Hz control versus 4.5 ± 3.0 Hz opto; $p < 10^{-6}$, n = 38; L6 FS sensory-driven: 8.3 ± 3.8 Hz control versus 7.0 ± 4.4 Hz opto; $p < 10^{-6}$, n = 9). These effects could potentially represent cascading changes in network activity caused by the loss of activity in L4 excitatory cells.

Photostimulating non-XC SST cells in X98-ChR2 mice yielded dramatically different effects. The activity of the L2/3 and L5 RS populations was substantially reduced both during spontaneous conditions (L2/3 RS spontaneous: 0.8 ± 0.6 Hz control versus 0.3 ± 0.2 Hz opto; $p < 10^{-6}$, n = 29; L5 RS spontaneous: 5.4 ± 1.5 Hz control versus 4.0 ± 1.8 Hz opto; $p < 10^{-6}$, n = 42), and during sensory stimulation (L2/3 RS sensory-driven: 2.4 ± 0.8 Hz control versus 1.2 ± 0.4 Hz opto; $p < 10^{-6}$, n = 29; L5 RS sensory-driven: 6.4 ± 1.6 Hz control versus 4.5 ± 1.8 Hz opto; $p < 10^{-6}$, n = 42), whereas the activity of the L4 RS population showed no change or small reductions under the same conditions (L4 RS spontaneous: 1.1 ± 0.4 Hz control versus 1.2 ± 0.5 Hz opto; p = 0.82, n = 12; L4 RS sensory-driven: 2.3 ± 0.8 Hz control versus 2.0 ± 0.6 Hz opto; $p < 0.01$, n = 12). No effect was observed in L6 RS units (L6 RS spontaneous: 4.3 ± 4.7 Hz control versus 3.2 ± 2.5 Hz opto; p = 0.13, n = 6; L6 RS sensory-driven: 4.6 ± 5.0 Hz control versus 4.1 ± 4.1 Hz opto; p = 0.24, n = 6), though we did not sample many of these. As with X94-ChR2 mice, we also observed a global suppression of FS units across all layers when photostimulating in X98-ChR2 mice; however, the magnitude of FS suppression was markedly smaller in X98-ChR2 mice relative to X94-ChR2 mice (L2/3 FS sensory-driven: 5.2 ± 4.2 Hz control versus 2.4 ± 1.6 Hz opto; $p < 10^{-6}$, n = 10; L4 FS sensory-driven: 7.2 ± 1.9 Hz control versus 5.4 ± 1.6 Hz opto; $p < 10^{-6}$, n = 47; L5 FS sensory-driven: 7.1 ± 1.9 Hz control versus 5.5 ± 1.9 Hz opto; $p < 10^{-6}$, n = 34; L6 FS sensory-driven: 7.8 ± 2.8 Hz control versus 5.6 ± 2.1 Hz opto; $p < 10^{-6}$, n = 6). Taken together with our X94-ChR2 data, these results are consistent with a parallel circuit model in which different SST subtypes suppressively modulate specific layers and cell-types.

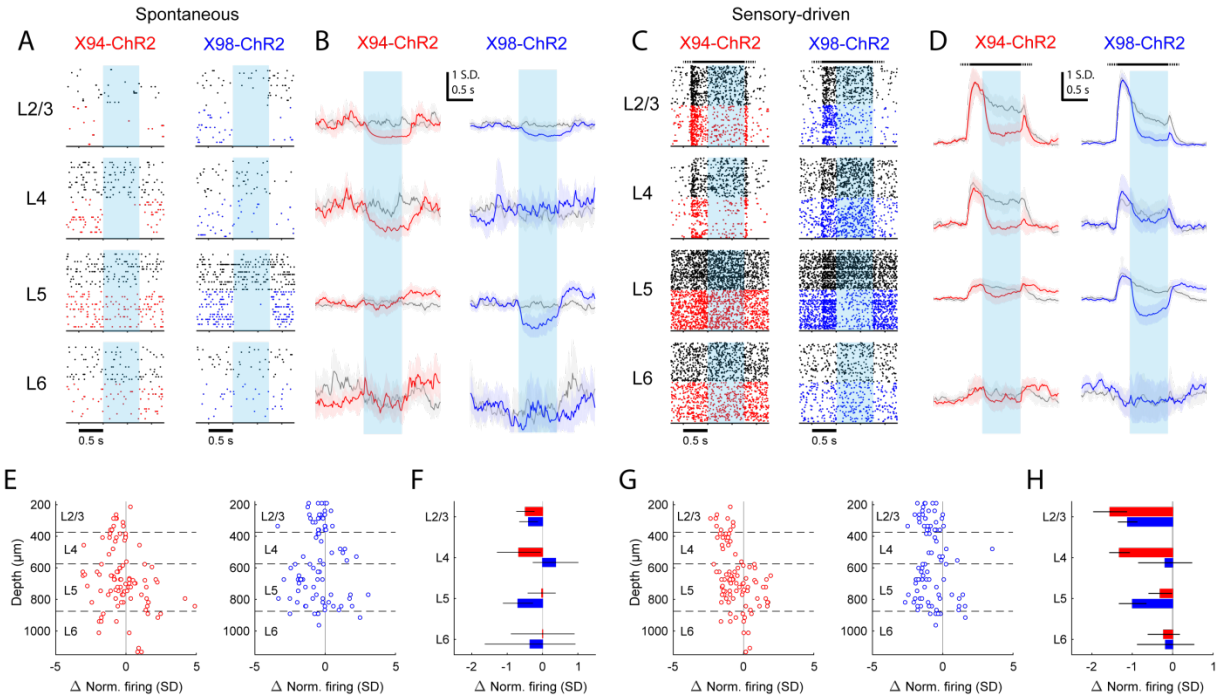

Figure 3.6 Differential layer-specific modulation of cortical activity by XCs and MCs

(A) Raster plots showing activity in example RS units recorded from different layers in X94-ChR2 and X98-ChR2 mice. Black rasters show trials with no stimulus i.e. spontaneous activity. Colored rasters show trials with photostimulation of X94-ChR2 (red) or X98-ChR2 (blue). Light blue region indicates photostimulation period.

(B) Grand averages of z-scored RS unit activity in L2/3, L4, L5, and L6 showing spontaneous activity (gray) and activity on photostimulation trials (red, X94-ChR2; blue, X98-ChR2). Responses have been smoothed with a 100ms alpha kernel and downsampled to 50 Hz. Shaded regions indicate 95% confidence interval.

(C) As in A, but for sensory-driven activity from trials in which a vertical pole is presented to the whiskers as a tactile stimulus

(D) As in B, but for sensory-driven activity

(E) Change in normalized spontaneous firing of RS units versus depth below pia for X94-ChR2 (left, red) and X98-ChR2 (right, blue) mice

(F) Mean change in normalized firing rate by layer for X94-ChR2 (red bars) and X98-ChR2 (blue bars). Errorbars indicate 95% confidence interval.

(G) As in E, but for change in sensory-driven activity

(H) As in F, but for change in sensory-driven activity

Discussion

Understanding of the organization of cortical inhibitory circuits has surged in recent years, but the integration of these new architectures with the established, layer-centric framework of the excitatory cortical microcircuit has proved elusive. Our data establish previously unknown excitatory-to-inhibitory and inhibitory-to-excitatory pathways involving two subnetworks of L5 SST interneurons, which are both layer and cell-type specific. Optogenetic circuit mapping shows that L5 MCs receive excitatory inputs chiefly from PCs in L2/3 and L5, the primary cortical output layers, while L5 XCs receive inputs mainly from PCs in L4 and upper L6, the primary input zones for afferent input from the ventral posteromedial thalamus (Wimmer et al., 2010). Paired recordings and 2-photon holographic optogenetic interrogation of common SST-mediated input indicate that in turn, these same SST subtypes selectively inhibit the same PC populations that excite them, at least within L4 and L5. Thus XCs and MCs, though spatially intermingled in L5, are functionally segregated into two disjoint networks with selective and complementary laminar connectivity (Fig. 4e).

Dense but selective inhibitory wiring

These results reveal a previously unknown, striking degree of specificity in the inhibitory cortical wiring diagram. In particular, the observation that L5 XCs exhibit nearly no intralaminar connectivity with L5 PCs, but do engage in dense, reciprocal connectivity with L4 PCs is inconsistent with the idea of a single, global blanket of SST-mediated inhibition. Instead, SST-PC circuits appear to more closely resemble a patchwork quilt, comprised of multiple networks of SST subtypes which independently service separate spatial domains. SST-PC connectivity can be extremely dense and non-selective within one of these domains (e.g. creating a blanket within a single laminar microcircuit), but highly selective on the scale of layers and columns. Though we did not investigate it in this study, it seems likely that selective connectivity on this scale could be achieved, at least in part, simply by SST subtypes having preferred laminar targets for axonal arborization (Packer et al., 2012).

Functional implications of separate, layer-specific SST feedback circuits

The circuit structure established here suggests that at least two different pools of SST-mediated inhibition separately modulate successive stages of cortical processing. XCs will chiefly be recruited as a function of the 'input' of the microcircuit, generating inhibition proportional to the amount of activity in the input layers and thalamus, which in turn varies widely depending on external sensory drive. Conversely, MCs will be recruited by activity in L2/3 and L5 PCs, whose projections represent the major feedforward pathways out of S1 (Harris and Shepherd, 2015); consequently, MCs will generate feedback inhibition as a function of the 'output' of the microcircuit. This raises the possibility that MC and XC-mediated feedback inhibition could differentially contribute to various forms of population gain control: XCs could perform input-scaling on the gain, whereas MCs could regulate output-scaling. These different modes of gain control have been proposed to perform myriad functions in perception and cognition (Carandini and Heeger, 2012; Miller, 2016; Salinas and Thier, 2000), and the circuit mechanisms of gain modulation are a topic of intense recent focus (Atallah et al., 2012; Fu et al., 2014; Lee et al., 2012; Litwin-Kumar et al., 2016; Pakan et al., 2016; Pouille et al., 2009a; Seybold et al., 2015; Wilson et al., 2012). Independent modulation of different SST circuits, either by the intracortical excitatory circuits described here, long range inputs from thalamus or higher cortical areas, or by other sources such as VIP-mediated inhibition (Lee et al., 2013; Muñoz et al., 2017; Pfeffer et al., 2013; Pi et al., 2013) or neuromodulation (Polack and

Contreras, 2012; Xiang et al., 1998; Xu et al., 2013) could represent a mechanism by which the brain dynamically fine-tunes the cortical population input-output function.

Furthermore, these parallel subnetworks of SST inhibition might also fine-tune how the sensory cortex integrates 'bottom-up' and 'top-down' inputs, as bottom-up is conveyed via thalamocortical axons primarily (though not exclusively; Constantinople and Bruno, 2013) to L4, and thus is most directly affected by XC-mediated inhibition, while top-down inputs are thought to be conveyed to the apical dendrites of L5 and L2/3, and thus are primarily modulated by MC-mediated inhibition (Murayama et al., 2009a; Petreanu et al., 2012). Therefore, the parallel structure of MC and XC networks could allow S1 to independently alter its sensitivity to top-down and bottom-up input streams to optimize the behavioral responses to sensory stimuli. Supporting this proposal, recent studies have observed that subtypes of SST cells with either wide or narrow spike waveforms (which might correspond to MCs and XCs) are differentially activated during various behavioral contingencies (Kim et al., 2016; Kvitsiani et al., 2013; Muñoz et al., 2017; Reimer et al., 2014). Pressing questions for future investigation will be to determine how excitatory drive from different laminar PC populations contributes to the unique activity patterns of SST subtypes, and conversely, to determine how distinct SST subtypes differentially shape the dynamics of the cortical microcircuit. Future experiments could address these questions by optogenetically manipulating specific SST subtypes using intersectional genetics (He et al., 2016) or with a Cre-DOG based approach (Tang et al., 2015b). Nearly all optogenetic manipulations of SST cells have employed the non-specific SST-Cre line, which could explain the somewhat heterogeneous results that have emerged, including both inhibition and disinhibition (Cottam et al., 2013; Lee et al., 2012; Seybold et al., 2015; Wilson et al., 2012; Xu et al., 2013). More precise manipulations of SST subtypes (e.g., MCs vs. XCs) could help reveal the functional impacts of distinct SST subnetworks.

The selective inhibitory 'pathways' described here also suggest specific predictions about how different SST subtypes shape the dynamics of cortical activity. For example, within layers, XCs and MCs will respectively mediate L4→L4 and L5→L5 feedback dendritic inhibition (Silberberg and Markram, 2007). Across layers, SST cells should contribute to L2/3→L5 feedforward inhibition (Adesnik and Scanziani, 2010; Apicella et al., 2012; Pouille et al., 2009b), but not to L4→L5 translaminar inhibition, implying that the latter operates solely through parvalbumin-expressing FS interneurons (Pluta et al., 2015a). Furthermore, XCs (but not MCs) receive strong thalamocortical input (Hu and Agmon, 2016; Ji et al., 2016; Tan et al., 2008) and are thought to generate feedforward inhibition in response to sustained thalamic activity; our data therefore imply that SST-mediated thalamocortical feedforward inhibition will impinge upon L4 neurons but not L5 PCs.

Diversity of L5 SST cells

We find that XCs comprise a large fraction of L5 SST cells and perhaps of SST cells more generally (see Fig. S1g and supplemental text). If XCs are so prevalent, one might ask why they have been reported on only sparingly. Beyond studies which used the X94 line (Hu and Agmon, 2016; Ma et al., 2006b; Tan et al., 2008), close examination of the literature reveals several reports of cells with L4-targeting morphologies and other properties characteristic of XCs (Fairén et al., 1986; Helmstaedter et al., 2009a; Kumar and Ohana, 2008; Porter et al., 2001), which have sometimes been called 'Lorente de Nó cells' in attribution to their earliest describer (Cobas et al., 1987; Fairén, 2007; Lorente de No, 1992). The previous lack of genetic tools to target these cells may have hindered detailed investigation of XCs until now; however, L5 XCs bear striking resemblances to non-Martinotti SST cells in L4 (see Fig. S4 and supplemental text) which are well studied by comparison (Beierlein et al., 2000, 2003; Ma et al., 2012; Xu et al., 2013). It is also likely that XCs have sometimes been misclassified as fast-spiking cells due to their quasi-fast-spiking intrinsic

properties, especially in studies done without genetic or immunohistochemical markers for somatostatin and parvalbumin. This issue likely also applies to studies performing *in vivo* extracellular recordings, since spike waveforms of XCs are similar to those of true parvalbumin-expressing FS cells (Kim et al., 2016; Kvitsiani et al., 2013; Muñoz et al., 2014).

Although our data clearly delineate two very distinct subtypes of SST cells in L5 and their intracortical circuits, an important limitation of this study is the need to use the GIN and X94 lines to target MCs and XCs. SST cells are highly heterogeneous, even within the subsets labeled by these lines (particularly the GIN line; Halabisky et al., 2006; McGarry et al., 2010) and other subtypes of SST cells not covered by these lines are known to exist, including long-range projecting SST cells that are most prevalent in L6 (He et al., 2016; Ma et al., 2006b; Tasic et al., 2016a; Yavorska and Wehr, 2016). It is likely that other subtypes also exhibit specific connectivity schemes which may be different from the ones described here. Most notably, L5 also contains at least one other type of 'T-shaped' MC which is labeled by the X98-GFP and the Chrna2-Cre transgenic lines (Hilscher et al., 2016; Ma et al., 2006b). T-shaped MCs are morphologically and electrophysiologically distinct from the L5 MCs labeled by the GIN line. Unlike L5 GIN MCs, which inhibit both thick and slender-tufted L5 PCs (data not shown), T-shaped MCs specifically inhibit thick-tufted but not slender-tufted L5 PCs and have been implicated in mediating frequency-dependent disynaptic inhibition between these neurons (Berger et al., 2010; Hilscher et al., 2016; Silberberg and Markram, 2007). Since we observed relatively little intralaminar excitatory input onto L5 GIN MCs, one possibility is that T-shaped MCs also possess their own unique circuit scheme, with relatively stronger intralaminar connectivity. Future work is needed to determine how closely laminar connectivity is tied to the cellular identity of other SST subtypes (and of cortical interneurons more generally) and whether this connectivity changes during development (Anastasiades et al., 2016; Marques-Smith et al., 2016b; Tuncdemir et al., 2016b) and learning (Kato et al., 2015; Kätzel and Miesenböck, 2014; Makino et al., 2015). Taken together, the data in this study establish two new fundamental inhibitory motifs in the cortex: two subnetworks of SST cells target specific cortical compartments – the input and output cortical layers, potentially providing a means to fine tune cortical computation during different sensory or behavioral demands.

Methods

All experiments were performed in accordance with the guidelines and regulations of the Animal Care and Use Committee of the University of California, Berkeley.

Transgenic mice

The following mouse lines were used for this study: the scnn1-tg3-Cre line (JAX stock # 009613), the emx1-IRES-Cre line (JAX stock #005628), the PV-IRES-cre line (B6;129P2-Pvalbtm1(cre)Arbr/J ; JAX stock #008069), the SST-IRES-cre line (JAX stock 013044), the GIN line (FVB-Tg(GadGFP)45704Swn/J; JAX stock #003718), the X94-GFP line (Tg(Gad1-EGFP)94Agmo/J; JAX stock 006334), the Ai9 Rosa-LSL-tdTomato line (JAX stock # 007909). Mice were housed in cohorts of five or fewer with a light:dark cycle of 12:12 hours, and were used for experimentation during their subjective night.

Viral Infection

Neonatal mice (p0-3) were deeply cryo-anesthetized and placed in a head mold. Viral aliquots were loaded into a Drummond Nanoject injector and injected into 4 sites in the barrel cortex of the left hemisphere. At each site, virus was injected at multiple depths (2 depths for scnn1-tg3-cre and drd3-cre mice, 3 depths for emx1-IRES-Cre and SST-IRES-cre mice) in increments of 18.4 nL or 36.8 nL (for multiphoton experiments), for a total of ~150-440 nL of virus injected per mouse. Following injections, mice were moved to an incubation chamber for recovery, and were returned to the dam once they regained color and began to move. For CRE-DOG experiments, we injected a mixture of 1 part AAV2/8.EF1a.C-CreintG.WPRE.hGH, 1 part and AAV2/8.EF1a.N-Cretrcintc.WPRE.hGH, and 1 part AAV9.CAGGS.Flex.ChR2-tdTomato.WPRE.SV40. In some initial slice experiments, we used a similar cocktail but with 2 parts AAV9.CAGGS.Flex.ChR2-tdTomato.WPRE.SV40.

Brain slice recording

Acute thalamocortical slices were prepared from mice (ages p14-29, at least 14 days after viral injection) as previously described (Adesnik and Scanziani, 2010b). Slices were placed in a recording chamber and constantly perfused with oxygenated artificial cerebro-spinal fluid (NaCl 119 mM, KCl 2.5 mM, $MgSO_4$ 1.3 mM, NaH_2PO_4 1.3 mM, glucose 20 mM, $NaHCO_3$ 26 mM, $CaCl_2$ 2.5 mM) maintained at 32° C (21° C for multiphoton mapping experiments). Slices were oriented with the caudal surface facing up in the recording chamber. To ensure minimal disruption of vertical connectivity, all slices used for recording were inspected under infrared illumination at 40x magnification and/or post-hoc confocal imaging to confirm that pyramidal cell apical dendrites stayed roughly parallel with the surface of the slice or receded slightly deeper as they progressed apically. Whole cell recordings were performed using glass micropipettes (2-5MΩ resistance) pulled on a Sutter P-1000 Micropipette Puller. Pipettes were filled with a Cs^+ based internal ($CsMeSO_4$ 135 mM, NaCl 8 mM, HEPES 10 mM, Na_3GTP 0.3 mM, MgATP 4 mM, EGTA 0.3 mM, QX-314-Cl 5 mM, TEA-Cl 5mM) or a potassium gluconate based internal (K-gluconate 135 mM, NaCl 8 mM, HEPES 10 mM, Na_3GTP 0.3 mM, MgATP 4 mM, EGTA 0.3 mM). In some experiments, biocytin (0.4-1%) was dissolved into the internal solution to enable morphological recovery. Voltage recordings were not corrected for the junction potential. Series resistance was monitored with negative voltage steps during each trial, and was compensated up to 60%. Data were analyzed from recordings in which series resistance remained stable and below 30MΩ. Data were acquired and filtered at 2.2 kHz using a Multiclamp 700B Amplifier (Axon Instruments) and digitized at 20 kHz

(National Instruments). All data were acquired using custom written MATLAB (Mathworks) software.

Characterization of intrinsic properties

In all recordings using K-based internal solution, an F-I curve was measured at the start of the experiment using a series of 1-second current injections, at -200 pA, -100 pA, and then proceeding in 50 pA increments from +50 to +500 pA. In some experiments, additional current steps were manually designated and performed online to aid in estimation of rheobase. Resting membrane potential was defined as the median membrane potential during a baseline period measured immediately after break-in. Input resistance was calculated with Ohm's law using the steady state membrane potential during subthreshold current injections steps (current clamp) and/or the steady state current during 5 mV voltage steps (voltage clamp). Action potential onset was detected using code adapted from the Berg lab's *Spike_threshold*_PS function, which defines onset as the point of maximum positive slope in the phase space of the membrane potential and its first derivative (Sekerli et al., 2004). Spike width was measured as the full-width of each spike at the voltage halfway between the action potential threshold and the peak amplitude (half-max). Rheobase was estimated using the average of 1) a linear fit (with coefficients constrained to be nonnegative using the *lsqnonneg* function in MATLAB) of the F-I relation during the last subthreshold current injection step and the first few suprathreshold steps and 2) linear extrapolation of the current necessary to reach threshold based on measurements of the resting membrane potential, input resistance, and average threshold value of the first action potentials evoked during suprathreshold injections. These two measures were usually in good agreement. Adaptation index was calculated (following the Allen Brain Institute's Cell Types Database protocol) for each current injection using the expression:

$$\frac{1}{N-1}\sum_{n=1}^{N-1}\frac{ISI_{n+1}-ISI_n}{ISI_{n+1}+ISI_n}$$

Where N is the number of spikes during that current step and ISI is the interspike interval.

Paired recording connectivity testing

We first targeted whole-cell recordings to a fluorescent (GFP+ or TdTomato+) SST cell, and then subsequently patched nearby neurons in the same slice. In some cases, we recorded serially from several neurons while maintaining the recording of the first neuron, in order to test multiple connections. Monosynaptic excitatory connectivity onto SST cells was tested by driving trains of 10 spikes in the presynaptic cell at 70 Hz via current injection, while monitoring for EPSCs in the postsynaptic cell. Stimulation was repeated at least 15 times in all pairs tested. Monosynaptic inhibitory connectivity from SST cells onto other neurons was tested by driving spikes in the presynaptic cell while monitoring postsynaptically for IPSCs (Cs-based internal, postsynaptic cell held at +10mV) or IPSPs (K-based internal, postsynaptic cell depolarized to approximately -52mV). Electrical connectivity between SST cells was tested by hyperpolarizing each cell with 1-second current injections (at least 15 trials) while monitoring for hyperpolarization in the other cell.

For L5SST-L5PC pairs, we recorded from both pyramidal tract and intratelencephalic type PCs, which could be distinguished by their laminar positions (preferentially L5B versus L5A), morphology visualized via infrared (large soma versus smaller soma) and post-hoc confocal imaging (thick-tufted apical dendrites versus slender-tufted), and/or their intrinsic properties (initial

burst/doublet spiking followed by non-adapting spikes versus continuously adapting regular-spiking phenotype; Hattox and Nelson, 2007; Kim et al., 2015; Schubert et al., 2001). We did not observe any significant differences in the connectivity of either L5PC type with L5MCs or XCs. For L5SST-L4PC pairs, we did not distinguish between spiny stellate and pyramidal/star-pyramidal excitatory cells.

For paired recordings between L5 SST cells and L4 FS/PV cells, we identified FS/PV cells using PV-Cre; LSL-TdTomato mice in some experiments (Fig. S7i). However, it was often difficult to visualize X94 cells using these animals due to the TdTomato fluorescence being much brighter than the GFP fluorescence. In other experiments (Fig. S7h), we targeted FS/PV cells in L4 by looking for L4 neurons with large cell bodies under IR, and then confirmed the identity of these cells electrophysiologically, with the primary criteria separating them from being narrow spike widths (slightly shorter than the average XC spike) and little or no spike frequency accommodation during high amplitude steps of current injection.

To classify SST-TdT cells as putative XCs or MCs, we fit a support vector machine (cross validated 10-fold) to perform binary classification of L5 GIN cells and L5 X94 cells using only their intrinsic electrophysiological properties. We found that a classifier based on only two measures (spike width and estimated rheobase) performed just as well as multivariate classification based on a large number of metrics (~85% accuracy).We then used this classifier to predict the identity of a different dataset of L5 SST cells recorded in SST-TdT mice. This approach is likely to have resulted in a small number of SST-TdT cells being misclassified; however, the connectivity of putative XCs and MCs were highly similar to the connectivity of XCs and MCs identified using the X94 and GIN lines. Furthermore, our conclusions about the differences in connectivity rates of L5 MCs and XCs with L4 and L5 PCs are unchanged by the exclusion of the SST-TdT dataset, with the exception of L5PC→L5SST connections – a circuit which has been studied in some detail by others. This approach also effectively assumes a dichotomy in L5 SST cells, since we have only two labels (MC and XC) to provide as training data, which is an important caveat since it is likely that further subdivisions of SST cells exist in L5 (Ma et al., 2006b). In a handful of cases, we recorded from SST-TdT cells which appeared to be FS cells (Hu et al., 2013), with very narrow spikes, low input resistances, and a near complete lack of spike-frequency accommodation during high amplitude current injection steps; these neurons were excluded from further analysis.

Using paired recordings, we tested 544 total possible connections between 146 L5 SST cells (39 L5 GIN cells, 53 L5 X94 cells, 54 L5 SST-TdT cells) and PCs/FS cells in L4 and L5. Data from a subset of these neurons (n = 17 L5 GIN cells) were included in a previous study (Pluta et al., 2015a). This dataset was unbalanced, and because in some cases we tested multiple connections onto the same L5 SST cell, included some non-independent observations. Because of this, we used Monte Carlo permutation tests to test for significant differences between the connectivity rates of MCs and XCs. We generated a permuted dataset with the same observation structure (same number of L5 SST cells and same number of connections tested per L5 SST cell) in place for MCs and XCs by randomly resampling with replacement at both levels. We then measured the difference in observed connectivity rate for the MC and XC groups, and repeated this procedure 100,000 times to generate a null distribution of rate differences. We used this distribution to perform a 1-tailed test for significant differences between MC and XC connectivity rates for each type of connection tested (Table S1).

Optogenetic connectivity mapping in vitro

Experiments were done in slices from Emx1-Cre; GIN or Emx1-Cre; X94 mice injected with an AAV driving Cre-dependent expression of ChR2 in all excitatory cells. Whole cell voltage clamp

recordings were performed in GFP+ L5 cells to target L5 MCs (Emx1-Cre; GIN) or L5 XCs (Emx1-Cre; X94). A digital micromirror device was used to focally photo-stimulate excitatory cells in different regions of the slice in order to map the spatial profile of excitatory inputs to recorded MCs and XCs.

Prior to experiments, slices were briefly visually inspected with epifluorescence under a 5x objective to confirm that a wide area containing dense, even expression of fluorescence (tagged to an opsin) was present in the barrel cortex. Recordings were targeted to within this region, which typically covered the entire lateral extent of barrel cortex in 4-5 slices. Slices in which expression appeared faint or uneven were discarded.

In some experiments, it was necessary to locate fluorophore-positive cells in slices also containing an excitatory opsin. To avoid excitotoxicity that can result from excessive illumination of opsin-containing neurons, we limited illumination to very brief intervals (1-2 seconds) while searching for fluorophore-positive cells. In some cases where the target cells were weakly fluorescent (young GIN and X94 animals), we searched for these cells while keeping the slice submerged in sucrose-substituted ACSF. Once target cells were located, this solution was washed out and replaced with normal recording ACSF prior to patching these cells and starting experiments.

DMD-based excitatory input mapping

Laser light was generated using a 1W 445nm diode laser (Ultralasers) and routed via a liquid light guide into a CEL5500 digital micromirror device (DMD) (Digital Light Innovations). The projection from the DMD was then collimated and integrated into the light path of the microscope, before being focused onto the slice chamber using a 5x (Olympus). For experiments using widefield illumination, the DMD passively reflected but not spatially modulate light. Prior to photo-stimulation, infrared and epifluorescence images were captured using an IR-1000 CCD camera (DAGE-MTI) and imported into MATLAB.

Excitatory mapping experiments were performed using a modified version of a previously described protocol (Pluta et al., 2015a). Mapping was performed over an area extending from pia to the white matter, covering 2-4 barrel columns laterally (~400 to ~800 μm). For mapping excitatory inputs to GIN and X94 cells, the DMD was used to pattern light into a square region (75 μm x 75 μm). Each stimulation site was spaced 40μm apart from adjacent ones, resulting in some overlap of adjacent stimuli. We chose to 'ramp' our photostimulation, starting each stimulus with the light off and linearly increasing the light intensity over time. Ramping in this manner minimizes activation of fibers of passage (Adesnik and Scanziani, 2010). In each trial, a 'sawtooth' light stimulus composed of three successive 25ms ramps of light (1.25 mW/mm^2 final intensity) was applied to one stimulus site. This protocol was chosen in order to maximize the short-term facilitation of excitatory inputs to L5 SST cells, though in practice we found it was usually possible to observe responses during the first ramp alone. Ten regions were stimulated per second in a serial, pseudorandom order, with 4 second breaks after every 10 seconds of mapping. Control experiments were performed using identical stimulation conditions while recording from $ChR2^+$ neurons in all layers. These experiments determined the spatial resolution of photostimulation and confirmed that spiking was elicited in ChR2+ neurons only when regions very close to the soma were stimulated. We also included n = 2 experiments mapping inputs to L5 X94 cells which were performed using the exact mapping protocol described in (Pluta et al., 2015), though our results and conclusions were not substantially altered by their exclusion.

All data were analyzed using custom written MATLAB software. Data preprocessing consisted of removing baseline offsets and slow fluctuations from recordings by subtracting a down-sampled and median-filtered versions. Charge was calculated as the integral of the preprocessed recordings during

photo-stimulation and the subsequent 25 milliseconds. To aggregate maps across cells, we first rotated the average map collected in each experiment in order to horizontally orient the laminar boundaries of the mapped area. Maps were next translated vertically to align the L4-L5 laminar boundary, and translated horizontally to align either the home column or the soma position of the recorded cell, before being horizontally cropped to an area ±300μm of their center and then averaged to yield a summary map.

For L4 stimulation experiments, we used widefield photostimulation through a 5x objective. We used two stimulation protocols: prolonged, 1-second ramps of linearly increasing light intensity and trains of ten pulses (1ms duration) at 40 Hz. We stimulated at 4 different intensities for each protocol. Since we sometimes recorded multiple neurons in the same slice (see Fig. S5), we fit generalized linear mixed effects models to the dose-response function of light-intensity versus evoked response (EPSC charge transfer or number of spikes), with fixed effects coefficients for the slope of this function for each cell-type and random effects slope coefficients for each slice and neuron in the dataset as well as a constant intercept term. F-tests were used to test for differences in fixed effects coefficients. For paired analysis of L4 XCs and L5 MCs/XCs (Fig. S5), paired t-tests were used to test for differences in L4-evoked responses at maximum stimulus intensity.

Multiphoton CGH-based inhibitory output mapping

Laser light was generated using a 5W 1040 nm femtoTrain laser (Sepctra-Physics) and power was modulated on short time scales using a Pockels cell (Conoptics) and a high speed shutter (UniBlitz). Light was delivered to the sample using a VIVO 2- Photon workstation (3i) based on a Sutter Moveable Objective Microscope (Sutter) and the hologram was created using a Phasor 2-Photon computer-generated holography system (3i) with Slidebook software (3i) (Fig. S9a). The holograms used for stimulation were 2D discs of diameter 15 um centered on points with 20 um spacing, making a 400 um x 400 um grid in the focal plane (Fig. S9b,c). Stimulation consisted of 4 or 10 ms square pulses to the Pockels cell with voltages calibrated to produce 200 or 250 mW average power on sample, respectively. The choice of 4 ms at 200 mW or 10 ms at 250 mW stimulation was determined slice to slice based on opsin expression. Power for each hologram was calibrated empirically to account for power loss due to diffraction efficiency degradation away from the zero-order of the SLM. There was an inter-trial interval of 100 ms between the end of one stimulation and the start of the next stimulation. Under these conditions, SST cells spiked reliably and with high radial resolution (Fig. 3c, Fig. S9c,d) and moderate axial resolution (Fig. S9f,g). Given the sparsity of SST neurons (Fig. 3b), this level of spatial resolution provided a good tradeoff between sampling many cells with fewer targets and spiking cells with high spatial resolution. In addition, reliably evoked spikes were produced with low latency and jitter when stimulating randomly through the target grid at 10 Hz. Under these conditions, most evoked spikes occurred in the first 20 ms after the onset of stimulation (Fig. S9e,h).

Space clamp error will inevitably affect somatic measurements of currents from distally located SST→PC synapses; however, we recorded IPSCs using a cesium-based internal solution (which included the ion channel blockers tetraethylammonium and QX-314) and performed experiments at room temperature, which ameliorate this to some extent (Williams and Mitchell, 2008). We also used a holding potential of +40 mV to increase the IPSC driving force. In these experiments, internal solutions also contained 5 μM Alexa 488 hydrazide (ThermoFisher Scientific) to aid visualization with multiphoton imaging, and ~5 mM kynurenic acid Sodium salt (abcam) was added to the external ACSF to block glutamatergic activity.

To determine which locations evoked responses in the voltage-clamp recordings, first we detected IPSCs using a Bayesian modeling approach via Gibbs sampling (Merel et al., 2016). Event

times were estimated by first binning all of the time samples at 1 ms resolution and then finding maxima of those timeseries (using *findpeaks* in MATLAB). Because the vast majority of evoked spikes recorded from opsin expressing SST cells occurred with short latency (Fig. S9c,f), we estimated the background rate of IPSCs for each patched cell from the last 25 ms of all inter-trial intervals and the evoked rate at each location from a time window of 30 ms starting 5ms after the onset of each stimulation. Taking a Poisson distribution of events with the estimated background rate as a null distribution for all locations for each cell, we could then calculate a p-value for the hypothesis that there is no evoked IPSCs each location. We then detected locations with evoked responses using the Benjamini-Hochberg False Detection Rate (FDR) procedure with $q = 0.1$ (Benjamini and Hochberg, 1995). We chose this relatively liberal FDR rate because any false positives will likely be thrown out after the temporal statistics are taken into account.

To determine if a location with evoked rates in both simultaneously patched cells was in fact a common input from a single source, we employed a statistical test that compares a computed synchrony statistic against a null distribution computed from resampled event time series. Specifically, the test we use employs a null distribution where all synchrony is a result of some processes at timescales longer than some given duration (Amarasingham et al., 2012). The intuition is that the chosen duration should match the general timing of evoked IPSCs such that any synchrony under this null arises only because IPSCs are being generated by two separate presynaptic SST cells at roughly the same time. When we reject this null, we have evidence that the synchrony is coming from a process that operates at a finer timescale than the general evoked IPSC statistics: that is, a single presynaptic SST cell is generating highly time-locked IPSCs in two postsynaptic PCs. In our case, the duration of the timescale we want to test against can be estimated from both the timing statistics of evoked spiking of SST cells as wells as the peristimulus time histogram (PSTH) of IPSCs for all trials at all detected input locations across all PC input maps (Fig. S9e,h, Fig. S10g). Using these statistics as guidance, we chose 10 ms as the timescale for our null distribution. In detail, we first summarize the synchrony of events between two simultaneously patched cells at each location where both cells receive input. The statistic we use is the sum of the center and two flanking bins of the cross correlation of the binary event time series for each cell. As mentioned, the event time series are binned at 1 ms. We then created a null distribution for this statistic at each of these locations using the event series resampling described in (Amarasingham et al., 2012) which allowed us to estimate a p-value for each location as well (Fig. S10h,i,j,k). We then detected common spatiotemporal input using these p-values and the Benjamini-Hochberg FDR procedure with $q = .05$, aggregating all tests across all paired maps. The common input probability for a simultaneously patched pair could then be computed as the total number of detected common input locations for that pair divided by the total number of unique detected input locations for the pair (i.e. the cardinality of the union of the sets of input locations for the two cells.

To align the input maps for each cell, we first aligned each input map to a two-photon image of the tissue taken at the time of recording based on previous calibrations between the SLM coordinate frame (e.g. the input map frame) and the two-photon imaging frame. Next, the tissue-aligned maps were then registered via an affine transform to a confocal image of the fixed slice which had been stained with DAPI and in which the opsin expressing cells could be visualized as well as the patched cells which had been filled with biocytin. This allowed each map to be registered to each other based on the laminar borders, in particular the L4-L5 boundary.

Biocytin staining and reconstruction

Following experiments, slices were transferred to 4% paraformaldehyde at 4° for several days. Slices were then repeatedly washed in TBS and subsequently incubated in block solution at room temperature for two hours. Next, 1:1000 streptavidin-Alexa647 conjugate was added to the solution and allowed to stain for 2 hours. Slices were then washed again and mounted/DAPI-stained on coverslips using VectaShield.

Stained neurons were imaged on a confocal microscope, along with the DAPI signal in order to identify laminar boundaries. These images allowed us to qualitatively assess whether recorded cells were L1-targeting MCs or L4-targeting XCs. We reconstructed a subset of filled neurons, with the goal of performing a bulk quantification of how MC and XC neurites are distributed with respect to the cortical layers (Fig. 1c, Fig S2e). Since detailed reconstructions of the morphologies of these neurons have already been carried out by others (He et al., 2016; Ma et al., 2006b; McGarry et al., 2010; Silberberg and Markram, 2007; Tan et al., 2008; Wang et al., 2004; Xu et al., 2013), we adopted a high-throughput, semi-automated approach to perform 2D reconstruct MCs and XCs (Fig. S2c). We imaged neurons using a 10x air objective and used the Imaris software package to automatically trace filled neurites. Subsequently, we manually edited these traces and annotated layer boundaries. These reconstructions did not distinguish between axon and dendrite and contained small scale errors (e.g. neurites passing near each other were sometimes spuriously connected). However, comparison of semi-automated reconstructions with detailed 3D reconstructions (performed manually in Imaris, after imaging with a 60x oil immersion objective and/or a 20x air objective) showed that the semi-automated approach yielded an accurate measurement of neurite density in each layer (Fig. S2a,b).

Miscellaneous

Supplemental Text

Comparison of L5 X94 cells and L4 non-Martinotti SST cells

Unlike L5 non-Martinotti SST cells, L4 non-Martinotti SST cells (sometimes identified as low-threshold spiking or 'LTS' cells) are well described (Beierlein et al., 2000, 2003; Gibson et al., 2005; Ma et al., 2006b, 2012; Xu et al., 2013). Several lines of evidence suggest that these L4 non-Martinotti SST cells belong to a similar or the same cell-type as the L5 cells labeled by the X94 line.

First, many L4 SST cells are labeled by the X94 line. Like L5 X94 cells, these neurons are non-Martinotti cells with axons that target L4 rather than L1. Furthermore, L4 X94 cells have intrinsic properties which are very similar to those of L5 X94 cells (Fig S3 b-e). A recent study reported that the L4 SST cells which are not labeled by X94 display the same phenotype as X94+ L4 SST cells (Xu et al., 2013), suggesting that all or nearly all L4 SST cells are X94-like, non-Martinotti cells.

Second, we observed that excitatory synapses from L4 PCs to L5 X94 cells exhibited what appeared to be asynchronous EPSCs during sustained high frequency firing in the presynaptic cell, which continued even after the cessation of presynaptic spiking (Fig. S8c). Elucidating the mechanism of this phenomenon was outside the scope of this study, but they can perhaps be attributed to asynchronous glutamatergic transmission. Asynchronous release of glutamate is uncommon in cortical circuits; to the best of our knowledge, the only other published observation is at the synapse from L4 PCs onto L4 SST cells (Beierlein et al., 2003). Similarly, were also able to observe asynchronous IPSCs in L4PCs during sustained high frequency firing of a connected L5 XC.

Third, excitatory input mapping to L4 X94 cells revealed that these neurons receive input from the same locations as L5 X94 cells- L4 and the L5B/L6 border (Fig. S3f, h, j). Additionally, during L4 stimulation experiments, L4 X94 cells recorded at the same time as L5 X94 cells had almost identical responses (Fig. S5), indicating similar degrees of L4 input to both L4 and L5 X94s. Furthermore, the connectivity of L5 X94s is broadly similar to the reported connectivity of L4 SST cells, since both are densely interconnected with L4 PCs and L4 FS cells. The connectivity of L5 X94 cells does differ from that of L4 SST cells in some respects. For example, L4FS cells appear to connect to L5 X94 cells less often than has been reported for L4FS→ L4SST connections (Fig. S7a-c). Additionally, whereas L4SST→L4FS synapses are also reported to be more powerful than L4SST→L4PC synapses, we found that L5X94→L4PCand L5X94→ L4FS synapses evoked IPSPs/IPSCs of similar amplitudes (Fig. S7d-j), though our sample size was relatively limited.

Overall L4 SST cells and L5 X94 cells exhibit strikingly similar electrophysiological, morphological, synaptic, and connective features, indicating that cells from both groups might be considered 'XCs'. Working under this assumption, roughly what fraction of SST cells in the barrel cortex are XCs? The X94 line labels approximately 15% of SST cells in the infragranular layers. This can be considered a lower bound on the fraction of XCs in L5, since the X94 line may not label all the cells with an XC phenotype, as is the case in L4. In the subset of L5 SST-TdT cells that we filled with biocytin and could successfully recover the morphology, we found that 19/52 cells (37%) possessed XC morphologies, 31/52 (60%) possessed MC morphologies, and 2/52 could not be placed in either category. Consistent with this, a support vector machine trained to distinguish L5 GIN cells from L5 X94 cells based on their intrinsic properties (Fig. S1g) labeled X% of L5 SST-TdT cells as putative XCs. However, L5 XCs often appeared to have larger cell bodies than MCs, which could potentially have made L5 XCs easier to locate or patch and thereby introduce a bias in

this assessment. Thus it is likely that between 15-40% of L5 SST cells are XCs. L4 and L5 respectively host approximately 10% and 40% of all SST cells in S1, so assuming nearly all L4 SST cells are XCs, we estimate that L4 and L5 XCs represent 16-26% of all SST cells in S1.

L4 GIN cells

Consistent with the idea that L4 SST cells are nearly all non-Martinotti, we observed that L4 cells labeled by the GIN line also exhibited non-Martinotti morphologies (Fig. S3a). L4 GIN cells had intrinsic properties which were significantly different from those of L5 GIN (MC) cells, but similar to those of L4 X94 cells and L5 X94 (XC) cells (Fig. S3b-e). Furthermore, the excitatory input maps for L4 GIN cells showed that these neurons received laminar patterns of input very similar to those of L4 and L5 X94 cells, which were dominated by L4 input. The input maps of L4 X94 cells, L5 X94 cells, and L4 GIN cells were all significantly different than the input maps for L5 GIN MCs in terms of the fraction of input originating from L4 and L6 (Fig. S3g,I,j). These results indicate that L4 GIN cells are distinct from L5 GIN MCs. and suggest that L4 GIN cells can also be considered XCs on the basis of their similarities with X94 cells. Thus, while the GIN line primarily labels MCs in L5, it is more heterogeneous across all the cortical layers, labeling a mixture of MCs and XCs.

We exploited this fact in order to implement a paired experimental design for our L4 stimulation experiments. The aim of these experiments was to compare the amount of L4 input received by L5 XCs and L5 MCs, which required us to perform experiments in two sets of animals (SCNN1-Cre; X94 mice and SCNN1-Cre; GIN mice). Whenever possible, while recording from an L5 X94 (XC) or L5 GIN (MC), we also recorded simultaneously from an L4 X94 or L4 GIN (both XCs). This configuration acts as a control for possible variability (e.g. in opsin expression, slice health) that is bound to occur to some extent between different slices and animals.

We observed that both L4 GIN cells and L4 X94 cells both received strong input during L4 photostimulation. Furthermore, we observed no significant difference in the responses of these two populations, indicating that we achieved the same degree of L4 activation in both experimental conditions ($p>0.05$ for EPSC charge transfer and spiking, for both types of photostimulation; F-test of linear mixed effects model coefficients). The responses of both L4 GIN and L4 X94 cells were similar to those of L5 X94 cells for all measures, suggesting that L4 provides a similar degree of drive to L4 XCs and L5 XCs (Fig. S5a-h).

In contrast, L5 GIN MCs received much less input from L4 than the other groups. In many conditions, we observed essentially no evoked excitation in L5 MCs; because we concurrently observed very strong excitation in L4 XCs, we can confidently conclude that this result is due to a near absence of L4PC→L5MC connectivity (Fig. S5a-h). When L5 GIN MCs did exhibit L4-evoked EPSCs (typically only during high intensity stimulation, Fig. S5c,d,i,j), their onset occurred at a considerably longer latency than in L5 XCs (Fig. 5k, 4.6 ms vs 3.6 ms; $p < 0.001$; two-sample t-test, $T(30) = -3.66$) suggesting that they were polysynaptic rather than monosynaptic.

Acknowledgements

We are grateful to Ariel Agmon (West Virginia University) for generously providing X94 mice. We thank Christopher Douglas, Desiree Chu, and Kirill Chesnov for technical assistance. We thank Ming-Chi Tsai, Alan Mardinly, Scott Pluta, Julia Veit, Evan Lyall, and Ian Oldenburg for helpful comments and discussion. This work was supported by National Institute of Neurological Disorders and Stroke grant DP2NS087725-01 and the New York Stem Cell Foundation. A.N. is supported by the National Institute of Neurological Disorders and Stroke of the National Institutes of Health under Ruth L. Kirschstein National Research Service Award F31NS093925. B.M.S. is supported by

a Fannie and John Hertz Foundation Fellowship and an NSF Graduate Research Fellowship. L.P. is supported by IARPA MICRONS contract D16PC00003 and DARPA SIMPLEX contract N66001-15-C-4032. H.A. is a New York Stem Cell Foundation Robertson Investigator.

Author contributions

Conceptualization, A.N. and H.A.; Methodology, A.N., B.M.S., L.P.; Investigation, A.N., B.M.S., B.S., and A.Y.E.; Resources, S.S.; Formal Analysis, A.N. and B.M.S.; Writing – Original Draft, A.N.; Writing – Review & Editing, A.N., B.M.S., L.P., and H.A.; Funding Acquisition, H.A.; Supervision, H.A. and L.P.

Supplemental Figures

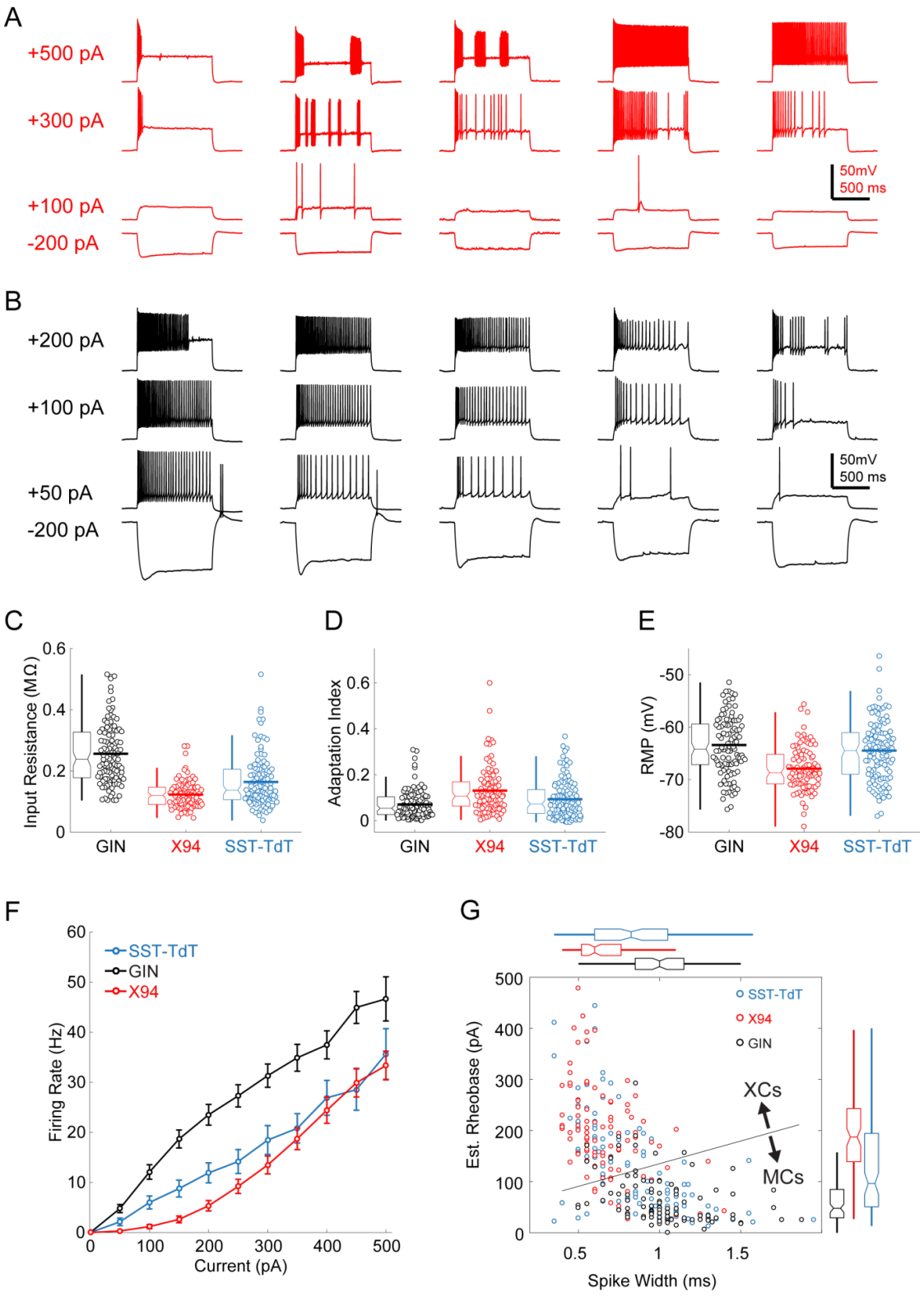

Supplemental Figure 3.1 Intrinsic properties of L5 SST cells

(A) Example traces showing diverse spiking responses of L5 X94 cells during current injection.
(B) As in A, but for L5 GIN cells. Note that less current is being injected due to the greater input resistance of these cells.
(C) Swarm and box-and-whisker plots of input resistance for L5 GIN cells (black), L5 X94 cells (red), and L5 SST-TdT cells (gray). Thick horizontal line indicates distribution mean.
(D,E) As in C, but for spike frequency adaptation index and resting membrane potential.
(F) FI curves from L5 cells recorded in the SST-TdT line (gray), GIN line (black), or X94 line (red).
(G) Scatter plot showing estimated rheobase and median spike width for L5 GIN cells (black), L5 X94 cells (red), and L5 SST-TdT cells (gray). Box and whisker plots summarizing population statistics for these variables are in the margins. The blue line indicates the decision boundary for a linear support vector machine trained to classify L5 GIN cells and L5 X94 cells based on these two variables; this classifier was in turn used to classify SST-TdT cells as putative SST_{L4T} cells or MCs.

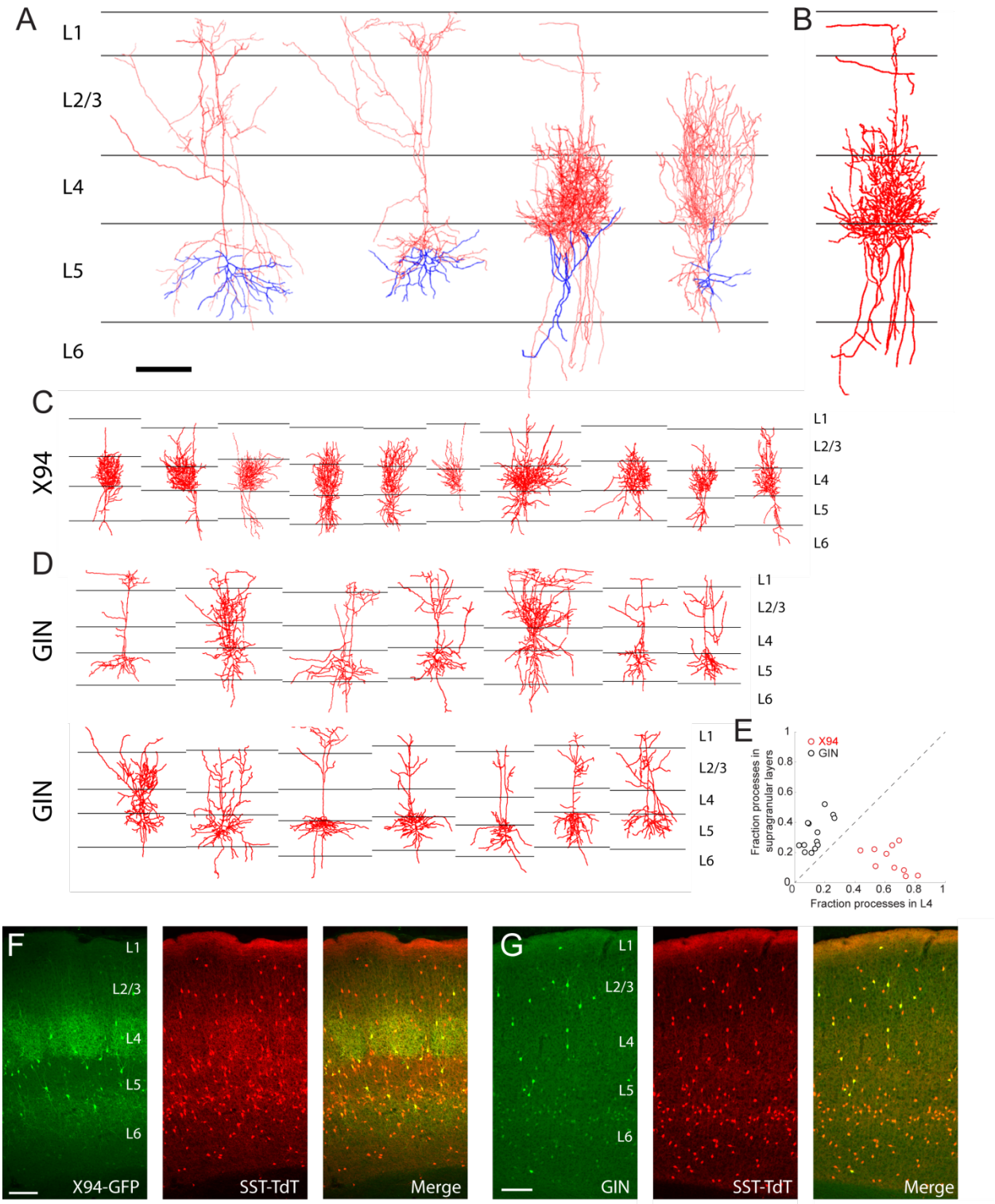

Supplemental Figure 3.2 Morphological reconstruction of L5 SST cells

(A) Examples of biocytin reconstructions done manually at high magnification of two L5 MCs (left two) and two L5 SST_{LAT} cells (right two) showing axonal (red) and dendritic (blue) morphology. Scale bar 150 µm.
(B) An example of a semi-automated reconstruction done at 10x magnification of an L5 SST_{LAT} (compare to the third reconstruction in A).
(C) Semi-automated reconstructions of L5 X94 cells
(D) As in C, but for L5 GIN cells.

(E) Comparison of neurite density of L5 GIN cells and L5 X94 cells in L4 versus the supragranular layers.
(F) Coronal section of barrel cortex in an X94-GFP; SST-TdT mouse. TdTomato fluorescence can be seen in all layers, with a dense band in L1 from the axons of MCs. Dense axonal arborization of X94-GFP cells is visible in L4, and upper L6 to a lesser extent, but not in L1.
(G) As in F, but for a GIN; SST-TdT mouse.

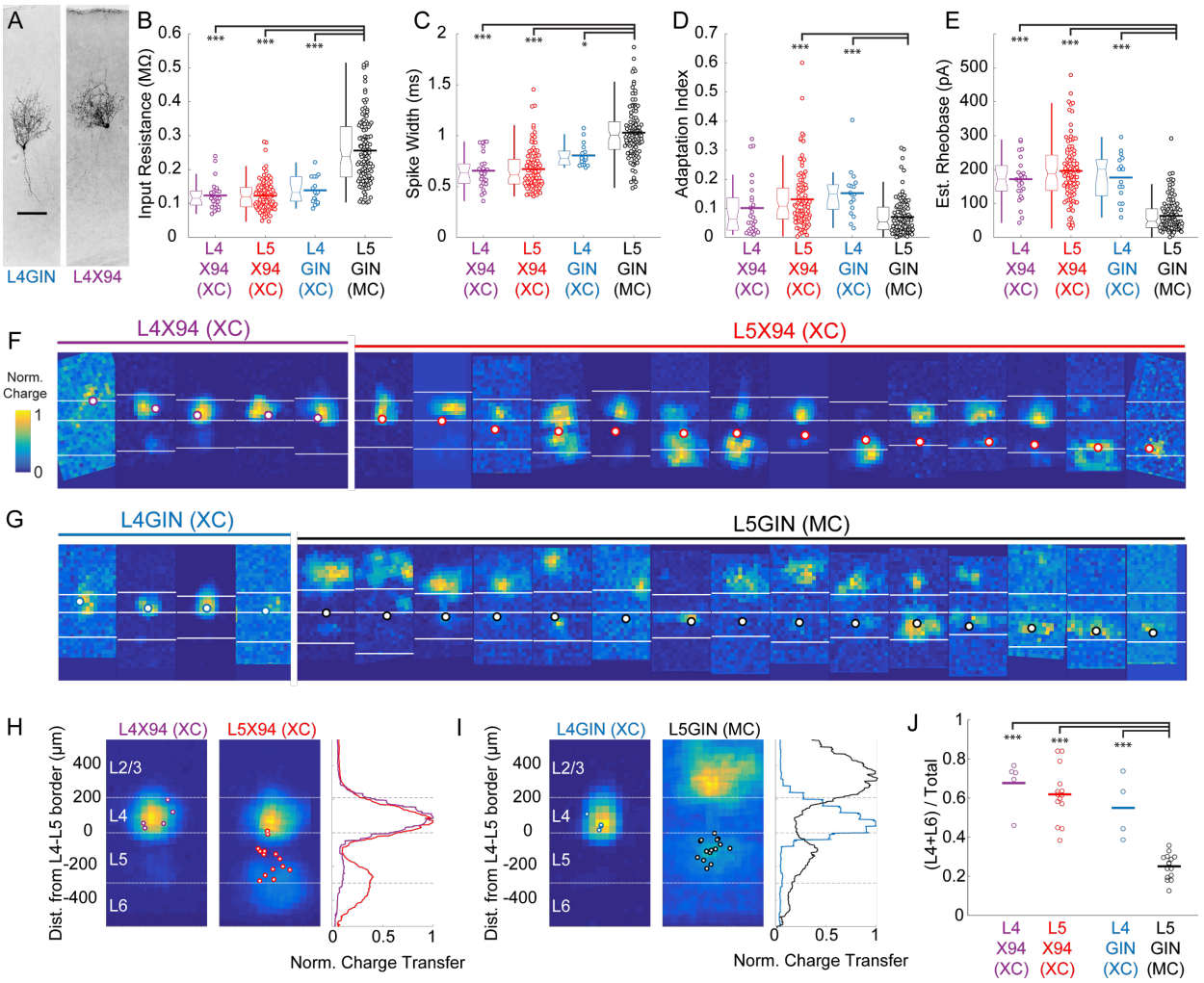

Supplemental Figure 3.3 Comparison of intrinsic properties and excitatory inputs for L4 and L5 SST cells

(A) Biocytin fills of an L4 GIN cell (left) and an L4 X94 cell (right), both exhibiting non-Martinotti morphology.
(B) Input resistances for L4X94, L5 X94, L4 GIN, and L5 GIN populations. Data are displayed as swarm plots, accompanied by Tukey box plots. The thick horizontal bar within the swarm indicates population mean. The L4 X94, L4 GIN, and L5 X94 populations have significantly lower input resistances than the L5 GIN population (L4 X94, $p = 3.8 \cdot 10^{-9}$; L5 X94, $p = 3.8 \cdot 10^{-9}$; L4 GIN, $p = 3.8 \cdot 10^{-5}$; Wilcoxon rank-sum test versus L5 GIN population).
(C) As in B, but for spike width. The L4 X94, L4 GIN, and L5 X94 populations have significantly shorter spike widths than the L5 GIN population (L4 X94, $p = 4.0 \cdot 10^{-9}$; L5 X94, $p = 3.8 \cdot 10^{-9}$; L4 GIN, $p = 0.029$; Wilcoxon rank-sum test versus L5 GIN population).
(D) As in B, but for adaptation index score. The L4 GIN and L5 X94 populations have significantly shorter spike widths than the L5 GIN population (L5 X94, $p = 1.5 \cdot 10^{-6}$; L4 GIN, $p = 1.4 \cdot 10^{-4}$; Wilcoxon rank-sum test) but the L4 X94 was not significantly different.
(E) As in B, but for estimated rheobase. The L4 X94, L4 GIN, and L5 X94 populations have significantly shorter spike widths than the L5 GIN population (L4 X94, $p = 7.2 \cdot 10^{-9}$; L5 X94, $p = 3.8 \cdot 10^{-9}$; L4 GIN, $p = 6.4 \cdot 10^{-7}$; Wilcoxon rank-sum test versus L5 GIN population).
(F) All excitatory input maps for X94 cells in L4 (left, orange) and L5 (right, red). Bordered white dots indicate the location of the recorded soma.
(G). As in F, but for GIN cells in L4 (gray) and L5 (black).
(H) Average maps for L4 and L5 XCs. Both groups receive strong input from L4. L5 XCs receive stronger inputs on average from the infragranular layers, though there was no significant difference between these groups nor a significant correlation of the depth of the recorded cell with the relative amount of input received from the deeper layers.
(I) As in H, but for GIN cells. L4 GIN cells (XCs) receive inputs primarily from L4 (similar to X94 cells) and are very different from L5 GIN cells (MCs).
(J) L5 GIN MCs received a significantly smaller proportion of excitatory charge transfer originating from L4 and L6 than other cell types (L4 X94, $p = 7.2 \cdot 10^{-9}$; L5 X94, $p = 3.8 \cdot 10^{-9}$; L4 GIN, $p = 6.4 \cdot 10^{-7}$; Wilcoxon rank-sum test versus L5 GIN population).
Single asterisk indicates $p<0.05$, three asterisks indicates $p<0.001$.

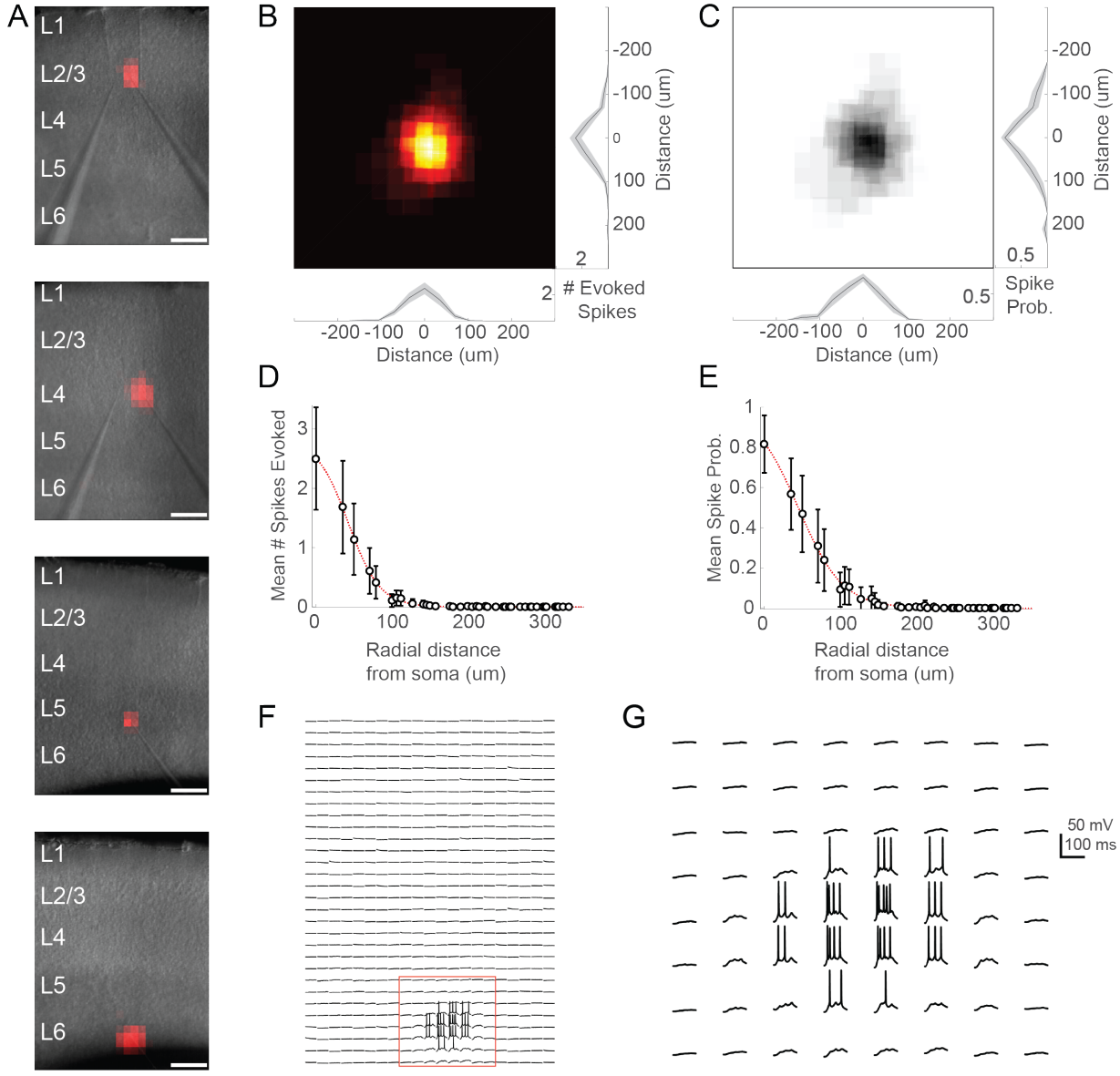

Supplemental Figure 3.4 Excitation profiles of ChR2+ cells in DMD-based mapping experiments

(A) Example spiking heatmaps recorded from cells in L2-6, overlaid on infrared images of slices. Scale bar indicates 175µm.
(B) Average map of # of evoked spikes per trial in n= 20 ChR2+ cells. Maps are centered on the somata of recorded cells.
(C) As in B, but for probability of evoking at least 1 spike per trial.
(D) Average number of spikes evoked as a function of radial distance from ChR2+ cell soma.
(E) As in D, but for probability of evoking at least one spike.
(F) Example traces corresponding to the bottom heatmap in A. Spiking is evoked only during perisomatic photostimulation.
(G) Expanded view of red boxed region in F. Bursts of spikes are evoked in a single trial during direct stimulation of the soma.

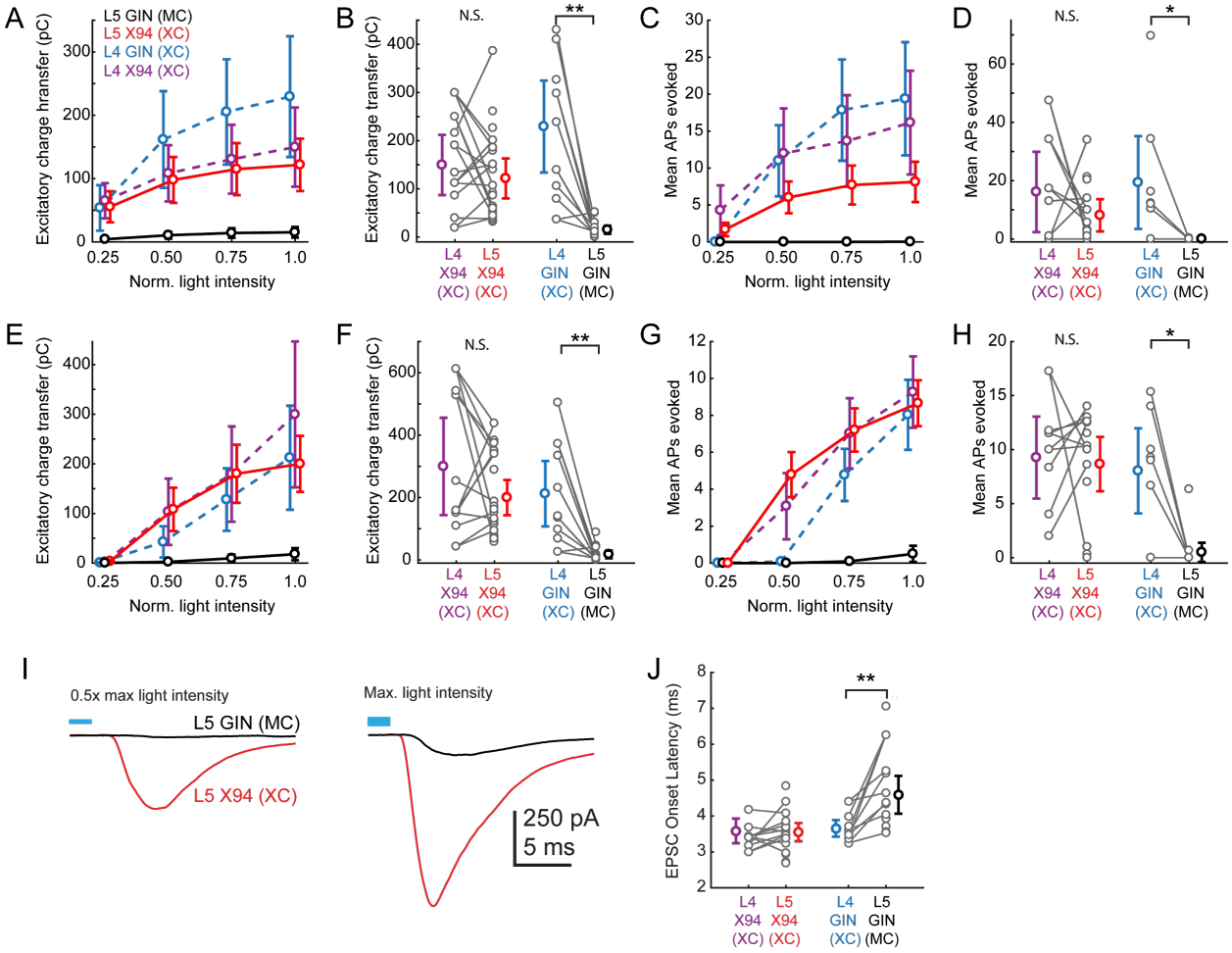

Supplemental Figure 3.5 Responses of L4 and L5 SST cells to L4 photo-stimulation

(A) Dose response profile of excitatory charge transfer evoked during 1 second ramp stimulation of L4 for X94 cells in L4 (purple) and L5 (red) and for GIN cells in L4 (blue) and L5 (black). To assess differences between groups, we fit a linear mixed-effects model with fixed effects parameters for the slope of the stimulus-response function and random effects slope parameters for each slice and cell recorded, along with a single intercept term. The L5 GIN cell group had a significantly lower fixed effects slope coefficient than the L5 X94 ($p = 2.1 \cdot 10^{-5}$), L4 X94 ($p = 3.1 \cdot 10^{-5}$), and L4 GIN groups ($p = 2.0 \cdot 10^{-9}$).

(B) Mean excitatory charge transfer evoked during maximum intensity 1 second ramp stimulation of L4. Gray lines indicate pairs of cells recorded in the same slice. Charge transfer was not significantly different between L4 X94 cells and L5 X94 cells on a pairwise basis (169.1 ± 91.5 pC versus 118.7 ± 44.0 pC ; $p = 0.10$, paired t-test), but was significantly different between L4 GIN cells and L5 GIN cells (229.4 ± 95.3 pC versus 15.2 ± 8.4 pC; $p = 0.002$, paired t-test).

(C,D) As in A,B, but for mean number of action potentials evoked in L5 SST cells recorded in current clamp during 1 second ramp photo-stimulation. F-tests on coefficients of a linear mixed-model indicated that the L5 GIN cell group had a significantly lower fixed effects slope coefficient than the L5 X94 ($p = 0.03$), L4 X94 ($p = 1.0 \cdot 10^{-3}$), and L4 GIN groups ($p = 1.7 \cdot 10^{-4}$). The mean number of spikes evoked was not significantly different between L4 X94 cells and L5 X94 cells on a pairwise basis (20.4 ± 23.7 spikes versus 9.0 ± 6.0 spikes ; $p = 0.14$, paired t-test), but was significantly different between L4 GIN cells and L5 GIN cells (19.4 ± 16.0 spikes versus 0.03 ± 0.05 spikes; $p = 0.034$, paired t-test).

(E,F). As in A,B, but for excitatory charge transfer in L5 SST cells recorded in voltage clamp during a train of ten 1ms pulses at 40 Hz. F-tests on coefficients of a linear mixed-model indicated that the L5 GIN cell group had a significantly lower fixed effects slope coefficient than the L5 X94 ($p = 1.2 \cdot 10^{-6}$), L4 X94 ($p = 3.5 \cdot 10^{-9}$), and L4 GIN groups ($p = 5.2 \cdot 10^{-16}$). Charge transfer was not significantly different between L4 X94 cells and L5 X94 cells on a pairwise basis (309.1 ± 220.6 pC versus 191.5 ± 58.8 pC ; $p = 0.055$, paired t-test), but was significantly different between L4 GIN cells and L5 GIN cells (212.2 ± 104.7 pC versus 18.0 ± 12.2 pC; $p = 0.002$, paired t-test).

(G,H). As in A,B, but for mean number of action potentials evoked in L5 SST cells recorded in current clamp during a train of ten 1ms pulses at 40 Hz. F-tests on coefficients of a linear mixed-model indicated that the L5 GIN cell group had a significantly lower fixed effects slope coefficient than the L5 X94 ($p = 1.2 \cdot 10^{-6}$), L4 X94 ($p = 5.3 \cdot 10^{-9}$), and L4 GIN groups ($p = 2.2 \cdot 10^{-14}$). The mean number of spikes evoked was not significantly different between L4 X94 cells and L5 X94 cells on a pairwise basis (9.8 ± 6.2 spikes versus 8.6 ± 2.6 spikes; $p = 0.56$, paired t-test), but was significantly different between L4 GIN cells and L5 GIN cells (8.0 ± 3.9 spikes versus 0.5 ± 0.9 spikes; $p = 0.0068$, paired t-test).

(I) Plots of the grand average EPSC evoked at mild intensity (top; 0.625 mW·mm^2) pulse and maximum intensity stimulation (bottom; 1.25 mW·mm^2) of L4 for L5 MCs (black) and L5 XCs (red). Low intensity stimulation produced robust EPSCs in L5 XCs but not L5 MCs. High intensity stimulation was able to evoke EPSCs L5 MCs but with a delayed onset.

(J) Plot of average EPSC onset latency in response to maximum intensity pulse stimulation of L4 (as seen in bottom panel of I) in different SST cell populations. Gray dots indicate individual cells in each group; cells connected by gray lines indicate neurons recorded in the same preparation (usually simultaneously). EPSC onset latency is uniformly longer for L5 MCs compared to paired L4 XCs.
Errorbars indicate mean ± confidence interval.

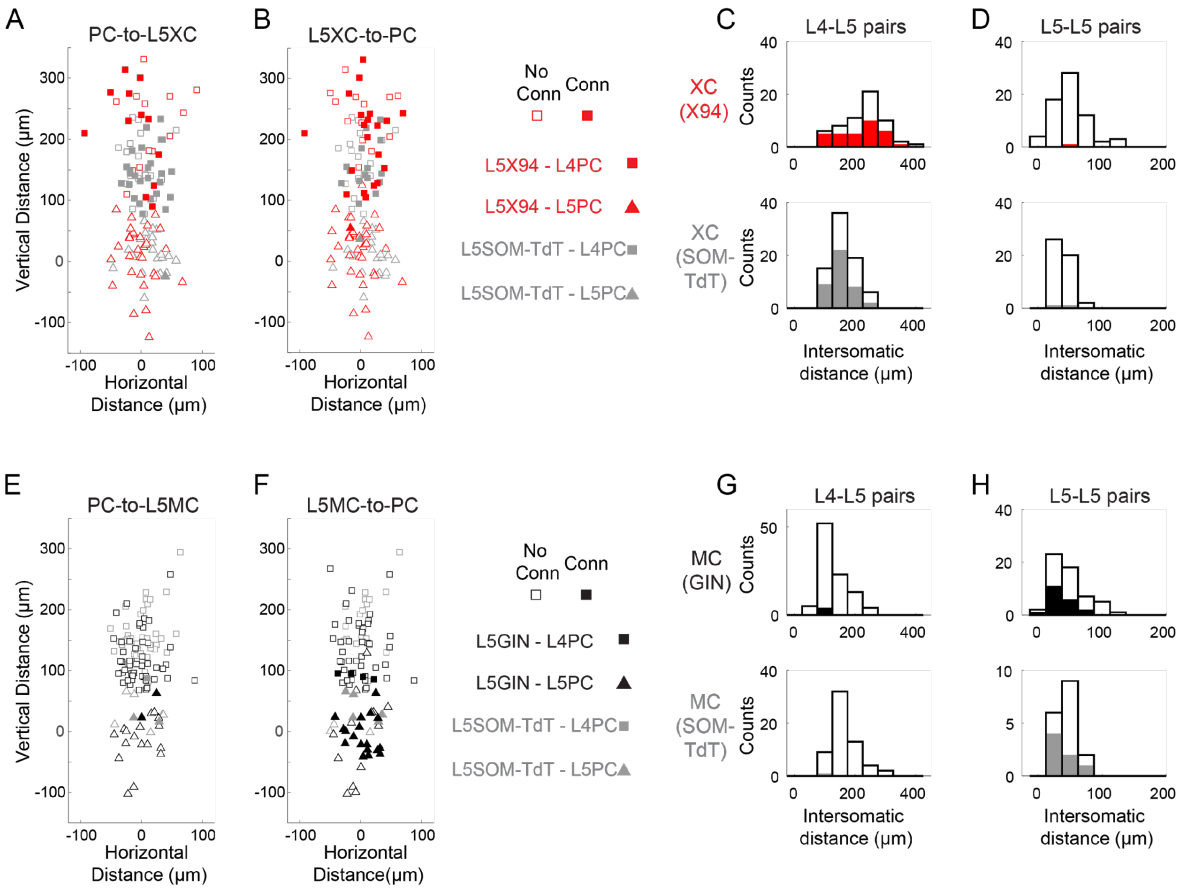

Supplemental Figure 3.6 Distances of connections tested in paired recordings

(A) Scatterplot showing the relative distances between pairs tested for monosynaptic excitatory connections from L4 and L5 PCs onto L5 XCs. Squares represent L5XC-L4 PC pairs; triangles represent L5XC-L5 PC pairs. Filled markers indicate that a connection was observed; open markers indicate no connection was observed. Red symbols indicate pairs tested in X94 mice; gray symbols indicate pairs tested in SST-TdT mice where the L5 XC was identified electrophysiologically. The origin represents the position of the L5 XC soma (note that these were located at variable distances from the L4-L5 border).
(B) As in A, but for monosynaptic inhibitory connections from L5 XCs onto L4 and L5 PCs.
(C) Histogram showing the distribution of intersomatic distances between pairs of L5 XCs and L4 PCs. Empty bars indicate the number of pairs tested per binned distance; filled bars indicate the number of positive connections (unidirectional in either direction or bidirectional) detected at that bin. Top: pairs in X94 mice. Bottom: pairs in SST-TdT mice.
(D) As in C, but for pairs of L5 XCs and L5 PCs.
(E-H) As in A-D, but for pairs of L5 MCs and L4/L5 PCs. Other than the layer-specific connectivity biases of MCs and XCs, we did not observe any significant relationship between intersomatic distance (vertical, horizontal, or Euclidean) and connection probability.

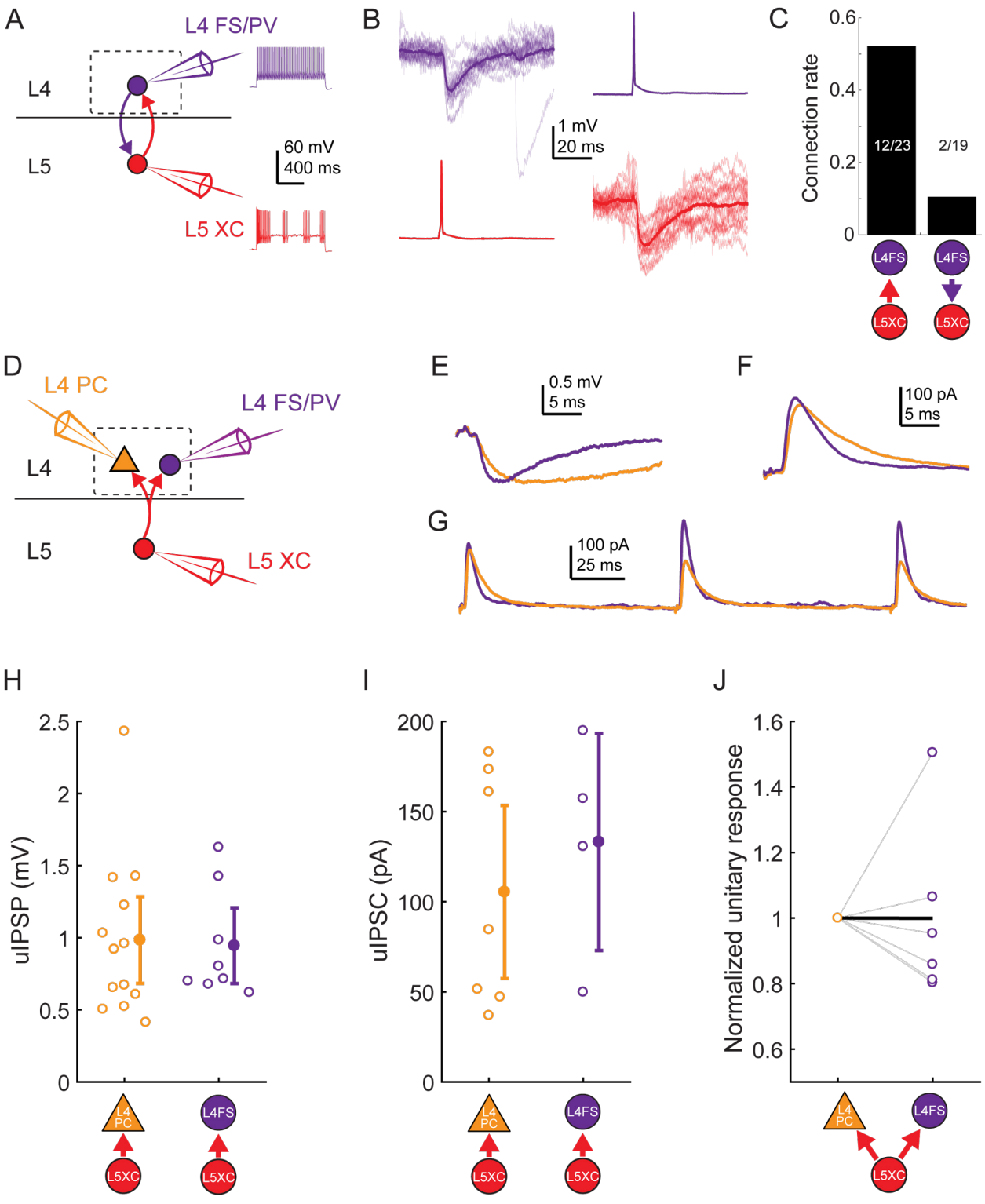

Supplemental Figure 3.7 L5 XC connectivity onto L4 FS cells

(A) Schematic of paired recordings between L4 FS/PV cells (purple) and L5 XCs. Inset: example spiking in response to depolarizing current injection.
(B) Monosynaptic IPSPs could be observed in L4 FS cells in response to single spikes in L5 XCs (left) and vice versa (right)
(C) Bar graph showing connection rates for L5XC-L4FS pairs. Connections from L5 XCs onto L4 FS cells were observed frequently, whereas connections from L4 FS cells onto L5 XCs occurred rarely.
(D) In some experiments, divergence from L5 XCs was observed by holding one L5 XC while serially patching L4 PCs and L4 FS/PV cells.

(E) Example IPSPs in an L4 PC and L4 FS/PV cell evoked by the same L5 XC.
(F) As in E, but while using a Cs-based internal to record IPSCs (holding potential +10mV) in an L4 PC and an L4 FS/PV cell.
(G) As in F, but while evoking multiple spikes in the L5 XC at 10 Hz.
(H) Amplitude of unitary IPSPs evoked by L5 XCs in L4 PCs (0.98 ± 0.30 mV) and L4 FS cells (0.94 ± 0.26 mV). Summary data are represented as mean ± 95% C.I.
(I) Amplitude of unitary IPSCs (recorded using cesium-based internal solution) evoked by L5 XCs in L4 PCs (105 ± 48 pA) and L4 FS cells (133 ± 60 pA). Summary data are represented as mean ± 95% C.I.
(J) Comparison of unitary response amplitudes (IPSPs or IPSCs) for pairs in which serial recordings were established for an L5XC-to-L4PC connection (left) and an L5XC-to-L4FS/PV connection (right), normalized to the amplitude of the L4PC response. Thick black line connects the mean normalized L4 PC unitary response (by definition, 1) and mean normalized L4 FS/PV unitary response (0.99 ± 0.52).

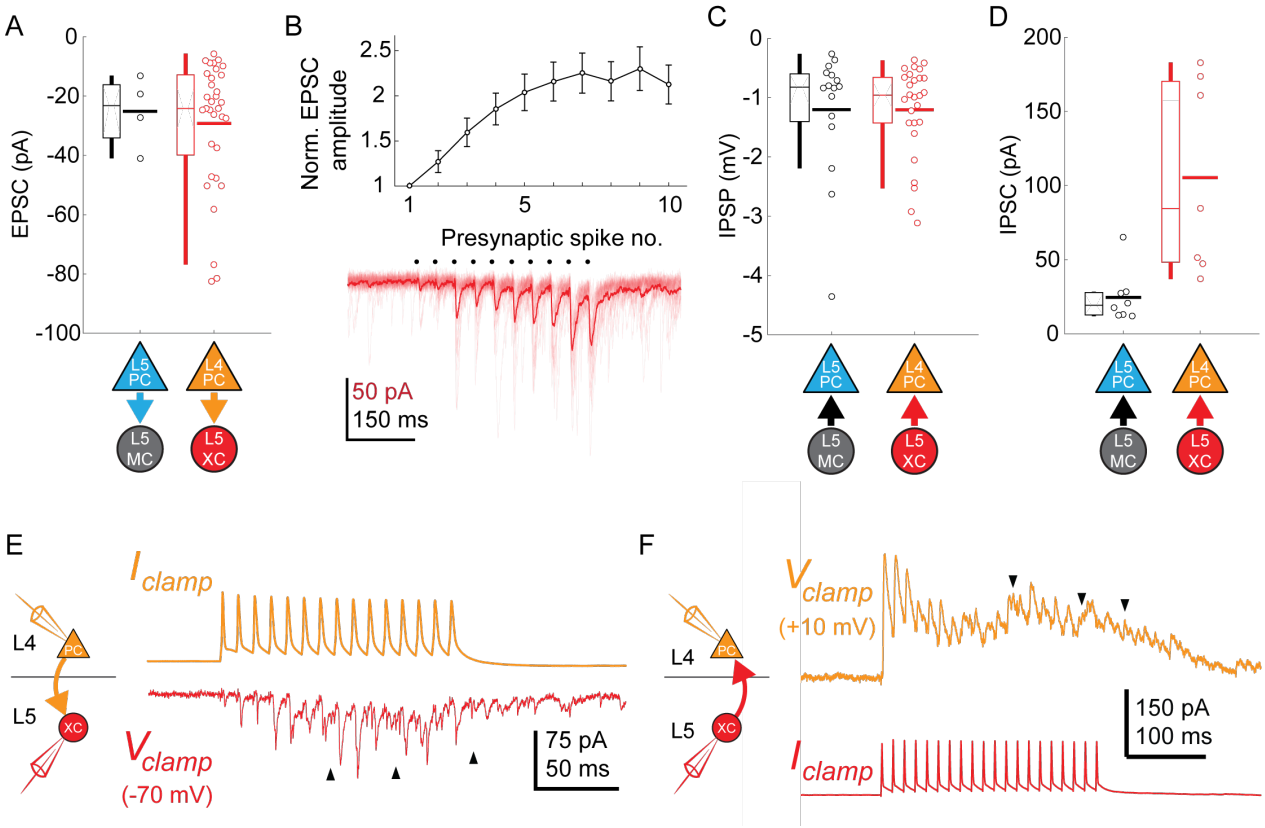

Supplemental Figure 3.8 Synaptic properties of L5 SST connections

(A) Swarm plots and Tukey box plots of evoked EPSC amplitude in connections onto L5 MCs (black) and L5 XCs (red), measured as the largest EPSC evoked during a train of presynaptic firing at 70 Hz.
(B) Facilitation dynamics of EPSCs onto L5 XCs. Bottom: example of facilitating EPSCs in response to a train of 10 spikes at 70 Hz in an L4 PC. Top: Mean EPSC amplitude evoked in L5XCs while stimulating L4 PCs at 70 Hz, normalized to EPSC amplitude after the initial spike. Errorbars represent mean ± S.E.M.
(C) Swarm plots and Tukey box plots of evoked IPSP amplitude in connections from L5 MCs (black) and L5 XCs (red) onto L4/L5 PCs.
(D) As in D, but for IPSCs recorded in L4/L5 PCs (holding potential +10mV) using a Cs-based internal. Unlike IPSPs, IPSCs evoked by L5XCs onto L4PCs are stronger than those evoked by L5 MCs onto L5 PCs; this may reflect differences in space clamp error when recording from L4 PCs vs L5 PCs.
(E) Sustained high frequency spiking in L4 PCs appeared to evoke asynchronous EPSCs in L5 XCs (indicated by black arrows) which continued even after the cessation of spiking.
(F) As in C, but for L5XC-to-L4PC connections. Sustained high frequency spiking in L5XCs appeared to evoke asynchronous IPSCs in L4 PCs (indicated by black arrows) which continued even after the cessation of spiking.

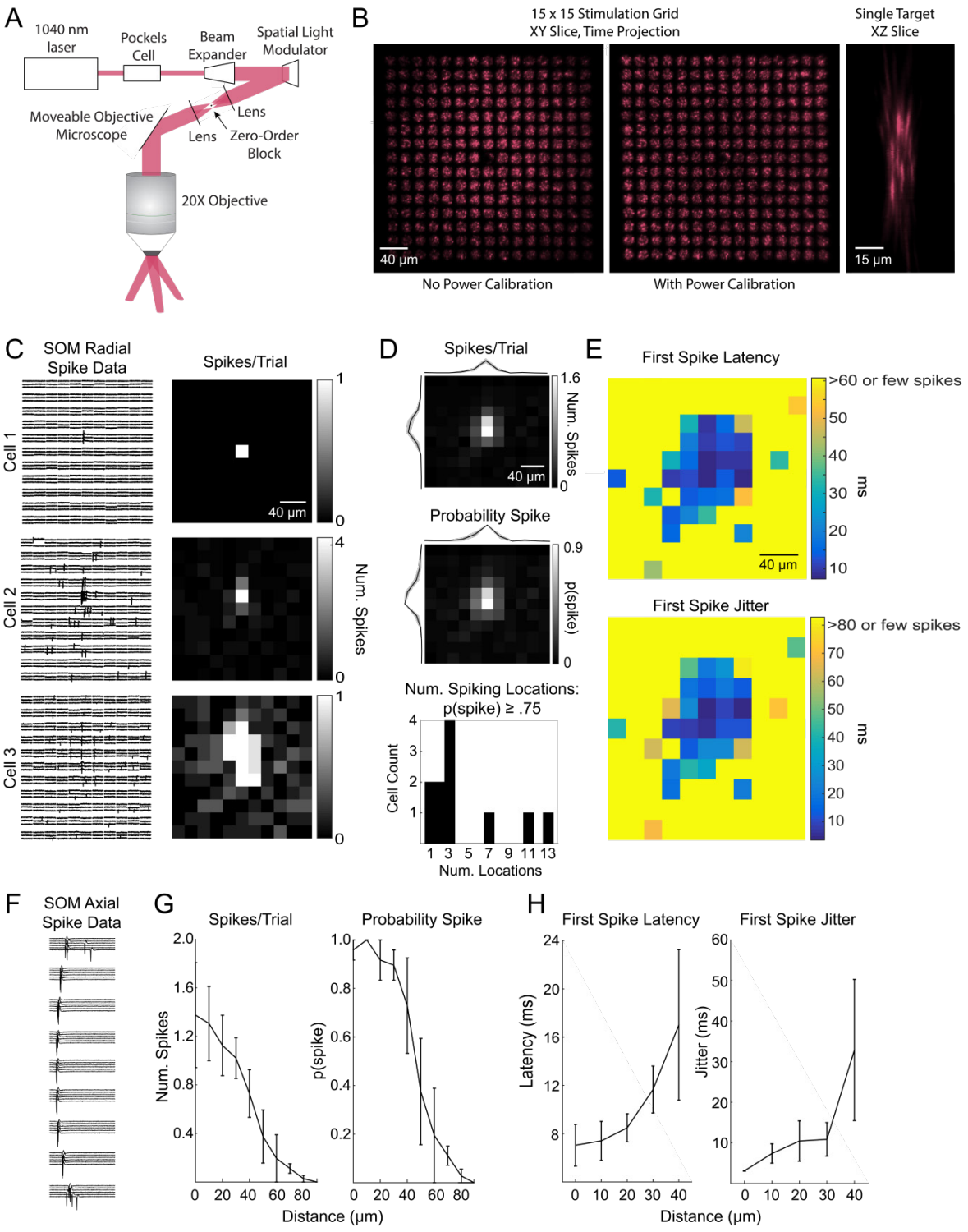

Supplemental Figure 3.9 Excitation profiles of st-ChrimsonR-expressing SST cells

(A) Schematic of the CGH-based stimulation microscope.
(B) Imaging stimulation holograms with two-photon induced fluorescence in a thin fluorescent slide. Left: Time projection of a stimulation sequence covering a 15 x 15 grid of targets at 20 µm spacing before power calibration. Middle: As in Left but with power calibration. Left: XZ slice of a single target. Note that excitation is confined to a small volume and that power calibration results in more uniform excitation radially. The decrease in fluorescence in the middle of the two stimulation grids is due to the zero-order block.

(C) Example plots of the lateral resolution of photo-stimulation. Left column: Raw cell-attached data of light-evoked spiking for example SST cells. Right column: average number of spikes evoked per trial at each location. Locations are 20 μm apart as in mapping experiments.
(D) Radial spike count statistics. Top: Average map of the number of evoked spikes per trial in st-ChrimsonR+ cells (n= 11). Maps are centered on the somata of recorded cells. Middle: As in top, but for probability of evoking at least 1 spike per trial. Bottom: Histogram of number of locations per cell which evoked a spike at least 75% of the trials.
(E) Radial spike timing statistics. Top: Average first spike latency for st-ChrimsonR+ cells (n = 11). Yellow indicates that the average was > 60 ms or that too few spikes were observed across cells at those locations to obtain a good estimate. Bottom: Average first spike jitter, computed as the full-width half-maximum of the first spike times. Yellow indicates a jitter of greater than 80 msec or that too few spikes were observed across cells at those locations.
(F) Data from an example cell as the hologram is moved axially. Distance between locations is 10 μm.
(G) Axial spike count statistics. Left: Average number of evoked spikes as a function of axial distance for st-ChrimsonR+ cells (n=4). Right: As in left, but for the probability of at least one spike per trial.
(H) Axial spike timing statistics. Left: Average first spike latency as a function of axial distance (n=4 cells). Right: First spike jitter as a function of axial distance for st-ChrimsonR+ cells (n = 3).

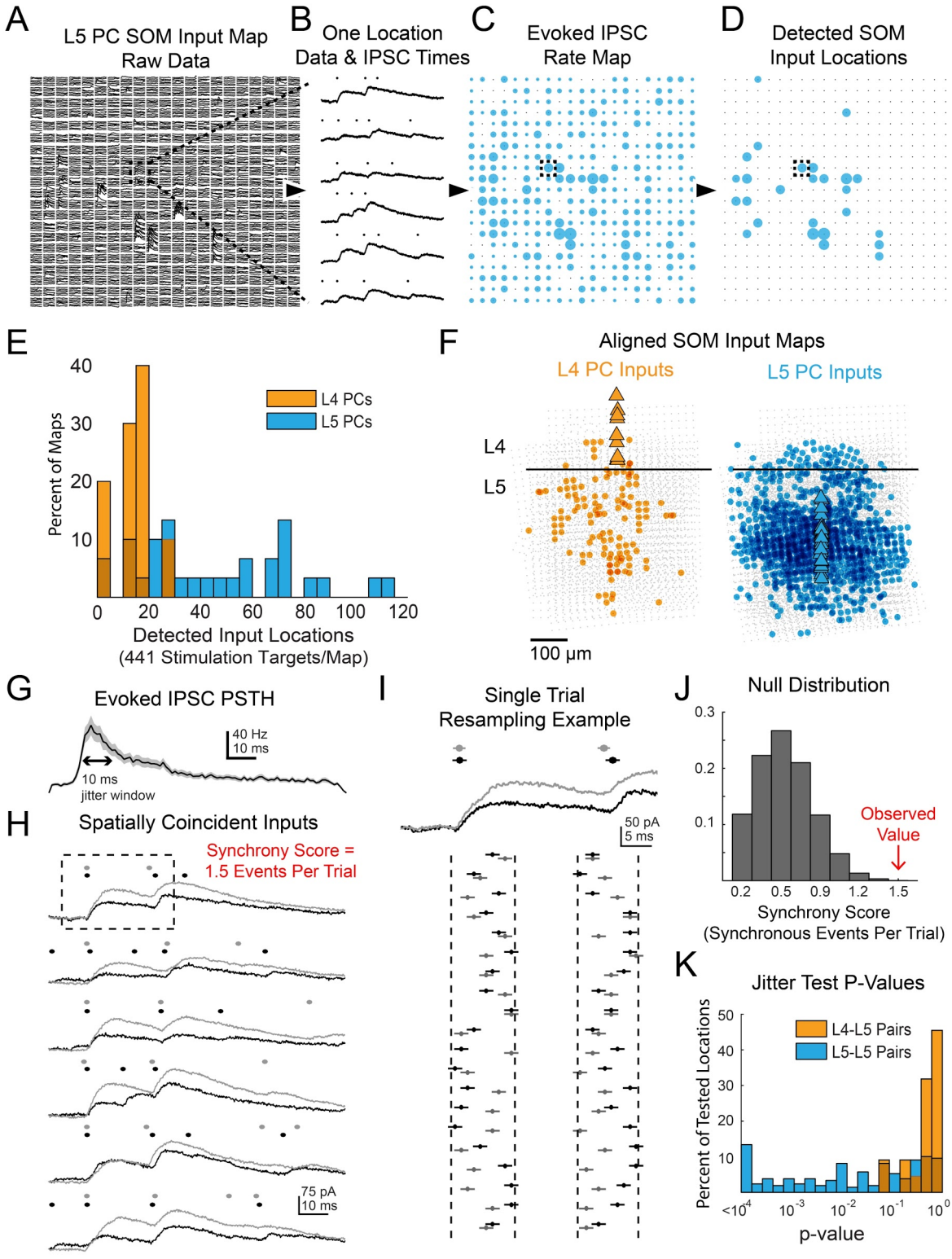
A
L5 PC SOM Input Map
Raw Data
B
One Location
Data & IPSC Times
C
Evoked IPSC
Rate Map
D
Detected SOM
Input Locations
E
Percent of Maps
L4 PCs
L5 PCs
Detected Input Locations
(441 Stimulation Targets/Map)
F
Aligned SOM Input Maps
L4 PC Inputs
L5 PC Inputs
L4
L5
100 µm
G
Evoked IPSC PSTH
40 Hz
10 ms
10 ms
jitter window
H
Spatially Coincident Inputs
Synchrony Score =
1.5 Events Per Trial
75 pA
10 ms
I
Single Trial
Resampling Example
50 pA
5 ms
J
Null Distribution
Observed
Value
Synchrony Score
(Synchronous Events Per Trial)
K
Jitter Test P-Values
L4-L5 Pairs
L5-L5 Pairs
Percent of Tested Locations
p-value

Supplemental Figure 3.10 Data processing and additional results for multiphoton SST output mapping

(A) Example of raw data a single map onto a L5 PC. Dashed box shows location for which data is shown in B.
(B) Example of Bayesian PSC detection on all 6 trials from a single location from the map in A.
(C) A map showing the evoked IPSC rates at each location for the map from A. Dashed box shows location of data from B.
(D) As in C except only locations which pass FDR detection are shown.
(E) Histograms showing the number of locations with evoked IPSCs for both L4 and L5 PCs.
(F) Overall spatial input distributions for SST cells in L5 to both L4 PCs (left, n = 10) and L5 PCs (right, n = 28). Maps are aligned vertically to the L4-L5 border and horizontally to the PC soma. For this representation all inputs are plotted with the same size circle.
(G). PSTH of IPSC times aggregated from all locations with detected evoked IPSC rates. A 10 ms duration which matches the jitter duration for temporal synchrony is marked for comparison.
(H) As in B except showing data and IPSC detection for two simultaneously recorded L5 PCs. The synchrony score for this location is 1.5 events/trial. Dashed box shows data used for I.
(I) Example of 20 resamplings of the events during the analysis window for the first trial shown in H. Vertical dashed lines show discrete event jittering windows. Horizontal lines on each event span 2ms such that if the lines from two events overlap then they would be counted as synchronous.
(J) Null distribution of synchrony score from event time series resampling of the data in H. The observed value is from the far right extreme of the distribution.
(K) Histograms of p-values for all spatially overlapping locations for all pairs from jitter synchrony tests.

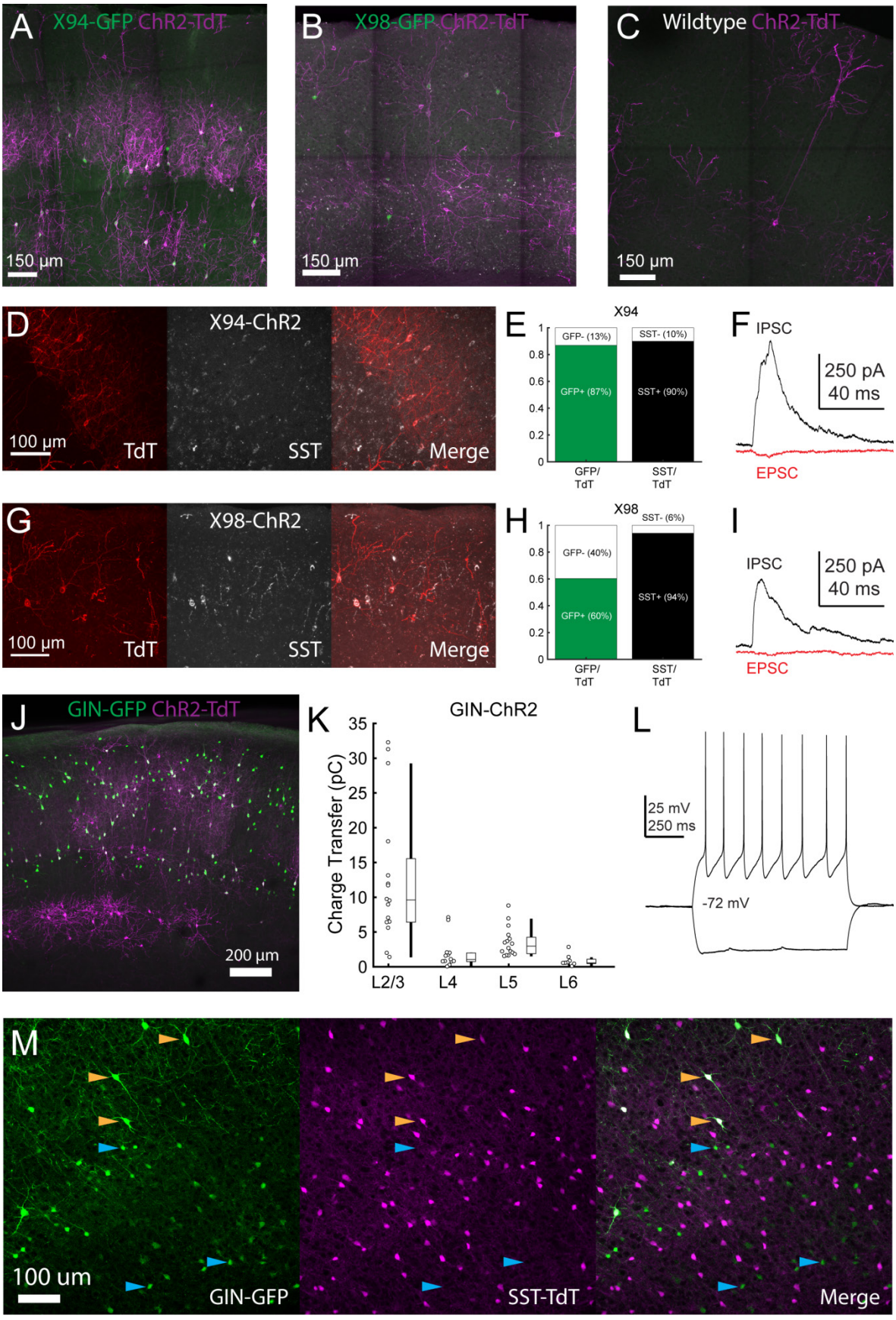
A
X94-GFP ChR2-TdT
150 µm
B
X98-GFP ChR2-TdT
150 µm
C
Wildtype ChR2-TdT
150 µm
D
X94-ChR2
100 µm
TdT
SST
Merge
E
X94
GFP- (13%)
SST- (10%)
GFP+ (87%)
SST+ (90%)
GFP/ TdT
SST/ TdT
F
IPSC
250 pA
40 ms
EPSC
G
X98-ChR2
100 µm
TdT
SST
Merge
H
X98
SST- (6%)
GFP- (40%)
GFP+ (60%)
SST+ (94%)
GFP/ TdT
SST/ TdT
I
IPSC
250 pA
40 ms
EPSC
J
GIN-GFP ChR2-TdT
200 µm
K
GIN-ChR2
Charge Transfer (pC)
L2/3
L4
L5
L6
L
25 mV
250 ms
-72 mV
M
100 um
GIN-GFP
SST-TdT
Merge

Supplemental Figure 3.11 Validation of Cre-DOG in X94, GIN, and X98 mice

(A) Max projection of confocal images of barrel cortex of an X94 mouse injected with Cre-DOG AAVs (AAV2/8. EF1a.C-CreintG WPRE.hGH and AAV2/8. EF1a. N-Cretrcintc WPRE.hGH) along with AAV9.CAGGS.Flex.ChR2-tdTomato.WPRE.SV40 showing expression of GFP (green) and ChR2-TdT (magenta) expression.
(B) As in A, but for an X98 mouse.
(C) As in A, but for a wildtype mouse.
(D) Immunohistochemical staining for SST in X94-ChR2 mice. Left: ChR2-TdT expression (red). Middle: SST staining (white) Right: Merge
(E) Quantification of the fraction of TdT+ cells in which GFP (left, green bar) and SST (right, black bar) was observed.
(F) Example EPSC and IPSC traces recorded in an L4 neuron during photostimulation in a slice from an X94-ChR2 mouse.
(G - I) As in D - F, but for X98-ChR2 mice.
(J) Max projection of a confocal image from a GIN mouse injected with Cre-DOG AAVs (AAV2/8. EF1a.C-CreintG WPRE.hGH and AAV2/8. EF1a. N-Cretrcintc WPRE.hGH) along with AAV9.CAGGS.Flex.ChR2-tdTomato.WPRE.SV40 showing expression of GFP (green) and ChR2-TdT (magenta) expression.
(K) Median charge transfer of evoked IPSCs in each PC recorded in GIN-ChR2 slices, grouped by layer and accompanied by box and whisker plots.
(L) Example current injection traces from an L6, TdT+ non-Martinotti neuron recorded in a GIN-ChR2 slice.
(M) Confocal images from a triple transgenic GIN; SST-TdT animal. Left: GFP (green). Middle: TdT (magenta). Right: merge. Yellow arrows indicate TdT+ cells with bright GFP expression, which are likely MCs. Blue arrows indicate TdT- cells with dimmer GFP expression, which are preferentially located in L6.

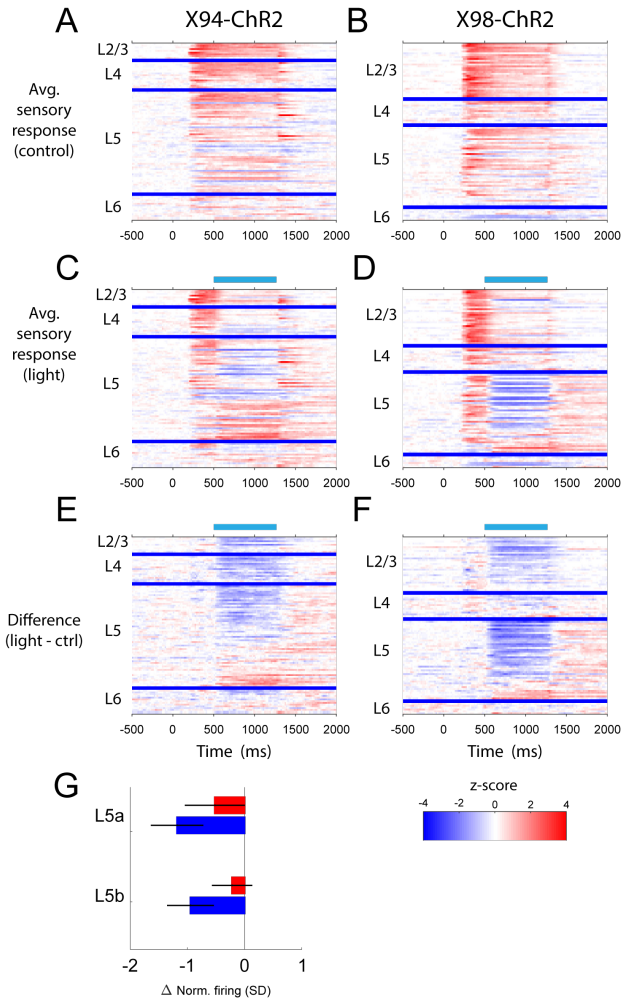

Supplemental Figure 3.12 RS unit sensory responses during optogenetic manipulation of MCs and XCs

(A) Heatmaps showing the mean normalized firing rate of all RS units recorded in X94-ChR2 mice during sensory stimulation, in the absence of optogenetic stimulation. Each row represents a single unit, and units are grouped according to the layer in which they were recorded. Within each layer group, units are sorted based on the degree to which they are modulated by optogenetic stimulation. Thick blue bars indicate divisions between layers.
(B) As in A, but for RS units recorded in X98-ChR2 mice.
(C) Heatmaps showing the mean normalized firing rate of all RS units recorded in X94-ChR2 mice during sensory stimulation along with optogenetic stimulation. Units are arranged as in A. Light blue bar indicates the period when optogenetic stimulation occurred.
(D) As in C, but for RS units recorded in X98-ChR2 mice.
(E) Heatmaps showing the difference in the mean normalized firing rate of all RS units recorded in X94-ChR2 mice between sensory stimulation with and without optogenetic stimulation, e.g. panel C subtracted from panel A.
(F) As in E, but for RS units recorded in X98-ChR2 mice.
(G) Bar graph summarizing the effect of X94-ChR2 (red) and X98-ChR2 (blue) optogenetic stimulation on RS units recorded in L5A and L5B.

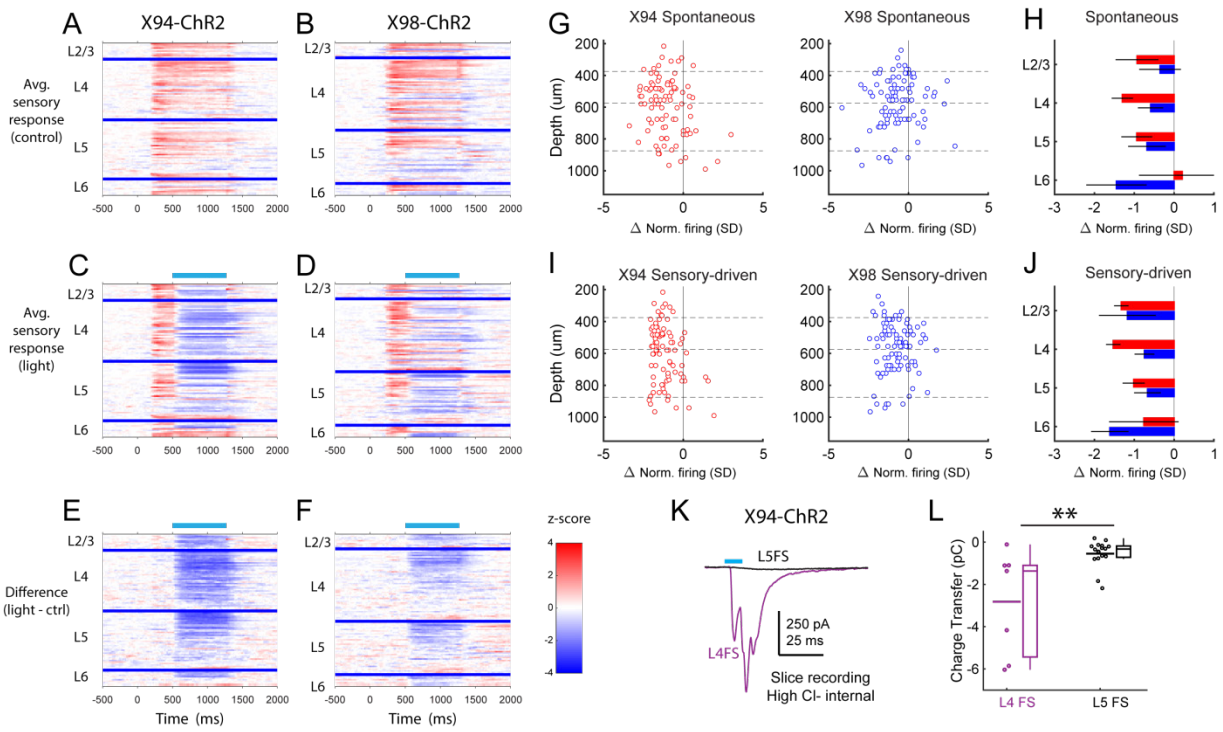

Supplemental Figure 3.13 FS unit sensory responses during optogenetic manipulation of MCs and XCs

(A) Heatmaps showing the mean normalized firing rate of all FS units recorded in X94-ChR2 mice during sensory stimulation, in the absence of optogenetic stimulation. Each row represents a single unit, and units are grouped according to the layer in which they were recorded. Within each layer group, units are sorted based on the degree to which they are modulated by optogenetic stimulation. Thick blue bars indicate divisions between layers.
(B) As in A, but for FS units recorded in X98-ChR2 mice.
(C) Heatmaps showing the mean normalized firing rate of all FS units recorded in X94-ChR2 mice during sensory stimulation along with optogenetic stimulation. Units are arranged as in A. Light blue bar indicates the period when optogenetic stimulation occurred.
(D) As in C, but for FS units recorded in X98-ChR2 mice.
(E) Heatmaps showing the difference in the mean normalized firing rate of all FS units recorded in X94-ChR2 mice between sensory stimulation with and without optogenetic stimulation, e.g. panel C subtracted from panel A.
(F) As in E, but for FS units recorded in X98-ChR2 mice.
(G) Change in normalized spontaneous firing of FS units versus depth below pia for X94-ChR2 (left, red) and X98-ChR2 (right, blue) mice.
(H) Mean change in normalized firing rate by layer for X94-ChR2 (red bars) and X98-ChR2 (blue bars). Errorbars indicate 95% confidence interval.
(I) As in G, but during sensory stimulation.
(J) As in H, but during sensory stimulation.
(K) Examples of L4 (purple) and L5 (black) FS cells recorded in X94-ChR2 slices under pharmacological blockade of glutamate. Traces show the average response to X94-ChR2 stimulation, which occurs during the light blue bar. Cells were recorded using a high chloride internal solution and voltage clamped at -70 mV; inward synaptic currents presumably reflect monosynaptic GABAergic conductances.
(L) Under the conditions described in K, X94-ChR2 stimulation evoked a significantly larger amount of charge transfer in L4 FS cells (n = 7) than in L5 FS cells (n = 16; p = 0.0021, student's T-test).

	GIN + X94			GIN + X94 + classified SST-TdT			All SST-TdT
	MCs	XCs	p	MCs	XCs	p	
L5SST→L4PC	**4/47** **9%** 2/20 10%	**21/34** **62%** 18/28 64%	$1.6 \cdot 10^{-4}$	**4/68** **6%** 2/35 6%	**36/67** **54%** 31/51 61%	$2.0 \cdot 10^{-5}$	**15/55** **27%** 33/86 38%
L4PC→L5SST	**0/50** **0%** 0/17 0%	**13/27** **48%** 11/23 48%	$5.8 \cdot 10^{-4}$	**1/95** **1%** 1/39 3%	**39/72** **54%** 31/51 61%	$<10^{-5}$	**27/91** **30%** 32/90 36%
L5SST→L5PC	**19/38** **50%** 13/23 57%	**1/38** **3%** 1/24 4%	$2.8 \cdot 10^{-4}$	**24/46** **52%** 17/30 57%	**2/65** **3%** 2/37 4%	$<10^{-5}$	**19/67** **28%** 6/35 17%
L5PC→L5SST	**2/22** **9%** 2/13 15%	**0/33** **0%** 0/22 0%	0.1431	**4/29** **14%** 4/20 20%	**1/60** **2%** 1/35 3%	0.02	**5/55** **9%** 3/34 9%

Supplementary Table 3.1 Connection rates for MCs and XCs recorded in different transgenic lines

Left columns show paired recording data collected using the GIN and X94 lines to respectively target MCs and XCs in L5. Right columns show the same data and additionally include data collected using the SST-TdT line, with L5 SST cells classified as putative MCs or XCs based on their intrinsic properties. Note that in many cases, more than one connection was tested per L5 SST cell recorded i.e. one SST cell can belong to multiple pairs. Bolded text at the top of each cell shows the number and fraction of SST-PC pairs in which a monosynaptic connection was detected for a given condition; regular font shows the number and fraction of SST cells tested in which at least one monosynaptic connection was observed for a given condition (for example, 39 connections were observed out of 72 connections tested from L4 PCs onto L5 XCs, with 31 out of 51 L5 XCs receiving at least one L4 PC connection.)

Chapter 4: Conclusions and future directions

Piecewise study of cortical circuits

The work described above can perhaps be fairly criticized as overly reductionist; our strategy has been to target individual elements in neural circuits and perform focused experiments interrogating their structure (here, mainly by mapping connectivity) and function (here, mainly by optogenetic manipulation). While neuroscientists are divided on what level of abstraction will be acceptable in a satisfactory model of cortical circuits, my own intuition is that for a model of cortex to produce useful insight into cortical pathologies of the cortex, it will at least be necessary for it to include a full 'parts-list' of cell-types and pathways, at least in an abstract sense. Studies like ours will hopefully contribute to achieving a full census of cortical cell-types, as well as a comprehensive understanding of the principles that govern cell-type specific connectivity. Understanding cell-type and cellular diversity will likely require a 'combined-arms' approach harnessing multiple experimental modalities. Future efforts to fill out the parts list will need to find ways to tie ever larger genomic/transcriptomic datasets to morphological, electrophysiological, connectivity, and *in vivo* functional data.

At the same time, it's unclear if investigating the function of individual components as we've done here is an approach that will scale up to understanding how the cortex works at large. As a closing thought, I offer a section from **Cracking the function of cortical layers** (see also Chapter 1) which provides a prospective view on the study of the cortex. [2]

Adesnik, H., Naka. A., (2018) Cracking the function of cortical layers. *In preparation*

A holistic attack on cortical layer function

Why has the extensive physiological data collected over the last few decades provided few concrete examples of new transformations that occur across layers? This absence is problematic since it has precluded the generation and validation of hypotheses concerning the differential roles of layers in sensory computation. We can consider several explanations: first, higher order feature selectivity might not emerge across layers within a single area, and only across cortical areas; second, physiologists have, until recently, lacked the proper tools to observe these higher order features; third, most measurements have been made in too impoverished conditions; or fourth, data have been analyzed in the wrong conceptual framework.

All of these issues, at least in part, have likely hindered progress towards a fuller understanding of cortical layers and cortical computation in general. Although it is difficult to argue from an absence of evidence, from the synthetic, hierarchical perspective it appears that major new transformations primarily emerge across cortical areas and not between layers of any individual layer.

[2] I note that this review is nominally devoted to studying layers, as opposed to pathways between layers (the main topic of this document). To me, this is a distinction without a difference; equivalent to asking if one should study a network by examining its nodes or examining its edges. Regardless, I believe that the thoughts contained within apply equally well to either framework.

Translaminar and recurrent circuits instead mediate various forms of linear and non-linear gain control that shape individual neuronal response properties, but do not necessarily generate entirely new ones. However, at the population level, and specifically for rich (i.e., naturalistic) stimuli, one can presume that there are yet to be discovered transformations across layers that change how neural ensembles encode the external world. These transformations have so far eluded observation because most physiological data has been collected on too few neurons at a time, to overly simple stimuli, and often in non-physiological conditions (e.g., under anesthesia or in the absence of explicit behavioral demands that require the neurons under study). By the same token, data analyzed from the pure synthetic perspective, rather than from view of cortical networks as operating through statistical inference or predictive coding, has also led to an impoverished view of the new transformations that are implemented across layers. This is not because investigators were unaware of these different viewpoints, but rather, because of technical difficulty in recording enough neurons simultaneously in behaviorally relevant contexts. Finally, the limited tools available for perturbing the activity of individual cortical layers with high specificity has prevented cortical physiologists from directly revealing their roles in generating novel responses properties or helping to construct generative models of the external world.

Taken together, the insight gained from the perturbations of cortical layers has led to a much more complex picture of the contributions of cortical lamina than what might be predicted from a simple understanding of the 'canonical' cortical microcircuit. While this may not be surprising given the over-simplified nature of this idealized circuit, the problem is that the existing approaches have yet to lead to a coherent picture for how different layers contribute to sensory computation. One possible explanation for this seeming complexity, albeit equally unsatisfying, is that these studies have been conducted under a variety of conditions, in different species, and with various tools, and have therefore yielded conflicting or ambiguous results. Yet even if these studies were all reproduced in the same species, brain state, and brain area, it is not even clear that they would lead to a more consistent picture. As proposed above, different layers (and even specific cell types within each layer) might selectively and independently contribute to certain computations, sensorimotor behaviors, or specific motivated brain states. However, even if this is the case, it is not guaranteed it will be possible to identify or satisfactorily understand these computations using standard methods for cell-type specific perturbations. Indeed, the lack of explanatory power of the canonical model suggests that cortical circuits cannot be approximated as feedforward architectures, probably due to the very high level of recurrence between cortical areas. Theoretically, highly recurrent networks can be dissected via simultaneous manipulations of multiple components, but even in very simple cases this is extremely challenging due to the combinatorial explosion of perturbations that might need to be performed (Kumar et al., 2013). Given this potential complexity, how can we obtain a more definitive view of the function of cortical layers?

The answer lies in abstraction: cortical scientists must strive to identify modules in cortical circuitry that might serve as building blocks in the bigger picture of how cortical computation is implemented (Koch, 2012). This is no simple task. It is clear that focused, small scale recording/manipulation of cortical populations will not be sufficient to achieve this goal. Mechanistically, the activity of any cortical neuron is fundamentally determined by the firings of other neurons, but these neurons number in the thousands and are widely distributed throughout the entire brain. By the same token, the effects of any neuron's synaptic outputs are incredibly widely distributed. Furthermore, understanding how synaptic input/output functionality relates to computation requires observing how neuronal activity relates to external covariates such as sensory stimuli and behavior. Furthermore, in the likely scenario that ensembles of neurons can be abstractly understood as computational modules, their function might only become apparent if large (and potentially distributed) populations are simultaneously observed.

The grand challenge of understanding cortical function calls for a holistic approach to monitoring and manipulating activity along the cortical axis. Rarely does one have enough *a priori* knowledge for the specific path afferent input will take under a specific condition such that that focused, small scale recording will be sufficient. Furthermore, key types of transformations might only become apparent at the population level, and across neurons that are not necessarily contiguous (Ma et al., 2006a; Pouget et al., 2000; Wohrer et al., 2013). Thus, the appropriate holistic approaches includes recording densely across all layers; identifying the cell types of the recorded cells within this volume; recording neural activity simultaneously in input and output areas (e.g., thalamus, secondary sensory areas, relevant motor cortices); and perturbing individual layers and cell types with high spatial and temporal precision. Applying this approach comparatively across different cortical areas and species will help reveal the circuit elements that are conserved in different cortical systems, which will be instrumental in identifying simplifying motifs. Whether one considers cortical computation from the synthetic or inferential vantage point, such an all-inclusive experimental approach can provide the comprehensive data needed to determine whether cortical circuits implement canonical computations, and if so, how specific layers and cell types contribute to specific computations or behaviors.

While we have focused on how the above approach would apply to sensory transformations, a holistic attack on cortical layer function will also require a holistic perspective on how cortical layers and cell types contribute to behavior, including perceptual learning, decision-making, and motor control. In primary motor cortex, a subtle but important conceptual advance has been to ask how cortical dynamics serve to robustly generate/execute movements, as opposed to asking how these populations might encode representations of movement parameters (Churchland et al., 2012; Gallego et al., 2017; Shenoy et al., 2013). By the same token, in the sensory cortex, it may be fruitful to shift the focus from asking how sensory information is represented and transformed *per se* and instead ask how sensory cortices and their component layers and cell types serve the broader function of allowing an animal to flexibly adapt its behavior to changing environmental conditions in its environment.

This is not a new proposal, but more widespread adoption of this approach might be ushered in by mounting evidence that the functional segregation of cortical areas is fuzzy at best. Instead, all cortical circuits appear to 'wear many hats.' For example, even primary sensory cortices appear to process heteromodal sensory input (Ibrahim et al., 2016; Iurilli et al., 2012), encode behavior/movement related information (Ayaz et al., 2013; Crochet and Petersen, 2006; Dipoppa et al., 2018; Reimer et al., 2014; Shimaoka et al., 2018; Stringer et al., 2018; Vinck et al., 2015; Zagha et al., 2013), and directly contribute to motor control (Liang et al., 2015; Liu et al., 2016a; Matyas et al., 2010). Accordingly, investigating the function of microcircuits in primary sensory cortex function by asking how they contribute to sensory transformations is unlikely to yield a full understanding of cortical computation. If there exists a canonical cortical microcircuit, then understanding its corresponding 'canonical computation' will likely require investigating how the circuit operates in its normal milieu: as a very small part that is subsumed by a much larger architecture. While the corticothalamic network at large is hierarchically organized (D'Souza and Burkhalter, 2017; Markov et al., 2013), it is also massively recurrent (Gămănuţ et al., 2018) and fundamentally sensorimotor. It may well be the case that the computational principles of cortical microcircuits will only be comprehensible in the context of naturalistic, sensorimotor behaviors (Juavinett et al., 2018; Krakauer et al., 2017).

Bibliography

Adesnik, H. (2017). Synaptic Mechanisms of Feature Coding in the Visual Cortex of Awake Mice. Neuron *95*, 1147–1159.e4.

Adesnik, H. (2018). Layer-specific excitation/inhibition balances during neuronal synchronization in the visual cortex. J. Physiol. *0*, 1–19.

Adesnik, H., and Scanziani, M. (2010). Lateral competition for cortical space by layer-specific horizontal circuits. Nature *464*, 1155–1160.

Adesnik, H., Bruns, W., Taniguchi, H., Huang, Z.J., and Scanziani, M. (2012). A neural circuit for spatial summation in visual cortex. Nature *490*, 226–231.

Agmon, A., and Connors, B.W. (1989). Repetitive burst-firing neurons in the deep layers of mouse somatosensory cortex. Neurosci. Lett. *99*, 137–141.

Agmon, A., and Connors, B.W. (1992). Correlation between intrinsic firing patterns and thalamocortical synaptic responses of neurons in mouse barrel cortex. J. Neurosci. *12*, 319–329.

Alonso, J.M., and Martinez, L.M. (1998). Functional connectivity between simple cells and complex cells in cat striate cortex. Nat. Neurosci. *1*, 395–403.

Amarasingham, A., Harrison, M.T., Hatsopoulos, N.G., and Geman, S. (2012). Conditional modeling and the jitter method of spike resampling. J. Neurophysiol. *107*, 517–531.

Anastasiades, P.G., Marques-Smith, A., Lyngholm, D., Lickiss, T., Raffiq, S., Kätzel, D., Miesenböck, G., and Butt, S.J.B. (2016). GABAergic interneurons form transient layer-specific circuits in early postnatal neocortex. Nat. Commun. *7*, 10584.

Andermann, M.L., Gilfoy, N.B., Goldey, G.J., Sachdev, R.N.S., Wölfel, M., McCormick, D.A., Reid, R.C., and Levene, M.J. (2013). Chronic Cellular Imaging of Entire Cortical Columns in Awake Mice Using Microprisms. Neuron *80*, 900–913.

Angelucci, A., and Bressloff, P.C. (2006). Contribution of feedforward, lateral and feedback connections to the classical receptive field center and extra-classical receptive field surround of primate V1 neurons. Prog. Brain Res. *154*, 93–120.

Angulo, M.C., Staiger, J.F., Rossier, J., and Audinat, E. (2003). Distinct local circuits between neocortical pyramidal cells and fast-spiking interneurons in young adult rats. J. Neurophysiol. *89*, 943–953.

Apicella, A.J., Wickersham, I.R., Seung, H.S., and Shepherd, G.M.G. (2012). Laminarly orthogonal excitation of fast-spiking and low-threshold-spiking interneurons in mouse motor cortex. J. Neurosci. *32*, 7021–7033.

Armañanzas, R., and Ascoli, G.A. (2015). Towards the automatic classification of neurons. Trends Neurosci. *38*, 307–318.

Armstrong-James, M., Fox, K., and Das-Gupta, A. (1992). Flow of excitation within rat barrel cortex on striking a single vibrissa. J. Neurophysiol. *68*, 1345–1358.

Aronoff, R., Matyas, F., Mateo, C., Ciron, C., Schneider, B., and Petersen, C.C.H. (2010). Long-range connectivity of mouse primary somatosensory barrel cortex. Eur. J. Neurosci. *31*, 2221–2233.

Ascoli, G.A., Alonso-Nanclares, L., Anderson, S.A., Barrionuevo, G., Benavides-Piccione, R., Burkhalter, A., Buzsáki, G., Cauli, B., Defelipe, J., Fairén, A., et al. (2008). Petilla terminology: nomenclature of features of GABAergic interneurons of the cerebral cortex. Nat. Rev. Neurosci. *9*, 557–568.

Atallah, B. V, Bruns, W., Carandini, M., and Scanziani, M. (2012). Parvalbumin-expressing interneurons linearly transform cortical responses to visual stimuli. Neuron *73*, 159–170.

Atasoy, D., Aponte, Y., Su, H.H., and Sternson, S.M. (2008). A FLEX Switch Targets Channelrhodopsin-2 to Multiple Cell Types for Imaging and Long-Range Circuit Mapping. J. Neurosci. *28*, 7025–7030.

Atencio, C.A., Sharpee, T., and Schreiner, C.E. (2009). Hierarchical computation in the canonical auditory cortical circuit. Proc. Natl. Acad. Sci. *106*, 21894–21899.

Ayaz, A., Saleem, A.B., Schölvinck, M.L., and Carandini, M. (2013). Locomotion Controls Spatial Integration in Mouse Visual Cortex. Curr. Biol. 890–894.

Bair, W., Cavanaugh, J.R., and Movshon, J.A. (2003). Time course and time-distance relationships for surround suppression in macaque V1 neurons. J. Neurosci. *23*, 7690–7701.

Baker, C.A., Elyada, Y.M., Parra-Martin, A., and Bolton, M. (2016). Cellular resolution circuit mapping in mouse brain with temporal-focused excitation of soma-targeted channelrhodopsin. Elife *5*, 1–15.

Barretto, R.P.J., Messerschmidt, B., and Schnitzer, M.J. (2009). In vivo fluorescence imaging with high-resolution microlenses. Nat. Methods *6*, 511–512.

Barth, A.L., and Poulet, J.F.A. (2012). Experimental evidence for sparse firing in the neocortex. Trends Neurosci. *35*, 345–355.

Bastos, A.M., Usrey, W.M., Adams, R. a, Mangun, G.R., Fries, P., and Friston, K.J. (2012). Canonical microcircuits for predictive coding. Neuron *76*, 695–711.

Bastos, A.M., Vezoli, J., Bosman, C.A., Schoffelen, J.M., Oostenveld, R., Dowdall, J.R., DeWeerd, P., Kennedy, H., and Fries, P. (2015). Visual areas exert feedforward and feedback influences through distinct frequency channels. Neuron *85*, 390–401.

Le Bé, J.-V., Silberberg, G., Wang, Y., and Markram, H. (2007). Morphological, electrophysiological, and synaptic properties of corticocallosal pyramidal cells in the neonatal rat neocortex. Cereb. Cortex *17*, 2204–2213.

Beierlein, M., and Connors, B.W. (2002). Short-term dynamics of thalamocortical and intracortical synapses onto layer 6 neurons in neocortex. J. Neurophysiol. *88*, 1924–1932.

Beierlein, M., Gibson, J.R., and Connors, B.W. (2000). A network of electrically coupled interneurons drives synchronized inhibition in neocortex. Nat. Neurosci. *3*, 904–910.

Beierlein, M., Gibson, J.R., and Connors, B.W. (2003). Two dynamically distinct inhibitory networks in layer 4 of the neocortex. J. Neurophysiol. *90*, 2987–3000.

Beltramo, R., D'Urso, G., Dal Maschio, M., Farisello, P., Bovetti, S., Clovis, Y., Lassi, G., Tucci, V., De Pietri Tonelli, D., and Fellin, T. (2013). Layer-specific excitatory circuits differentially control recurrent network dynamics in the neocortex. Nat. Neurosci. *16*, 227–234.

Benjamini, Y., and Hochberg, Y. (1995). Controlling the False Discovery Rate : A Practical and Powerful Approach to Multiple Testing Author (s): Yoav Benjamini and Yosef Hochberg Source : Journal of the Royal Statistical Society . Series B (Methodological), Vol . 57 , No . 1 Published by : J. R. Stat. Soc. *57*, 289–300.

Berger, T.K., Perin, R., Silberberg, G., and Markram, H. (2009). Frequency-dependent disynaptic inhibition in the pyramidal network: a ubiquitous pathway in the developing rat neocortex. J. Physiol. *587*, 5411–5425.

Berger, T.K., Silberberg, G., Perin, R., and Markram, H. (2010). Brief bursts self-inhibit and correlate the pyramidal network. PLoS Biol. *8*.

Binzegger, T. (2004). A Quantitative Map of the Circuit of Cat Primary Visual Cortex. J. Neurosci. *24*, 8441–8453.

Blazquez-Llorca, L., Woodruff, A., Inan, M., Anderson, S.A., Yuste, R., DeFelipe, J., and Merchan-Perez, A. (2014). Spatial distribution of neurons innervated by chandelier cells. Brain Struct. Funct. *220*, 2817–2834.

Bloss, E.B., Cembrowski, M.S., Karsh, B., Colonell, J., Fetter, R.D., and Spruston, N. (2016). Structured Dendritic Inhibition Supports Branch-Selective Integration in CA1 Pyramidal Cells. Neuron *89*, 1–15.

Bock, D.D., Lee, W.-C.A., Kerlin, A.M., Andermann, M.L., Hood, G., Wetzel, A.W., Yurgenson, S., Soucy, E.R., Kim, H.S., and Reid, R.C. (2011). Network anatomy and in vivo physiology of visual cortical neurons. Nature *471*, 177–182.

Bolz, J., and Gilbert, C.D. (1986). Generation of end-inhibition in the visual cortex via interlaminar connections. Nature *320*, 362–365.

Bortone, D.S., Olsen, S.R., and Scanziani, M. (2014). Translaminar inhibitory cells recruited by layer 6 corticothalamic neurons suppress visual cortex. Neuron *82*, 474–485.

Bourassa, J., and Deschênes, M. (1995). Corticothalamic projections from the primary visual cortex in rats: a single fiber study using biocytin as an anterograde tracer. Neuroscience *66*, 253–263.

Bovetti, S., and Fellin, T. (2015). Optical dissection of brain circuits with patterned illumination through the phase modulation of light. J. Neurosci. Methods *241*, 66–77.

Brecht, M. (2017). The Body Model Theory of Somatosensory Cortex. Neuron *94*, 985–992.

Brecht, M., Roth, A., and Sakmann, B. (2003a). Dynamic receptive fields of reconstructed pyramidal cells in layers 3 and 2 of rat somatosensory barrel cortex. J. Physiol. *553*, 243–265.

Brecht, M., Roth, A., and Sakmann, B. (2003b). Dynamic receptive fields of reconstructed pyramidal cells in layers 3 and 2 of rat somatosensory barrel cortex. J. Physiol. *553*, 243–265.

Briggs, F. (2010). Organizing principles of cortical layer 6. Front. Neural Circuits *4*, 1–8.

Briggs, F., and Callaway, E.M. (2001). Layer-specific input to distinct cell types in layer 6 of monkey primary visual cortex. J. Neurosci. *21*, 3600–3608.

Briggs, F., and Usrey, W.M. (2008). Emerging views of corticothalamic function. Curr. Opin. Neurobiol. *18*, 403–407.

Brill, J., and Huguenard, J.R. (2010). Enhanced infragranular and supragranular synaptic input onto layer 5 pyramidal neurons in a rat model of cortical dysplasia. Cereb. Cortex *20*, 2926–2938.

Brill, J., Mattis, J., Deisseroth, K., and Huguenard, J.R. (2016). LSPS/Optogenetics to Improve Synaptic Connectivity Mapping: Unmasking the Role of Basket Cell Mediated Feed-Forward Inhibition. eNeuro *3*, ENEURO.0142-15.2016.

Brown, S.P., and Hestrin, S. (2009). Intracortical circuits of pyramidal neurons reflect their long-range axonal targets. Nature *457*, 1133–1136.

Bruce, C., Desimone, R., and Gross, C.G. (1981). Visual properties of neurons in a polysensory area in superior temporal sulcus of the macaque. J. Neurophysiol. *46*, 369–384.

Brumberg, J.C., Pinto, D.J., and Simons, D.J. (1996). Spatial gradients and inhibitory summation in the rat whisker barrel system. J. Neurophysiol. *76*, 130–140.

Brunet, N., Bosman, C.A., Roberts, M., Oostenveld, R., Womelsdorf, T., De Weerd, P., and Fries, P. (2015). Visual cortical gamma-band activity during free viewing of natural images. Cereb. Cortex *25*, 918–926.

Bruno, R.M. (2011). Synchrony in sensation. Curr. Opin. Neurobiol. *21*, 701–708.

Bruno, R.M., and Simons, D.J. (2002). Feedforward mechanisms of excitatory and inhibitory cortical receptive fields. J Neurosci *22*, 10966–10975.

Buchanan, K.A., Blackman, A.V., Moreau, A.W., Elgar, D., Costa, R.P., Lalanne, T., Tudor Jones, A.A., Oyrer, J., and Sjöström, P.J. (2012a). Target-Specific Expression of Presynaptic NMDA Receptors in Neocortical Microcircuits. Neuron *75*, 451–466.

Buchanan, K.A., Blackman, A. V., Moreau, A.W., Elgar, D., Costa, R.P., Lalanne, T., Tudor Jones, A.A., Oyrer, J., and Sjöström, P.J. (2012b). Target-Specific Expression of Presynaptic NMDA Receptors in Neocortical Microcircuits. Neuron *75*, 451–466.

Callaway, E.M. (1998). Local circuits in primary visual cortex of the macaque monkey. Annu. Rev. Neurosci. *21*, 47–74.

Carandini, M., and Heeger, D. (2012). Normalization as a canonical neural computation. Nat. Rev. Neurosci. 1–12.

Cauller, L.J., and Connors, B.W. (1994). Synaptic physiology of horizontal afferents to layer I in slices of rat SI neocortex. J. Neurosci. *14*, 751–762.

Cauller, L.J., Clancy, B., and Connors, B.W. (1998). Backward cortical projections to primary somatosensory cortex in rats extend long horizontal axons in layer I. J. Comp. Neurol. *390*, 297–310.

Chagnac-Amitai, Y., Luhmann, H.J., and Prince, D. a. (1990). Burst generating and regular spiking layer 5 pyramidal neurons of rat neocortex have different morphological features. J. Comp. Neurol. *296*, 598–613.

Chakrabarti, S., and Alloway, K.D. (2006). Differential origin of projections from SI barrel cortex to the whisker representations in SII and MI. J. Comp. Neurol. *498*, 624–636.

Chen, G., Zhang, Y., Li, X., Zhao, X., Ye, Q., Lin, Y., Tao, H.W., Rasch, M.J., and Zhang, X. (2017). Distinct Inhibitory Circuits Orchestrate Cortical beta and gamma Band Oscillations. Neuron *96*, 1403–1418.e6.

Chen, J.L., Carta, S., Soldado-Magraner, J., Schneider, B.L., and Helmchen, F. (2013). Behaviour-dependent recruitment of long-range projection neurons in somatosensory cortex. Nature *499*, 336–340.

Chen, N., Sugihara, H., and Sur, M. (2015). An acetylcholine-activated microcircuit drives temporal dynamics of cortical activity. Nat. Neurosci. *18*, 892–902.

Chisum, H.J., and Fitzpatrick, D. (2004). The contribution of vertical and horizontal connections to the receptive field center and surround in V1. Neural Networks *17*, 681–693.

Chiu, C.Q., Lur, G., Morse, T.M., Carnevale, N.T., Ellis-Davies, G.C.R., and Higley, M.J. (2013). Compartmentalization of GABAergic inhibition by dendritic spines. Science *340*, 759–762.

Churchland, M.M., Cunningham, J.P., Kaufman, M.T., Foster, J.D., Nuyujukian, P., Ryu, S.I., Shenoy, K. V., and Shenoy, K. V. (2012). Neural population dynamics during reaching. Nature *487*, 51–56.

Cichon, J., and Gan, W.-B. (2015). Branch-specific dendritic Ca2+ spikes cause persistent synaptic plasticity. Nature *520*, 180–185.

Clack, N.G., O'Connor, D.H., Huber, D., Petreanu, L., Hires, A., Peron, S., Svoboda, K., and Myers, E.W. (2012). Automated tracking of whiskers in videos of head fixed rodents. PLoS Comput. Biol. *8*.

Clancy, K.B., Schnepel, P., Rao, A.T., and Feldman, D.E. (2015). Structure of a single whisker representation in layer 2 of mouse somatosensory cortex. J. Neurosci. *35*, 3946–3958.

Cobas, a, Welker, E., Fairén, a, Kraftsik, R., and Van der Loos, H. (1987). GABAergic neurons in the barrel cortex of the mouse: an analysis using neuronal archetypes. J. Neurocytol. *16*, 843–870.

Constantinople, C.M., and Bruno, R.M. (2013). Deep cortical layers are activated directly by thalamus. Science *340*, 1591–1594.

Cottam, J.C.H., Smith, S.L., and Häusser, M. (2013). Target-specific effects of somatostatin-expressing interneurons on neocortical visual processing. J. Neurosci. *33*, 19567–19578.

Crandall, S.R., Cruikshank, S.J., and Connors, B.W. (2015). A Corticothalamic Switch: Controlling the Thalamus with Dynamic Synapses. Neuron *86*, 768–782.

Crandall, S.R., Patrick, S.L., Cruikshank, S.J., and Connors, B.W. (2017). Infrabarrels Are Layer 6 Circuit Modules in the Barrel Cortex that Link Long-Range Inputs and Outputs. Cell Rep. *21*, 3065–3078.

Crochet, S., and Petersen, C.C.H. (2006). Correlating whisker behavior with membrane potential in barrel cortex of awake mice. Nat. Neurosci. *9*, 608–610.

Crochet, S., Poulet, J.F. a, Kremer, Y., and Petersen, C.C.H. (2011). Synaptic mechanisms underlying sparse coding of active touch. Neuron *69*, 1160–1175.

Cruikshank, S.J., Lewis, T.J., and Connors, B.W. (2007). Synaptic basis for intense thalamocortical activation of feedforward inhibitory cells in neocortex. Nat. Neurosci. *10*, 462–468.

Cruikshank, S.J., Urabe, H., Nurmikko, A. V, and Connors, B.W. (2010). Pathway-Specific Feedforward Circuits between Thalamus and Neocortex Revealed by Selective Optical Stimulation of Axons. Neuron *65*, 230–245.

Curtis, J.C., and Kleinfeld, D. (2009). Phase-to-rate transformations encode touch in cortical neurons of a scanning sensorimotor system. Nat. Neurosci. *12*, 492–501.

D'Souza, R.D., and Burkhalter, A. (2017). A Laminar Organization for Selective Cortico-Cortical Communication. Front. Neuroanat. *11*.

Dávid, C., Schleicher, A., Zuschratter, W., and Staiger, J.F. (2007). The innervation of parvalbumin-containing interneurons by VIP-immunopositive interneurons in the primary somatosensory cortex of the adult rat. Eur. J. Neurosci. *25*, 2329–2340.

Daw, M.I., Ashby, M.C., and Isaac, J.T.R. (2007). Coordinated developmental recruitment of latent fast spiking interneurons in layer IV barrel cortex. Nat. Neurosci. *10*, 453–461.

DeFelipe, J., López-Cruz, P.L., Benavides-Piccione, R., Bielza, C., Larrañaga, P., Anderson, S., Burkhalter, A., Cauli, B., Fairén, A., Feldmeyer, D., et al. (2013). New insights into the classification and nomenclature of cortical GABAergic interneurons. Nat. Rev. Neurosci. *14*, 202–216.

Denardo, L.A., Berns, D.S., Deloach, K., and Luo, L. (2015). Connectivity of mouse somatosensory and prefrontal cortex examined with trans-synaptic tracing. Nat. Neurosci. *18*, 1687–1697.

DeNardo, L.A., Berns, D.S., DeLoach, K., and Luo, L. (2015). Connectivity of mouse somatosensory and prefrontal cortex examined with trans-synaptic tracing. Nat. Neurosci. 1–13.

Denman, D.J., and Contreras, D. (2015). Complex Effects on In Vivo Visual Responses by Specific Projections from Mouse Cortical Layer 6 to Dorsal Lateral Geniculate Nucleus. J. Neurosci. *35*, 9265–9280.

Diamond, M.E., Von Heimendahl, M., Knutsen, P.M., Kleinfeld, D., and Ahissar, E. (2008). "Where" and "what" in the whisker sensorimotor system. Nat. Rev. Neurosci. *9*, 601–612.

Dipoppa, M., Ranson, A., Krumin, M., Pachitariu, M., Carandini, M., and Harris, K.D. (2018). Vision and Locomotion Shape the Interactions between Neuron Types in Mouse Visual Cortex. Neuron 1–14.

Douglas, R.J., and Martin, K.A.C. (2004). Neuronal Circuits of the Neocortex. Annu. Rev. Neurosci. *27*, 419–451.

Douglas, R.J., Martin, K. a. C., and Whitteridge, D. (1989). A Canonical Microcircuit for Neocortex. Neural Comput *1*, 480–488.

Elstrott, J., Clancy, K.B., Jafri, H., Akimenko, I., and Feldman, D.E. (2014). Cellular mechanisms for response heterogeneity among L2/3 pyramidal cells in whisker somatosensory cortex. J. Neurophysiol. *112*, 233–248.

Erişir, A., Van Horn, S.C., and Sherman, S.M. (1997). Relative numbers of cortical and brainstem inputs to the lateral geniculate nucleus. Proc. Natl. Acad. Sci. U. S. A. *94*, 1517–1520.

Fairén, A. (2007). Cajal and Lorente de Nó on cortical interneurons: Coincidences and progress. Brain Res. Rev. *55*,

430–444.

Fairén, A., Cobas, A., and Fonseca, M. (1986). Times of generation of glutamic acid decarboxylase immunoreactive neurons in mouse somatosensory cortex. J. Comp. Neurol. *251*, 67–83.

Fanselow, E.E., and Nicolelis, M.A. (1999). Behavioral modulation of tactile responses in the rat somatosensory system. J. Neurosci. *19*, 7603–7616.

Fanselow, E.E., Richardson, K.A., and Connors, B.W. (2008). Selective , State-Dependent Activation of Somatostatin-Expressing Inhibitory Interneurons in Mouse Neocortex. J. Neurophysiol. *100*, 2640–2652.

Fariñas, I., and DeFelipe, J. (1991). Patterns of synaptic input on corticocortical and corticothalamic cells in the cat visual cortex. II. The axon initial segment. J. Comp. Neurol. *304*, 70–77.

Favorov, O. V., and Kursun, O. (2011). Neocortical layer 4 as a pluripotent function linearizer. J. Neurophysiol. *105*, 1342–1360.

Feldmeyer, D. (2012). Excitatory neuronal connectivity in the barrel cortex. Front. Neuroanat. *6*, 24.

Feldmeyer, D., and Sakmann, B. (2000). Synaptic efficacy and reliability of excitatory connections between the principal neurones of the input (layer 4) and output layer (layer 5) of the neocortex. J. Physiol. *525*, 31–39.

Feldmeyer, D., Roth, A., and Sakmann, B. (2005). Monosynaptic connections between pairs of spiny stellate cells in layer 4 and pyramidal cells in layer 5A indicate that lemniscal and paralemniscal afferent pathways converge in the infragranular somatosensory cortex. J. Neurosci. *25*, 3423–3431.

Ferster, D., Chung, S., and Wheat, H. (1996). Orientation selectivity of thalamic input to simple cells of cat visual cortex. Nature *380*, 249–252.

Fino, E., and Yuste, R. (2011). Dense inhibitory connectivity in neocortex. Neuron *69*, 1188–1203.

Fino, E., Packer, A.M., and Yuste, R. (2013). The logic of inhibitory connectivity in the neocortex. Neuroscientist *19*, 228–237.

Fox, K., Wright, N., Wallace, H., and Glazewski, S. (2003). The origin of cortical surround receptive fields studied in the barrel cortex. J. Neurosci. *23*, 8380–8391.

Frick, A., Feldmeyer, D., Helmstaedter, M., and Sakmann, B. (2008). Monosynaptic connections between pairs of L5A pyramidal neurons in columns of juvenile rat somatosensory cortex. Cereb. Cortex *18*, 397–406.

Froudarakis, E., Berens, P., Ecker, A.S., Cotton, R.J., Sinz, F.H., Yatsenko, D., Saggau, P., Bethge, M., and Tolias, A.S. (2014). Population code in mouse V1 facilitates readout of natural scenes through increased sparseness. Nat. Neurosci. *17*, 851–857.

Fu, Y., Tucciarone, J.M., Espinosa, J.S., Sheng, N., Darcy, D.P., Nicoll, R. a., Huang, Z.J., and Stryker, M.P. (2014). A cortical circuit for gain control by behavioral state. Cell *156*, 1139–1152.

Fukushima, K. (1980). Neocognitron: A self-organizing neural network model for a mechanism of pattern recognition unaffected by shift in position. Biol. Cybern. *36*, 193–202.

Gabernet, L., Jadhav, S.P., Feldman, D.E., Carandini, M., and Scanziani, M. (2005a). Somatosensory integration controlled by dynamic thalamocortical feed-forward inhibition. Neuron *48*, 315–327.

Gabernet, L., Jadhav, S.P., Feldman, D.E., Carandini, M., and Scanziani, M. (2005b). Somatosensory integration controlled by dynamic thalamocortical feed-forward inhibition. Neuron *48*, 315–327.

Galarreta, M., and Hestrin, S. (1998). Frequency-dependent synaptic depression and the balance of excitation and inhibition in the neocortex. Nat. Neurosci. *1*, 587–594.

Galarreta, M., and Hestrin, S. (1999). A network of fast-spiking cells in the neocortex connected by electrical synapses. Nature *402*, 72–75.

Galarreta, M., and Hestrin, S. (2002). Electrical and chemical synapses among parvalbumin fast-spiking GABAergic interneurons in adult mouse neocortex. Proc. Natl. Acad. Sci. U. S. A. *99*, 12438–12443.

Gallego, J.A., Perich, M.G., Miller, L.E., and Solla, S.A. (2017). Neural Manifolds for the Control of Movement. Neuron *94*, 978–984.

Gămănuţ, R., Kennedy, H., Toroczkai, Z., Ercsey-Ravasz, M., Van Essen, D.C., Knoblauch, K., and Burkhalter, A. (2018). The Mouse Cortical Connectome, Characterized by an Ultra-Dense Cortical Graph, Maintains Specificity by Distinct Connectivity Profiles. Neuron *97*, 698–715.e10.

Ganguli, S., and Sompolinsky, H. (2012). Compressed Sensing, Sparsity, and Dimensionality in Neuronal Information Processing and Data Analysis. Annu. Rev. Neurosci. *35*, 485–508.

Gentet, L.J. (2012). Functional diversity of supragranular GABAergic neurons in the barrel cortex. Front. Neural Circuits *6*, 1–13.

Gentet, L.J., Kremer, Y., Taniguchi, H., Huang, Z.J., Staiger, J.F., and Petersen, C.C.H. (2012). Unique functional properties of somatostatin-expressing GABAergic neurons in mouse barrel cortex. Nat. Neurosci. *15*, 607–612.

Gibson, J.R., Beierlein, M., and Connors, B.W. (1999). Two networks of electrically coupled inhibitory neurons in neocortex. Nature *402*, 75–79.

Gibson, J.R., Beierlein, M., and Connors, B.W. (2005). Functional Properties of Electrical Synapses Between Inhibitory Interneurons of Neocortical Layer 4. J Neurophysiol *93*, 467–480.

Gieselmann, M.A., and Thiele, A. (2008). Comparison of spatial integration and surround suppression characteristics in spiking activity and the local field potential in macaque V1. Eur. J. Neurosci. *28*, 447–459.

Gilbert, C.D., and Kelly, J.P. (1975). The projections of cells in different layers of the cat's visual cortex. J. Comp. Neurol. *163*, 81–105.

Glickfeld, L.L., Roberts, J.D., Somogyi, P., and Scanziani, M. (2009). Interneurons hyperpolarize pyramidal cells along their entire somatodendritic axis. Nat. Neurosci. *12*, 21–23.

Gonchar, Y. (2008). Multiple distinct subtypes of GABAergic neurons in mouse visual cortex identified by triple immunostaining. Front. Neuroanat. *1*.

Gong, S., Doughty, M., Harbaugh, C.R., Cummins, A., Hatten, M.E., Heintz, N., and Gerfen, C.R. (2007). Targeting Cre Recombinase to Specific Neuron Populations with Bacterial Artificial Chromosome Constructs. J. Neurosci. *27*, 9817–9823.

Gong, Y., Huang, C., Li, J.Z., Grewe, B.F., Zhang, Y., Eismann, S., and Schnitzer, M.J. (2015). High-speed recording of neural spikes in awake mice and flies with a fluorescent voltage sensor. Science *350*, 1361–1366.

Gorski, J. a, Talley, T., Qiu, M., Puelles, L., Rubenstein, J.L.R., and Jones, K.R. (2002). Cortical excitatory neurons and glia, but not GABAergic neurons, are produced in the Emx1-expressing lineage. J. Neurosci. *22*, 6309–6314.

Gradinaru, V., Zhang, F., Ramakrishnan, C., Mattis, J., Prakash, R., Diester, I., Goshen, I., Thompson, K.R., and Deisseroth, K. (2010). Molecular and Cellular Approaches for Diversifying and Extending Optogenetics. Cell *141*, 154–165.

Gray, C.M. (1999). The temporal correlation hypothesis of visual feature integration: Still alive and well. Neuron *24*, 31–47.

Gray, C.M., König, P., Engel, A.K., and Singer, W. (1989). Oscillatory responses in cat visual cortex exhibit inter-columnar synchronization which reflects global stimulus properties. Nature *338*, 334–337.

Greenhill, S.D., Ranson, A., and Fox, K. (2015). Hebbian and Homeostatic Plasticity Mechanisms in Regular Spiking and Intrinsic Bursting Cells of Cortical Layer 5. Neuron *88*, 539–552.

Grewe (2010). Back-propagation of physiological action potential output in dendrites of slender-tufted L5A pyramidal neurons. Front. Cell. Neurosci. *4*, 1–11.

Grieve, K.L., and Sillito, A.M. (1991). A re-appraisal of the role of layer VI of the visual cortex in the generation of cortical end inhibition. Exp. Brain Res. *87*, 521–529.

Groh, A., Meyer, H.S., Schmidt, E.F., Heintz, N., Sakmann, B., and Krieger, P. (2010). Cell-type specific properties of pyramidal neurons in neocortex underlying a layout that is modifiable depending on the cortical area. Cereb. Cortex *20*, 826–836.

Grosenick, L., Marshel, J.H., and Deisseroth, K. (2015). Closed-loop and activity-guided optogenetic control. Neuron *86*, 106–139.

Gross, C.G., Rocha-Miranda, C.E., and Bender, D.B. (1972). Visual properties of neurons in inferotemporal cortex of the Macaque. J. Neurophysiol. *35*, 96–111.

Gupta, A., Wang, Y., Markram, H., Thomson, A.M., Deuchars, J., Kawaguchi, Y., Kubota, Y., DeFelipe, J., Cauli, B., Connors, B.W., et al. (2000). Organizing principles for a diversity of GABAergic interneurons and synapses in the neocortex. Science *287*, 273–278.

Haider, B., Häusser, M., and Carandini, M. (2013). Inhibition dominates sensory responses in the awake cortex. Nature *493*, 97–102.

Halabisky, B., Shen, F., Huguenard, J.R., and Prince, D.A. (2006). Electrophysiological classification of somatostatin-positive interneurons in mouse sensorimotor cortex. J. Neurophysiol. *96*, 834–845.

Harris, K.D. (2013). Top-down control of cortical state. Neuron *79*, 408–410.

Harris, K.D., and Mrsic-Flogel, T.D. (2013). Cortical connectivity and sensory coding. Nature *503*, 51–58.

Harris, K.D., and Shepherd, G.M.G. (2015). The neocortical circuit: themes and variations. Nat. Neurosci. *18*, 170–181.

Hassabis, D., Kumaran, D., Summerfield, C., and Botvinick, M. (2017). Neuroscience-Inspired Artificial Intelligence. Neuron *95*, 245–258.

Hasse, J.M., and Briggs, F. (2017). Corticogeniculate feedback sharpens the temporal precision and spatial resolution of visual signals in the ferret. Proc. Natl. Acad. Sci. 201704524.

Hattox, A.M., and Nelson, S.B. (2007). Layer V neurons in mouse cortex projecting to different targets have distinct physiological properties. J. Neurophysiol. *98*, 3330–3340.

He, M., Tucciarone, J., Lee, S., Nigro, M.J., Kim, Y., Levine, J.M., Kelly, S.M., Krugikov, I., Wu, P., Chen, Y., et al. (2016). Strategies and tools for combinatorial targeting of GABAergic neurons in mouse cerebral cortex. Neuron 1–16.

Helmstaedter, M., Staiger, J.F., Sakmann, B., and Feldmeyer, D. (2008). Efficient recruitment of layer 2/3 interneurons by layer 4 input in single columns of rat somatosensory cortex. J. Neurosci. *28*, 8273–8284.

Helmstaedter, M., Sakmann, B., and Feldmeyer, D. (2009a). Neuronal Correlates of Local, Lateral, and Translaminar Inhibition with Reference to Cortical Columns. Cereb. Cortex *19*, 926–937.

Helmstaedter, M., Sakmann, B., and Feldmeyer, D. (2009b). L2/3 interneuron groups defined by multiparameter analysis of axonal projection, dendritic geometry, and electrical excitability. Cereb. Cortex *19*, 951–962.

Helmstaedter, M., Sakmann, B., and Feldmeyer, D. (2009c). The relation between dendritic geometry, electrical excitability, and axonal projections of L2/3 interneurons in rat barrel cortex. Cereb. Cortex *19*, 938–950.

Hermes, D., Miller, K.J., Wandell, B.A., and Winawer, J. (2015). Stimulus dependence of gamma oscillations in human visual cortex. Cereb. Cortex *25*, 2951–2959.

Hestrin, S., and Galarreta, M. (2005). Electrical synapses define networks of neocortical GABAergic neurons. Trends Neurosci. *28*, 304–309.

Hill, D.N., Mehta, S.B., and Kleinfeld, D. (2011). Quality Metrics to Accompany Spike Sorting of Extracellular Signals. J. Neurosci. *31*, 8699–8705.

Hilscher, M.M., Le, R.N., Edwards, S.J., Le, K.E., and Kullander, K. (2016). Chrna2-Martinotti Cells Synchronize layer 5 type A Pyramidal Cells via Rebound Excitation. 1–26.

Hioki, H., Okamoto, S., Konno, M., Kameda, H., Sohn, J., Kuramoto, E., Fujiyama, F., and Kaneko, T. (2013). Cell type-specific inhibitory inputs to dendritic and somatic compartments of parvalbumin-expressing neocortical interneuron. J. Neurosci. *33*, 544–555.

Hires, S.A., Gutnisky, D.A., Yu, J., O'Connor, D.H., Svoboda, K., Andrew Hires, S., Gutnisky, D.A., Yu, J., O'Connor, D.H., and Svoboda, K. (2015). Low-noise encoding of active touch by layer 4 in the somatosensory cortex. Elife *4*, e06619.

Hirsch, J. a., Alonso, J.-M., Reid, R.C., and Martinez, L.M. (1998). Synaptic Integration in Striate Cortical Simple Cells. J. Neurosci. *18*, 9517–9528.

Hofer, S.B., Ko, H., Pichler, B., Vogelstein, J., Ros, H., Zeng, H., Lein, E., Lesica, N.A., and Mrsic-Flogel, T.D. (2011). Differential connectivity and response dynamics of excitatory and inhibitory neurons in visual cortex. Nat. Neurosci. *14*, 1045–1052.

Hooks, B.M., Hires, S.A., Zhang, Y.X., Huber, D., Petreanu, L., Svoboda, K., and Shepherd, G.M.G. (2011). Laminar analysis of excitatory local circuits in vibrissal motor and sensory cortical areas. PLoS Biol. *9*.

Horton, N.G., Wang, K., Kobat, D., Clark, C.G., Wise, F.W., Schaffer, C.B., and Xu, C. (2013). In vivo three-photon microscopy of subcortical structures within an intact mouse brain. Nat. Photonics *7*, 205–209.

House, D.R.C., Elstrott, J., Koh, E., Chung, J., and Feldman, D.E. (2011). Parallel regulation of feedforward inhibition and excitation during whisker map plasticity. Neuron *72*, 819–831.

Hu, H., and Agmon, A. (2016). Differential Excitation of Distally versus Proximally Targeting Cortical Interneurons by Unitary Thalamocortical Bursts. J. Neurosci. *36*, 6906–6916.

Hu, H., Cavendish, J.Z., and Agmon, A. (2013). Not all that glitters is gold: off-target recombination in the somatostatin–IRES-Cre mouse line labels a subset of fast-spiking interneurons. Front. Neural Circuits *7*, 1–4.

Hu, H., Gan, J., and Jonas, P. (2014). Fast-spiking, parvalbumin+ GABAergic interneurons: From cellular design to microcircuit function. Science (80-.). *345*, 1255263–1255263.

Huang, Z.J. (2014). Toward a genetic dissection of cortical circuits in the mouse. Neuron *83*, 1284–1302.

Huang, Y.-L., Walker, A.S., and Miller, E.W. (2015). A Photostable Silicon Rhodamine Platform for Optical Voltage Sensing. J. Am. Chem. Soc. *2*, 150813160848005.

Hubel, D.H., and Wiesel, T.N. (1959). Receptive fields of single neurones in the cat's striate cortex. J. Physiol. *148*, 574–591.

Hubel, D.H., and Wiesel, T.N. (1962). Receptive fields, binocular interaction and functional architecture in the cat's visual cortex. J. Physiol. *160*, 106–154.

Hubel, D.H., and Wiesel, T.N. (1965). Receptive Fields and Functional Architecture in Two Nonstriate Visual Areas (18 and 19) of the Cat. J. Neurophysiol. *28*, 229–289.

Ibrahim, L.A., Mesik, L., Ji, X. ying, Fang, Q., Li, H. fu, Li, Y. tang, Zingg, B., Zhang, L.I., and Tao, H.W. (2016). Cross-Modality Sharpening of Visual Cortical Processing through Layer-1-Mediated Inhibition and Disinhibition. Neuron *89*, 1031–1045.

Inda, M.C., DeFelipe, J., and Muñoz, A. (2009). Morphology and distribution of chandelier cell axon terminals in the mouse cerebral cortex and claustroamygdaloid complex. Cereb. Cortex *19*, 41–54.

Inoue, M., Takeuchi, A., Horigane, S., Ohkura, M., Gengyo-Ando, K., Fujii, H., Kamijo, S., Takemoto-Kimura, S., Kano, M., Nakai, J., et al. (2014). Rational design of a high-affinity, fast, red calcium indicator R-CaMP2. Nat. Methods *12*, 64–70.

Isaacson, J.S., and Scanziani, M. (2011). How inhibition shapes cortical activity. Neuron *72*, 231–243.

Iurilli, G., Ghezzi, D., Olcese, U., Lassi, G., Nazzaro, C., Tonini, R., Tucci, V., Benfenati, F., and Medini, P. (2012). Sound-Driven Synaptic Inhibition in Primary Visual Cortex. Neuron *73*, 814–828.

Jacob, V., Petreanu, L., Wright, N., Svoboda, K., and Fox, K. (2012). Regular spiking and intrinsic bursting pyramidal cells show orthogonal forms of experience-dependent plasticity in layer V of barrel cortex. Neuron *73*, 391–404.

Jadhav, S.P., Wolfe, J., and Feldman, D.E. (2009). Sparse temporal coding of elementary tactile features during active whisker sensation. Nat. Neurosci. *12*, 792–800.

Ji, X. -y., Zingg, B., Mesik, L., Xiao, Z., Zhang, L.I., and Tao, H.W. (2015). Thalamocortical Innervation Pattern in Mouse Auditory and Visual Cortex: Laminar and Cell-Type Specificity. Cereb. Cortex bhv099-.

Ji, X.Y., Zingg, B., Mesik, L., Xiao, Z., Zhang, L.I., and Tao, H.W. (2016). Thalamocortical Innervation Pattern in Mouse Auditory and Visual Cortex: Laminar and Cell-Type Specificity. Cereb. Cortex *26*, 2612–2625.

Jiang, X., Wang, G., Lee, A.J., Stornetta, R.L., and Zhu, J.J. (2013). The organization of two new cortical interneuronal circuits. Nat. Neurosci. *16*, 210–218.

Jiang, X., Shen, S., Cadwell, C.R., Berens, P., Sinz, F., Ecker, A.S., Patel, S., and Tolias, A.S. (2015). Principles of connectivity among morphologically defined cell types in adult neocortex. Science (80-.). *350*, aac9462-aac9462.

Jin, X., Jiang, K., and Prince, D. a (2014). Excitatory and Inhibitory Synaptic Connectivity to Layer V Fast-spiking Interneurons in the Freeze Lesion Model of Cortical Microgyria. J. Neurophysiol. 1703–1713.

Juavinett, A.L., Erlich, J.C., and Churchland, A.K. (2018). Decision-making behaviors: weighing ethology, complexity, and sensorimotor compatibility. Curr. Opin. Neurobiol. *49*, 42–50.

Kampa, B.M., Letzkus, J.J., and Stuart, G.J. (2006). Cortical feed-forward networks for binding different streams of sensory information. Nat. Neurosci. *9*, 1472–1473.

Kapfer, C., Glickfeld, L.L., Atallah, B. V, and Scanziani, M. (2007). Supralinear increase of recurrent inhibition during sparse activity in the somatosensory cortex. Nat. Neurosci. *10*, 743–753.

Karayannis, T., Huerta-Ocampo, I., and Capogna, M. (2006). GABAergic and Pyramidal Neurons of Deep Cortical Layers Directly Receive and Differently Integrate Callosal Input. Cereb. Cortex *17*, 1213–1226.

Karnani, M.M., Agetsuma, M., and Yuste, R. (2014). A blanket of inhibition: functional inferences from dense inhibitory connectivity. Curr. Opin. Neurobiol. *26*, 96–102.

Karnani, M.M., Jackson, J., Ayzenshtat, I., Tucciarone, J., Manoocheri, K., Snider, W.G., and Yuste, R. (2016a). Cooperative Subnetworks of Molecularly Similar Interneurons in Mouse Neocortex. Neuron.

Karnani, M.M., Jackson, J., Ayzenshtat, I., Hamzehei Sichani, A., Manoocheri, K., Kim, S., and Yuste, R. (2016b). Opening Holes in the Blanket of Inhibition: Localized Lateral Disinhibition by VIP Interneurons. J. Neurosci. *36*, 3471–3480.

Karnani, M.M.M., Jackson, J., Ayzenshtat, I., Tucciarone, J., Manoocheri, K., Snider, W.G.G., and Yuste, R. (2016c). Cooperative Subnetworks of Molecularly Similar Interneurons in Mouse Neocortex. Neuron *90*, 86–100.

Kato, H.K., Gillet, S.N., and Isaacson, J.S. (2015). Flexible Sensory Representations in Auditory Cortex Driven by Behavioral Relevance. Neuron *88*, 1027–1039.

Katz, L.C. (1987). Local circuitry of identified projection neurons in cat visual cortex brain slices. J. Neurosci. *7*, 1223–1249.

Kätzel, D., and Miesenböck, G. (2014). Experience-Dependent Rewiring of Specific Inhibitory Connections in Adult Neocortex. PLoS Biol. *12*.

Kätzel, D., Zemelman, B. V, Buetfering, C., Wölfel, M., and Miesenböck, G. (2011). The columnar and laminar organization of inhibitory connections to neocortical excitatory cells. Nat. Neurosci. *14*, 100–107.

Kawaguchi, Y. (1993). Groupings of nonpyramidal and pyramidal cells with specific physiological and morphological characteristics in rat frontal cortex. J. Neurophysiol. *69*, 416–431.

Kepecs, A., and Fishell, G. (2014). Interneuron cell types are fit to function. Nature *505*, 318–326.

Kerlin, A.M., Andermann, M.L., Berezovskii, V.K., and Reid, R.C. (2010). Broadly tuned response properties of diverse inhibitory neuron subtypes in mouse visual cortex. Neuron *67*, 858–871.

Kerr, J.N., de Kock, C.P.J., Greenberg, D.S., Bruno, R.M., Sakmann, B., and Helmchen, F. (2007). Spatial organization of neuronal population responses in layer 2/3 of rat barrel cortex. J Neurosci *27*, 13316–13328.

Khatri, V. (2004). Adaptation in Thalamic Barreloid and Cortical Barrel Neurons to Periodic Whisker Deflections Varying in Frequency and Velocity. J. Neurophysiol. *92*, 3244–3254.

Kim, D., Jeong, H., Lee, J., Ghim, J., Her, E.S., Lee, S., Kim, D., Jeong, H., Lee, J., Ghim, J., et al. (2016). Distinct Roles of Parvalbumin- and Somatostatin- Expressing Interneurons in Working Memory Article Distinct Roles of Parvalbumin- and Somatostatin-Expressing Interneurons in Working Memory. Neuron *92*, 1–14.

Kim, E.J., Juavinett, A.L., Kyubwa, E.M., Jacobs, M.W., and Callaway, E.M. (2015a). Three Types of Cortical Layer 5 Neurons That Differ in Brain-wide Connectivity and Function. Neuron *88*, 1253–1267.

Kim, E.J., Juavinett, A.L., Kyubwa, E.M., Jacobs, M.W., Callaway, E.M., Kim, E.J., Juavinett, A.L., Kyubwa, E.M., Jacobs, M.W., and Callaway, E.M. (2015b). Three Types of Cortical Layer 5 Neurons That Differ in Brain-wide Connectivity and Function. Neuron *88*, 1–15.

Kim, J., Matney, C.J., Blankenship, A., Hestrin, S., and Brown, S.P. (2014). Layer 6 Corticothalamic Neurons Activate a Cortical Output Layer, Layer 5a. J. Neurosci. *34*, 9656–9664.

Kinnischtzke, A.K., Sewall, A.M., Berkepile, J.M., and Fanselow, E.E. (2012). Postnatal maturation of somatostatin-expressing inhibitory cells in the somatosensory cortex of GIN mice. Front. Neural Circuits *6*, 33.

Kinnischtzke, A.K., Simons, D.J., and Fanselow, E.E. (2014). Motor Cortex Broadly Engages Excitatory and Inhibitory Neurons in Somatosensory Barrel Cortex. Cereb. Cortex *24*, 2237–2248.

Kinnischtzke, A.K., Fanselow, E.E., and Simons, D.J. (2016). Target-specific M1 inputs to infragranular S1 pyramidal neurons. J. Neurophysiol. *116*, 1261–1274.

Kiritani, T., Wickersham, I.R., Seung, H.S., and Shepherd, G.M.G. (2012). Hierarchical Connectivity and Connection-Specific Dynamics in the Corticospinal-Corticostriatal Microcircuit in Mouse Motor Cortex. J. Neurosci. *32*, 4992–5001.

Koch, C. (2012). Modular biological complexity. Science (80-.). *337*, 531–532.

de Kock, C.P.J., and Sakmann, B. (2009). Spiking in primary somatosensory cortex during natural whisking in awake head-restrained rats is cell-type specific. Proc. Natl. Acad. Sci. U. S. A. *106*, 16446–16450.

de Kock, C.P.J., Bruno, R.M., Spors, H., and Sakmann, B. (2007). Layer- and cell-type-specific suprathreshold stimulus representation in rat primary somatosensory cortex. J. Physiol. *581*, 139–154.

Koelbl, C., Helmstaedter, M., L'bke, J., and Feldmeyer, D. (2015). A barrel-related interneuron in layer 4 of rat somatosensory cortex with a high intrabarrel connectivity. Cereb. Cortex *25*, 713–725.

Krakauer, J.W., Ghazanfar, A.A., Gomez-Marin, A., MacIver, M.A., and Poeppel, D. (2017). Neuroscience Needs Behavior: Correcting a Reductionist Bias. Neuron *93*, 480–490.

Krieger, P., Kuner, T., and Sakmann, B. (2007). Synaptic Connections between Layer 5B Pyramidal Neurons in Mouse Somatosensory Cortex Are Independent of Apical Dendrite Bundling. J. Neurosci. *27*, 11473–11482.

Krook-Magnuson, E., Varga, C., Lee, S.-H., and Soltesz, I. (2012). New dimensions of interneuronal specialization unmasked by principal cell heterogeneity. Trends Neurosci. *35*, 175–184.

Kruglikov, I., and Rudy, B. (2008). Perisomatic GABA release and thalamocortical integration onto neocortical excitatory cells are regulated by neuromodulators. Neuron *58*, 911–924.

Krupa, D.J., Wiest, M.C., Shuler, M.G., Laubach, M., and Nicolelis, M. a L. (2004a). Layer-specific somatosensory cortical activation during active tactile discrimination. Science *304*, 1989–1992.

Krupa, D.J., Wiest, M.C., Shuler, M.G., Laubach, M., and Nicolelis, M. a L. (2004b). Layer-specific somatosensory cortical activation during active tactile discrimination. Science *304*, 1989–1992.

Kubota, Y. (2014). Untangling GABAergic wiring in the cortical microcircuit. Curr. Opin. Neurobiol. *26*, 7–14.

Kubota, Y., Shigematsu, N., Karube, F., Sekigawa, A., Kato, S., Yamaguchi, N., Hirai, Y., Morishima, M., and Kawaguchi, Y. (2011). Selective coexpression of multiple chemical markers defines discrete populations of neocortical gabaergic neurons. Cereb. Cortex *21*, 1803–1817.

Kumar, P., and Ohana, O. (2008). Inter- and intralaminar subcircuits of excitatory and inhibitory neurons in layer 6a of the rat barrel cortex. J. Neurophysiol. *100*, 1909–1922.

Kumar, A., Vlachos, I., Aertsen, A., and Boucsein, C. (2013). Challenges of understanding brain function by selective modulation of neuronal subpopulations. Trends Neurosci. *36*, 579–586.

Kvitsiani, D., Ranade, S., Hangya, B., Taniguchi, H., Huang, J.Z., and Kepecs, a (2013). Distinct behavioural and network correlates of two interneuron types in prefrontal cortex. Nature *498*, 363–366.

Kwan, A.C., and Dan, Y. (2012). Dissection of cortical microcircuits by single-neuron stimulation in vivo. Curr. Biol. *22*, 1459–1467.

Larkum, M. (2013). A cellular mechanism for cortical associations: an organizing principle for the cerebral cortex. Trends Neurosci. *36*, 141–151.

Larkum, M.E., and Zhu, J.J. (2002). Signaling of layer 1 and whisker-evoked Ca2+ and Na+ action potentials in distal and terminal dendrites of rat neocortical pyramidal neurons in vitro and in vivo. J. Neurosci. *22*, 6991–7005.

Larkum, M.E., Zhu, J.J., and Sakmann, B. (1999a). A new cellular mechanism for coupling inputs arriving at different cortical layers. Nature *398*, 338–341.

Larkum, M.E., Kaiser, K.M.M., and Sakmann, B. (1999b). Calcium electrogenesis in distal apical dendrites of layer 5 pyramidal cells at a critical frequency of back-propagating action potentials. Proc. Natl. Acad. Sci. *96*, 14600–14604.

Larkum, M.E., Senn, W., and Lüscher, H.-R. (2004). Top-down dendritic input increases the gain of layer 5 pyramidal neurons. Cereb. Cortex *14*, 1059–1070.

Larkum, M.E., Nevian, T., Sandler, M., Polsky, A., and Schiller, J. (2009). Synaptic integration in tuft dendrites of layer 5 pyramidal neurons: a new unifying principle. Science *325*, 756–760.

Larsen, D.D., and Callaway, E.M. (2006). Development of layer-specific axonal arborizations in mouse primary somatosensory cortex. J. Comp. Neurol. *494*, 398–414.

Larsen, D.D., Wickersham, I.R., and Callaway, E.M. (2007). Retrograde tracing with recombinant rabies virus reveals correlations between projection targets and dendritic architecture in layer 5 of mouse barrel cortex. Front. Neural Circuits *1*, 5.

Lavzin, M., Rapoport, S., Polsky, A., Garion, L., and Schiller, J. (2012). Nonlinear dendritic processing determines angular tuning of barrel cortex neurons in vivo. Nature *490*, 397–401.

Leão, R.N., Mikulovic, S., Leão, K.E., Munguba, H., Gezelius, H., Enjin, A., Patra, K., Eriksson, A., Loew, L.M., Tort, A.B.L., et al. (2012). OLM interneurons differentially modulate CA3 and entorhinal inputs to hippocampal CA1 neurons. Nat. Neurosci. *15*, 1524–1530.

Lee, A.J., Wang, G., Jiang, X., Johnson, S.M., Hoang, E.T., Lanté, F., Stornetta, R.L., Beenhakker, M.P., Shen, Y., and Julius Zhu, J. (2014a). Canonical Organization of Layer 1 Neuron-Led Cortical Inhibitory and Disinhibitory Interneuronal Circuits. Cereb. Cortex *2*, 1–13.

Lee, A.T., Gee, S.M., Vogt, D., Patel, T., Rubenstein, J.L., and Sohal, V.S. (2014b). Pyramidal neurons in prefrontal cortex receive subtype-specific forms of excitation and inhibition. Neuron *81*, 61–68.

Lee, S., Hjerling-Leffler, J., Zagha, E., Fishell, G., and Rudy, B. (2010). The largest group of superficial neocortical GABAergic interneurons expresses ionotropic serotonin receptors. J Neurosci *30*, 16796–16808.

Lee, S., Kruglikov, I., Huang, Z.J., Fishell, G., and Rudy, B. (2013). A disinhibitory circuit mediates motor integration in the somatosensory cortex. Nat. Neurosci. *16*, 1662–1670.

Lee, S.-H., Kwan, A.C., Zhang, S., Phoumthipphavong, V., Flannery, J.G., Masmanidis, S.C., Taniguchi, H., Huang, Z.J., Zhang, F., Boyden, E.S., et al. (2012). Activation of specific interneurons improves V1 feature selectivity and visual perception. Nature *488*, 379–383.

Lefort, S., Tomm, C., Floyd Sarria, J.-C., and Petersen, C.C.H. (2009). The excitatory neuronal network of the C2 barrel column in mouse primary somatosensory cortex. Neuron *61*, 301–316.

Legéndy, C.R., and Salcman, M. (1985). Bursts and recurrences of bursts in the spike trains of spontaneously active striate cortex neurons. J. Neurophysiol. *53*, 926–939.

Leinweber, M., Ward, D.R., Sobczak, J.M., Attinger, A., and Keller, G.B. (2017). A Sensorimotor Circuit in Mouse Cortex for Visual Flow Predictions. Neuron *95*, 1420–1432.e5.

Lévesque, M., Charara, A., Gagnon, S., Parent, A., and Deschênes, M. (1996). Corticostriatal projections from layer V cells in rat are collaterals of long-range corticofugal axons. Brain Res. *709*, 311–315.

Levy, R.B., and Reyes, A.D. (2012). Spatial profile of excitatory and inhibitory synaptic connectivity in mouse primary auditory cortex. J. Neurosci. *32*, 5609–5619.

Li, L., and Ebner, F.F. (2007). Cortical Modulation of Spatial and Angular Tuning Maps in the Rat Thalamus. J. Neurosci. *27*, 167–179.

Li, L. -y., Ji, X. -y., Liang, F., Li, Y. -t., Xiao, Z., Tao, H.W., and Zhang, L.I. (2014). A Feedforward Inhibitory Circuit Mediates Lateral Refinement of Sensory Representation in Upper Layer 2/3 of Mouse Primary Auditory Cortex. J. Neurosci. *34*, 13670–13683.

Li, L.Y., Li, Y.T., Zhou, M., Tao, H.W., and Zhang, L.I. (2013a). Intracortical multiplication of thalamocortical signals in mouse auditory cortex. Nat. Neurosci. *16*, 1179–1181.

Li, Y.T., Ibrahim, L.A., Liu, B.H., Zhang, L.I., and Tao, H.W. (2013b). Linear transformation of thalamocortical input by intracortical excitation. Nat. Neurosci. *16*, 1324–1330.

Liang, F., Xiong, X.R., Zingg, B., Ji, X. ying, Zhang, L.I., and Tao, H.W. (2015). Sensory Cortical Control of a Visually Induced Arrest Behavior via Corticotectal Projections. Neuron *86*, 755–767.

Lien, A.D., and Scanziani, M. (2013). Tuned thalamic excitation is amplified by visual cortical circuits. Nat. Neurosci. *16*, 1315–1323.

Litwin-Kumar, A., Rosenbaum, R., and Doiron, B. (2016). Inhibitory stabilization and visual coding in cortical circuits with multiple interneuron subtypes. J. Neurophysiol. jn.00732.2015.

Liu, B.H., Huberman, A.D., and Scanziani, M. (2016a). Cortico-fugal output from visual cortex promotes plasticity of innate motor behaviour. Nature *538*, 383–387.

Liu, L., She, L., Chen, M., Liu, T., Lu, H.D., Dan, Y., and Poo, M. (2016b). Spatial structure of neuronal receptive field in awake monkey secondary visual cortex (V2). Proc. Natl. Acad. Sci. *113*, 1913–1918.

Lorente de No, R. (1992). The Cerebral Cortex of the Mouse. Somat. Mot. Res. *9*, 3–36.

Lu, J., Tucciarone, J., Padilla-Coreano, N., He, M., Gordon, J.A., and Josh Huang, Z. (2017). Selective inhibitory control of pyramidal neuron ensembles and cortical subnetworks by chandelier cells. Nat. Neurosci. *20*, 1377–1383.

Lur, G., Vinck, M.A., Tang, L., Cardin, J.A., and Higley, M.J. (2016a). Projection-Specific Visual Feature Encoding by Layer 5 Cortical Subnetworks. Cell Rep. *14*, 2538–2545.

Lur, G., Vinck, M.A., Tang, L., Cardin, J.A., and Higley, M.J. (2016b). Projection-Specific Visual Feature Encoding by Layer 5 Cortical Subnetworks. Cell Rep. *14*, 2538–2545.

Ma, W., Liu, B., Li, Y., Huang, Z.J., Zhang, L.I., and Tao, H.W. (2010). Visual representations by cortical somatostatin inhibitory neurons--selective but with weak and delayed responses. J. Neurosci. *30*, 14371–14379.

Ma, W.J., Beck, J.M., Latham, P.E., and Pouget, A. (2006a). Bayesian inference with probabilistic population codes. Nat. Neurosci. *9*, 1432–1438.

Ma, Y., Hu, H., Berrebi, A.S., Mathers, P.H., and Agmon, A. (2006b). Distinct subtypes of somatostatin-containing neocortical interneurons revealed in transgenic mice. J. Neurosci. *26*, 5069–5082.

Ma, Y., Hu, H., and Agmon, a. (2012). Short-Term Plasticity of Unitary Inhibitory-to-Inhibitory Synapses Depends on the Presynaptic Interneuron Subtype. J. Neurosci. *32*, 983–988.

Madisen, L., Zwingman, T.A., Sunkin, S.M., Oh, S.W., Zariwala, H.A., Gu, H., Ng, L.L., Palmiter, R.D., Hawrylycz, M.J., Jones, A.R., et al. (2010). A robust and high-throughput Cre reporting and characterization system for the whole mouse brain. Nat. Neurosci. *13*, 133–140.

Major, G., Larkum, M.E., and Schiller, J. (2013). Active properties of neocortical pyramidal neuron dendrites. Annu. Rev. Neurosci. *36*, 1–24.

Makino, H., Komiyama, T., Xu, J., Harvey, N., Saito, T., Fukai, A., Mabuchi, A., Ikeda, T., Yano, F., Ohba, S., et al. (2015). Learning enhances the relative impact of top-down processing in the visual cortex. Nat Neurosci *18*, 1116–1122.

Malina, K.C.K., Mohar, B., Rappaport, A.N., and Lampl, I. (2016). Local and thalamic origins of correlated ongoing and sensory-evoked cortical activities. Nat. Commun. *7*.

Malpeli, J.G. (1983). Activity of cells in area 17 of the cat in absence of input from layer a of lateral geniculate nucleus. J. Neurophysiol. *49*, 595–610.

Manita, S., Suzuki, T., Homma, C., Matsumoto, T., Odagawa, M., Yamada, K., Ota, K., Matsubara, C., Inutsuka, A., Sato, M., et al. (2015a). A Top-Down Cortical Circuit for Accurate Sensory Perception. Neuron *86*, 1304–1316.

Manita, S., Suzuki, T., Homma, C., Matsumoto, T., Odagawa, M., Yamada, K., Ota, K., Matsubara, C., Inutsuka, A., Sato, M., et al. (2015b). A Top-Down Cortical Circuit for Accurate Sensory Perception. Neuron *86*, 1–6.

Manns, I.D., Sakmann, B., and Brecht, M. (2004). Sub- and suprathreshold receptive field properties of pyramidal neurones in layers 5A and 5B of rat somatosensory barrel cortex. J. Physiol. *556*, 601–622.

Mao, T., Kusefoglu, D., Hooks, B.M., Huber, D., Petreanu, L., and Svoboda, K. (2011a). Supplemental Information Long-Range Neuronal Circuits Underlying the Interaction between Sensory and Motor Cortex. Neuron *72*, 111–123.

Mao, T., Kusefoglu, D., Hooks, B.M., Huber, D., Petreanu, L., and Svoboda, K. (2011b). Long-range neuronal circuits underlying the interaction between sensory and motor cortex. Neuron *72*, 1–22.

Markov, N.T., Ercsey-Ravasz, M., Van Essen, D.C., Knoblauch, K., Toroczkai, Z., and Kennedy, H. (2013). Cortical high-density counterstream architectures. Science (80-.). *342*, 1238406.

Markram, H. (1997). A network of tufted layer 5 pyramidal neurons. Cereb. Cortex *7*, 523–533.

Markram, H., Toledo-Rodriguez, M., Wang, Y., Gupta, A., Silberberg, G., and Wu, C. (2004). Interneurons of the neocortical inhibitory system. Nat. Rev. Neurosci. *5*, 793–807.

Markram, H., Muller, E., Ramaswamy, S., Reimann, M.W., Abdellah, M., Sanchez, C.A., Ailamaki, A., Alonso-Nanclares, L., Antille, N., Arsever, S., et al. (2015). Reconstruction and Simulation of Neocortical Microcircuitry. Cell *163*, 456–492.

Marlin, J.J., and Carter, a. G. (2014). GABA-A Receptor Inhibition of Local Calcium Signaling in Spines and Dendrites. J. Neurosci. *34*, 15898–15911.

Marques-Smith, A., Lyngholm, D., Kaufmann, A.-K., Stacey, J.A., Hoerder-Suabedissen, A., Becker, E.B.E., Wilson, M.C., Molnár, Z., and Butt, S.J.B. (2016a). A Transient Translaminar GABAergic Interneuron Circuit Connects Thalamocortical Recipient Layers in Neonatal Somatosensory Cortex. Neuron *89*, 536–549.

Marques-Smith, A., Lyngholm, D., Kaufmann, A.K., Stacey, J.A., Hoerder-Suabedissen, A., Becker, E.B.E., Wilson, M.C., Molnár, Z., and Butt, S.J.B. (2016b). A Transient Translaminar GABAergic Interneuron Circuit Connects Thalamocortical Recipient Layers in Neonatal Somatosensory Cortex. Neuron *89*, 536–549.

Marr (1982). Vision: A Computational Investigation into the Human Representation and Processing of Visual Information. Book.

Martinez, L.M., and Alonso, J.M. (2001). Construction of complex receptive fields in cat primary visual cortex. Neuron *32*, 515–525.

Martinez, L.M., Wang, Q., Reid, R.C., Pillai, C., Alonso, J.M., Sommer, F.T., and Hirsch, J.A. (2005). Receptive field structure varies with layer in the primary visual cortex. Nat Neurosci *8*, 372–379.

Matyas, F., Sreenivasan, V., Marbach, F., Wacongne, C., Barsy, B., Mateo, C., Aronoff, R., and Petersen, C.C.H. (2010). Motor control by sensory cortex. Science *330*, 1240–1243.

McGarry, L.M., Packer, A.M., Fino, E., Nikolenko, V., Sippy, T., and Yuste, R. (2010). Quantitative classification of somatostatin-positive neocortical interneurons identifies three interneuron subtypes. Front. Neural Circuits *4*, 12.

McGuire, B. a, Hornung, J.P., Gilbert, C.D., and Wiesel, T.N. (1984). Patterns of synaptic input to layer 4 of cat striate cortex. J. Neurosci. *4*, 3021–3033.

Merel, J., Shababo, B., Naka, A., Adesnik, H., and Paninski, L. (2016). Bayesian methods for event analysis of intracellular currents. J. Neurosci. Methods *269*, 21–32.

Meyer, H.S., Wimmer, V.C., Oberlaender, M., de Kock, C.P.J., Sakmann, B., and Helmstaedter, M. (2010a). Number and laminar distribution of neurons in a thalamocortical projection column of rat vibrissal cortex. Cereb. Cortex *20*, 2277–2286.

Meyer, H.S., Wimmer, V.C., Hemberger, M., Bruno, R.M., de Kock, C.P.J., Frick, A., Sakmann, B., and Helmstaedter, M. (2010b). Cell type-specific thalamic innervation in a column of rat vibrissal cortex. Cereb. Cortex *20*, 2287–2303.

Meyer, H.S., Schwarz, D., Wimmer, V.C., Schmitt, A.C., Kerr, J.N.D., Sakmann, B., and Helmstaedter, M. (2011). Inhibitory interneurons in a cortical column form hot zones of inhibition in layers 2 and 5A. Proc. Natl. Acad. Sci. U. S. A. *108*, 16807–16812.

Mignard, M., and Malpeli, J.G. (1991). Paths of information flow through visual cortex. Science *251*, 1249–1251.

Miller, K.D. (2016). Canonical computations of cerebral cortex. Curr. Opin. Neurobiol. *37*, 75–84.

Mittmann, W., Wallace, D.J., Czubayko, U., Herb, J.T., Schaefer, A.T., Looger, L.L., Denk, W., and Kerr, J.N.D. (2011). Two-photon calcium imaging of evoked activity from L5 somatosensory neurons in vivo. Nat. Neurosci. *14*, 1089–1093.

Morgenstern, N.A., Bourg, J., and Petreanu, L. (2016). Multilaminar networks of cortical neurons integrate common inputs from sensory thalamus. Nat. Neurosci. *19*, 1034–1040.

Müllner, F.E., Wierenga, C.J., and Bonhoeffer, T. (2015). Precision of Inhibition: Dendritic Inhibition by Individual GABAergic Synapses on Hippocampal Pyramidal Cells Is Confined in Space and Time. Neuron *87*, 576–589.

Muñoz, W., Tremblay, R., and Rudy, B. (2014). Channelrhodopsin-Assisted Patching: InVivo Recording of Genetically and Morphologically Identified Neurons throughout the Brain. Cell Rep. *9*, 2304–2316.

Muñoz, W., Tremblay, R., Levenstein, D., and Rudy, B. (2017). Layer-specific modulation of neocortical dendritic inhibition during active wakefulness. Science (80-.). *355*, 954 LP-959.

Murayama, M., Pérez-Garci, E., Nevian, T., Bock, T., Senn, W., and Larkum, M.E. (2009a). Dendritic encoding of sensory stimuli controlled by deep cortical interneurons. Nature *457*, 1137–1141.

Murayama, M., Pérez-Garci, E., Nevian, T., Bock, T., Senn, W., and Larkum, M.E. (2009b). Dendritic encoding of sensory stimuli controlled by deep cortical interneurons. Nature *457*, 1137–1141.

Naka, a. (2015). Cell-Type-Specific Manipulation Reveals New Specificity in the Neocortical Microcircuit. J. Neurosci. *35*, 8976–8978.

Nakajima, M., Görlich, A., and Heintz, N. (2014). Oxytocin modulates female sociosexual behavior through a specific class of prefrontal cortical interneurons. Cell *159*, 295–305.

Narayanan, R.T., Egger, R., Johnson, A.S., Mansvelder, H.D., Sakmann, B., De Kock, C.P.J., and Oberlaender, M. (2015a). Beyond columnar organization: Cell type- and target layer-specific principles of horizontal axon projection patterns in rat vibrissal cortex. Cereb. Cortex *25*, 4450–4468.

Narayanan, R.T., Egger, R., Johnson, A.S., Mansvelder, H.D., Sakmann, B., de Kock, C.P.J., and Oberlaender, M. (2015b). Beyond Columnar Organization: Cell Type- and Target Layer-Specific Principles of Horizontal Axon Projection Patterns in Rat Vibrissal Cortex. Cereb. Cortex bhv053-.

Narayanan, R.T., Udvary, D., and Oberlaender, M. (2017). Cell Type-Specific Structural Organization of the Six Layers in Rat Barrel Cortex. Front. Neuroanat. *11*, 1–10.

Nassi, J.J., Lomber, S.G., and Born, R.T. (2013). Corticocortical Feedback Contributes to Surround Suppression in V1 of the Alert Primate. J. Neurosci. *33*, 8504–8517.

Nicholson, C., and Freeman, J.A. (1975). Theory of current source-density analysis and determination of conductivity tensor for anuran cerebellum. J. Neurophysiol. *38*, 356–368.

Niell, C.M., and Stryker, M.P. (2008). Highly selective receptive fields in mouse visual cortex. J. Neurosci. *28*, 7520–7536.

Niell, C.M., and Stryker, M.P. (2010). Modulation of Visual Responses by Behavioral State in Mouse Visual Cortex. Neuron *65*, 472–479.

Nienborg, H., Hasenstaub, A., Nauhaus, I., Taniguchi, H., Huang, Z.J., and Callaway, E.M. (2013). Contrast

Dependence and Differential Contributions from Somatostatin- and Parvalbumin-Expressing Neurons to Spatial Integration in Mouse V1. J. Neurosci. *33*, 11145–11154.

Nowak, L.G., Azouz, R., Sanchez-Vives, M. V, Gray, C.M., and McCormick, D. a (2003). Electrophysiological classes of cat primary visual cortical neurons in vivo as revealed by quantitative analyses. J. Neurophysiol. *89*, 1541–1566.

Nurminen, L., and Angelucci, A. (2014). Multiple components of surround modulation in primary visual cortex: Multiple neural circuits with multiple functions? Vision Res. *104*, 47–56.

O'Connor, D.H., Peron, S.P., Huber, D., and Svoboda, K. (2010). Neural activity in barrel cortex underlying vibrissa-based object localization in mice. Neuron *67*, 1048–1061.

Oberlaender, M., Boudewijns, Z.S.R.M., Kleele, T., Mansvelder, H.D., Sakmann, B., and de Kock, C.P.J. (2011). Three-dimensional axon morphologies of individual layer 5 neurons indicate cell type-specific intracortical pathways for whisker motion and touch. Proc. Natl. Acad. Sci. U. S. A. *108*, 4188–4193.

Oberlaender, M., de Kock, C.P.J., Bruno, R.M., Ramirez, A., Meyer, H.S., Dercksen, V.J., Helmstaedter, M., and Sakmann, B. (2012). Cell type-specific three-dimensional structure of thalamocortical circuits in a column of rat vibrissal cortex. Cereb. Cortex *22*, 2375–2391.

Oláh, S., Füle, M., Komlósi, G., Varga, C., Báldi, R., Barzó, P., and Tamás, G. (2009). Regulation of cortical microcircuits by unitary GABA-mediated volume transmission. Nature *461*, 1278–1281.

Oliva, a a, Jiang, M., Lam, T., Smith, K.L., and Swann, J.W. (2000). Novel hippocampal interneuronal subtypes identified using transgenic mice that express green fluorescent protein in GABAergic interneurons. J. Neurosci. *20*, 3354–3368.

Olsen, S.R., Bortone, D.S., Adesnik, H., and Scanziani, M. (2012). Gain control by layer six in cortical circuits of vision. Nature *483*, 47–52.

Olshausen, B.A., and Field, D.J. (2004). Sparse coding of sensory inputs. Curr. Opin. Neurobiol. *14*, 481–487.

Otchy, T.M., Wolff, S.B.E., Rhee, J.Y., Pehlevan, C., Kawai, R., Kempf, A., Gobes, S.M.H., and Ölveczky, B.P. (2015). Acute off-target effects of neural circuit manipulations. Nature *528*, 358–363.

Otsuka, T., and Kawaguchi, Y. (2009). Cortical inhibitory cell types differentially form intralaminar and interlaminar subnetworks with excitatory neurons. J. Neurosci. *29*, 10533–10540.

Otsuka, T., and Kawaguchi, Y. (2013). Common excitatory synaptic inputs to electrically connected cortical fast-spiking cell networks. J. Neurophysiol. *110*, 795–806.

Ozeki, H., Finn, I.M., Schaffer, E.S., Miller, K.D., and Ferster, D. (2009). Inhibitory Stabilization of the Cortical Network Underlies Visual Surround Suppression. Neuron *62*, 578–592.

Packer, A.M., and Yuste, R. (2011). Dense, unspecific connectivity of neocortical parvalbumin-positive interneurons: a canonical microcircuit for inhibition? J. Neurosci. *31*, 13260–13271.

Packer, A.M., McConnell, D.J., Fino, E., and Yuste, R. (2012). Axo-Dendritic Overlap and Laminar Projection Can Explain Interneuron Connectivity to Pyramidal Cells. Cereb. Cortex *23*, 2790–2802.

Pakan, J.M.P., Lowe, S.C., Dylda, E., Keemink, S.W., Currie, S.P., Coutts, C.A., and Rochefort, N.L. (2016). Behavioral-state modulation of inhibition is context-dependent and cell type specific in mouse visual cortex. Elife *5*, 1–18.

Pala, A., and Petersen, C.C.H. (2015). InVivo Measurement of Cell-Type-Specific Synaptic Connectivity and Synaptic Transmission in Layer 2/3 Mouse Barrel Cortex. Neuron *85*, 68–76.

Palmer, L.M., Schulz, J.M., Murphy, S.C., Ledergerber, D., Murayama, M., and Larkum, M.E. (2012). Interhemispheric Inhibition. Science (80-.). *39*, 989–993.

Palmer, L.M., Schulz, J.M., and Larkum, M.E. (2013). Layer-specific regulation of cortical neurons by interhemispheric inhibition. Commun. Integr. Biol. 1–5.

Perin, R., Berger, T.K., and Markram, H. (2011). A synaptic organizing principle for cortical neuronal groups. Proc. Natl. Acad. Sci. U. S. A. *108*, 5419–5424.

Peron, S.P., Freeman, J., Iyer, V., Guo, C., and Svoboda, K. (2015). A Cellular Resolution Map of Barrel Cortex Activity during Tactile Behavior. Neuron *86*, 783–799.

Peters, A., Proskauer, C.C., and Ribak, C.E. (1982). Chandelier cells in rat visual cortex. J. Comp. Neurol. *206*, 397–416.

Petersen, C.C.H. (2014). Cell-type specific function of GABAergic neurons in layers 2 and 3 of mouse barrel cortex. Curr. Opin. Neurobiol. *26*, 1–6.

Petersen, C.C.H., and Crochet, S. (2013). Synaptic Computation and Sensory Processing in Neocortical Layer 2/3. Neuron *78*, 28–48.

Petersen, C.C.H., and Sakmann, B. (2000). The excitatory neuronal network of rat layer 4 barrel cortex. J. Neurosci. *20*, 7579–7586.

Petersen, R.S., Panzeri, S., and Diamond, M.E. (2002). Population coding in somatosensory cortex. Curr. Opin. Neurobiol. *12*, 441–447.

Petreanu, L., Huber, D., Sobczyk, A., and Svoboda, K. (2007). Channelrhodopsin-2-assisted circuit mapping of long-range callosal projections. Nat. Neurosci. *10*, 663–668.

Petreanu, L., Mao, T., Sternson, S.M., and Svoboda, K. (2009). The subcellular organization of neocortical excitatory connections. Nature *457*, 1142–1145.

Petreanu, L., Gutnisky, D. a., Huber, D., Xu, N., O'Connor, D.H., Tian, L., Looger, L., and Svoboda, K. (2012). Activity in motor–sensory projections reveals distributed coding in somatosensation. Nature 0–7.

Pfeffer, C.K., Xue, M., He, M., Huang, Z.J., and Scanziani, M. (2013). Inhibition of inhibition in visual cortex: the logic of connections between molecularly distinct interneurons. Nat. Neurosci. *16*, 1068–1076.

Pi, H.-J., Hangya, B., Kvitsiani, D., Sanders, J.I., Huang, Z.J., and Kepecs, A. (2013). Cortical interneurons that specialize in disinhibitory control. Nature *503*, 521–524.

Pinto, D.J. (2003). Cortical Damping: Analysis of Thalamocortical Response Transformations in Rodent Barrel Cortex. Cereb. Cortex *13*, 33–44.

Pitas, A., Albarracín, A.L., Molano-Mazón, M., and Maravall, M. (2016). Variable Temporal Integration of Stimulus Patterns in the Mouse Barrel Cortex. Cereb. Cortex bhw006-.

Pluta, S., Naka, A., Veit, J., Telian, G., Yao, L., Hakim, R., Taylor, D., and Adesnik, H. (2015a). A direct translaminar inhibitory circuit tunes cortical output. Nat Neurosci *18*, 1631–1640.

Pluta, S., Naka, A., Veit, J., Telian, G., Yao, L., Hakim, R., Taylor, D., and Adesnik, H. (2015b). A direct translaminar inhibitory circuit tunes cortical output. Nat. Neurosci. *advance on*.

Pluta, S.R., Lyall, E.H., Telian, G.I., Ryapolova-Webb, E., and Adesnik, H. (2017). Surround Integration Organizes a Spatial Map during Active Sensation. Neuron *94*, 1220–1233.e5.

Polack, P.-O., and Contreras, D. (2012). Long-range parallel processing and local recurrent activity in the visual cortex of the mouse. J. Neurosci. *32*, 11120–11131.

Polack, P.P.-O., Friedman, J., and Golshani, P. (2013). Cellular mechanisms of brain state-dependent gain modulation in visual cortex. Nat. Neurosci. *16*, 1–11.

Poo, C., and Isaacson, J.S. (2009). Odor Representations in Olfactory Cortex: "Sparse" Coding, Global Inhibition, and Oscillations. Neuron *62*, 850–861.

Porter, J.T., Johnson, C.K., and Agmon, A. (2001). Diverse types of interneurons generate thalamus-evoked feedforward inhibition in the mouse barrel cortex. J. Neurosci. *21*, 2699–2710.

Potjans, T.C., and Diesmann, M. (2011). The cell-type specific connectivity of the local cortical network explains prominent features of neuronal activity. Arxiv 57.

Potjans, T.C., and Diesmann, M. (2014). The cell-type specific cortical microcircuit: Relating structure and activity in a full-scale spiking network model. Cereb. Cortex *24*, 785–806.

Pouget, A., Dayan, P., and Zemel, R. (2000). Information processing with population codes. Nat. Rev. Neurosci. *1*, 125–132.

Pouille, F., and Scanziani, M. (2001). Enforcement of temporal fidelity in pyramidal cells by somatic feed-forward inhibition. Science *293*, 1159–1163.

Pouille, F., and Scanziani, M. (2004). Routing of spike series by dynamic circuits in the hippocampus. Nature *429*, 717–723.

Pouille, F., Marin-Burgin, A., Adesnik, H., Atallah, B. V, and Scanziani, M. (2009a). Input normalization by global feedforward inhibition expands cortical dynamic range. Nat. Neurosci. *12*, 1577–1585.

Pouille, F., Marin-Burgin, A., Adesnik, H., Atallah, B. V, and Scanziani, M. (2009b). Input normalization by global feedforward inhibition expands cortical dynamic range. Nat. Neurosci. *12*, 1577–1585.

Priebe, N.J., and Ferster, D. (2008). Inhibition, Spike Threshold, and Stimulus Selectivity in Primary Visual Cortex. Neuron *57*, 482–497.

Prönneke, A., Scheuer, B., Wagener, R.J., Möck, M., Witte, M., and Staiger, J.F. (2015). Characterizing VIP Neurons in the Barrel Cortex of VIPcre/tdTomato Mice Reveals Layer-Specific Differences. Cereb. Cortex bhv202.

Przybyszewski, A.W., Gaska, J.P., Foote, W., and Pollen, D.A. (2000). Striate cortex increases contrast gain of macaque LGN neurons. Vis. Neurosci. *17*, 485–494.

Radnikow, G., and Feldmeyer, D. (2018). Layer- and Cell Type-Specific Modulation of Excitatory Neuronal Activity in the Neocortex. Front. Neuroanat. *12*.

Rah, J.-C., Bas, E., Colonell, J., Mishchenko, Y., Karsh, B., Fetter, R.D., Myers, E.W., Chklovskii, D.B., Svoboda, K., Harris, T.D., et al. (2013). Thalamocortical input onto layer 5 pyramidal neurons measured using quantitative large-scale array tomography. Front. Neural Circuits *7*, 1–16.

Raizada, R.D.S. (2003). Towards a Theory of the Laminar Architecture of Cerebral Cortex: Computational Clues from the Visual System. Cereb. Cortex *13*, 100–113.

Ramaswamy, S., and Markram, H. (2015). Anatomy and physiology of the thick-tufted layer 5 pyramidal neuron. Front. Cell. Neurosci. *9*, 233.

Rao, R.P.N., and Ballard, D.H. (1999). Predictive coding in the visual cortex: A functional interpretation of some extra-classical receptive-field effects. Nat. Neurosci. *2*, 79–87.

Reimer, J., Froudarakis, E., Cadwell, C.R., Yatsenko, D., Denfield, G.H., and Tolias, A.S. (2014). Pupil Fluctuations Track Fast Switching of Cortical States during Quiet Wakefulness. Neuron *84*, 355–362.

Reyes, A., Lujan, R., Rozov, A., Burnashev, N., Somogyi, P., and Sakmann, B. (1998). Target-cell-specific facilitation and depression in neocortical circuits. Nat. Neurosci. *1*, 279–285.

Reyes-Puerta, V., Sun, J.-J., Kim, S., Kilb, W., and Luhmann, H.J. (2015a). Laminar and Columnar Structure of Sensory-

Evoked Multineuronal Spike Sequences in Adult Rat Barrel Cortex In Vivo. Cereb. Cortex *25*, 2001–2021.

Reyes-Puerta, V., Kim, S., Sun, J.J., Imbrosci, B., Kilb, W., and Luhmann, H.J. (2015b). High Stimulus-Related Information in Barrel Cortex Inhibitory Interneurons. PLoS Comput. Biol. *11*, 1–32.

Rock, C., and Apicella, A.J. (2015). Callosal projections drive neuronal-specific responses in the mouse auditory cortex. J. Neurosci. *35*, 6703–6713.

Rockland, K., and Lund, J. (1982). Widespread periodic intrinsic connections in the tree shrew visual cortex. Science (80-.). *215*, 1532–1534.

Rodney, B.Y., Douglas, J., and Martin, K.A.C. (1991). A functional microcircuit for cat visual cortex. 735–769.

Roux, L., and Buzsáki, G. (2014). Tasks for inhibitory interneurons in intact brain circuits. Neuropharmacology *88*, 10–23.

Rubin, D.B., VanHooser, S.D., and Miller, K.D. (2015). The stabilized supralinear network: A unifying circuit motif underlying multi-input integration in sensory cortex. Neuron *85*, 402–417.

Rudy, B., Fishell, G., Lee, S., and Hjerling-Leffler, J. (2011). Three groups of interneurons account for nearly 100% of neocortical GABAergic neurons. Dev. Neurobiol. *71*, 45–61.

Runyan, C. a, Schummers, J., Van Wart, A., Kuhlman, S.J., Wilson, N.R., Huang, Z.J., and Sur, M. (2010). Response features of parvalbumin-expressing interneurons suggest precise roles for subtypes of inhibition in visual cortex. Neuron *67*, 847–857.

Sachdev, R.N.S., Krause, M.R., and Mazer, J. a (2012). Surround suppression and sparse coding in visual and barrel cortices. Front. Neural Circuits *6*, 43.

Sakata, S., and Harris, K.D. (2009a). Laminar Structure of Spontaneous and Sensory-Evoked Population Activity in Auditory Cortex. Neuron *64*, 404–418.

Sakata, S., and Harris, K.D. (2009b). Laminar structure of spontaneous and sensory-evoked population activity in auditory cortex. Neuron *64*, 404–418.

Salinas, E., and Thier, P. (2000). Gain Modulation : A Major Computational Principle of the Central Nervous System. Neuron *27*, 15–21.

Schnepel, P., Kumar, A., Zohar, M., Aertsen, A., and Boucsein, C. (2015). Physiology and Impact of Horizontal Connections in Rat Neocortex. Cereb. Cortex *25*, 3818–3835.

Scholl, B., Pattadkal, J.J., Dilly, G.A., Priebe, N.J., and Zemelman, B.V. (2015a). Local Integration Accounts for Weak Selectivity of Mouse Neocortical Parvalbumin Interneurons. Neuron *87*, 424–436.

Scholl, B., Pattadkal, J.J., Dilly, G.A., Priebe, N.J., and Zemelman, B. V. (2015b). Local Integration Accounts for Weak Selectivity of Mouse Neocortical Parvalbumin Interneurons. Neuron *87*, 424–437.

Schubert, D., Staiger, J.F., Cho, N., Kötter, R., Zilles, K., and Luhmann, H.J. (2001). Layer-specific intracolumnar and transcolumnar functional connectivity of layer V pyramidal cells in rat barrel cortex. J. Neurosci. *21*, 3580–3592.

Schubert, D., Kötter, R., Luhmann, H.J., and Staiger, J.F. (2006). Morphology, electrophysiology and functional input connectivity of pyramidal neurons characterizes a genuine layer va in the primary somatosensory cortex. Cereb. Cortex *16*, 223–236.

Sekerli, M., Del Negro, C.A., Lee, R.H., and Butera, R.J. (2004). Estimating action potential thresholds from neuronal time-series: New metrics and evaluation of methodologies. IEEE Trans. Biomed. Eng. *51*, 1665–1672.

Self, M.W., Lorteije, J.A.M., Vangeneugden, J., van Beest, E.H., Grigore, M.E., Levelt, C.N., Heimel, J.A., and Roelfsema, P.R. (2014). Orientation-Tuned Surround Suppression in Mouse Visual Cortex. J. Neurosci. *34*, 9290–9304.

Seybold, B.A., Phillips, E.A.K., Schreiner, C.E., and Hasenstaub, A.R. (2015). Inhibitory Actions Unified by Network Integration. Neuron *87*, 1181–1192.

Shenoy, K. V., Sahani, M., and Churchland, M.M. (2013). Cortical Control of Arm Movements: A Dynamical Systems Perspective. Annu. Rev. Neurosci. *36*, 337–359.

Shepherd, G.M.G., Pologruto, T.A., and Svoboda, K. (2003). Circuit analysis of experience-dependent plasticity in the developing rat barrel cortex. Neuron *38*, 277–289.

Shima, Y., Sugino, K., Hempel, C., Shima, M., Taneja, P., Bullis, J.B., Mehta, S., Lois, C., and Nelson, S.B. (2016). A mammalian enhancer trap resource for discovering and manipulating neuronal cell types. Elife *5*, e13503.

Shimaoka, D., Harris, K.D., and Carandini, M. (2018). Effects of Arousal on Mouse Sensory Cortex Depend on Modality. Cell Rep. *22*, 3160–3167.

Silberberg, G. (2008). Polysynaptic subcircuits in the neocortex: spatial and temporal diversity. Curr. Opin. Neurobiol. *18*, 332–337.

Silberberg, G., and Markram, H. (2007). Disynaptic inhibition between neocortical pyramidal cells mediated by Martinotti cells. Neuron *53*, 735–746.

Sillito, A.M., Jones, H.E., Gerstein, G.L., and West, D.C. (1994). Feature-linked synchronization of thalamic relay cell firing induced by feedback from the visual cortex. Nature *369*, 479–482.

Sofroniew, N.J., Vlasov, Y.A., Andrew Hires, S., Freeman, J., and Svoboda, K. (2015). Neural coding in barrel cortex during whisker-guided locomotion. Elife *4*, e12559.

Sohn, J., Hioki, H., Okamoto, S., and Kaneko, T. (2014). Preprodynorphin-expressing neurons constitute a large subgroup of somatostatin-expressing GABAergic interneurons in the mouse neocortex. J. Comp. Neurol. *522*, 1506–1526.

Song, S., Sjöström, P.J., Reigl, M., Nelson, S., and Chklovskii, D.B. (2005). Highly nonrandom features of synaptic connectivity in local cortical circuits. PLoS Biol. *3*, e68.

Staiger, J.F. (1997). Interneurons immunoreactive for vasoactive intestinal polypeptide (VIP) are extensively innervated by parvalbumin-containing boutons in rat primary somatosensory cortex. Eur. J. Neurosci. *9*, 2259–2268.

Staiger, J.F., Schubert, D., Zuschratter, W., Kotter, R., and Luhmann, H.J. (2002). Innervation of interneurons immunoreactive for VIP by intrinsically bursting pyramidal cells and fast-spiking interneurons in infragranular layers of juvenile rat neocortex. Eur. J. Neurosci. *16*, 11–20.

Stanisor, L., van der Togt, C., Pennartz, C.M.A., and Roelfsema, P.R. (2013). A unified selection signal for attention and reward in primary visual cortex. Proc. Natl. Acad. Sci. *110*, 9136–9141.

Stokes, C.C.A., and Isaacson, J.S. (2010). From dendrite to soma: dynamic routing of inhibition by complementary interneuron microcircuits in olfactory cortex. Neuron *67*, 452–465.

Stringer, C., Pachitariu, M., Steinmetz, N., Reddy, C., Carandini, M., and Harris, K.D. (2018). Spontaneous behaviors drive multidimensional , brain-wide neural activity. 1–26.

Sun, Q.-Q. (2006). Barrel Cortex Microcircuits: Thalamocortical Feedforward Inhibition in Spiny Stellate Cells Is Mediated by a Small Number of Fast-Spiking Interneurons. J. Neurosci. *26*, 1219–1230.

Sun, W., Tan, Z., Mensh, B.D., and Ji, N. (2016). Thalamus provides layer 4 of primary visual cortex with orientation- and direction-tuned inputs. Nat. Neurosci. *19*, 308–315.

Sun, Y.J., Kim, Y.-J., Ibrahim, L.A., Tao, H.W., and Zhang, L.I. (2013). Synaptic mechanisms underlying functional dichotomy between intrinsic-bursting and regular-spiking neurons in auditory cortical layer 5. J. Neurosci. *33*, 5326–5339.

Swadlow, H.A. (2003). Fast-spike Interneurons and Feedforward Inhibition in Awake Sensory Neocortex. Cereb. Cortex *13*, 25–32.

Szabadics (2006). Excitatory Effect of GABAergic. Science (80-.). *311*, 233–235.

Takahashi, N., Oertner, T.G., Hegemann, P., and Larkum, M.E. (2016). Modulate Perception. Science (80-.). *354*, 1587–1590.

Tamamaki, N., Yanagawa, Y., Tomioka, R., Miyazaki, J.I., Obata, K., and Kaneko, T. (2003). Green Fluorescent Protein Expression and Colocalization with Calretinin, Parvalbumin, and Somatostatin in the GAD67-GFP Knock-In Mouse. J. Comp. Neurol. *467*, 60–79.

Tan, Z., Hu, H., Huang, Z.J., and Agmon, A. (2008). Robust but delayed thalamocortical activation of dendritic-targeting inhibitory interneurons. Proc. Natl. Acad. Sci. U. S. A. *105*, 2187–2192.

Tang, J.C.Y., Rudolph, S., Dhande, O.S., Abraira, V.E., Choi, S., Lapan, S.W., Drew, I.R., Drokhlyansky, E., Huberman, A.D., Regehr, W.G., et al. (2015a). Cell type–specific manipulation with GFP-dependent Cre recombinase. Nat. Neurosci. *18*, 1334–1341.

Tang, J.C.Y., Rudolph, S., Dhande, O.S., Abraira, V.E., Choi, S., Lapan, S.W., Drew, I.R., Drokhlyansky, E., Huberman, A.D., Regehr, W.G., et al. (2015b). Cell type–specific manipulation with GFP-dependent Cre recombinase. Nat. Neurosci. *18*, 1334–1341.

Taniguchi, H. (2014). Genetic dissection of GABAergic neural circuits in mouse neocortex. Front. Cell. Neurosci. *8*, 1–22.

Taniguchi, H., He, M., Wu, P., Kim, S., Paik, R., Sugino, K., Kvitsani, D., Fu, Y., Lu, J., Lin, Y., et al. (2011a). A Resource of Cre Driver Lines for Genetic Targeting of GABAergic Neurons in Cerebral Cortex. Neuron *71*, 995–1013.

Taniguchi, H., He, M., Wu, P., Kim, S., Paik, R., Sugino, K., Kvitsani, D., Fu, Y., Lu, J., Lin, Y., et al. (2011b). A Resource of Cre Driver Lines for Genetic Targeting of GABAergic Neurons in Cerebral Cortex. Neuron *71*, 995–1013.

Taniguchi, H., He, M., Wu, P., Kim, S., Paik, R., Sugino, K., Kvitsani, D., Fu, Y., Lu, J., Lin, Y., et al. (2011c). A Resource of Cre Driver Lines for Genetic Targeting of GABAergic Neurons in Cerebral Cortex. Neuron *71*, 995–1013.

Taniguchi, H., Lu, J., and Huang, Z.J. (2013). The spatial and temporal origin of chandelier cells in mouse neocortex. Science *339*, 70–74.

Tarczy-Hornoch, K., Martin, K.A.C., Jack, J.J.B., and Stratford, K.J. (1998). Synaptic interactions between smooth and spiny neurones in layer 4 of cat visual cortex in vitro. J. Physiol. *508*, 351–363.

Tasic, B., Menon, V., Nguyen, T.N.T., Kim, T.T.K., Jarsky, T., Yao, Z., Levi, B.B., Gray, L.T., Sorensen, S.A., Dolbeare, T., et al. (2016a). Adult mouse cortical cell taxonomy revealed by single cell transcriptomics. Nat. Neurosci. *advance on*, 1–37.

Tasic, B., Menon, V., Nguyen, T., Kim, T., Levi, B., Yao, Z., Lee, C., Shapovalova, N., Parry, S., Madisen, L., et al. (2016b). Adult cortical cell taxonomy by single cell transcriptomics. Nat. Neurosci.

Temereanca, S., and Simons, D.J. (2004). Functional Topography of Corticothalamic Feedback Enhances Thalamic Spatial Response Tuning in the Somatosensory Whisker/Barrel System. Neuron *41*, 639–651.

Thomson, A.M. (2007). Functional maps of neocortical local circuitry. Front. Neurosci. *1*, 19–42.

Thomson, A.M. (2010). Neocortical layer 6, a review. Front. Neuroanat.

Thorpe, S., Fize, D., and Marlot, C. (1996). Speed of processing in the human visual system. Nature *381*, 520–522.

Tremblay, R., Lee, S., and Rudy, B. (2016). GABAergic Interneurons in the Neocortex: From Cellular Properties to Circuits. Neuron *91*, 260–292.

Tuncdemir, S.N., Wamsley, B., Stam, F.J., Osakada, F., Goulding, M., Callaway, E.M., Rudy, B., and Fishell, G. (2016a). Early Somatostatin Interneuron Connectivity Mediates the Maturation of Deep Layer Cortical Circuits. Neuron *89*, 521–535.

Tuncdemir, S.N., Wamsley, B., Stam, F.J., Osakada, F., Goulding, M., Callaway, E.M., Rudy, B., and Fishell, G. (2016b). Early Somatostatin Interneuron Connectivity Mediates the Maturation of Deep Layer Cortical Circuits. Neuron *89*, 521–535.

Urban-Ciecko, J., and Barth, A.L. (2016). Somatostatin-expressing neurons in cortical networks. Nat. Rev. Neurosci. *17*, 401–409.

Urban-Ciecko, J., Fanselow, E.E., and Barth, A.L. (2015). Neocortical somatostatin neurons reversibly silence excitatory transmission via GABAb receptors. Curr. Biol. *25*, 722–731.

Veinante, P., Lavallée, P., and Deschênes, M. (2000). Corticothalamic projections from layer 5 of the vibrissal barrel cortex in the rat. J. Comp. Neurol. *424*, 197–204.

Veit, J., Hakim, R., Jadi, M.P., Sejnowski, T.J., and Adesnik, H. (2017). Cortical gamma band synchronization through somatostatin interneurons. Nat. Neurosci. *20*, 951–959.

Vélez-Fort, M., Rousseau, C. V., Niedworok, C.J., Wickersham, I.R., Rancz, E.A., Brown, A.P.Y., Strom, M., and Margrie, T.W. (2014). The stimulus selectivity and connectivity of layer six principal cells reveals cortical microcircuits underlying visual processing. Neuron *83*, 1431–1443.

Vinck, M., Batista-Brito, R., Knoblich, U., and Cardin, J.A. (2015). Arousal and Locomotion Make Distinct Contributions to Cortical Activity Patterns and Visual Encoding. Neuron *86*, 740–754.

Vinje, W.E., and Gallant, J.L. (2000). Sparse coding and decorrelation in primary visual cortex during natural vision. Science (80-.). *287*, 1273–1276.

Vucurovic, K., Gallopin, T., Ferezou, I., Rancillac, A., Chameau, P., Van Hooft, J.A., Geoffroy, H., Monyer, H., Rossier, J., and Vitalis, T. (2010). Serotonin 3A receptor subtype as an early and protracted marker of cortical interneuron subpopulations. Cereb. Cortex *20*, 2333–2347.

Walker, F. (2016). Functional connectivity of layer II/III and V GABAergic Martinotti cells in the primary somatosensory (barrel) cortex of mice [dissertation]. Georg. Univ. Sch. Sci.

Wang, K., Sun, W., Richie, C.T., Harvey, B.K., Betzig, E., and Ji, N. (2015). Direct wavefront sensing for high-resolution in vivo imaging in scattering tissue. Nat. Commun. *6*, 7276.

Wang, Y., Gupta, A., Toledo-Rodriguez, M., Wu, C.Z., and Markram, H. (2002). Anatomical, physiological, molecular and circuit properties of nest basket cells in the developing somatosensory cortex. Cereb. Cortex *12*, 395–410.

Wang, Y., Toledo-Rodriguez, M., Gupta, A., Wu, C., Silberberg, G., Luo, J., and Markram, H. (2004). Anatomical, physiological and molecular properties of Martinotti cells in the somatosensory cortex of the juvenile rat. J. Physiol. *561*, 65–90.

Wilent, W.B., and Contreras, D. (2005). Dynamics of excitation and inhibition underlying stimulus selectivity in rat somatosensory cortex. Nat. Neurosci. *8*, 1364–1370.

Williams, S.R., and Mitchell, S.J. (2008). Direct measurement of somatic voltage clamp errors in central neurons. Nat. Neurosci. *11*, 790–798.

Wilson, D.E., Smith, G.B., Jacob, A.L., Walker, T., Dimidschstein, J., Fishell, G., and Fitzpatrick, D. (2017). GABAergic Neurons in Ferret Visual Cortex Participate in Functionally Specific Networks. Neuron *93*, 1058–1065.e4.

Wilson, N.R., Runyan, C. a., Wang, F.L., and Sur, M. (2012). Division and subtraction by distinct cortical inhibitory networks in vivo. Nature *488*, 1–6.

Wimmer, V.C., Bruno, R.M., de Kock, C.P.J., Kuner, T., and Sakmann, B. (2010). Dimensions of a Projection Column and Architecture of VPM and POm Axons in Rat Vibrissal Cortex. Cereb. Cortex *20*, 2265–2276.

Wise, S.P., and Jones, E.G. (1977). Cells of origin and terminal distribution of descending projections of the rat somatic sensory cortex. J. Comp. Neurol. *175*, 129–157.

Wiser, a K., and Callaway, E.M. (1996). Contributions of individual layer 6 pyramidal neurons to local circuitry in macaque primary visual cortex. J. Neurosci. *16*, 2724–2739.

Wohrer, A., Humphries, M.D., and Machens, C.K. (2013). Population-wide distributions of neural activity during perceptual decision-making. Prog. Neurobiol. *103*, 156–193.

Womelsdorf, T., Valiante, T. a, Sahin, N.T., Miller, K.J., and Tiesinga, P. (2014). Dynamic circuit motifs underlying rhythmic gain control, gating and integration. Nat. Neurosci. *17*, 1031–1039.

Woodruff, A.R., Anderson, S.A., and Yuste, R. (2010). The Enigmatic Function of Chandelier Cells. Front. Neurosci. *4*, 1–11.

Woodruff, a. R., McGarry, L.M., Vogels, T.P., Inan, M., Anderson, S. a., and Yuste, R. (2011). State-Dependent Function of Neocortical Chandelier Cells. J. Neurosci. *31*, 17872–17886.

Wright, N., and Fox, K. (2010). Origins of cortical layer V surround receptive fields in the rat barrel cortex. J. Neurophysiol. *103*, 709–724.

Wu, C., Ivanova, E., Zhang, Y., and Pan, Z.H. (2013). rAAV-Mediated Subcellular Targeting of Optogenetic Tools in Retinal Ganglion Cells In Vivo. PLoS One *8*, 1–10.

Xiang, Z., Huguenard, J.R., and Prince, D. a (1998). Cholinergic Switching Within Neocortical Inhibitory Networks. Science (80-.). *281*, 985–988.

Xiang, Z., Huguenard, J.R., and Prince, D. a (2002). Synaptic inhibition of pyramidal cells evoked by different interneuronal subtypes in layer v of rat visual cortex. J. Neurophysiol. *88*, 740–750.

Xing, D., Yeh, C.-I., Burns, S., and Shapley, R.M. (2012). Laminar analysis of visually evoked activity in the primary visual cortex. Proc. Natl. Acad. Sci. U. S. A. *109*, 13871–13876.

Xu, X., and Callaway, E.M. (2009). Laminar specificity of functional input to distinct types of inhibitory cortical neurons. J. Neurosci. *29*, 70–85.

Xu, H., Jeong, H.Y., Tremblay, R., and Rudy, B. (2013). Neocortical Somatostatin-Expressing GABAergic Interneurons Disinhibit the Thalamorecipient Layer 4. Neuron *77*, 155–167.

Xu, N., Harnett, M.T., Williams, S.R., Huber, D., O'Connor, D.H., Svoboda, K., and Magee, J.C. (2012). Nonlinear dendritic integration of sensory and motor input during an active sensing task. Nature *492*, 247–251.

Xu, X., Roby, K.D., and Callaway, E.M. (2010). Immunochemical characterization of inhibitory mouse cortical neurons: Three chemically distinct classes of inhibitory cells. J. Comp. Neurol. *518*, 389–404.

Xue, M., Atallah, B. V., and Scanziani, M. (2014). Equalizing excitation–inhibition ratios across visual cortical neurons. Nature *511*, 596–600.

Yamawaki, N., and Shepherd, G.M.G. (2015). Synaptic circuit organization of motor corticothalamic neurons. J. Neurosci. *35*, 2293–2307.

Yang, H., Kwon, S.E., Severson, K.S., and O'Connor, D.H. (2016). Origins of choice-related activity in mouse somatosensory cortex. Nat. Neurosci. *19*.

Yavorska, I., and Wehr, M. (2016). Somatostatin-Expressing Inhibitory Interneurons in Cortical Circuits. Front. Neural Circuits *10*, 1–18.

Ye, Z., Mostajo-Radji, M.A., Brown, J.R., Rouaux, C., Tomassy, G.S., Hensch, T.K., and Arlotta, P. (2015). Instructing Perisomatic Inhibition by Direct Lineage Reprogramming of Neocortical Projection Neurons. Neuron *88*, 475–483.

Yoshimura, Y., and Callaway, E.M. (2005). Fine-scale specificity of cortical networks depends on inhibitory cell type and connectivity. Nat. Neurosci. *8*, 1552–1559.

Yoshimura, Y., Dantzker, J., and Callaway, E. (2005). Excitatory cortical neurons form fine-scale functional networks. Nature *433*.

Yu, J., Gutnisky, D.A., Hires, S.A., and Svoboda, K. (2016). Layer 4 fast-spiking interneurons filter thalamocortical signals during active somatosensation. Nat. Neurosci. *19*, 1647–1657.

Zagha, E., Casale, A.E., Sachdev, R.N.S., McGinley, M.J., and McCormick, D. a (2013). Motor cortex feedback influences sensory processing by modulating network state. Neuron *79*, 567–578.

Zarrinpar, A., and Callaway, E.M. (2014). Functional Local Input to Layer 5 Pyramidal Neurons in the Rat Visual Cortex. Cereb. Cortex bhu268-.

Zeisel, A., Manchado, A.B.M., Codeluppi, S., Lonnerberg, P., La Manno, G., Jureus, A., Marques, S., Munguba, H., He, L., Betsholtz, C., et al. (2015). Cell types in the mouse cortex and hippocampus revealed by single-cell RNA-seq. Science (80-.). *347*, 1138–1142.

Zhang, S., Xu, M., Kamigaki, T., Hoang Do, J.P., Chang, W.-C., Jenvay, S., Miyamichi, K., Luo, L., and Dan, Y. (2014). Long-range and local circuits for top-down modulation of visual cortex processing. Science *345*, 660–665.

Zhou, Y., Liu, B. hua, Wu, G.K., Kim, Y.J., Xiao, Z., Tao, H.W., and Zhang, L.I. (2010). Preceding Inhibition Silences Layer 6 Neurons in Auditory Cortex. Neuron *65*, 706–717.

Zmarz, P., and Keller, G.B. (2016). Mismatch Receptive Fields in Mouse Visual Cortex. Neuron *92*, 766–772.

Znamenskiy, P., and Zador, A.M. (2013). Corticostriatal neurons in auditory cortex drive decisions during auditory discrimination. Nature *497*, 482–485.

Znamenskiy, P., Kim, M.-H., Muir, D.R., Iacaruso, M.F., Hofer, S.B., and Mrsic-Flogel, T.D. (2018). Functional selectivity and specific connectivity of inhibitory neurons in primary visual cortex. bioRxiv 294835.

Endnotes

[A] For haircuts and straight-talk
[B] For being able to tolerate living with me
[C] For being one of the most fun people I know; I once described you as being a lot like me, except with cats, a Nintendo, and more attitude.
[D] For being unfalteringly kind and cheerful
[E] For being an incredible source of inspiration, wisdom, love, and support; for unfailingly seeking out and fighting for what is good in the world; for reminding me to see beauty in the world and in us.
[F] For getting my back at tough times for the last 15 years, and for cooking me the best meal I've ever had.
[G] For all your help in the lab, and for putting up with my tempestuously disorganized behavior
[H] For being on the dreamteam
[I] For greeting me with a small smile at the exact moment I came up for air; for finding the best and the worst in me; for sharing wonder and wanderlust
[J] One million dollars. For being an incredible friend and one of the best and kindest people I know. You are one of the best daily influences on me.
[K] For being a longtime friend and confidant
[L] For your advice, friendship, and (excessively) erudite witticisms
[M] For sharing ideas, whiskey, and an unhealthy interest in whiskers with me
[N] For looking out for me and infusing novelty into my life
[O] For teaching me to climb; for being the chairman
[P] For being the brother I never had; for remembering the things that I forget; for generally thinking about others a lot
[Q] For being able to tolerate living with me *and* working with me
[R] For being a worthy adversary; for being someone who makes every situation more fun with her presence
[S] For being thoughtful, honest, and frank; for giving a damn about the people around you and for giving a damn about doing good science
[T] For being one of the smartest and most compassionate people I know; for having a good sense of humor, for embracing teachable moments like when I'm using the word 'ergodic' or 'zeitgeist' incorrectly
[U] For having a strong moral compass; for your humor and honest insight; for teaching me to throw a flick
[V] For being hard-working and generous; for being a rock in the lab and a stalwart friend; for being professor science.
[W] For smiling every day; for helping me remember to not take life too seriously
[X] For reminding me that we are not alone.
[Y] For advice and friendship over the years; for being a pushover in chess
[Z] For your incredible drive and work ethic; for teaching me a great deal that I did not know; for always watching and listening thoughtfully; for calling things out; for thinking mapping is cool
[AA] For your humor and quiet, grgly goodwill
[BB] For being a hard worker, a good friend and a good listener
[CC] For love and support; for finding beauty in the small good things in the world; for being one of the best people I've ever known
[DD] For your goodwill and good humor; for being social glue and always getting lunch; for noticing when things are wrong; for throwing ball with me; for helping me stay sane
[EE] For the nicknames
[FF] Ryan, Cara, Jack, Uncle Ken, and Auntie Donna; for basically being my second nuclear family
[GG] Far too many Nakas, Huttars, and various permutations thereof to possibly name! I love you all.
[HH] The neurofiends
[II] Hell on Wheels
[JJ] To everyone I need to thank but don't realize I need to thank
[KK] For being a warm and loving spirit through many years; for making me feel at home whenever I see you
[LL] I'm so happy to live near you and it's been such an incredible joy to grow to be friends with you (even if it took a while). I'm awed by your compassion for other people and your enthusiasm for life. When I describe you to other people, I say that you're a lot like me, but cooler.
[MM] To gardengnomes and squeeb: I'm so impressed by the people you have become. I've watched you grow into two of the smartest, kindest, and most clever people I know. And I love how you are both incredible goofballs, each in your own way. Be good.